Study of the Quasielastic ^{3}He(e,e′p) Reaction at $Q^2 = 1.5$ (GeV/c)^2 up to Missing Momenta of 1 GeV/c

by

Marat M. Rvachev

Submitted to the Department of Physics
in partial fulfillment of the requirements for the degree of

Doctor of Philosophy

at the

MASSACHUSETTS INSTITUTE OF TECHNOLOGY

September 2003

Author . . . .
Department of Physics
July 18, 2003

Certified by . . . .
William Bertozzi
Professor of Physics
Thesis Supervisor

Certified by . . . .
Dr. Shalev Gilad
Principal Research Scientist
Thesis Co-Supervisor

Accepted by . . . .
Prof. Thomas J. Greytak
Associate Department Head for Education

Study of the Quasielastic ^{3}He(e,e$'$p) Reaction at $Q^2 = 1.5$ (GeV/c)^2 up to Missing Momenta of 1 GeV/c

by

Marat M. Rvachev

Submitted to the Department of Physics
on July 18, 2003, in partial fulfillment of the
requirements for the degree of
Doctor of Philosophy

Abstract

As a part of the E89044 experiment at Hall A of Jefferson Lab, we have studied the quasielastic ^{3}He(e,e$'$p) reaction in perpendicular coplanar kinematics, with energy and momentum transfer by the electron fixed at 837 MeV and 1500 MeV/c respectively, at three beam energies of 1255, 1954 and 4807 MeV. ^{3}He(e,e$'$p)D and ^{3}He(e,e$'$p)pn cross sections and distorted spectral functions were measured up to missing momenta of 1000 MeV/c, and, for the three-body breakup channel, up to missing energy of 30 MeV. The A_{TL} asymmetry, R_T and R_{TL} response functions, and the combination $R_L + R_{TT}V_{TT}/V_L$ of response functions were separated for the ^{3}He(e,e$'$p)D reaction channel up to missing momenta of 550 MeV/c.

In the low missing momentum regime, measured ^{3}He(e,e$'$p)D cross sections agree with available calculations based on variational ground state wave functions, and disagree with calculations based on Faddeev-type ground state wave functions. For missing momenta from 100 to 740 MeV/c, strong final state interaction effects, in general consistent with Glauber-type and diagrammatic calculations, are observed. On a finer detail, meson exchange currents, isobaric currents and dynamical relativistic effects might be isolated with further theoretical work, in view of remaining disagreements between available calculations and the measurements. For missing momenta from 740 to 1000 MeV/c, measured ^{3}He(e,e$'$p)D cross sections are more than an order of magnitude greater than predicted by available theories. Further theoretical work is needed for understanding the nature of processes in this region.

Thesis Supervisor: William Bertozzi
Title: Professor of Physics

Thesis Co-Supervisor: Dr. Shalev Gilad
Title: Principal Research Scientist

Contents

List of Figures

List of Tables

Chapter 1

Introduction

1.1 Motivation of the experiment

The recent achievement of the 100% duty factor, high-current and high-energy electron beam at the Jefferson Laboratory (e.g., [1]) is helping to overcome the traditional limitation of electron scattering, weakness of electromagnetic interaction of the electron probe with nuclei. Thus, one can fully utilize advantages of electron scattering – low distortion of the incident and scattered electron waves in the nucleus, ease of interpretation of the scattering process in the well-grounded (for light and medium nuclei) one-photon exchange approximation, and kinematic flexibility of the reaction by which one can vary energy and momentum transfer to the nucleus independently.

The ^{3}He nucleus belongs to the group of light nuclei studied for their simple-to-intermediate position in the nuclear systems. The deuteron, the simplest system of bound nucleons, is a basic testing ground for realistic nucleon-nucleon (NN) potentials derived from NN scattering data [2, 3]. Low deuteron density limits possible medium modifications of the bound nucleons; still, subnucleonic degrees of freedom, manifested as meson exchange currents, have been identified to play a significant role [2, 3]. In the quasielastic regime, meson exchange currents are unimportant relative to single-particle aspects of the reaction, and the deuteron is used for study of the electromagnetic structure of the neutron.

As a more tightly bound system, ^{3}He nucleus is better suited for study of structural modifications of bound nucleons, and for investigation of short-range part of NN interaction [2, 4]. The ^{3}He nucleus provides a laboratory for studying three-body NN forces. At the same time, the ^{3}He nucleus is more susceptible to accurate theoretical calculations, compared to medium and heavy nuclei. Hence, the ^{3}He nucleus provides a unique combination of structural complexity and susceptibility to accurate theoretical treatment, setting the stage for fruitful interaction between theory and experiment.

In quasielastic ^{3}He(e,e′p) experiments, the process in which a single bound nucleon absorbs all the transferred energy and momentum is emphasized [2, 4]. Detection of both the scattered electron and the proton provides knowledge of momentum and excitation energy of the undetected residual system, allowing separation of ^{3}He(e,e′p)D and ^{3}He(e,e′p)pn reaction channels. In the first approximation, (e,e′p) experiments sample the Fourier transform of the single-nucleon wave function. Thus, with modern Faddeev and variational techniques of solution of the non-relativistic three-body problem [3], one can hope to test state-of-the-art realistic NN potentials.

However, additional effects, such as final state interactions (FSI), meson exchange currents (MEC) and relativity, have to be taken into account in data interpretation, providing another testing ground for theoretical models [2, 4]. Normally, experimentalists try to avoid kinematic settings with large expression of FSI and MEC, to have an unobstructed access to the nucleon wave function. This has proved not to be an easy task, with earlier predictions of both FSI and MEC suppressed in a high momentum transfer quasielastic regime, and the current view that MEC are indeed suppressed but FSI are enhanced in this regime [5]. For the ^{3}He(e,e′p) reaction, FSI can be treated precisely in the non-relativistic Faddeev three-body calculations [2, 3, 4]. However, at high ($\gtrsim$ 1 GeV/c) momenta of the knocked-out proton the more relevant treatments are the Laget's diagrammatic expansion [6], Glauber-type [7] and other eikonal approximations [8].

Relativistic effects are expected to manifest themselves at high ($Q^2 \gtrsim 1$ (GeV/c)^2) momentum transfers, in particular in the TL interference term [2, 9]. Fully relativistic calculations of the ^{3}He ground state and the knockout process are not currently available, but various degrees of inclusion of relativity, such as the treatment of the nucleon current operator relativistically [10, 11] and corrections to the bound and scattered nucleon wave functions [10, 11], are becoming available.

Up to now, quasielastic ^{3}He(e,e$'$p) experiments have provided data with momentum transfers up to 700 MeV/c and recoil momenta up to 600 MeV/c. However, a strong motivation exists to expand exploration of the reaction in the following directions:

1. One would like to increase the momentum transfer (decrease wavelength of the exchanged photon), to test limits of nucleonic models of nuclear structure and to search for possible hadronic and quark degrees of freedom.

2. One would like to map out the components of the nucleon wave function at as high a momentum as possible, in view of study of short-range part of NN interaction.

3. One would like to vary the momentum transfer to the nucleus over a wide range, while keeping the recoil momentum fixed. These measurements can help one understand whether the electromagnetic structure of nucleons is modified in the nuclear medium (one would extract an analog of the electromagnetic form factor for the bound nucleon and compare it to the electromagnetic form factor of the free nucleon).

4. High-precision and systematic studies of the reaction, including separation of response functions, are desirable, to help disentangle various reaction mechanisms.

With these aims in mind, the E89044 experiment at Hall A of the Jefferson Laboratory was planned. This thesis reports on the E89044 measurements in quasielastic perpendicular kinematics, at fixed energy and at a momentum transfer of 837 MeV and 1500 MeV/c. The ^{3}He(e,e$'$p)D and ^{3}He(e,e$'$p)pn cross sections and distorted spectral functions were measured up to recoil momenta of 1000 MeV/c, with the ^{3}He(e,e$'$p)D response functions and A_{TL} asymmetry separated up to recoil momenta

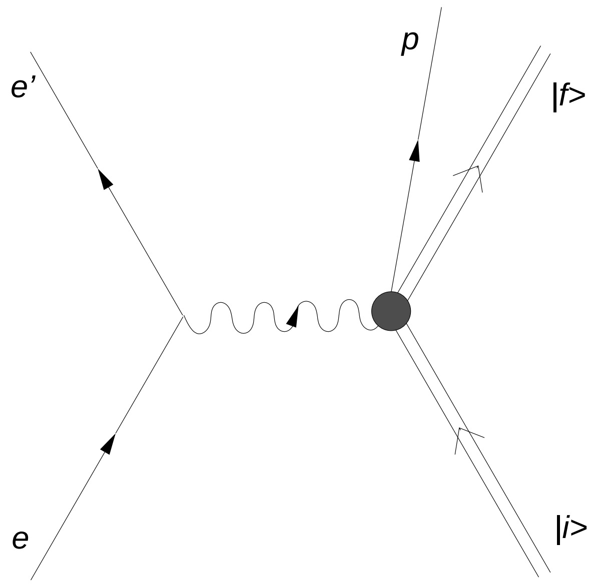

Figure 1-1: Feynman diagram for the (e,e′p) reaction in one-photon exchange approximation.

of 550 MeV/c. The ^{3}He(e,e′p)pn measurements reported in this thesis are only up to missing energy of 30 MeV, measurements above 30 MeV, as well as analysis of the parallel kinematic settings of the E89044 experiment, are reported elsewhere [12, 13].

Nuclear Physics is well-known for its great variety of theoretical models, with some based on fundamental physical laws, some on approximations, some on phenomenology, or on combinations of the above. Rephrasing Russian physicist and Nobel Laureate P. L. Kapitza: "Theories come and go, but a correct experiment stays forever." This statement seems to be very relevant to the field of Nuclear Physics, which the theorists are still trying to transform into a more fundamental and consistent form, to advance our understanding of nuclear structure.

1.2 Plane Wave Born Approximation

In Plane Wave Born Approximation (PWBA), also known as the one-photon exchange approximation, electrons incident and scattered from a nucleus are described as Dirac plane waves, with the interaction mediated by an exchange of a single virtual photon [2, 4]. A diagram of the (e,e′p) reaction in PWBA is shown in Fig. 1-1. Validity of

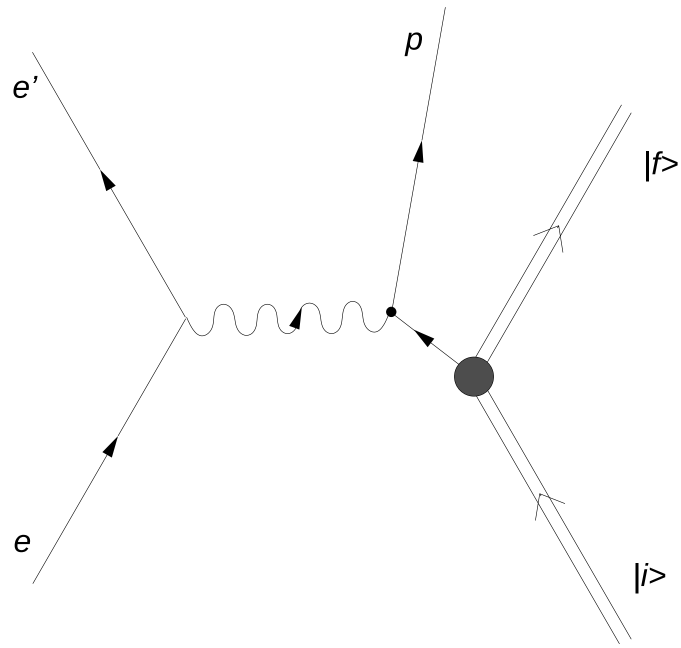

Figure 1-2: Feynman diagram for the (e,e′p) reaction in Plane Wave Impulse Approximation.

PWBA for light and medium nuclei stems from the smallness of the electromagnetic coupling constant.

Corrections to the approximation are treated in Distorted Wave Born Approximation (DWBA). One of the simplest and most useful corrections to PWBA is through substitution of the momentum transfer by the electron by an "effective momentum transfer" (Effective Momentum Approximation, EMA) [14], with the rest of PWBA formalism preserved.

1.3 Plane Wave Impulse Approximation

In Plane Wave Impulse Approximation (PWIA), in addition to the one-photon exchange approximation, it is assumed that the virtual photon is absorbed at a single bound nucleon, which leaves the nucleus without further interaction, and that this nucleon is detected in the (e,e′N) measurement (Fig. 1-2) [4]. In non-relativistic

PWIA, the six-fold differential (e,e′p) cross section factorizes as

$$\frac{d^6\sigma}{dE_f d\Omega_e dE_p d\Omega_p} = \frac{E_p p_p}{(2\pi)^3}\sigma_{ep} S(E_{miss}, \vec{P}_{miss}), \tag{1.1}$$

where σ_{ep} is the off-shell electron-nucleon cross section, $S(E_{miss}, P_{miss})$ is the spectral function, with the rest of the quantities defined in Sec. 1.4. In PWIA, the spectral function is interpreted as the probability of finding a nucleon with momentum P_{miss} and separation energy E_{miss} within the nucleus [4].

In the independent particle model (IPM) [4], the spectral function can be represented as

$$S(E_{miss}, \vec{P}_{miss}) = \sum_{\alpha} N_\alpha |\phi_\alpha(\vec{P}_{miss})|^2 \delta(E_\alpha - E_{miss}), \tag{1.2}$$

where $\phi_\alpha(\vec{P}_{miss})$ is the nucleon wave function in the momentum representation, E_α is the corresponding energy eigenvalue, and N_α is the occupation number, all for orbital α.

1.4 Definition of kinematic variables

In the present experiment, the reaction under study is the true coincidence ^{3}He(e,e′p) reaction, in which the incident electron, detected electron and detected proton are involved in a reaction on the same ^{3}He nucleus. A schematic view of the ^{3}He(e,e′p) reaction is shown in Fig. 1-3. Using a standard notation, we designate four-momenta, total energies and three-momenta of the participants of the reaction, in the laboratory coordinate system, as:

incident electron: $k_i = (E_i, \vec{k}_i)$,

detected electron: $k_f = (E_f, \vec{k}_f)$,

detected proton: $p_p = (E_p, \vec{p}_p)$,

target nucleus: $p_A = (E_A, \vec{p}_A)$,

undetected residual system: $p_B = (E_B, \vec{p}_B)$,

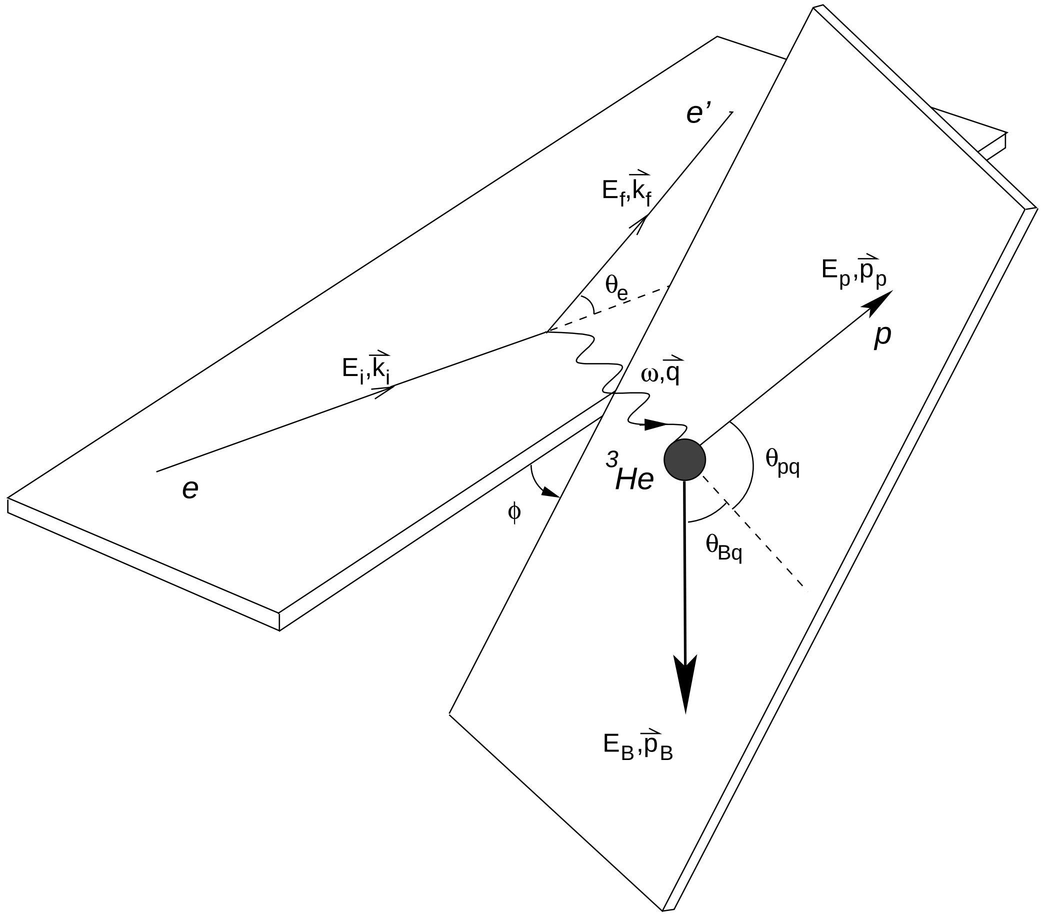

Figure 1-3: Schematic view of the ^{3}He(e,e$'$p) reaction and definition of kinematic variables.

energy-momentum transferred to the target nucleus: $q = (\omega, \vec{q})$.

The electron scattering plane is defined as the plane containing both the incident and the scattered electron; the reaction plane is defined as the plane containing the detected proton and the three-momentum transfer $\vec{q}$. The angle between the electron scattering plane and the reaction plane ("out-of-plane angle") is denoted as ϕ (Fig. 1-3); the electron scattering angle is denoted as θ_e; the angle between the three-momentum transfer $\vec{q}$ and the proton momentum $\vec{p}_p$ is denoted as θ_{pq}. The kinematic setting with $\phi = 0°$ is referred to as "in-plane forward of $\vec{q}$", or "coplanar forward of $\vec{q}$"; the kinematic setting with $\phi = 180°$ is referred to as "in-plane back of $\vec{q}$", or "coplanar back of $\vec{q}$".

In ^{3}He(e,e$'$p) measurements, the experimentally determined quantities are $\vec{k}_i$, $\vec{k}_f$ and $\vec{p}_p$. The total energy of the detected proton E_p is obtained with $E_p = \sqrt{M_p^2 + p_p^2}$, where M_p is the proton rest mass. Masses of ultra-relativistic electrons are neglected to yield $E_i = k_i$, $E_f = k_f$. Neglecting the initial momentum of the target ^{3}He nucleus yields $\vec{p}_A = \vec{0}$, $p_A = (M_A, \vec{0})$, where M_A is the rest mass of the ^{3}He nucleus.

The transferred four-momentum q is found from the energy-momentum conservation relation:

$$q = k_i - k_f = (\omega, \vec{q}). \tag{1.3}$$

It can be shown that $q^2 \leq 0$; Q^2 is defined as $Q^2 = -q^2 \geq 0$.

Missing momentum $\vec{P}_{miss}$ is defined as the three-momentum of the undetected residual nuclear system, and is found using the momentum conservation relation:

$$\vec{P}_{miss} \equiv \vec{p}_B = \vec{q} - \vec{p}_p. \tag{1.4}$$

Missing energy E_{miss}[1] is defined as

$$E_{miss} = \omega - T_p - T_B, \tag{1.5}$$

where T_p and T_B are kinetic energies of the detected proton and the residual nucleus. Missing energy can be found for each (e,e$'$p) event with

$$E_{miss} = \omega - (\sqrt{p_p^2 + M_p^2} - M_p) - (\sqrt{p_B^2 + M_B^2} - M_B). \tag{1.6}$$

One can see that the missing energy E_{miss} is related to the excitation energy of the residual nucleus with

$$E_{miss} = E_S + \epsilon^*, \tag{1.7}$$

where E_S is the energy of separation of a proton from the target nucleus A, and ϵ^* is the excitation energy of the residual nucleus B. Therefore, for the ^{3}He(e,e$'$p) reaction, the lowest possible E_{miss} value is $\sim$ 5.49 MeV (energy of separation of

[1] Also known as missing mass.

a proton from the ^{3}He nucleus), corresponding to the deuteron in the final state (reaction ^{3}He(e,e$'$p)D). Since the deuteron does not possess discrete excited states and has binding energy of $\sim$ 2.22 MeV, the continuum spectrum of allowed E_{miss} values starts at $\sim$ 7.72 MeV, corresponding to the unbound neutron and proton in the final state (reaction ^{3}He(e,e$'$p)pn). Further, at higher excitation energies ϵ^*, pions and other particles can appear in the final state.

1.5 Previous ^{3}He(e,e$'$p) measurements

Reviews of ^{3}He(e,e$'$p) measurements are available in Frullani and Mougey [4] and Kelly [2]. Here we provide references to the ^{3}He(e,e$'$p) measurements made to date [15, 16, 17, 18, 19, 20, 21, 22]. Below, several of the experiments are summarized.

The first ^{3}He(e,e$'$p) measurements were made at the Stanford Mark III linear accelerator [15, 23] using an incident electron energy of 550 MeV, in quasielastic perpendicular kinematics[2] with momentum transfer of 443.5 MeV/c. Covered missing momentum range was 0 – 100 MeV/c. The missing energy resolution was poor and prevented a clean separation of the ^{3}He(e,e$'$p)D and ^{3}He(e,e$'$p)pn reaction channels.

^{3}He(e,e$'$p) measurements at the Kharkov LUE-2000 accelerator [16] were also performed in quasielastic perpendicular kinematics at beam energies of 1200 MeV, 806 MeV and 643 MeV, with a missing energy resolution of 10 MeV, 4 MeV and 2.6 MeV respectively. The ^{3}He(e,e$'$p)D reaction channel was separated from the ^{3}He(e,e$'$p)pn reaction channel only for the 806 MeV and 643 MeV datasets. The missing momentum range of the 806 MeV and 643 MeV measurements was 0 – 100 MeV/c. Fig. 1-4 shows ^{3}He(e,e$'$p)D distorted momentum distributions extracted from the Stanford and the Kharkov data (positive q_R in the figure corresponds to the detected proton in perpendicular kinematics and back of $\vec{q}$).

The first clean separation of the ^{3}He(e,e$'$p)D reaction channel can be attributed

[2]For the ^{3}He(e,e$'$p) reaction, the quasielastic kinematics is defined by $Q^{*2} = 2M_p\omega^*$, where $Q^{*2} = |\vec{q}|^2 - \omega^{*2}$, $\omega^* = \omega - E_S$, and $E_S = 5.49$ MeV is the binding energy of a proton, and the other quantities are defined in Sec. 1.4. For large Q^2 and ω, $Q^2/(2M_p\omega) \approx 1$. In perpendicular kinematics, Q^2 and the center of mass energy of the final system W are held constant, while the recoil momentum is varied [4].

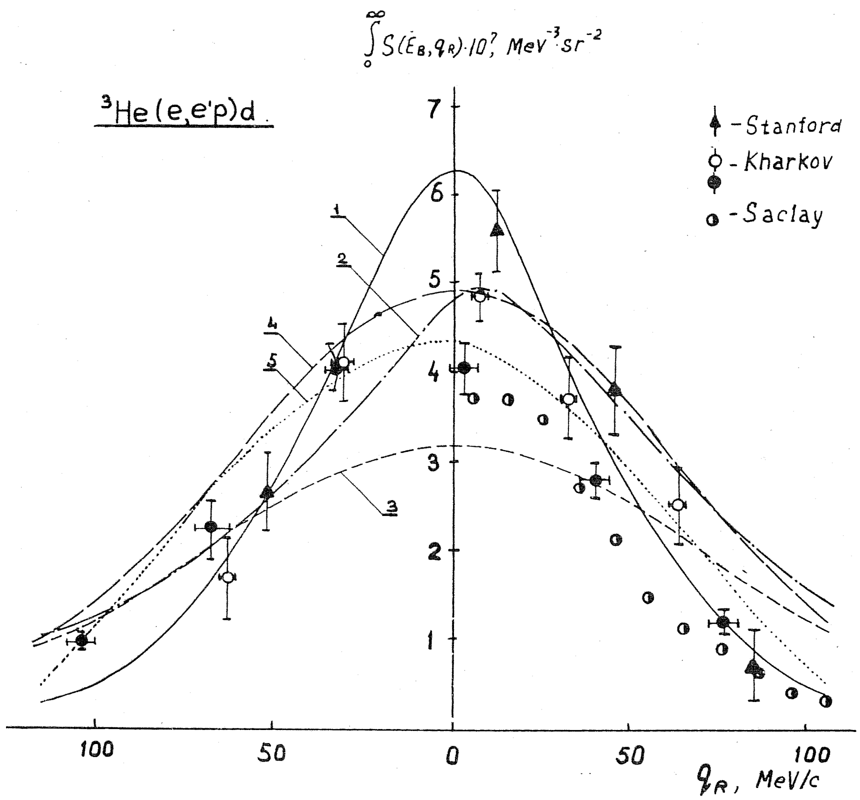

Figure 1-4: Distorted momentum distribution of proton in the ^{3}He nucleus, measured in Stanford and Kharkov prior to 1982. Figure from [16].

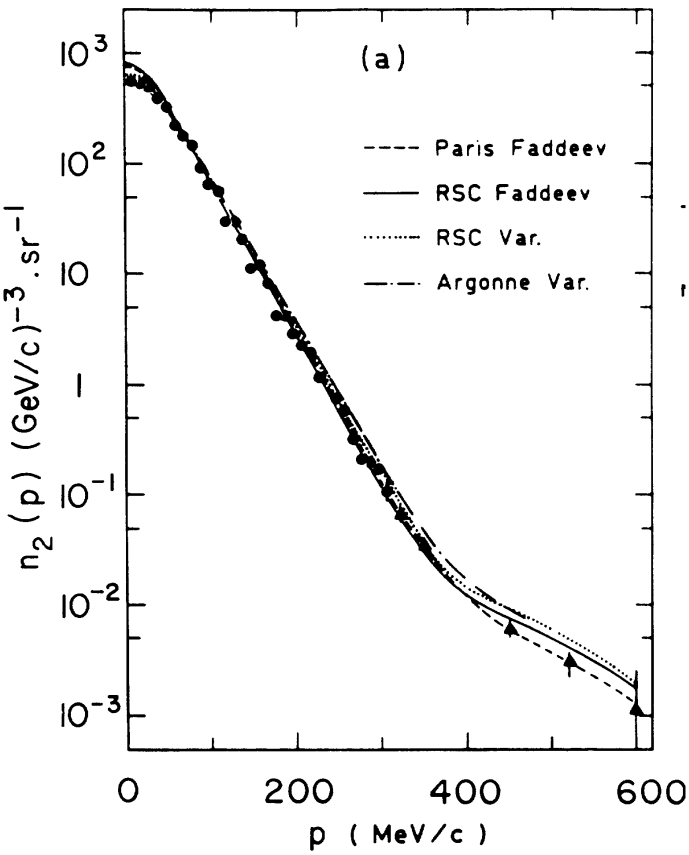

Figure 1-5: Momentum distribution of proton in ^{3}He measured in the two Saclay experiments. Figure from [19].

to a Saclay experiment [17], which achieved a missing energy resolution of 1.2 MeV. The data was collected in quasielastic perpendicular kinematics, with beam energies 509 – 528 MeV, missing momenta 0 – 310 MeV/c, with momentum transfers of 300 – 430 MeV/c.

In another Saclay experiment [19], the ^{3}He(e,e′p)D reaction channel was separated in "dip" perpendicular kinematics, with energy and momentum transfers of 200 MeV and 279 MeV/c respectively. The incident electron energy was 560 MeV, with a covered missing momentum range from 300 to 600 MeV/c. Fig. 1-5 shows the ^{3}He(e,e′p)D momentum distribution obtained in the two Saclay experiments.

Fig. 1-6 shows ^{3}He(e,e′p)D distorted momentum distribution extracted in a recent experiment at Mainz microtron MAMI [22, 24]. Richard Florizone and the Nuclear Interactions Group at MIT (W. Bertozzi, J. P. Chen, D. Dale, S. Gilad, A. J. Sarty,

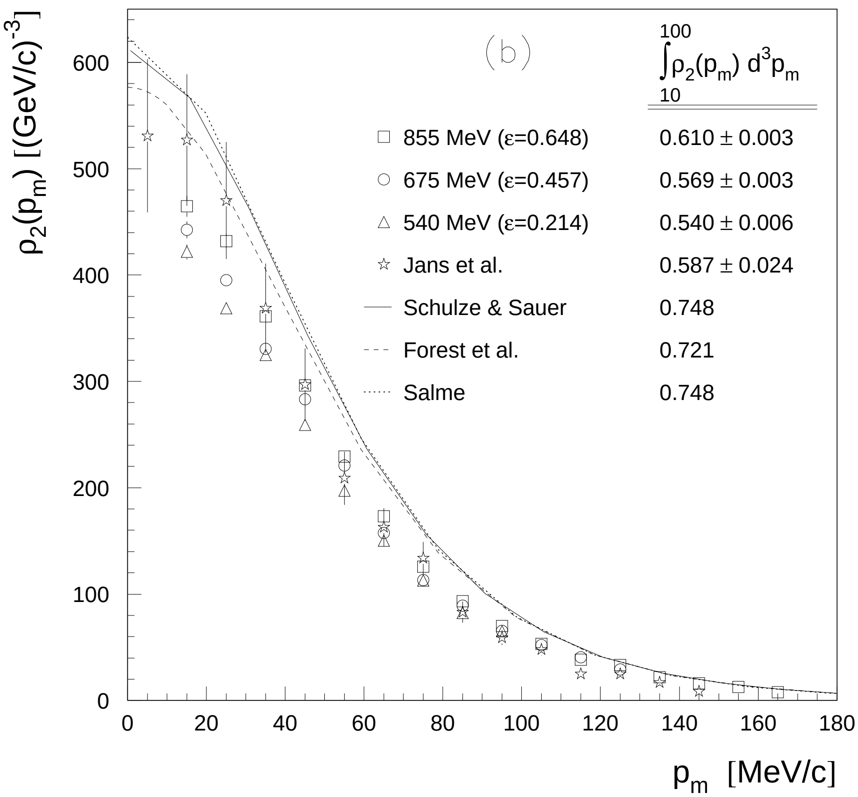

Figure 1-6: ^{3}He distorted momentum distribution obtained in Mainz experiment. Figure courtesy R. Florizone.

J. A. Templon, J. Zhao, Z.-L. Zhou, K. Fissum, J. Gao, N. Liyanage and D. Rowntree) played a leading role in planning, execution and analysis of the experiment. The measurements were made in parallel kinematics at a fixed momentum transfer of 685 MeV/c, incident electron energies of 540, 675 and 855 MeV, with a missing momentum range of 10 – 95, 10 – 125 and 10 – 165 MeV/c respectively. The ^{3}He(e,e$'$p)D reaction channel was cleanly separated from the ^{3}He(e,e$'$p)pn reaction channel. The dependence of the measured ^{3}He(e,e$'$p)D cross sections on polarization of the exchanged virtual photon was found to be described well by the cc1 prescription for the off-shell e-p cross section [25]. This observation was further confirmed by a calculation of the integral [22, 24]

$$N(\epsilon) = 4\pi \int_{10MeV/c}^{100MeV/c} \rho_2(P_{miss}) P_{miss}^2 dP_{miss},$$

where $\rho_2(P_{miss})$ is the measured momentum distribution for the ^{3}He(e,e$'$p)D reaction channel, and the limits of the integral correspond to the region of overlap of the three datasets. The values of the integral calculated for the three beam energies are shown in Fig. 1-6. The values were found to vary by $\sim$ 10% for a range of the virtual photon polarization from 0.214 to 0.648. It was concluded that the meson exchange and isobar currents are not important for the kinematics of the experiment, while the final state interactions could have an effect of an overall decrease of the ^{3}He(e,e$'$p)D cross sections by $\sim$ 10 – 20% [22, 24].

The covered missing energy range of the Mainz measurements was up to 80 MeV, but no ^{3}He(e,e$'$p)pn strength was observed at missing energies above 20 MeV. The ^{3}He(e,e$'$p)D R_L and R_T response functions were separated. As was the case for the measured ^{3}He(e,e$'$p)D cross sections, the transverse/longitudinal behavior of the response functions was found to agree with the PWIA factorization with the cc1 [22, 24].

^{3}He(e,e$'$p) data available to date showed, in general, a reasonable agreement with most PWIA Faddeev and variational calculations using realistic NN potentials, in several cases indicating that a theoretical treatment of FSI is necessary for a good description of data. The Saclay measurement in dip perpendicular kinematics [19] suggested the existence of short-range two-body correlations. Several measurements in parallel kinematics away from the quasielastic peak [20, 21] suggested suppressed R_L relative to R_T at the momentum transfers below 500 MeV/c, which only partially could be accounted for in calculations by MEC and FSI. As described above, the Mainz measurement [22, 24] in parallel kinematics at a fixed momentum transfer of 685 MeV/c found that in general the transverse/longitudinal behavior of the ^{3}He(e,e$'$p)D cross sections and R_L and R_T response functions is described well by the PWIA factorization with the cc1, and the overall $\sim$ 10 – 20% decrease in the measured ^{3}He(e,e$'$p)D strength relative to PWIA calculations was possibly due to effects of FSI.

Although a wealth of ^{3}He(e,e$'$p) data was obtained to date, the limitations of the duty factors, energies and currents of the electron beams prevented the experiments from extending the measurements above recoil momenta of about 600 MeV/c and momentum transfers of about 700 MeV/c. As described in Sec. 1.1, this regime of high recoil momenta and momentum transfers, especially in the quasielastic kinematics, is expected to yield new and intriguing information on the nucleonic models of nuclear structure, nucleon-nucleon interaction and the mechanisms of the ^{3}He(e,e$'$p) reaction.

1.6 Overview of kinematic settings and results

The ^{3}He(e,e$'$p) kinematic settings analyzed in this thesis are summarized in Table 1.1, Table 1.2 and Fig. 1-7. The data was collected at three values of beam energy, 4.8068 GeV, 1.9542 GeV and 1.2553 GeV[3,4]. At each beam energy, scattered electrons were detected by the Hall A electron spectrometer, set at a fixed scattering angle and momentum, both corresponding to the quasielastic knockout of protons with transferred momentum $|\vec{q}| = 1.5$ GeV/c and energy $\omega = 837$ MeV.

In coincidence with the scattered electron, the knocked out proton was detected by the Hall A hadron spectrometer, in perpendicular coplanar (e,e$'$p) kinematics. With $\vec{q}$ and ω fixed and coplanar detection of the knocked out proton, the requirement of observing the ^{3}He(e,e$'$p)D reaction provides a relationship between the angle and momentum of the detected proton. The central angle and momentum of the hadron spectrometer were varied while in fact keeping the ^{3}He(e,e$'$p)D reaction within the spectrometer acceptance, thus providing ^{3}He(e,e$'$p)D measurements over a range of momentum of the undetected recoil.

This thesis uses both a digit and a letter notation to designate ^{3}He(e,e$'$p) kinematic settings. The digit notation (e.g., kinematics 15) refers to an angle and momentum

[3] For convenience, in the following these values are referred to as 4.8 GeV, 1.9 GeV and 1.2 GeV.

[4] After energy loss corrections, the average energy of incident electron at the interaction vertex was 4.8055 GeV, 1.9530 GeV and 1.2538 GeV respectively.

Part 1 ^{3}He(e,e'p)d Perpendicular Kinematics

Kin #	Kin	$\vec{q}$ (GeV/c)	E_0 (GeV)	ω (GeV)	ϵ	P_m (GeV/c)	E_e (GeV)	θ_e (deg)	P_p (GeV/c)	θ_p (deg)	t (hr)
1-2	Σ_1	1.500	4.803	0.837	0.943	0.000	3.966	16.40	1.500	48.30	0.7
3	Σ_3	1.500	1.254	0.837	0.108	0.000	0.417	118.72	1.500	14.13	1.3
4	Σ_1	1.500	4.803	0.837	0.943	0.150	3.966	16.40	1.493	54.04	0.9
5	Σ_2	1.500	4.803	0.837	0.943	0.150	3.966	16.40	1.493	42.56	0.7
6	Σ_3	1.500	1.254	0.837	0.108	0.150	0.417	118.72	1.493	19.87	3.4
7	Σ_1	1.500	4.803	0.837	0.943	0.300	3.966	16.40	1.472	59.83	10.1
8	Σ_2	1.500	4.803	0.837	0.943	0.300	3.966	16.40	1.472	36.76	6.6
9	Σ_3	1.500	1.254	0.837	0.108	0.300	0.417	118.72	1.472	25.67	33.3
10	Σ_1	1.500	4.803	0.837	0.943	0.425	3.966	16.40	1.444	64.76	19.9
11	Σ_2	1.500	4.803	0.837	0.943	0.425	3.966	16.40	1.444	31.84	15.5
12	Σ_3	1.500	1.254	0.837	0.108	0.425	0.417	118.72	1.444	30.59	64.6
13	Σ_1	1.500	4.803	0.837	0.943	0.550	3.966	16.40	1.406	69.80	35.2
14	Σ_2	1.500	4.803	0.837	0.943	0.550	3.966	16.40	1.406	26.79	42.8
15	Σ_3	1.500	1.254	0.837	0.108	0.550	0.417	118.72	1.406	35.63	122.0

Part 1a ^{3}He(e,e'p)d Very High Pm in Perpendicular Kinematics

Kin #	Kin	$\vec{q}$ (GeV/c)	E_0 (GeV)	ω (GeV)	ϵ	P_m (GeV/c)	E_e (GeV)	θ_e (deg)	P_p (GeV/c)	θ_p (deg)	t (hr)
28	Σ_1	1.500	4.803	0.837	0.943	0.750	3.966	16.40	1.327	78.28	23.0
29	Σ_1	1.500	4.803	0.837	0.943	1.000	3.966	16.40	1.171	89.95	23.0

Part 2 ^{3}He(e,e'p)d 3rd epsilon value in Perpendicular Kinematics

Kin #	Kin	$\vec{q}$ (GeV/c)	E_0 (GeV)	ω (GeV)	ϵ	P_m (GeV/c)	E_e (GeV)	θ_e (deg)	P_p (GeV/c)	θ_p (deg)	t (hr)
33	Σ_4	1.500	1.953	0.837	0.615	0.000	1.117	49.87	1.500	34.69	1.2
34	Σ_4	1.500	1.953	0.837	0.615	0.150	1.117	49.87	1.493	40.43	3.5
35	Σ_5	1.500	1.953	0.837	0.615	0.150	1.117	49.87	1.493	28.95	2.9

Table 1.1: Kinematic settings analyzed in this thesis. Given are nominal values of spectrometer settings, beam energies and other kinematic parameters. Table courtesy Jean Mougey, Grenoble, France.

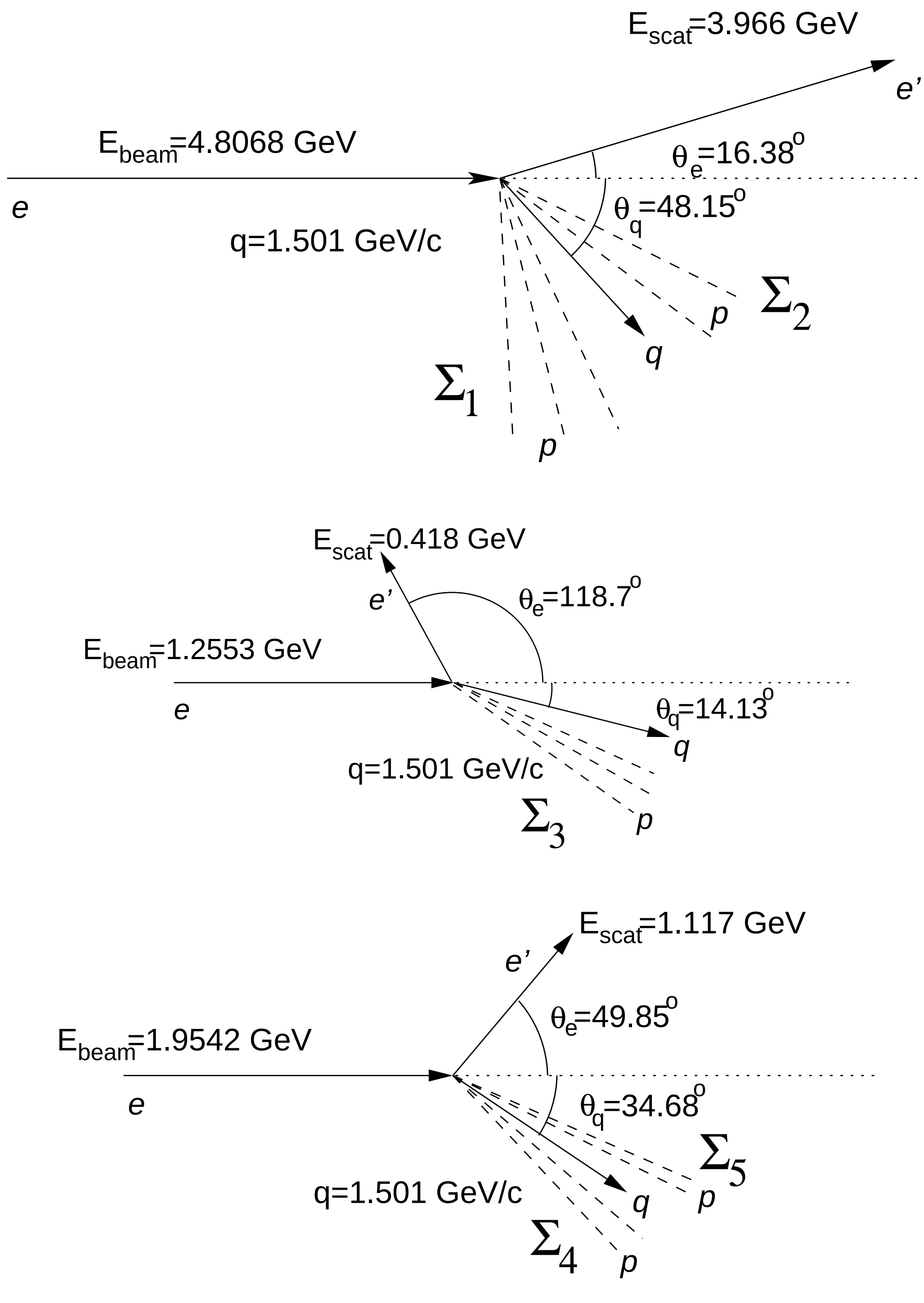

Figure 1-7: Graphical view of kinematic settings analyzed in this thesis. Given are actual beam energies and central angles and momenta of the electron spectrometer.

Kinematics	Beam energy GeV	Forw/back of $\vec{q}$	P_{miss} range MeV
Σ_1	4.8	back	0 – 1000
Σ_2	4.8	forw	0 – 550
Σ_3	1.2	back	0 – 550
Σ_4	1.9	back	0 – 150
Σ_5	1.9	forw	0 – 150

Table 1.2: Missing momentum ranges of measured ^{3}He(e,e$'$p)D and ^{3}He(e,e$'$p)pn cross sections and distorted spectral functions.

setting of both electron and hadron spectrometers, and is defined in the first column of Table 1.1. The letter notation (Σ_1, Σ_2, Σ_3, Σ_4, or Σ_5) is used to designate a beam energy, and whether the proton was detected forward (closer to the beam dump) or back from the momentum transfer $\vec{q}$. The letter notation is defined in the second column of Table 1.1, in Table 1.2 and in Fig. 1-7. Hence, a "Σ_n" kinematic setting contains several "digit" kinematic (spectrometer) settings, with the correspondence following from Table 1.1.

^{3}He(e,e$'$p)D and ^{3}He(e,e$'$p)pn cross sections and distorted spectral functions were extracted as a function of P_{miss} at all spectrometer settings (covered ranges of P_{miss} at each beam energy are given in Table 1.2). ^{3}He three-body breakup data was analyzed only up to $E_{miss} = 30$ MeV, E89044 data above $E_{miss} = 30$ MeV is the subject of thesis of Fatiha Benmokhtar [12]. Data collected at Σ_1, Σ_2 and Σ_3 settings was used for separation of ^{3}He(e,e$'$p)D R_T, R_{TL} and $R_L + V_{TT}R_{TT}/V_L$ response functions up to P_{miss} of 550 MeV/c. Σ_4 and Σ_5 data (the beam energy of 1.9 GeV) provided a check of systematic errors in the separation procedure with the Rosenbluth technique [4], up to P_{miss} of 150 MeV/c. A_{TL} asymmetry for the ^{3}He(e,e$'$p)D reaction was extracted from Σ_1 and Σ_2 data (the beam energy of 4.8 GeV) up to P_{miss} of 550 MeV/c.

Parallel kinematics data collected by the E89044 experiment is the subject of thesis of Emilie Penel [13].

Chapter 2

Experimental setup

The E89044 experiment was performed at the Thomas Jefferson National Accelerator Facility (TJNAF, or Jefferson Lab), also known as CEBAF (Continuous Electron Beam Accelerator Facility), located in Newport News, Virginia. The facility features a continuous wave 6 GeV electron accelerator and three state-of-the-art experimental halls. The experiment ran in Hall A, from December of 1999 until April of 2000, and used standard Hall A equipment: systems for measurement of properties and manipulation of the incoming electron beam; a high-power unpolarized ^{3}He target; a set of solid targets for auxiliary measurements; and, two high-resolution magnetic spectrometers with associated detector packages and data acquisition systems. In this chapter an overview of the experimental apparatus, as employed by the E89044, is presented. A more detailed discussion of JLab and Hall A instrumentation is available in [26, 27].

2.1 CEBAF accelerator

The accelerator was approved for construction in 1987 and became operational in 1994 [1]. It was designed to provide the nuclear physics community with a state-of-the-art laboratory for studying the nuclear structure. As such, its design combined the latest achievements in the accelerator technology to produce a continuous, high energy, high current, and high polarization electron beam.

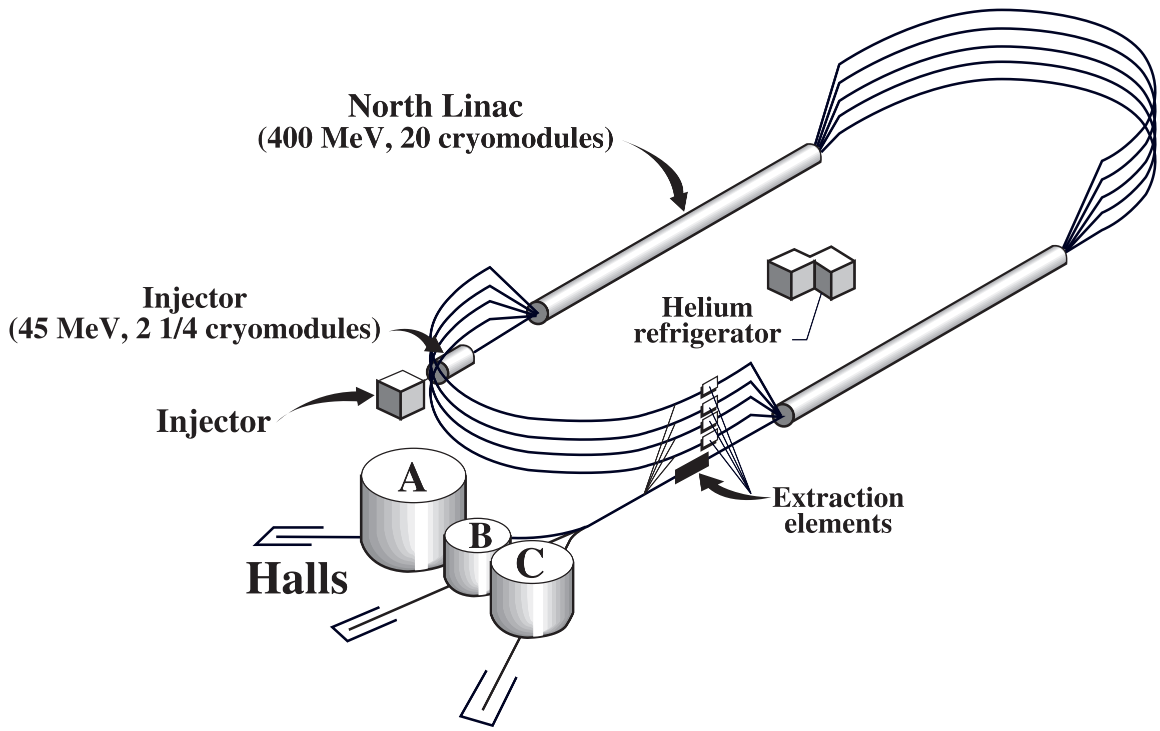

Figure 2-1: Schematic layout of JLab accelerator.

A schematic layout of the accelerator is shown in Fig. 2-1. The accelerator has the form of a racetrack, with accelerating structures located 10 m below ground. Unpolarized electrons are delivered from a conventional thermionic gun, while polarized electrons are knocked-out from a GaAs photocathode by an infrared laser. The electrons are accelerated to 45 MeV in the injector, and are directed into the first (North) linac. In the linac electrons are accelerated by the electric field of 1497 MHz microwaves injected in superconducting niobium cavities. The cavities are kept at a temperature of $\sim 2^\circ$ K by superfluid ^{4}He bathing their outside surfaces. The superconducting state of the cavities allows the transfer of almost the entire microwave power into the acceleration of the beam.

After acceleration in the first linac, electrons with different energies are magnetically separated, magnetically recirculated by 180°, and injected in the second (South) linac. The second linac uses the same principle of acceleration as the first linac. At the exit from the second linac, electrons with different energies are again separated, recirculated and again injected in the first linac. The process can be repeated for up to 5 total passes of the electrons through the accelerator, each pass increasing the energy of the electrons by a maximum of 1.2 GeV. After each pass the electrons can be directed into an experimental hall.

Due to the relatively low electron mass, $\approx$ 0.5 MeV/c^2, electrons with different energies move through the linacs at close velocities (close to the speed of light, $c \approx 3 \cdot 10^8$ m/s), and are accelerated together in the same electron packets. The distance between the moving packets is $3{\cdot}10^8$ m/s / 1497 MHz $\approx$ 20 cm, which is equal to the longitudinal periodicity of the cavity shape; the length of the electron packets is $\sim$ 0.5 mm.

At the time of this writing, the Jefferson Lab accelerator provides the Hall A with a high-quality continuous-wave electron beam with energies in the range of 0.8 – 6 GeV (in multipass operation), currents of 1 – 190 μA, beam energy spread $\sigma_E/E < 5{\cdot}10^{-5}$, and > 70% polarization for currents up to 100 μA. The E89044 experiment collected data at 7 beam energies in the range of 0.644 – 4.8 GeV, currents of 1 – 140μA, with the beam polarization not required (in the study of the ^{3}He(e,e$'$p) reaction) and averaged over by a 30 Hz beam helicity reversal.

2.2 Hall A

A schematic layout of the experimental Hall A is shown in Fig. 2-2. The hall is circular in shape, with a diameter of 53 m and a height of about 20 m. The electron beam enters the hall in a vacuum pipe, and passes through several quadrupole magnets and through systems for beam rastering and measurement of beam current, position and energy. Just before reaching the center of the hall, the electron beam enters a cylindrical aluminum scattering chamber. The scattering chamber contains a vertical assembly of targets. The whole assembly inside the chamber can be remotely moved in the vertical direction, exposing the desired target to the beam.

The majority of electrons in the beam do not substantially interact with the material in the scattering chamber and pass through to a shielded beam dump. Some of the scattered electrons and knocked-out protons enter either of the two high resolu-

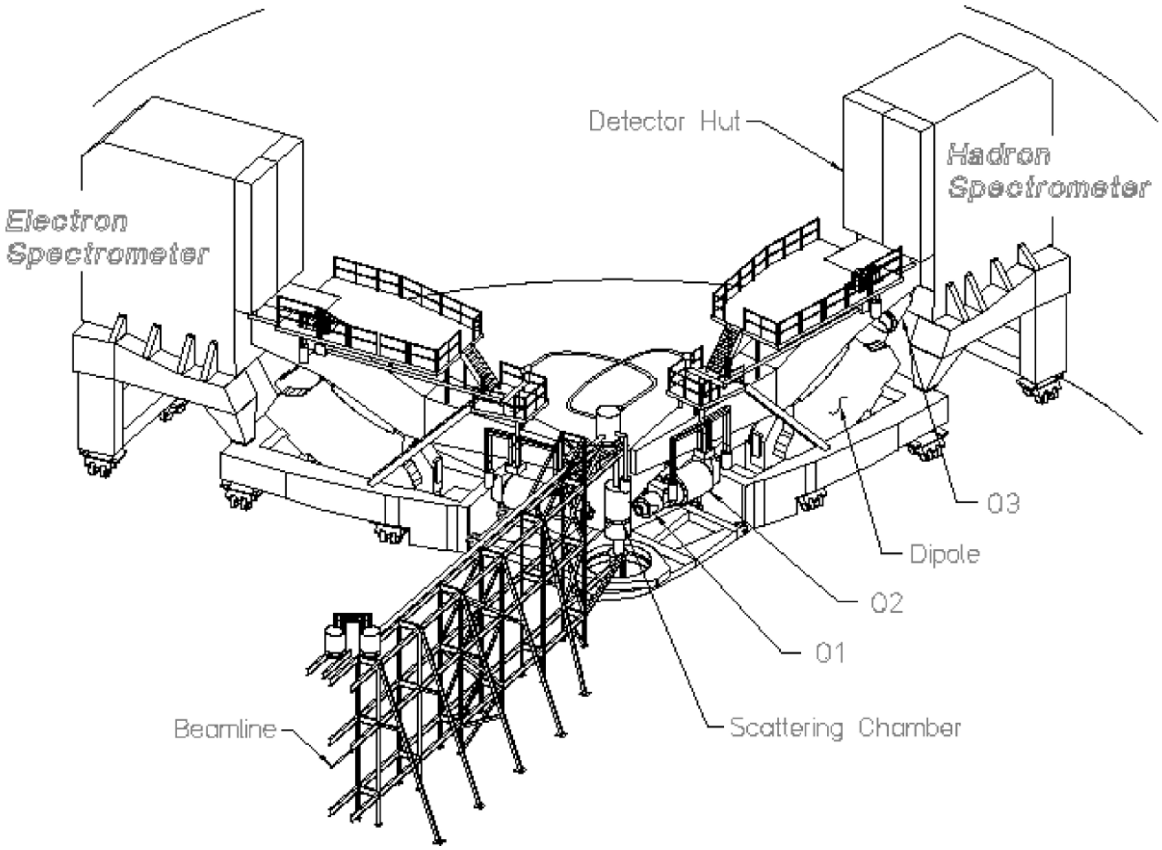

Figure 2-2: Schematic layout of Hall A.

tion magnetics spectrometers, labeled electron high resolution spectrometer (HRSE) and hadron high resolution spectrometer (HRSH). The spectrometers are used for measurement of particle trajectories, momenta, relative timing, and for particle identification.

2.3 Beamline

2.3.1 Beam position monitors

The beam position monitor (BPM) is a device for non-invasive continuous measurement of the position of the beam. Each of the employed BPMs has a cavity with four antennae, each oriented parallel to the nominal beam direction and located symmetrically around the nominal beam position (Fig. 2-3). The electron beam passing

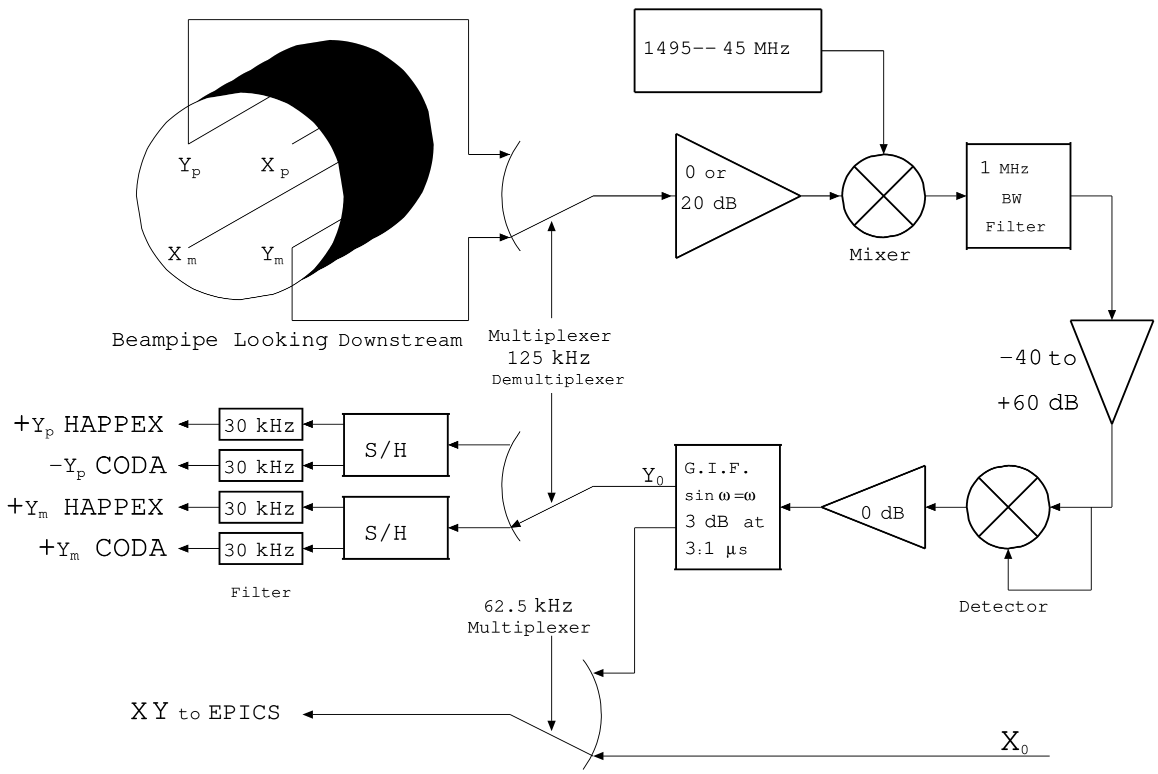

Figure 2-3: Beam position monitor readout electronics. Figure modified from [28].

through the cavity induces signals in the antennae, with amplitudes inversely proportional to the distance from the beam to each of the antennae. The Analog-to-Digital Converter (ADC) readouts from pairs of antennae are combined with calibration coefficients to yield the beam position in each of the two directions.

In the E89044 experiment setup, position and direction of the beam at the target for each physics event was measured by the last two BPMs, located 7.524 m and 1.286 m upstream from the nominal target center. Immediately prior to the start of the E89044, Hall A switched to a "burst mode" readout of the BPMs [29]. In this regime, the beam position in the last two BPMs is read out 6 times per trigger, with intervals of 4 μs. This allowed one to precisely track the motion of the beam due to rastering for each event. After corrections for a phase shift, the beam positions at the two BPMs are extrapolated linearly to the interaction point in the target during event reconstruction. The precision of the measurement of both the vertical and horizontal angles of the beam at the target is ~ 0.3 mrad [30]. The influence of the uncertainties on extracted cross sections was calculated with the code “systerr” (Sec. 6.6). For the E89044 experiment, Michael Kuss calibrated the burst mode readout and implemented the beam position reconstruction in the analysis code ESPACE.

The beam position given by the last before target BPM, averaged over the raster cycle, was restricted to 0.1 mm from the beamline axis throughout the collection of data.

A wire (harp) scanner [26] is a device for precise measurement of the beam profile and position. It operates by moving differently-oriented wires across a low current beam and a readout of induced wire signals. Harp scanners are positioned adjacent to each of the two last before target BPMs, are surveyed relative to the hall coordinates, and are used for calibration of the BPMs in a procedure called “bull's eye”.

2.3.2 Beam current monitors

The beam current monitor (BCM) is a device for non-invasive continuous measurement of the beam current. Hall A beam currents are measured by two identical BCMs located ~ 25 m upstream from the target center [26].

Hall A BCM is a stainless steel cylindrical cavity, 15.48 cm in diameter and 15.24 cm in length, with the cylinder axis coinciding with the nominal beam position. Resonant frequencies of the cavities are tuned to the frequency of the beam. Inside each cavity there are two loop antennae, one of which provides an output signal proportional to the beam current. The output signal is amplified and split into two parts. One part is sent to a high-precision digital AC voltmeter, which provides a measurement of the beam current averaged over 1 s periods. The other part of the signal is converted by an RMS-to-DC converter into an analog DC voltage level, which is then converted to a frequency signal by a V-to-F converter. This frequency signal is sent to scalers gated by the start and the end of each run, providing a measurement of the beam charge accumulated during the runs. Fig. 2-4 shows a block-diagram of the Hall A implementation of the BCM readout.

The two BCMs are calibrated at high beam currents, relative to an Unser monitor located between the BCMs. The Unser monitor is a parametric current transformer,

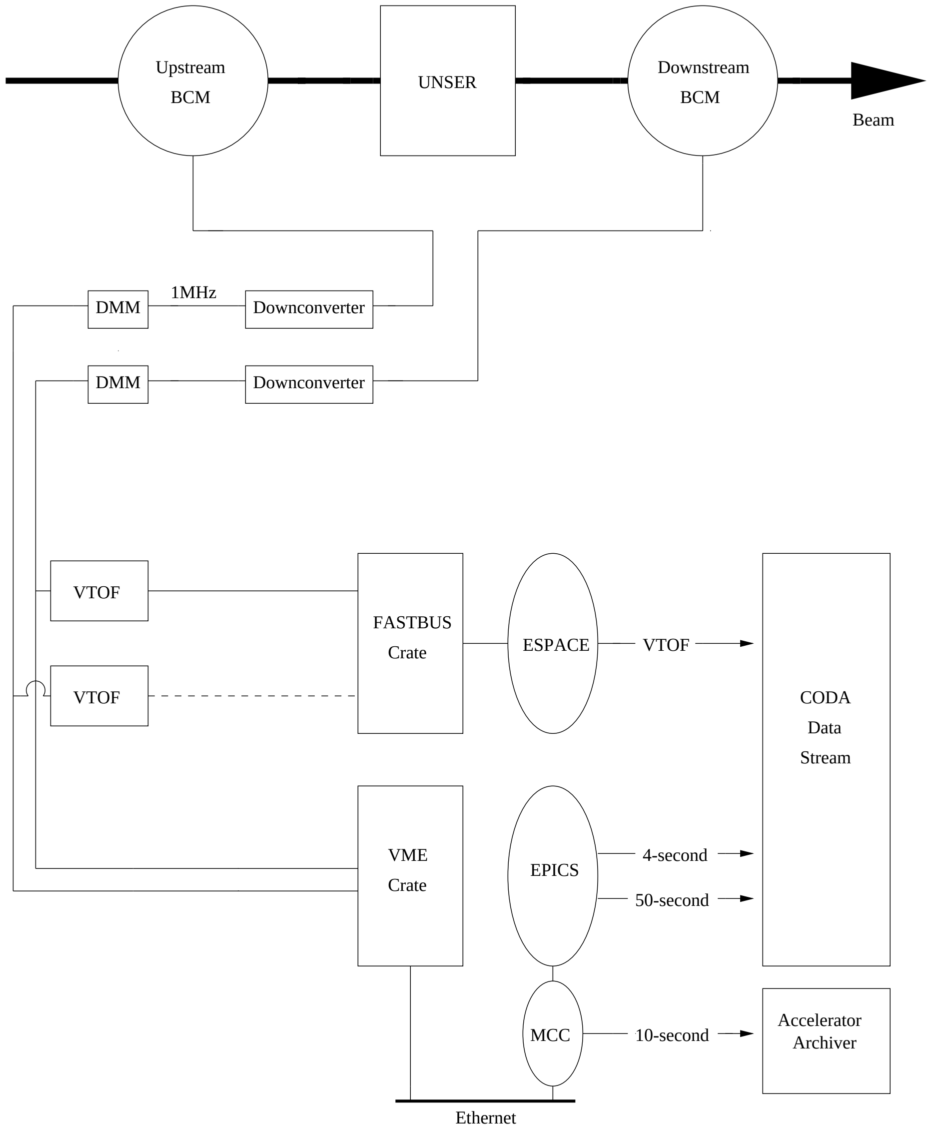

Figure 2-4: Block-diagram of BCM readout. Figure courtesy of Brian Diederich.

calibrated by passing a precisely known current through a wire going through the Unser monitor [26].

2.4 Targets

Fig. 2-5 shows a photograph of the vertical assembly of the Hall A cryogenic targets [26, 31]. The four lower cells are liquid hydrogen and deuterium targets; the upper "tuna can" shaped cell is the unpolarized ^{3}He target employed in the present experiment.

The ^{3}He cell was designed, fabricated and tested by the CalState L. A. group (D. Margaziotis, K. Aniol, M. Epstein and others). Mechanical drawing of the cell was done at JLab (P. Brindza and J. Miller), with the gas handling system designed and built at JLab.

The "tuna can" target is capable of carrying either ^{3}He or ^{4}He. During the commissioning period of the experiment, several test runs were made with the target filled with ^{4}He. During the rest of the experiment the target contained ^{3}He at a temperature of 6.3 K and pressures from 60 to 120 psi.

Fig. 2-6 shows a photograph of the aluminum side wall and flanges of the ^{3}He cell (the photograph was taken at the manufacturing stage). The cell is cylindrical in shape, with a diameter of 10.32 cm and a wall thickness of 0.33 mm. Gas is propelled along the axis of the cylinder at a velocity of $\sim$ 30 m/s; the electron beam is directed perpendicularly to the axis of the cylinder, and is positioned close to the target center. To minimize damage from local heating by the electron beam, during the experiment the beam was rastered to a square 4×4 mm profile.

Fig. 2-7 shows a schematic diagram of the ^{3}He target loop. ^{3}He gas is cooled in the heat exchanger, by ^{4}He supplied by the ESR (End Station Refrigerator) at a temperature of $\sim$ 4.5 K. Low power and high power heaters, shown in the figure in zigzag lines, are controlled by a PID (proportion, integral and derivative) feedback system, keeping the ^{3}He gas in the target at the temperature of 6.3 K. During the experiment, two heat exchangers were connected in parallel, dramatically increasing

Figure 2-5: Photograph of Hall A cryogenic targets. Helium "tuna can" target is at the top of the assembly. Photograph courtesy of D. Margaziotis, CalState L. A.

Figure 2-6: Aluminum side wall and flanges of the "tuna can" target. Photograph courtesy of D. Margaziotis, CalState LA.

the amount of available cooling power. The idea was proposed by P. Brindza, JLab, and allowed to substantially increase the beam currents on the target.

During the whole experiment, the ^{3}He target operated very stably, with maximum sustained currents of 140 μA at full ~ 0.072 g/cm^3 density. The following aspects of operation of the "tuna can" target are discussed in other chapters: measurements of density of the ^{3}He gas in the target (Sec. 4.2.2), the analysis of stability of the ^{3}He density (Sec. 4.3), the analysis of changes in the ^{3}He density due to heating by the beam (Sec. 4.4).

Other targets employed in the experiment were: a carbon foil target, three aluminum "dummy" targets, and a BeO target. The carbon foil target is a thin carbon foil positioned perpendicularly to the nominal beam direction. It was used for a measurement of mispointing of spectrometers (Sec. 3.3). The aluminum "dummy" targets are pairs of thin aluminum plates, positioned vertically at a distance of 4, 10 or 15 cm. The dummy targets are normally used for the measurement of contributions from aluminum walls of other targets. In this experiment the dummy targets were used for checks of quality of reconstruction of the reaction point along the beam.

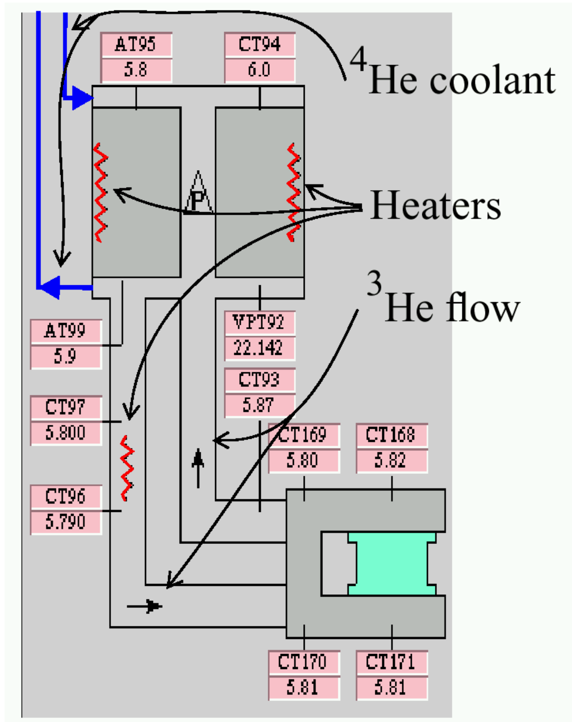

Figure 2-7: Diagram of ^{3}He target loop. During E89044, ^{3}He gas in the target was cooled by two heat exchangers connected in parallel.

The BeO target was used to visually (through cameras) check the beam position, by observing the fluorescent light emitted from the place of impingement of the target by the beam. Hall A targets are arranged in a vertical assembly, which can be remotely moved (in the vertical direction) within the scattering chamber in order to expose a desired target to the beam.

2.5 Spectrometers

Fig. 2-8 shows a schematic view of the experimental Hall A, with a cross section of one of the two high-resolution spectrometers (HRS). The two spectrometers [26] are nominally identical, and use the QQDQ configuration of superconducting magnets to deflect charged particles into their focal planes. At the focal planes the particles, dispersed vertically in momentum, are detected in the detector packages. The optical length of the spectrometers is 23.4 m; the nominal bend angle of the central ray is

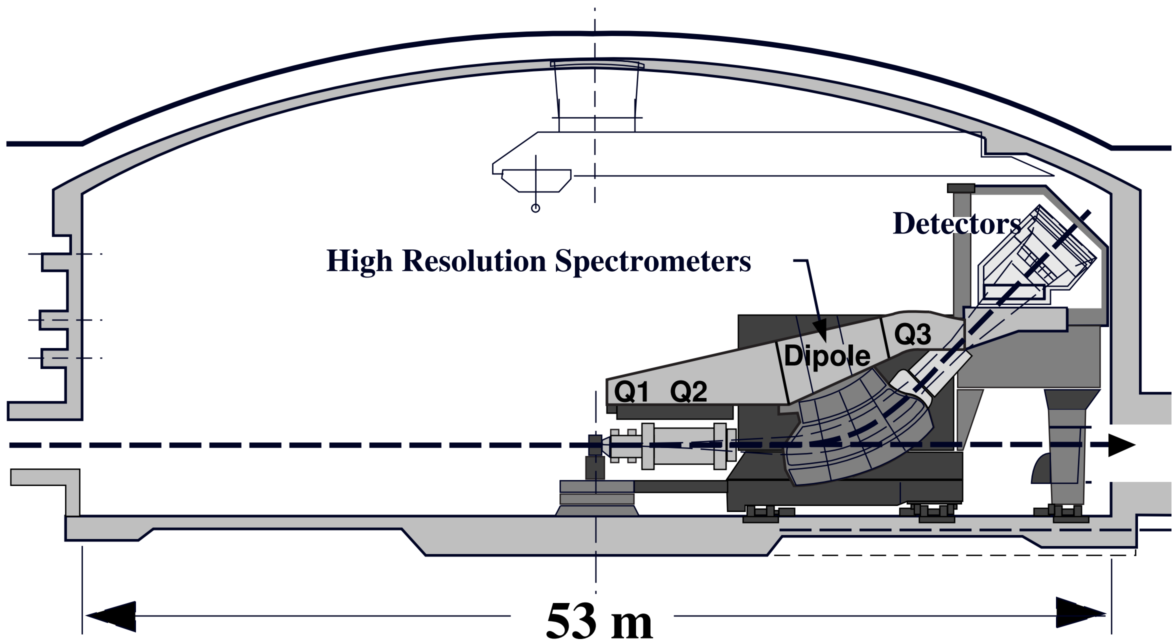

Figure 2-8: Cross section view of Hall A and of a high-resolution spectrometer.

45°. Each of the spectrometers can operate in either polarity, with a nominal central momentum range of 0.3 – 4 GeV/c. The scattering angle of the detected particles is varied through rotation of the spectrometers around the hall center, with a central scattering angle range of 12.5 – 150°. Nominal acceptance of the spectrometers is ± 28 mrad in the horizontal direction, ± 60 mrad in the vertical direction, with ± 4.5 % momentum bite, and ± 5 cm length acceptance. During collection of ^{3}He quasielastic data the spectrometer located left from the beamline (labeled "electron spectrometer", or "HRSE"), as shown in Fig. 2-2, was normally in negative polarity and detected negatively charged particles, while the spectrometer right from the beamline (labeled "hadron spectrometer", or "HRSH") was in positive polarity and detected positively charged particles. The following is discussed in other chapters: the spectrometer acceptance (Sec. 5.3), the spectrometer mispointing (Sec. 3.3), residual distortions in the spectrometer optics and the quadrupole magnet cycling procedure (Sec. 3.2.3).

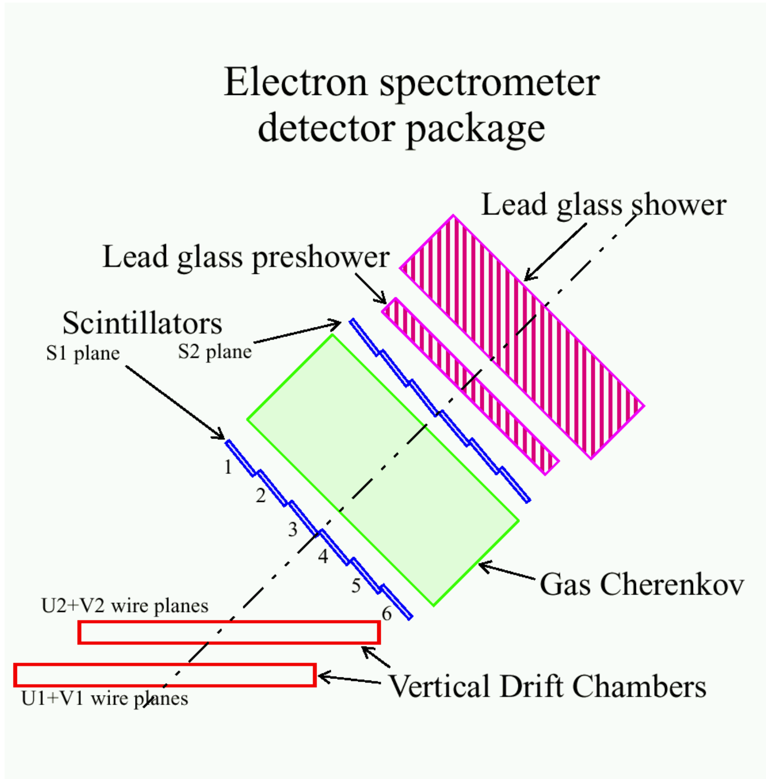

Figure 2-9: Electron spectrometer detectors employed in the experiment.

2.6 Detector packages

Figs. 2-9 and 2-10 show schematic views of the detectors employed in the experiment, and their arrangement at the spectrometer focal planes. In analysis presented in this thesis, the electron spectrometer lead glass shower and preshower detectors were not used.

Detector packages of both spectrometers [26] contain two planes of scintillators used for triggering, and two vertical drift chambers used for tracking of particles. Gas Cherenkov detector, located in the electron spectrometer detector package, was employed for separation of electrons from negative pions, and for generation of an auxiliary trigger used for a measurement of efficiency of main trigger types (Sec. 2.8). In the hadron spectrometer detector package, auxiliary triggers were generated by the S0 scintillator paddle.

During the collection of data, the detector packages and the data acquisition

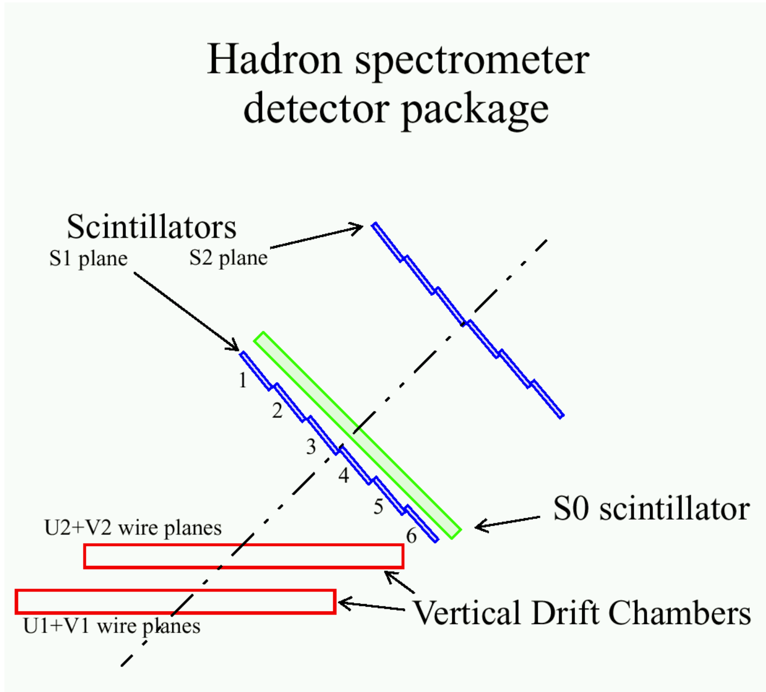

Figure 2-10: Hadron spectrometer detectors employed in the experiment.

(DAQ) electronics are located inside a shielded "detector hut", protected from most radiation. The detectors and the DAQ are mounted on a retractable steel frame, and are moved out from the hut for maintenance or reconfiguration. In the following, each detector is briefly described.

2.6.1 Scintillators

Triggering of singles and coincidence events was provided by the scintillators [26], arranged in two planes on each spectrometer. The two planes are parallel to each other, are perpendicular to the spectrometer nominal central ray, and are spaced apart by $\sim$ 2 m along the central ray (Figs. 2-9 and 2-10). The lower scintillator plane is labeled "S1" scintillator plane. The upper scintillator plane is labeled "S2" scintillator plane. Each plane is formed by 6 identical overlapping scintillator paddles, numbered from top to bottom, as shown in the figures. The paddles are 5 mm thick plastic, with two photomultiplier tubes (PMTs) at each end. The active area of the S1 scintillator plane is about 170 cm $\times$ 35 cm, and that of the S2 scintillator plane is about 220 cm $\times$ 54 cm.

The hadron spectrometer detector package contained a 10 mm thick scintillator paddle, named the S0 detector. The active area of the paddle is, approximately, 190 cm $\times$ 40 cm. The paddle was installed shortly prior to the start of the experiment, and was positioned immediately behind the S1 scintillator plane, and parallel to the plane (Fig. 2-10). The S0 paddle is viewed by 2 PMTs, labeled top (T) and bottom (B). The E89044 trigger setup is described in Sec. 2.8.1.

2.6.2 Vertical Drift Chambers

Two Vertical Drift Chambers (VDCs) [32], located at the focal planes of each of the two spectrometers, were used for tracking of particles at the focal planes. All four VDCs are nominally identical, with the active area of 240 cm $\times$40 cm. The VDC located near the spectrometer nominal focal surface[1] is labeled "VDC1"; the other VDC, labeled "VDC2", is offset 50 cm along the spectrometer nominal central ray. Both VDCs are parallel to each other and to a horizontal plane, and intersect the spectrometer central ray at an angle of 45°. Fig. 2-11 shows a side and top view of a VDC pair, as mounted in the detector hut.

Each VDC contains two sets of parallel 20 μm-diameter gold-coated tungsten wires (386 wires in each plane), sandwiched in between gold-coated mylar planes. A gas mixture of argon (62%) and ethane (38%) is supplied in between the mylar planes at a rate of 5 liters per hour. During the operation, the mylar planes are kept at a negative voltage of 4 kV, while the tungsten (sense) wires are grounded. A charged particle crossing a VDC ionizes atoms in the gas mixture, creating a trace of released electrons. The electrons are accelerated by the electric field created by the high voltage, and drift along the field lines toward the wires. In the close vicinity of the sense wires (where the electric field is the strongest) the drifting electrons initiate electron avalanches. The electron avalanches hit the wires and induce wire signals, which are amplified, discriminated, and sent to multihit TDCs [32].

[1]Actual focal surfaces of the spectrometers have a complex shape and are located between the two VDCs, due to a manufacturing problem known as the "Hall A sextupole crisis" [33].

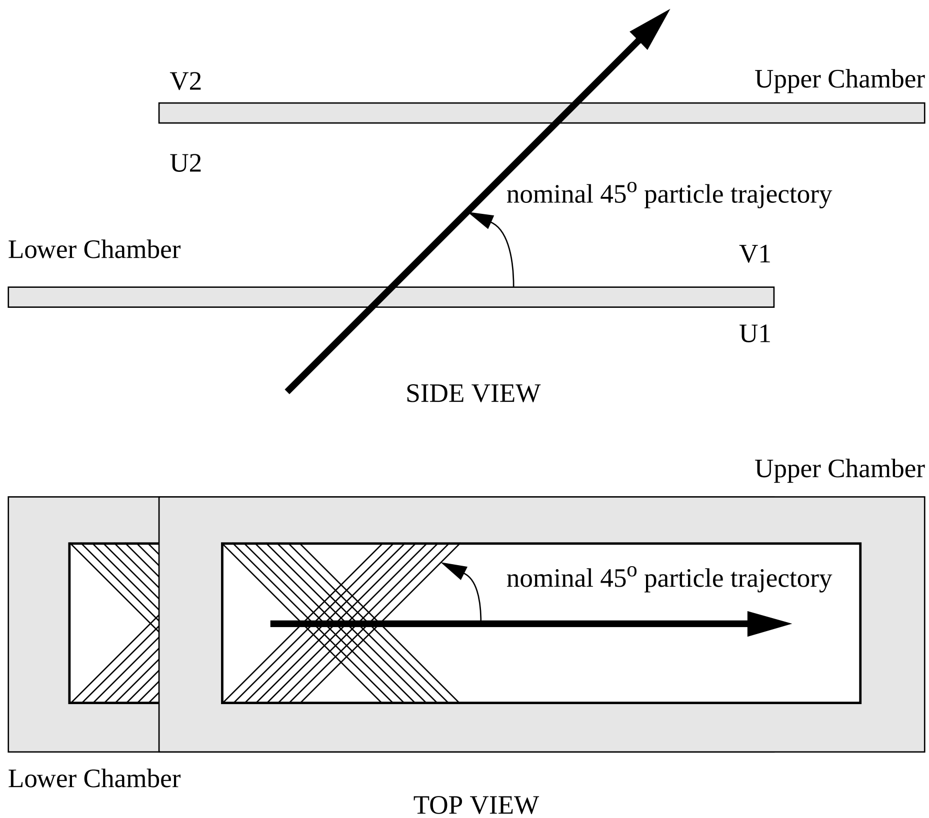

Figure 2-11: A pair of vertical drift chambers, as mounted at the focal plane. Figure courtesy Kevin Fissum, [32].

As shown in Fig. 2-11, the wires in the two wire planes are perpendicular to each other, and are oriented at 45° to the projection of the nominal central ray on the VDC surface. The lower (upper) wire plane of the lower VDC is denoted "U1" ("V1") plane, the lower (upper) wire plane of the upper VDC is denoted "U2" ("V2") plane. TDC readouts from wires hit in any "U" and "V" planes allow one to fully reconstruct the particle trajectory. However, the resolution can be substantially improved by combining the TDC information from wires hit in all four wire planes. The overall position resolution of the two wire chambers is $\sim 100\ \mu$m; the angular resolution is $\sim$ 0.5 mrad. Algorithms of reconstruction of particle trajectories in the wire chambers are described in Sec. 3.1.2 and Sec. 3.2.

Throughout the experiment VDCs provided reliable tracking with virtually absent noise. The VDCs were constructed, commissioned and installed by K. Fissum, J. Gao,

N. Liyanage, W. Bertozzi, S. Gilad and the Nuclear Interactions Group at MIT. A detailed description of the Hall A VDC package is available in [32].

2.6.3 Gas Cherenkov

The Gas Cherenkov detector [34, 26] was mounted between the S1 and S2 scintillator planes in the electron spectrometer detector package (Fig. 2-9). The Gas Cherenkov detector is a rectangular chamber filled with the CO_2 gas at the atmospheric pressure [34]. Charged particles traversing the chamber at velocities larger than $1/n$, where n is the refractive index of the gas, emit Cherenkov radiation. 10 spherical mirrors located at the chamber walls focus the radiation on 10 PMT photocathodes. The refractive index of CO_2 at the atmospheric pressure is $n \approx 1.00041$, with a corresponding Cherenkov radiation threshold of 4.8 GeV/c for pions, and 17 MeV/c for electrons.

The Gas Cherenkov detector provided separation of electrons from π^- in the electron spectrometer (Sec. 3.1.3). In addition, the analog sum of the 10 PMT signals was used for triggering of particles missed by the main trigger (Sec. 2.8.1). Fig. 3-6 shows the distribution of the sum of the 10 Gas Cherenkov ADCs corrected for pedestals and gains.

2.7 Coordinate systems

Reconstructed trajectories of particles in Hall A are specified in one of five coordinate systems: hall coordinate system, target coordinate system, and three coordinate systems linked to the detector packages. Three of these coordinate systems, used in the analysis presented in the next chapters, are described below.

1. Hall Coordinate System (HCS): The origin of this coordinate system is defined as the point of intersection of the unrastered beam, centered in the last two BPMs, with the plane perpendicular to the beam and containing the axis of rotation of the target assembly. The $\hat{z}$ axis points in the direction of the beam, the $\hat{y}$ axis points vertically upward, vectors $\hat{x}$, $\hat{y}$, $\hat{z}$ form a right-handed triplet

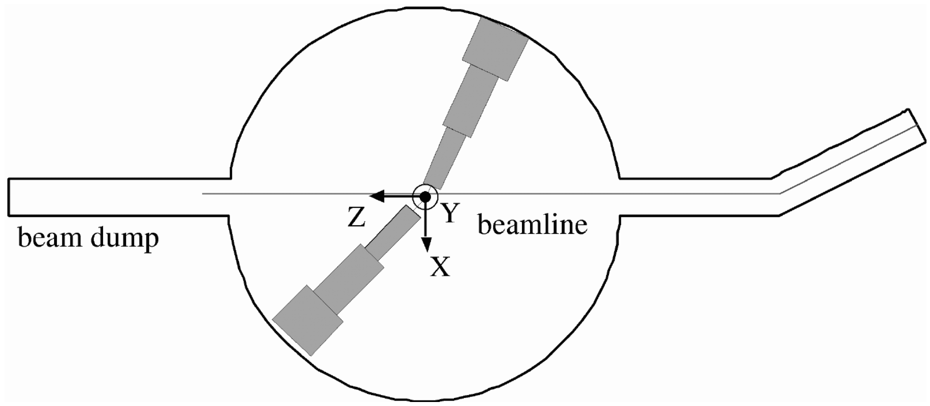

Figure 2-12: Definition of the Hall Coordinate System. Figure modified from [29].

(Fig. 2-12). This is the "laboratory" coordinate system, used for calculating the kinematic variables of events.

2. Target coordinate system (TCS). The origin of this coordinate system is defined as the point at a distance of 1.25 m from the center of the central sieve slit hole[2], along a ray perpendicular to the sieve slit surface and pointing toward the target. The $\hat{z}$ axis points toward the center of the central sieve slit hole; the $\hat{x}$ axis points vertically downward. The triplet $\hat{x}$, $\hat{y}$, $\hat{z}$ is right-handed. Variables referring to this coordinate system are designated by the subscript "tg". Variables x_{tg} and y_{tg} are defined as the x and y coordinates of the point of intersection of a particle trajectory with the $z_{tg} = 0$ plane. Variables θ_{tg} and ϕ_{tg} are defined as

$$\tan\theta_{tg} = \frac{dx}{dz}, \tag{2.1}$$

$$\tan\phi_{tg} = \frac{dy}{dz}. \tag{2.2}$$

δ_{tg} is defined with $\delta_{tg} = (p - p_0)/p_0$, where p is the particle momentum and p_0 is the spectrometer central momentum. Additional subscripts "e" and "h"

[2]The sieve slit [26, 35] is a 5 mm-thick tungsten plate with dimensions of, approximately, 200 × 300 mm. A regular pattern of circular holes is drilled through the sieve slit surface. The sieve slit is used for experimental study of the spectrometer optics. During the study, the sieve slit is moved in across the spectrometer entrance window and limits events entering the spectrometer to the area of the holes. A detailed description of the study of the spectrometer optics using the sieve slit is available in [36, 37].

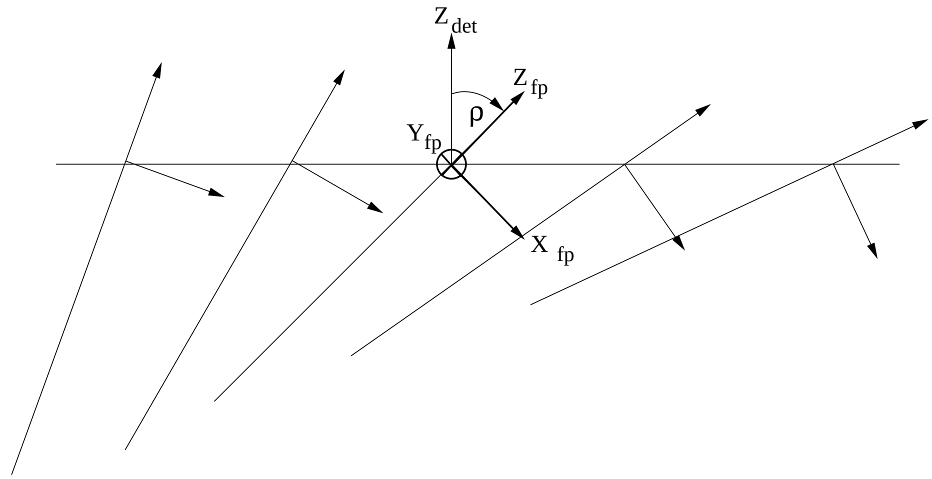

Figure 2-13: Definition of the Focal Plane Coordinate system. Figure modified from [36].

on x_{tg}, y_{tg}, θ_{tg}, ϕ_{tg} and δ_{tg} denote whether the coordinate system is that of the electron or hadron spectrometer.

3. Focal plane coordinate system (FPCS). The origin of this coordinate system is defined as the point of intersection of wire 184 of the U1 VDC wire plane with the projection of wire 184 of the V1 wire plane on the U1 wire plane (the VDC notation is described in Sec. 2.6.2). The $\hat{y}$ axis lies in the U1 wire plane and is parallel to the short symmetry axis of the VDC1; the $\hat{z}$ axis points in the direction of the projection of the local central ray ($x_{tg} = y_{tg} = \theta_{tg} = \phi_{tg} = 0$) on a plane perpendicular to the $\hat{y}$ axis (Fig. 2-13). Variables referring to the focal plane coordinate system are designated by the subscript "fp". Coordinates y_{fp} and ϕ_{fp} are corrected for misalignments in the VDC package by a set of polynomial coefficients y_{i000} and p_{i000} acting on powers of x_{fp} [38, 37, 29]. The dependence of the angle between the local central ray ($x_{tg} = y_{tg} = \theta_{tg} = \phi_{tg} = 0$) and the central ray ($x_{tg} = y_{tg} = \theta_{tg} = \phi_{tg} = \delta_{tg} = 0$) on the particle momentum is contained in another set of polynomial coefficients, t_{i000}, also acting on powers of x_{fp} [38, 37, 29]. Coefficients y_{i000}, p_{i000} and t_{i000} are determined during calibration of the spectrometer optics database (Sec. 3.2).

2.8 Electronics and data acquisition

2.8.1 Trigger setup

Triggers are electronic signals that prompt the data acquisition system (Sec. 2.8.2) to start a readout of the detector information. In the E89044 experiment setup, the main physics trigger types were: an electron spectrometer singles trigger (denoted “T1”, or “type 1”), a hadron spectrometer singles trigger (“T3”, or “type 3”), and a coincidence trigger (“T5”, or “type 5”). Auxiliary physics triggers, used for measurements of efficiencies of the main triggers, were an electron spectrometer trigger (denoted “T2”, or “type 2”), and a hadron spectrometer trigger (“T4”, or “type 4”).

The configuration of the electronics for the singles trigger T1 and the coincidence trigger T5 are given in Appendix C. Fig. 2-14 shows a simplified schematic view of the setup of the main physics triggers. As described in Sec. 2.6.1, the main physics triggers were generated using scintillator signals. The scintillators were arranged in two planes in each of the two detector packages, with six scintillator paddles in each plane, and two photomultiplier tubes (PMTs) viewing each paddle. Therefore, the PMTs of the two scintillator planes provided $2 \times 2 \times 6 = 24$ signals for each spectrometer. In Fig. 2-14 “S1” and “S2” denote signals from the lower and the upper scintillator planes, respectively. “S1-L” (“S1-R”) denotes scintillator signals from the left (the right) PMTs of the lower scintillator plane. “S2-L” (“S2-R”) denotes scintillator signals from the left (the right) PMTs of the upper scintillator plane.

Analog signals from the scintillator PMTs were first sent to a discriminator (LeCroy Model 4413/200) providing both analog and digitized outputs. The analog signals were sent to ADCs. The digitized signals were split in three parts: one part was sent to TDCs, another part was sent to scalers gated by the start and the end of each run, and the third part was sent to a logical AND unit making a coincidence between pairs of PMTs viewing the same paddle. For each spectrometer, 12 outputs of the logical AND unit were fed into the Memory Lookup Unit (MLU, LeCroy Model 2372). The MLU is a programmable device that, given a combination of logical signals at its inputs, provides a corresponding (programmed) combination of logical signals at its

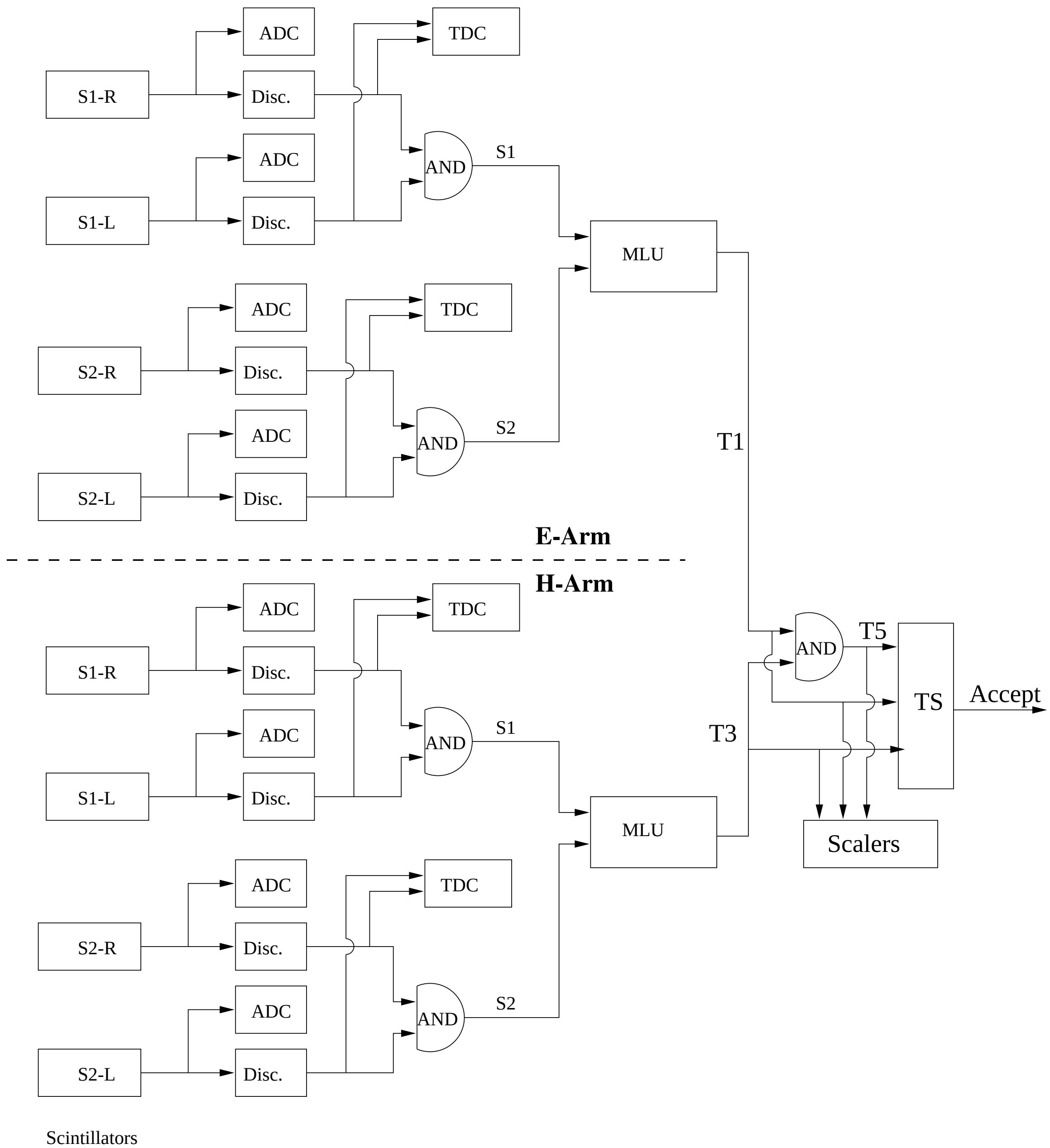

Figure 2-14: Simplified block-diagram of setup of the main physics triggers.

outputs. In the experiment, the electron and the hadron spectrometer MLUs were programmed to issue a logical signal "S-ray" when:

1. Coincident hits were present in both PMTs of a scintillator paddle in the S1 scintillator plane.

2. Coincident hits were present in both PMTs of a scintillator paddle in the S2 scintillator plane.

3. These two paddles were either adjacent or coincided in their relative position in the planes (Figs. 2-9 and 2-10).

The coincidence between the S-rays from the two spectrometers within a ~ 100 ns time window formed the coincidence trigger T5. The absence of a coincidence, but the presence of an S-ray, formed either the electron singles trigger T1, from the electron spectrometer S-ray, or the hadron spectrometer singles trigger T3, from the hadron spectrometer S-ray.

The auxiliary trigger type 2 for the electron spectrometer was generated when the electron S-ray was not present and any two of the three following "events" were coincident:

1. A coincidence between both PMTs of a scintillator paddle in the S1 scintillator plane of the electron spectrometer.

2. A coincidence between both PMTs of a scintillator paddle in the S2 scintillator plane of the electron spectrometer.

3. The analog sum of the 10 Gas Cherenkov PMTs (electron spectrometer) is above a threshold.

Similarly, the auxiliary trigger type 4 for the hadron spectrometer was generated when the hadron S-ray was not present and any two of the three following "events" were coincident:

1. A coincidence between both PMTs of a scintillator paddle in the S1 scintillator plane of the hadron spectrometer.

2. A coincidence between both PMTs of a scintillator paddle in the S2 scintillator plane of the hadron spectrometer.

3. A coincidence between both PMTs of the S0 scintillator paddle (hadron spectrometer).

From the description above it can be seen that the five trigger types are exclusive, i.e. any given trigger can have only a single type, T1, T2, T3, T4, or T5[3]. Scalers counting the number of issued T1 and T3 triggers in fact counted the number of S-rays that occurred in the electron and hadron spectrometers, and therefore their number had to be corrected by the number of coincidence triggers (the correction is described in Sec. 3.4).

The electron and hadron spectrometer MLUs that issued the S-rays were operated in a "strobed" mode. In this mode, the MLUs were issuing an S-ray only 45 ns after arrival of an "enable" signal. The enable signal was formed by the logical OR of the signals from the right PMTs of the S1 and S2 scintillator planes, with the signals from the S1 plane delayed in time relative to the signals from the S2 plane. This setup guaranteed that the timing of generation of the main physics triggers was always defined by the right PMTs of the S2 scintillator plane. This definitiveness of the timing simplifies reconstruction of events (Sec. 3.2.1).

Generated trigger signals were fed into a custom-built Trigger Supervisor (TS) module, which prescaled the triggers and, based on the current state of the data acquisition system (DAQ), decided whether to prompt the DAQ to start the event readout. Trigger prescale factors were downloaded into the TS at the start of runs. In the Hall A TS setup, the prescale factor n for the trigger type i means that the TS attempts to read out every nth event of type i.

[3]Another physics trigger type, T14, occurred (very infrequently) when there was an overlap of 10 ns or less between the five main trigger types (T1 – T5) at the Trigger Supervisor.

2.8.2 Data acquisition system

Fig. 2-15 shows a block-diagram of the Hall A data acquisition system (DAQ). The DAQ software is based on the "CEBAF online data acquisition" (CODA) package [39]. The hardware components are either custom made, such as the trigger supervisor module, or commercially acquired, such as the Analog-to-Digital Converter (ADC), Time-to-Digital Converter (TDC) and scaler modules. The E89044 experiment used a standard Hall A DAQ in two-spectrometer configuration [40], without readout of the focal plane polarimeter data.

The ADC, TDC and scaler modules are either Fastbus [41] or VME-type [42][4], and are housed in either Fastbus or VME crates. After registering hits from detectors, the crates are read out by the Read Out Controllers (ROCs), which are CODA routines running under the VxWorks operating system [43]. The ROC's function is to receive a trigger from the trigger supervisor, execute a corresponding readout list, structure the information and over the network pass it to the next CODA component, the Event Builder (EB). The Event Builder is a routine that waits for connection requests from the ROCs, collects their event fragments, and orders and merges the pieces into a single data structure in the CODA format. The events are then passed to the Event Recorder (ER), which is a CODA routine that writes the events to disk. Written data files are eventually transferred to JLab silo tapes.

A physics event during the experiment contained a ROC1 readout of a Fastbus crate in the electron spectrometer detector package, a ROC2 readout of a Fastbus crate in the hadron spectrometer detector package, and a ROC14 readout of a VME crate with the BPM and raster information. Readouts of most scalers were inserted in the data stream as event type 140, every few seconds, as well at the end of each run. All scalers were gated by the start and the end of each run.

The BPM and BCM data from the EPICS (Experimental Physics and Industrial Control System) databases [44] is inserted in the datastream as event type 131, ap-

[4]Fastbus and VME are standards that specify mechanical circuit board characteristics, such as board and connector dimensions, and electronic specifications, such as signal voltage levels, signal timing and functions.

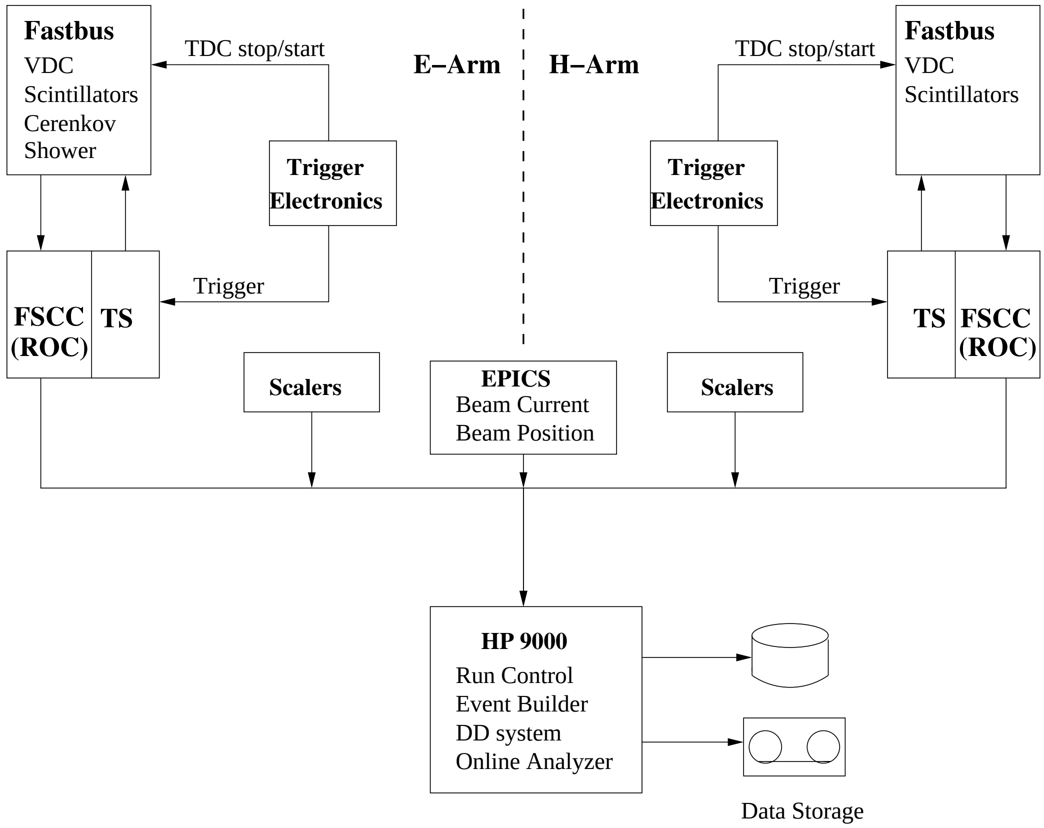

Figure 2-15: Block-diagram of the Hall A DAQ system.

proximately every 5 seconds. A longer list of EPICS data, including the ^{3}He target temperature and pressure, magnetic fields in the spectrometers and currents in the spectrometer magnets, are inserted every 30 seconds, as well as at the start and at the end of runs.

Chapter 3

Calibrations and auxiliary measurements

In this chapter we describe the calculation of trigger efficiency (Sec. 3.1.1), tracking efficiency (Sec. 3.1.2), Gas Cherenkov efficiency (Sec. 3.1.3), proton absorption (Sec. 3.1.4), the calibration of the optics and detector databases (Sec. 3.2), the measurement of the mispointing of the spectrometers (Sec. 3.3), and the calculation of computer and electronic deadtimes (Sec. 3.4).

3.1 Efficiencies

3.1.1 Trigger efficiency

The scintillator inefficiency arises due to: 1. statistical fluctuations of energy deposited by the charged particles in the scintillator paddles (when little or no energy is deposited); 2. imperfect transmission of light emitted by the particles in the paddles to the photomultiplier tubes (PMTs); 3. inefficiencies of the PMTs; 4. other inefficiencies. Since the triggers are generated based on the scintillator signals (Sec. 2.8.1), the scintillator inefficiency causes the trigger inefficiency[1].

[1]In addition, at proton momenta below $\sim 0.8 - 1$ GeV/c, p-N rescattering in the S1 scintillator plane can cause the protons to miss the S2 scintillator plane [45]. The analysis of inefficiencies of detection of protons is presented in Sec. 3.1.4.

The setup of all physics triggers used in the experiment is described in Sec. 2.8.1. Most events missed by the main physics trigger types 1, 3 and 5 (T1, T3 and T5) due to the trigger inefficiency still caused a trigger, type 2 (T2) in the electron spectrometer or type 4 (T4) in the hadron spectrometer. During the experiment, the T2 and T4 triggers were prescaled so that 50 Hz of each was recorded to disk. The recorded triggers T2 and T4 allowed us to calculate the trigger efficiencies (and inefficiencies), as described below.

Events (triggers) of types 2 and 4 can be classified in the following categories:

1. Background events with trajectories outside the focal plane envelope, hitting a "large-angle" combination of the scintillator paddles in the two scintillator planes S1 and S2.

2. Background events with trajectories outside the focal plane envelope, hitting a scintillator paddle in one of the two scintillator planes, and producing a signal in the Gas Cherenkov (HRSE) or in the S0 detector (HRSH).

3. "Good" events falling within the focal plane envelope and generally having a track in the VDCs, but failing to generate a singles or a coincidence trigger due to the trigger inefficiency, and producing a signal in the Gas Cherenkov (HRSE) or in the S0 detector (HRSH).

As a first step in finding the trigger efficiency, one has to filter out the background events (falling outside the focal plane envelope) from a run containing a large number of recorded T2 and T4 events. Then, one has to separate electrons from π^- in the electron spectrometer (for the T2 events), and protons from π^+ and other positive particles (such as ^{2}H and ^{3}H) in the hadron spectrometer (for the T4 events). These steps are described next.

The background events with trajectories outside the focal plane envelope were filtered out by a software cut requiring a good VDC track reconstructing to the target (both for T2 and T4 events). For T2 events, electrons were separated from the π^- by a cut requiring the sum of the 10 Gas Cherenkov ADC signals to be above

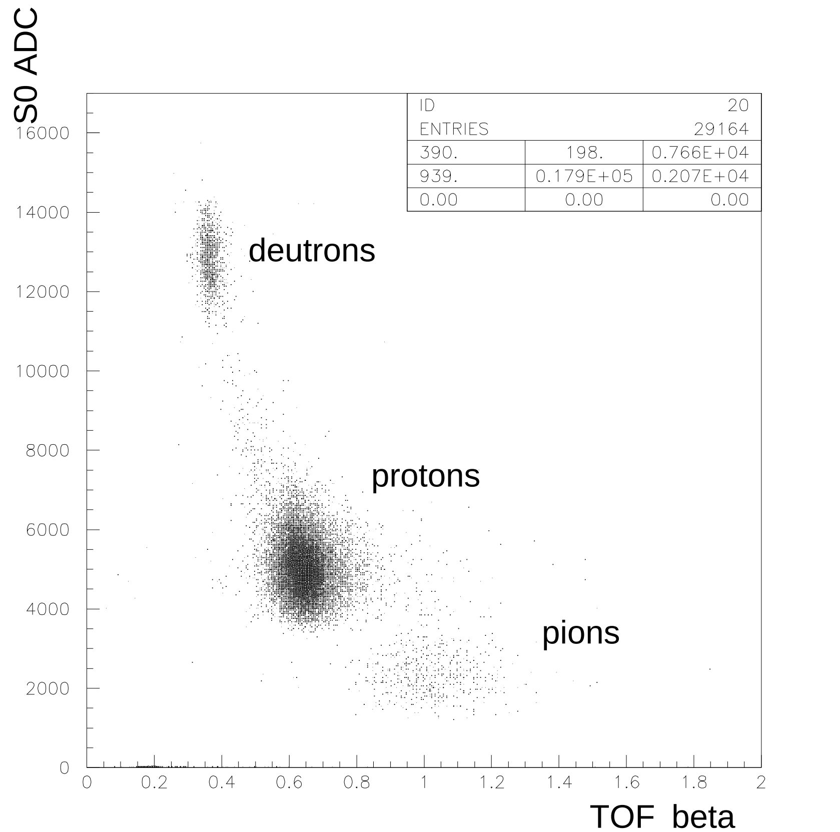

Figure 3-1: Sum of the two S0 ADC signals vs particle velocity β calculated from the time of flight (TOF) between the S1 and S2 scintillator planes. The S0 ADC signals were corrected for gains, pedestals and light attenuation in the S0 scintillator paddle. Kinematics 8.

a cutoff value. The ADC signals in the sum were corrected for pedestals and gains, as described in Sec. 3.2.2. For T4 events, the protons were separated from other positive particles by a cut requiring the sum of the two S0 ADC signals to be in the range corresponding to protons (Fig. 3-1). The two S0 ADC signals were corrected for pedestals, gains and light attenuation in the S0 scintillator paddle (Sec. 3.2.2). Then, to ensure uniform sampling of events of all trigger types, the cuts described above were applied to the recorded good physics events (types 1, 3 and 5).

The trigger efficiency ϵ_e (ϵ_p) for detection of electrons (protons), averaged over the focal plane, was then calculated from the number of (corrected for prescaling, computer and electronic deadtimes) events N_i of trigger types $i = 1, ..., 5$ in the

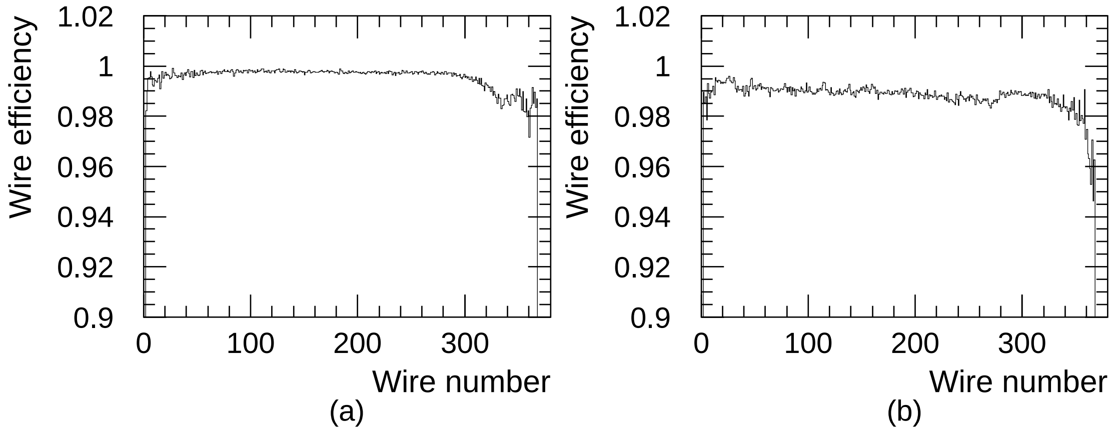

Figure 3-2: Efficiency of VDC wires calculated with the formula (3.2): (a) HRSE V2 wire plane; (b) HRSH U2 wire plane. Kinematics 1.

remaining sample, as

$$\epsilon_{e(p)} = \frac{N_{1(3)} + N_5}{N_{1(3)} + N_5 + N_{2(4)}}. \tag{3.1}$$

The trigger efficiency determined at different kinematic settings and at different times during the experiment gave consistent results, with 99.9% efficiency of detection of electrons in the electron spectrometer, and 99.8% efficiency of detection of protons in the hadron spectrometer. Statistical errors of the measurements were less than 0.05%.

3.1.2 Wire chamber and tracking efficiency

The efficiency of a single sense wire in the wire chambers is the probability that the wire fires when a charged particle passes sufficiently close to it. It can be estimated with the formula:

$$\epsilon_{wire} = \frac{N_1}{N_0 + N_1}, \tag{3.2}$$

where N_1 (N_0) is the number of times the wire fired (did not fire) when 2 wires adjacent to it fired. The efficiency determined with this formula was monitored during the experiment with the online code "dplot", and is shown in Fig. 3-2 for the electron spectrometer V2 wire plane and the hadron spectrometer U2 wire plane (^{3}He(e,e$'$p) data, kinematics 1). The efficiency was determined to be greater than 0.98 for all wires within the acceptance region of the spectrometers used in cross section analysis.

This estimate of wire efficiency should be considered as a lower bound of actual wire efficiency, since formula (3.2) takes no account of situations when two clusters of hit wires with a gap of one wire in between were produced by two different particles. Such an event is shown in Fig. 3-3 (top). In this figure, as well as in Fig. 3-3 (bottom), Fig. 3-4 and Fig. 3-5, the edges of the drift chambers are represented by horizontal lines, and dots in between the edges represent locations of hit wires. Small circles in the figures denote locations of the particles reconstructed by the analysis code ESPACE (only 16 locations for a cluster are plotted). Dashed lines are "local" fits to trajectories of the particles[2], for individual clusters of hit wires in a wire plane, and solid sloped lines are "global" fits to the trajectories, for pairs of clusters from the two wire planes deemed to be produced by the same particle by the "minimum spanning tree" algorithm (the algorithm is described later in the section).

The event shown in Fig. 3-3 (top) has two clusters of hit wires in the hadron spectrometer V1 wire plane, with the right cluster most probably produced by a delta-ray electron knocked-on just before the particle entered the V1 plane. The two clusters of hit wires are separated by one wire, and therefore the efficiency of this wire, if determined with (3.2), would be lower than its actual efficiency. Fig. 3-3 (top) demonstrates several features of the trajectory reconstruction algorithm implemented in ESPACE: if two clusters are separated by only 1 wire, they are in fact considered as one cluster (and therefore only one "local" fit is made); the judgment whether to put the reconstructed location of the particle below or above a hit wire is poor for clusters that are produced by more than 1 particle, probably because the code assumes that a cluster can belong only to a single particle[3].

[2]That is, the fits are to the small circles in the figures.

[3]As described in Sec. 3.2.1, an experimentally measured quantity is the absolute distance from the hit wire to the particle location. Therefore, in order to fit the particle trajectory, the analysis code has to make a determine whether the particle passed below or above each of the hit wires. It is here observed that the analysis code ESPACE makes the determination very well for clusters that are produced only by a single particle, but is performing worse for clusters produced by more than one particle.

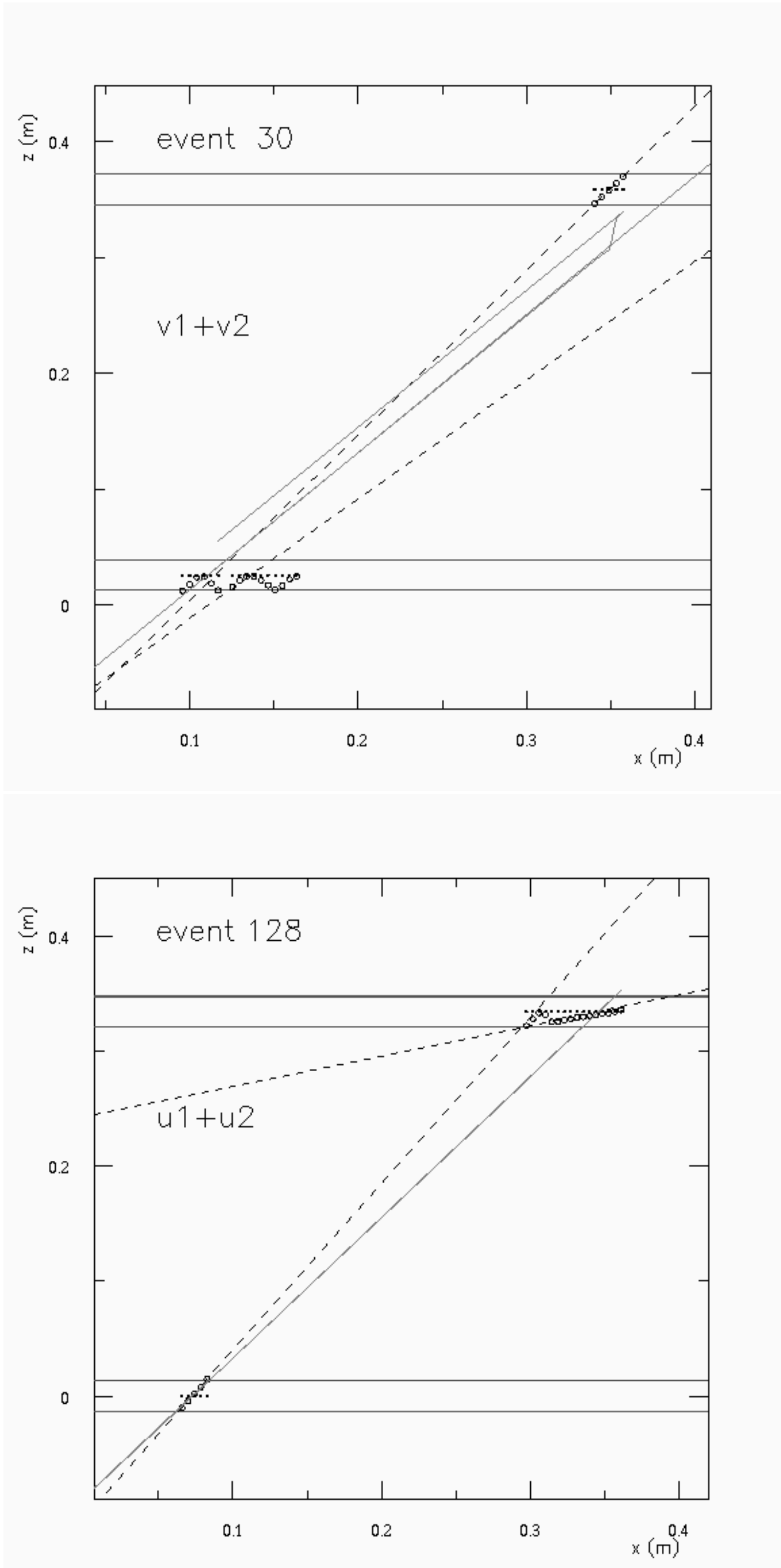

Figure 3-3: Reconstruction of tracks with delta-rays: (top) hadron spectrometer V1 and V2 wire planes; (bottom) electron spectrometer U1 and U2 wire planes.

This latter feature is also apparent in the event shown in Fig. 3-3 (bottom), where (most probably) a delta-ray was knocked-on from the lower foil of the electron spectrometer U2 wire plane. Reconstructed locations of the original (making the trigger) particle above the U2 wire plane are incorrectly flipped below the plane. As mentioned above, this is probably because the analysis code has no special algorithm for treating clusters produced by more than one particle. As a result, as in the case of the event in Fig. 3-3 (top), the code treated the large cluster in the U2 wire plane as belonging only to one particle, and the "global" fit significantly deviates from the particle trajectory.

For fitting separate tracks crossing the wire chambers, the analysis code has to assign clusters of hit wires from different wire planes to a particular track. For that, ESPACE employs the "minimum spanning tree" algorithm. For the two wire planes determining the particle trajectory in each direction, the algorithm effectively amounts to searching for a combination of clusters from the two planes having the lowest chi-square straight-line fit, with the time offset t_0 [32, 29] left as a free parameter[4]. Then, the two found clusters are assigned to a track, and the procedure is repeated for the remaining clusters until all the tracks are found.

In most cases the algorithm performed very well. For example, the event shown in Fig. 3-4 (shown are the electron spectrometer U1 and U2 planes) demonstrates how the code correctly assigned 8 clusters in the two wire planes to 4 tracks. The remaining task for the code was to select the "golden" track that made the trigger, by analyzing the timing of the tracks and the locations of their intersects with the scintillator planes. As will be discussed below, this event was incorrectly reconstructed by the electron spectrometer. Therefore, in this situation either ESPACE incorrectly selected the "golden" track, or, less likely, the trajectory of the scattered electron was significantly altered by secondary interactions.

Fig. 3-5 shows an apparent breakdown of the implementation of the minimum spanning tree algorithm, where a delta-ray electron knocked-on between the wire

[4]Having the time offset t_0 as a free parameter allows one to fit trajectories of particles with shifted timing (by t_0) relative to the particle that makes the trigger [29]. Timing of particles at the focal planes is discussed in Sec. 3.2.1 and in [29].

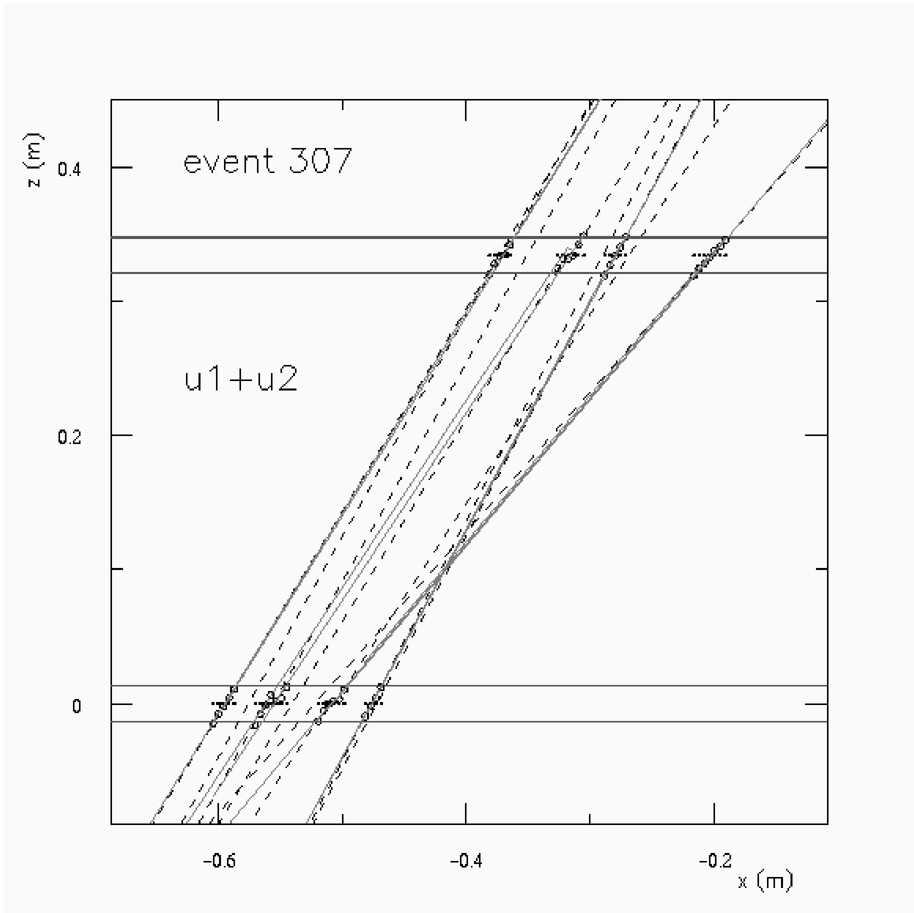

Figure 3-4: Reconstruction of a multiple-track event, electron spectrometer U1 and U2 wire planes.

chambers was confused for the continuation of an original track (Fig. 3-5 (top)), and a situation where the algorithm incorrectly assigned 4 clusters to 2 tracks (Fig. 3-5 (bottom)).

Events shown in Figs. 3-3, 3-4 and 3-5 were ^{3}He(e,e$'$p) coincidence events taken at kinematics 1 (E_{beam} = 4.8 GeV, nominal $P_{miss} = 0$), with the coincidence time between the spectrometers belonging to the real coincidence peak, and with one good track in the other spectrometer (not shown). In all these cases one spectrometer had a single good track with the reconstructed interaction point along the beam within the (-5.16 cm, 5.16 cm) target boundary. The other (shown) spectrometer had the reconstructed interaction point along the beam more than 6 cm outside the target boundary. Therefore, y_{tg} (and possibly other reconstructed coordinates) of the shown

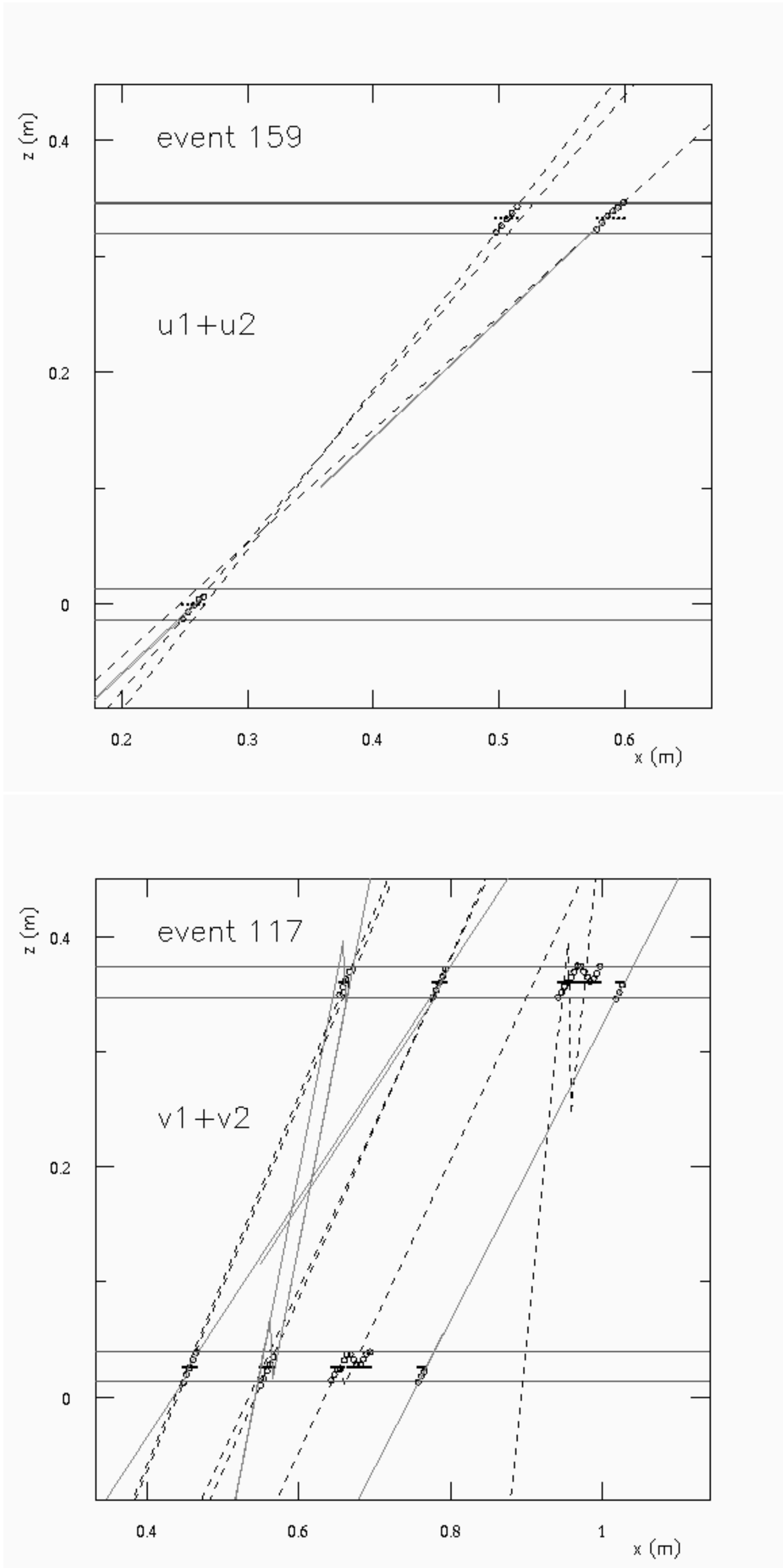

Figure 3-5: Reconstruction of multiple-cluster tracks: (top) hadron spectrometer U1 and U2 wire planes; (bottom) hadron spectrometer V1 and V2 wire planes.

tracks were reconstructed incorrectly.

To exclude poorly reconstructed events from the analysis, the following "tracking" cuts were imposed:

1. The number of clusters in each wire chamber plane equal to 1.

2. The multiplicity[5] of each cluster greater than or equal to 3 and less than or equal to 7.

For the singles events these cuts were imposed only on the spectrometer that issued the trigger; for the coincidence events these cuts were applied to both spectrometers. In addition to eliminating events with high cluster multiplicity (created mostly by delta-rays) and events with multiple tracks, these cuts also excluded events with low multiplicity or a missing cluster of hit wires in any of the wire planes. Such events formed a tiny ($< 0.1\%$) fraction of all recorded events and were mostly background particles that happened to have a trajectory satisfying a "good" trigger logic. In general, these background events reconstructed outside the target boundary.

The tracking efficiency $\epsilon_{tr,i}$ for events of type i was then calculated as

$$\epsilon_{tr,i} = \frac{N_i'}{N_i}, \qquad i = 1, 3, 5, \tag{3.3}$$

where N_i' is the number of events of type i passing the tracking cuts, and N_i is the total number of recorded events of type i.

In the cross section analysis, the detected yield was corrected for events eliminated by the tracking cuts by, essentially, dividing the detected yield by the tracking efficiencies $\epsilon_{tr,i}$ (Sec. 4.5). It was assumed that all events eliminated by the tracking cuts were "good" events that either knocked-on a delta-ray (or another secondary particle), or formed a multiple track with another "good" event. This assumption is precise to $\sim< 0.1\%$, the relative rate of the background events. Another assumption was that the tracking efficiency is uniform over the active area of the drift chambers.

[5]The multiplicity of a cluster of hit wires is defined as the number of hit wires in the cluster. From the geometry of the wire chambers and the spectrometers it follows that a typical single-track event forming 45° with the VDC surface has the multiplicity of 5 [32].

This assumption was found to be correct by a calculation of the tracking efficiency in different regions of the drift chambers [46].

The magnitude of tracking efficiencies $\epsilon_{tr,i}$ varied between kinematic settings and depended mostly on the rate of particles at the focal planes, through changes in the rate of events with multiple tracks. Overall, the tracking efficiency was rather low, ~ 0.8 for the singles and ~ 0.6 for the coincidence events. For the coincidence events, the tracking cuts required a single good track in both spectrometers, while for the singles events the tracking cuts required a single good track in one of the two spectrometers. This is the reason why the tracking efficiency for the coincidence events is lower.

Despite the low tracking efficiencies, the absolute systematic error due to correcting for the efficiencies was found to be $\sim 0.5\%$ for the singles events and $\sim 1\%$ for the coincidence events. These estimates were obtained by observing changes in the rate (per Coulomb of the beam charge) of particles entering the electron spectrometer at different kinematic settings, after correcting the number of particles for the tracking efficiencies and the computer and electronic deadtimes (Sec. 4.3)[6]. The effect of the errors on the ^{3}He(e,e′p) results is estimated in Sec. 6.6.

3.1.3 Gas Cherenkov efficiency

The electron spectrometer Gas Cherenkov detector is described in Sec. 2.6.3. Fig. 3-6 shows the distribution of the sum of the 10 Gas Cherenkov ADCs corrected for pedestals and gains (kinematics 1). The electrons detected in the electron spectrometer were separated from the π^- by a software cut requiring that the sum ($\mathrm{ADC_{sum}}$) is greater than 50.

The Gas Cherenkov inefficiency is defined as the fraction of electrons eliminated by the cut $\mathrm{ADC_{sum}} > 50$. The inefficiency can be found by considering a sample of data containing purely electrons (and no π^-), and calculating the fraction of events eliminated by the cut.

[6]With a wide range of the beam currents used at different kinematics ($10 - 140$ μA), the tracking efficiencies and the deadtimes varied widely between the kinematics. Therefore, the stability of the rate discussed in Sec. 4.3 could be used as a measure of quality of the corrections for the tracking efficiencies and the deadtimes.

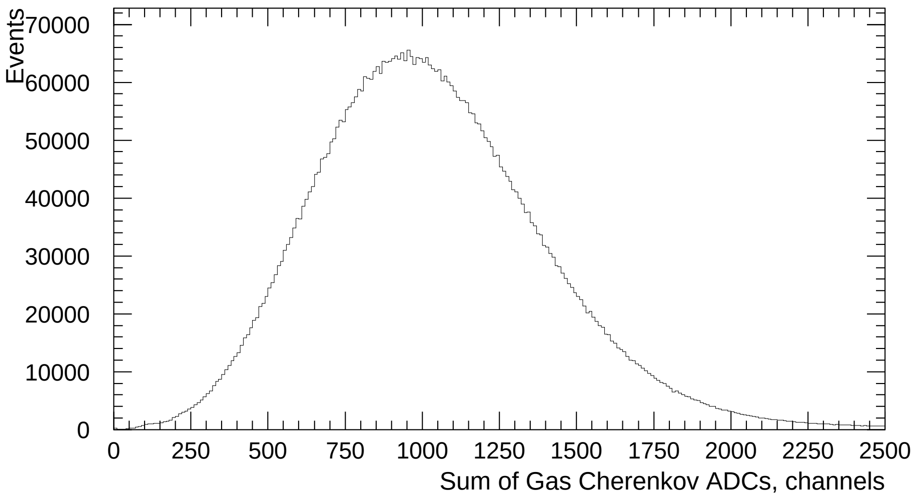

Figure 3-6: Distribution of sum of the 10 Gas Cherenkov ADCs corrected for pedestals and gains. Kinematics 1.

A simple calculation [36] shows that the π^-, truly coincident with a positively charged particle in the hadron spectrometer, are kinematically not allowed in the ^{3}He(e,e′p)D two-body breakup (2bbu) peak. Therefore, to obtain the required pure sample of electrons, one has to apply the E_{miss} cut selecting the 2bbu peak on a sample containing very few accidental coincidence events. Such a sample was obtained from the ^{3}He(e,e′p) data collected at nominal $P_{miss} = 0$ kinematics (where the rate of the accidental coincidences is extremely low), by applying a tight cut on the real coincidence peak (Fig. 5-9). In summary, the required pure sample of electrons was obtained from the ^{3}He(e,e′p)D data collected at nominal $P_{miss} = 0$ kinematics by application of two cuts: 1. the cut selecting the ^{3}He 2bbu peak; 2. the cut selecting the real coincidence peak.

Then, the Gas Cherenkov efficiency was found with

$$\epsilon_{GC} = \frac{N_{cut}}{N_{tot}}, \tag{3.4}$$

where N_{cut} is the number of events in the sample after application of the cut $\mathrm{ADC_{sum}} >$

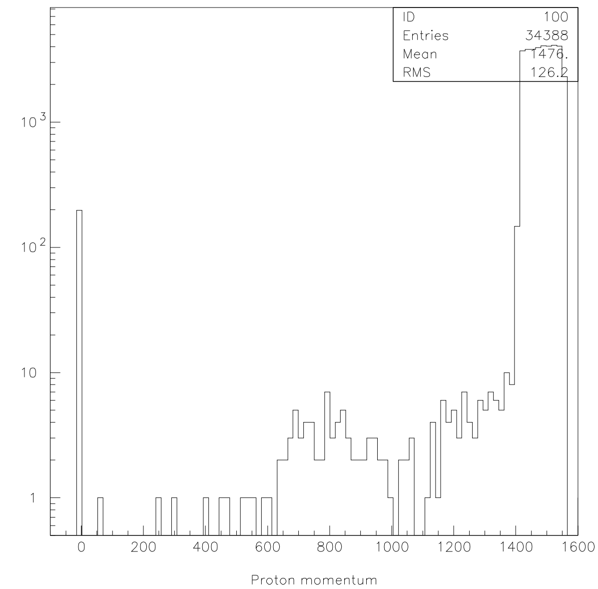

Figure 3-7: Distribution of momentum of protons knocked-out from ^{3}He at the hadron spectrometer entrance window, simulated with GEANT. Figure courtesy of G. Chang, Univ. of Maryland.

50, N_{tot} is the total number of events in the sample. The Gas Cherenkov efficiency determined with the described technique at kinematics 1 and 3 was found to be $\sim$ 0.99994. Statistical errors of the measurements are $< 0.005\%$.

3.1.4 Proton absorption

The fraction of the protons knocked-out from ^{3}He that was lost before reaching the hadron spectrometer scintillators was calculated with a GEANT simulation by George Chang, Univ. of Maryland. The protons are lost due to the energy losses, absorption and p-N rescattering in the target and spectrometer material, and in the air.

The simulation proceeded in 3 phases. In the first phase, events were distributed uniformly over the target length. In the second phase, at each interaction site momenta and angles of the scattered electron and the knocked-out proton were generated using the 3-body kinematics, and the protons were transported through the ^{3}He gas in the target, the Al target walls and air up to the spectrometer entrance. In the third phase, the particles were transferred to the focal plane using the spectrometer forward transfer functions, and transported through the Ti spectrometer exit window and air.

The number of events within the acceptance with and without simulation of energy losses yielded the estimate of proton absorption, $\sim 2.3\%$. This estimate was obtained for the kinematic setting 1 (nominal $P_{miss} = 0$, $E_{beam} = 4.8$ GeV), but is applicable to all kinematic settings analyzed in this thesis, since the hadron spectrometer central momenta were close to 1.5 GeV/c at all kinematic settings. The largest proton absorption, as expected, was due to the proton absorption in the ^{3}He gas in the target. Fig. 3-7 shows the distribution of momentum of the protons at the hadron spectrometer entrance window after the second stage of the simulation with energy losses.

3.2 Calibration of detector and optics databases

3.2.1 Reconstruction of events by ESPACE

Steps performed by the analysis code ESPACE during its reconstruction of each event can be summarized as follows:

1. Reconstruct particle trajectories at the focal plane:

   determine the drift times of electrons in the wire chambers; find the drift distances;

   identify and fit trajectories;

   calculate time-of-flight β and other focal plane variables.

2. Reconstruct trajectories at the target:

   apply optics database (a transformation matrix between the focal plane and the target coordinate systems);

   find the beam position from the BPM information;

   determine x_{tg} from the beam position and known 1st order particle trajectory at the target; apply extended target corrections to θ_{tg} and δ_{tg}.

3. Calculate kinematic variables:

    correct for the mean energy losses of the particles before and after the interaction point;

    calculate kinematic variables;

    correct the coincidence time between the spectrometers for the time of flight of the particles through the spectrometers.

Algorithms used by ESPACE for the identification and fitting of particle trajectories at the focal plane are discussed in Sec. 3.1.2. The transformation between the focal plane and the target coordinate systems and the extended target corrections to θ_{tg} and δ_{tg} are described in Sec. 3.2.3. Here the principles of ESPACE's calculation of the drift times of the ionized electrons in the wire chambers are outlined.

Signals from VDC wires are sent to TDCs that count times between arrival of start signals from the wires and stop signals from the trigger. The trigger was issued based on information from scintillators, and therefore its timing was defined by timing of the scintillator signals. More precisely, the trigger electronics was set up so that the trigger timing was determined by signals from the right phototubes of paddles in the S2 scintillator plane (Sec. 2.8.1).

As a result, the time of arrival of the start signal at the wire chamber TDCs was defined by: the time when a particle ionized atoms in the VDC gas mixture; the drift time of the ionized electrons to the wire; and the time for the signal to pass through the wire, electronics and cables to the start input of the TDC. On the other hand, the time of arrival of the stop signal at the TDC was defined by: the time when the particle emitted light in a paddle in the S2 scintillator plane; the time for the light to reach the right phototube of the paddle; the time for the signal to get converted to an electronic pulse; and the time for the electronic pulse to pass through the cables and trigger electronics to the stop input of the TDC.

The time consumed by the first sequence of events is larger than the time taken by the second, by the time of flight of the particles from the wire chamber plane to the scintillator paddles, less the time counted by the TDC. The time of flight of the particles from the wire chambers to the scintillator paddles can be determined from the reconstructed trajectory of the particle at the focal plane and the particle velocity measured by the TOF between the scintillator planes. Therefore, the drift times of the ionized electrons can be found from a knowledge of timing of signals in the trigger electronics, determined during calibration of the system, and from periods of time calculated on event by event basis.

This is, in fact, how ESPACE calculates the drift times of the ionized electrons [29]. The drift time Δt is converted to the drift distance x with the linear formula $x = v\Delta t$, where $v \approx 4.9 \cdot 10^4$ m/s is the calibrated value of the velocity of propagation of the ionized electrons through the VDC gas mixture. Then, higher-order polynomial corrections, calculated with a GARFIELD [47] simulation of the VDCs, are applied [32].

Timing of signals in the trigger electronics, as well as pedestals of ADCs and gains of the phototubes, are found during the detector calibration, described in the next section.

3.2.2 Detector calibration

The detectors were calibrated in the first phase of analysis. The procedure of calibration of ADC gains and pedestals is similar for both scintillator and Gas Cherenkov ADCs. It is described below, using as an example the calibration of the S0 detector.

The hadron spectrometer detector package included a wide scintillator paddle, named "S0", with two phototubes at its ends, named "top" and "bottom" (Sec. 2.6.1). The paddle was located immediately behind the S1 scintillator plane and was used for the calculation of the hadron trigger efficiency (Sec. 3.1.1). Fig. 3-8 shows the distribution of raw ADC signals from the bottom phototube of the paddle as a function of the position of particle hit along the paddle. The lower band of events corresponds to pions, having the lowest dE/dx. The middle band corresponds to the protons, and the higher band corresponds to the deuterons. The two S0 ADCs were calibrated for ADC pedestals, photomultiplier tube (PMT) gains and light attenuation in the paddle.

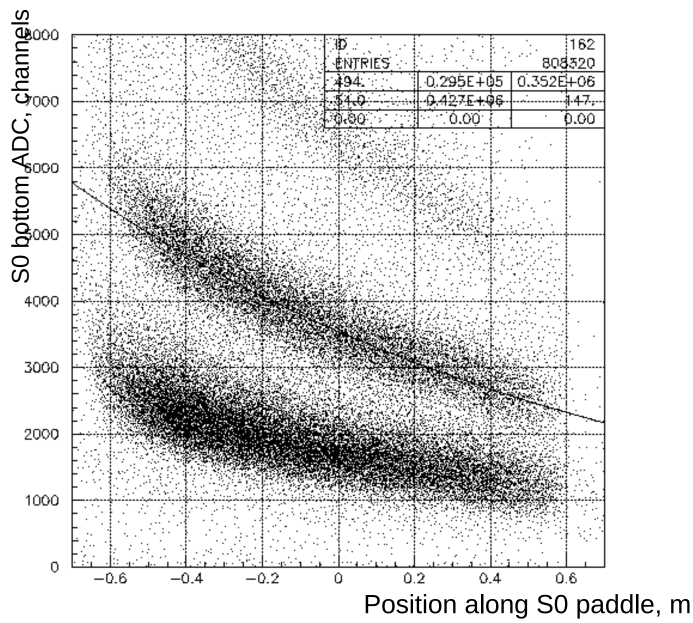

Figure 3-8: The "bottom" S0 ADC corrected for pedestal and gain vs position of particle hit along the S0 paddle. The lower band of events corresponds to π^+, the middle band of events corresponds to protons, and the upper band corresponds to deuterons.

The scintillator ADC pedestal is defined as the ADC readout when there is no signal in the scintillator. ADC values below a set threshold (usually the pedestal value + 10 channels) are normally not read out ("suppressed") during data acquisition, to decrease the event size. The pedestals are found in dedicated "pedestal" runs, when the DAQ is instructed to read out all ADCs, irrespective of their values. ADCs are corrected for pedestals by subtraction of the pedestal values from the raw ADC readout.

The correction for phototube gains is done by multiplication of the ADCs corrected for pedestals by a calibration coefficient. The calibration coefficient is found by requiring that the ADC spectra of the two phototubes, after the corrections for the pedestals and gains, have the same peak values for data uniformly illuminating the focal plane.

The coefficient for the light attenuation in the scintillator paddle is defined as the paddle length over which the ADC signal corrected for the pedestals and gains decreases e times. It is obtained by fitting an exponential[7] to the ADC distribution corrected for the pedestals and gains versus the position of the particle hit along the paddle (Fig. 3-8). The ADC signals are corrected for the light attenuation in the paddle by dividing the ADC variable corrected for the pedestals and gains by the fitted exponential. The resulting ADC variable (corrected for the pedestals, gains and light attenuation) can be used for particle identification (Fig. 3-1).

Timing-related calibrated quantities included:

- the relative signal delays in the scintillator cables and the phototubes;
- the speed of light in the scintillators;
- the relative signal delays in the wire chamber electronics and cables;
- the coefficient for timewalk correction, accounting for the dependence of the time spent to digitize a signal at the discriminator on the signal amplitude.

Many of these quantities were calibrated with a “beta optimization” code written by Nilanga Liyanage: data uniformly illuminating the focal plane is preanalyzed with ESPACE, with particle velocities, scintillator TDCs, the numbers of paddles hit and other parameters of events selected for the detector optimization written to a file. The file is read by the optimization code, which uses various algorithms [29, 35] for calibration of the timing-related coefficients.

In particular, the relative delays in the scintillator cables and the phototubes of adjacent paddles can be found from the events in which a particle hits an overlapping region of the paddles. Then, the difference between the TDCs of the PMTs of the paddles yields the relative delay[8]. The events in which a particle hits a pair of the paddles from the two scintillator planes can be used to find the relative delays between the paddles, from a knowledge of the particle velocity and the trajectory at the focal plane. The speed of light in the scintillators can be found by plotting the difference

[7]The exponential has the form $A\exp(-x/x_0)$, where x is the position of particle hit along the paddle, x_0 is the attenuation coefficient, and A is a free parameter.

[8]This technique assumes that the timewalk correction and the speed of light are the same for both paddles, which in fact is a good approximation for the E89044 experimental setup.

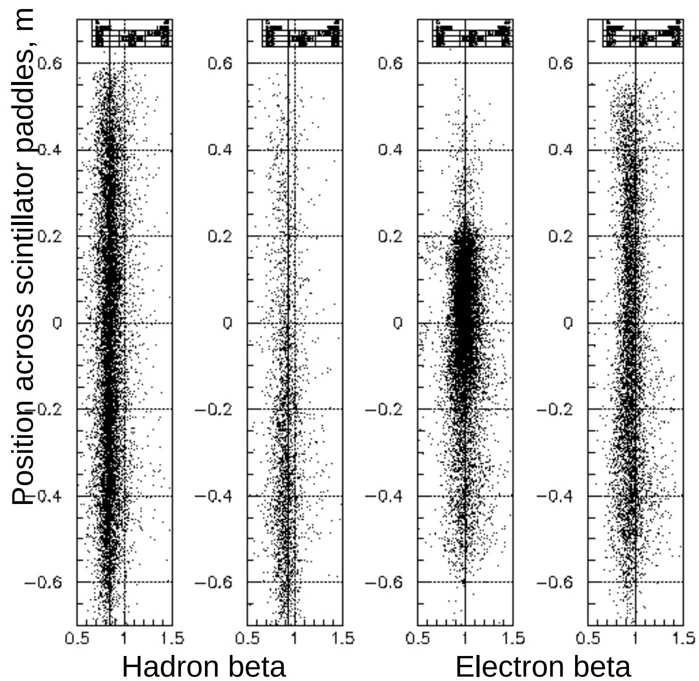

Figure 3-9: Position of particle hit across scintillator paddles vs particle velocity β calculated from TOF between the scintillator planes, after detector calibration. Solid vertical lines indicate β calculated from the particle momentum and rest mass. The beam energies of 1.2 and 4.8 GeV. The four panels from left to right: protons (4.8 GeV, hadron spectrometer), protons (1.2 GeV, hadron spectrometer), electrons (4.8 GeV, electron spectrometer), electrons (1.2 GeV, electron spectrometer).

between the raw TDCs of both PMTs of a paddle, versus the position of the particle hit along the paddle. The slope of the distribution yields the speed of light in the paddle.

The timing-related coefficients are involved in the reconstruction of the particle velocity β from TOF between the scintillator planes. Therefore, one can check the quality of the calibration by comparing β reconstructed from the TOF to β calculated from the particle rest mass and momentum. It is especially useful to make the comparison across the scintillator paddles, to be able to see how well β is reconstructed by each pair of the paddles. This comparison is shown in Fig. 3-9. From the figure one can see that the β reconstructed from the TOF between the scintillator planes closely follows the β calculated from the particle rest mass and momentum at different kinematic settings, for both spectrometers. Therefore, the timing-related coefficients of the spectrometers were optimized well.

3.2.3 Optics calibration

The target coordinate system, denoted by the subscript "tg", and the focal plane coordinate system, denoted by the subscript "fp", are defined in Sec. 2.7. The transformation from the focal plane to the target coordinate system is done through matrix elements Y_{ijkl}, T_{ijkl}, P_{ijkl}, D_{ijkl}, as:

$$y_{tg} = \sum_{i,j,k,l} Y_{ijkl} x^i_{fp} \tan^j \theta_{fp} y^k_{fp} \tan^l \phi_{fp}, \tag{3.5}$$

$$\tan\theta_{tg} = \sum_{i,j,k,l} T_{ijkl} x^i_{fp} \tan^j \theta_{fp} y^k_{fp} \tan^l \phi_{fp}, \tag{3.6}$$

$$\tan\phi_{tg} = \sum_{i,j,k,l} P_{ijkl} x^i_{fp} \tan^j \theta_{fp} y^k_{fp} \tan^l \phi_{fp}, \tag{3.7}$$

$$\delta_{tg} = \sum_{i,j,k,l} D_{ijkl} x^i_{fp} \tan^j \theta_{fp} y^k_{fp} \tan^l \phi_{fp}, \tag{3.8}$$

The symmetry of the spectrometers with respect to their vertical mid-planes implies that

$$T_{ijkl} = D_{ijkl} = 0 \qquad \text{for odd} \quad k+l, \tag{3.9}$$

$$Y_{ijkl} = P_{ijkl} = 0 \qquad \text{for even} \quad k+l. \tag{3.10}$$

The trajectory and the momentum of the particle at the target is fully characterized by 5 target coordinates: y_{tg}, θ_{tg}, ϕ_{tg}, δ_{tg}, x_{tg}. The fifth coordinate x_{tg}, not given by (3.5) – (3.8), is obtained by combining the first-order trajectory given by (3.5) – (3.8) with the beam position information. Then θ_{tg} and δ_{tg} are corrected for non-zero x_{tg} (described below).

It is important to realize that even with the beam position centered exactly at (0,0) in the hall coordinate system (HCS), for extended targets the x_{tg} coordinate of the trajectories can be quite large [29], leading to relatively large corrections to θ_{tg}

and δ_{tg}. The x_{tg} corrections are linear in the first order: $\Delta\theta_{tg} = \alpha x_{tg}$, $\Delta\delta_{tg} = \beta x_{tg}$, and therefore asymmetric with respect to x_{tg}. Up to the spring of 1999, this has led to so called "spectrometer mid-plane asymmetry problem", depicted in Fig. 3-10. Shown are the θ_{tg} vs ϕ_{tg} distributions for the ^{12}C(e,e) sieve slit data of the E94010 experiment. The electron spectrometer was located at the scattering angle of 15.5°, the beam was unrastered and centered at (0, 0) in the HCS. The top (bottom) figure corresponds to elastic scattering from a thin carbon foil located 13.2 cm downstream (upstream) from the target center. The squares in the figures denote the "correct" θ_{tg} and ϕ_{tg} values, calculated from the geometry of the sieve slit, the targets and the beam position.

The θ_{tg} values for the downstream foil are reconstructed at larger than the correct absolute values, while for the upstream foil – at lower than the correct absolute values. This apparently breaks the mid-plane symmetry of the electron spectrometer (given by (3.9)). For some time this effect was attempted to be corrected by introduction of "asymmetric" matrix elements in the optics databases, following a suspicion of an asymmetry allowed during manufacturing of the spectrometers. The author of this thesis is proud to be the one to realize that the source of the asymmetry was in fact not in an asymmetry of the spectrometers, but in the absence of the extended target corrections both in the optimization and in the reconstruction routines. Fig. 3-10 gives an idea of the magnitude and the sign of the extended θ_{tg} corrections.

In general, the matrix elements Y_{ijkl}, T_{ijkl}, P_{ijkl}, D_{ijkl} of the optics databases are calibrated by: 1. Collection of data so that some of kinematic quantities of the detected particles are known. 2. Adjustment of the matrix elements so that the known kinematic quantities of the particles are correctly reconstructed by the analysis code. Normally, the data used for the calibration is a ^{12}C(e,e) elastic sieve slit data, such as the one described above. Then, the Y_{ijkl} matrix elements are calibrated using the events scattered from the thin carbon foils and a knowledge of the location of the foils. The T_{ijkl} and P_{ijkl} matrix elements are calibrated using the events passing through the sieve slit holes and a knowledge of the geometry of the sieve slit and the location of the targets. Finally, the D_{ijkl} matrix elements are calibrated using the electrons

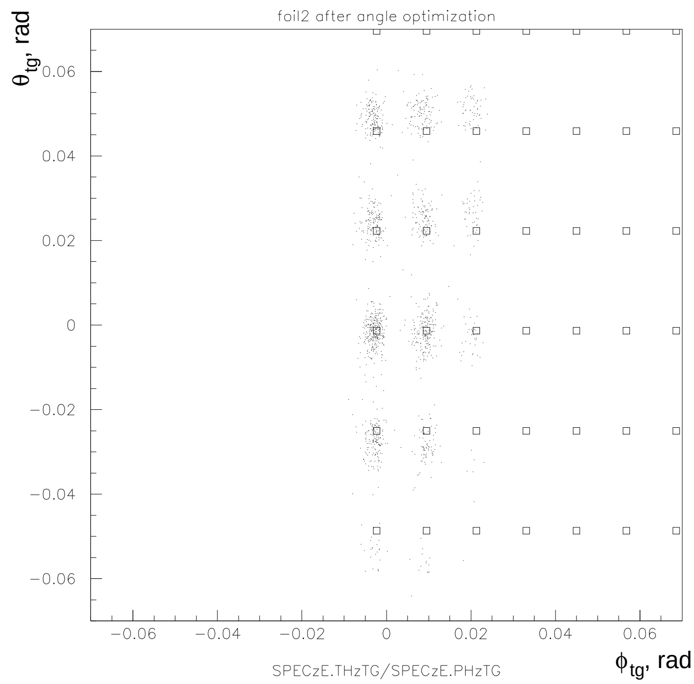

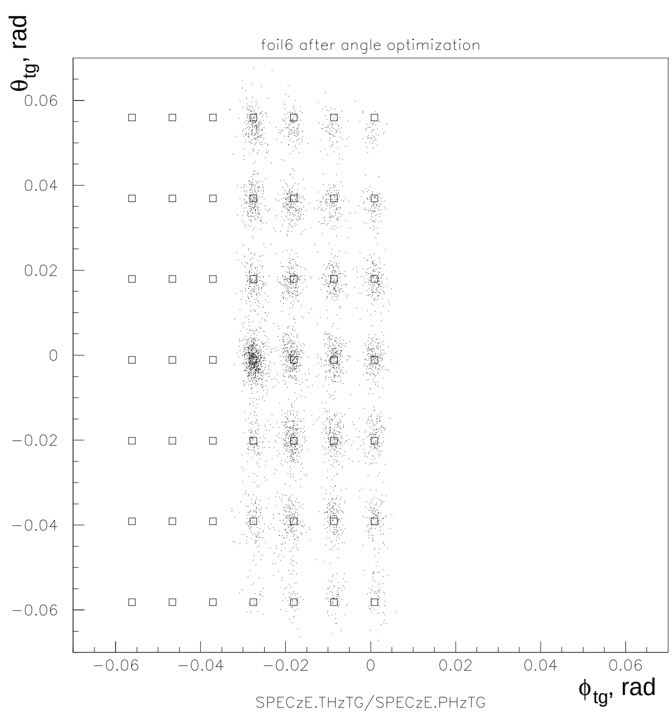

Figure 3-10: Reconstruction of events without extended target corrections to θ_{tg}; sieve slit ^{12}C(e,e) data for scattering from a carbon foil located 13.2 cm downstream (top), and 13.2 cm upstream (bottom) from the target center.

scattered elastically from the carbon foils and a knowledge of the momentum of the electrons. The calibration procedures are documented in detail in [35, 36, 37].

The ^{12}C(e,e) sieve slit data can be collected with high enough statistics only at relatively low momentum settings of the spectrometers and the beam energies, where the cross section for the ^{12}C(e,e) elastic scattering is sufficiently high. At higher spectrometer momenta, a different set of data must be used. For example, Nilanga Liyanage has developed a "C-optimizer" software package [35] that calibrates a chosen set of the matrix elements by requiring the correct reconstruction of a discrete missing energy peak for a generic A(e,e$'$p)B reaction.

The distribution of magnetic field lines in the spectrometers (the "spectrometer optics") is attempted to be kept alike at all spectrometer central momentum settings, by the variation of the currents through the Q1, Q2 and Q3 quadrupole magnets proportionally to a measured magnetic field in the dipole magnet, so that the optics database obtained at lower spectrometer momentum settings is applicable at other spectrometer momenta. However, just before the start of the experiment it was found that hysteresis effects in the iron collars of the Q2 and Q3 magnets of both spectrometers do appreciably distort the optics. A cycling procedure, involving increasing the currents in the Q2 and Q3 magnets to 1600 A with each increase in their momentum setting, did rectify some of the optics distortions. Nevertheless, residual distortions in the optics warranted the use of different optics databases at different momentum settings.

Most data presented in this thesis was collected with the electron spectrometer central momentum set at 418 MeV/c (Σ_3 kinematic settings) or at 3966 MeV/c (Σ_1 and Σ_2 kinematic settings), and with the hadron spectrometer momentum kept in the range 1170 – 1480 MeV/c. Separate optics databases were used for the two electron spectrometer central momenta, while a single optics database was used for the hadron spectrometer.

The Y_{ijkl} matrix elements of the three databases and the T_{ijkl}, P_{ijkl} and D_{ijkl} matrix elements of the 417 MeV/c electron spectrometer database were calibrated using the ^{12}C(e,e) elastic sieve slit data collected during the commissioning period of the

E89044 experiment. The calibration procedure is documented in detail in [35, 36, 37]. The calibration was performed by Nilanga Liyanage. Using his "C-optimizer" code [35], Nilanga Liyanage also calibrated the D_{ijkl} (momentum) matrix elements of the hadron spectrometer database and the 3966 MeV/c electron spectrometer database, by requiring the correct reconstruction of the ^{3}He(e,e$'$p)D peak position in the E_{miss} spectrum. This calibration procedure uses the fact that the E_{miss} variable for the ^{3}He(e,e$'$p) events at Σ_1 and Σ_2 kinematics (the beam energy of 4.8 GeV) is very sensitive to the quality of the reconstruction of momentum of the detected electron and the proton (Sec. 5.7, [35]). The P_{ijkl} and T_{ijkl} (angular) matrix elements of the hadron spectrometer database and the 3966 MeV/c electron spectrometer database were calibrated by Zhengwei Chai using H(e,ep) elastic sieve slit data of the E91011 experiment. The E91011 experiment was conducted in the summer of 2000 in the Hall A and used spectrometer settings close to the E89044 spectrometer settings. This calibration procedure is documented in detail in [48].

With the extensive help from Nilanga Liyanage and Zhengwei Chai, the author of this thesis only had to calibrate the E89044 detectors (Sec. 3.2.2) and the central momenta of the spectrometers (Sec. 5.7), to make corrections for small errors in the 3966 MeV/c electron spectrometer database (discussed below and in Sec. 5.7), and to select the optics matrix elements that perform best at the kinematics of the E89044 experiment from all available optics databases[9].

The resolution of the reconstruction of the target variables using the final set of the databases is discussed in Sec. 5.2.2. The E_{miss} resolution is represented in Figs. 5-21 through 5-39, which show the reconstructed ^{3}He(e,e$'$p)D peak in the E_{miss} spectrum for each spectrometer setting. The achieved resolution in the reconstruction of the reaction point along the beam is represented in Figs. 5-7 and 5-8. Fig. 5-9 shows the distribution of the coincidence time between the spectrometers corrected for the time of flight of particles to the focal planes. The full width at half maximum of $\sim$ 1.3 ns for the real (e,e$'$p) coincidence peak is indicative of a good reconstruction of

[9]The author has a deep practical knowledge of calibration of the optics of the Hall A spectrometers from his calibration of both the detectors and the optics for the E94010 experiment in the spring of 1999.

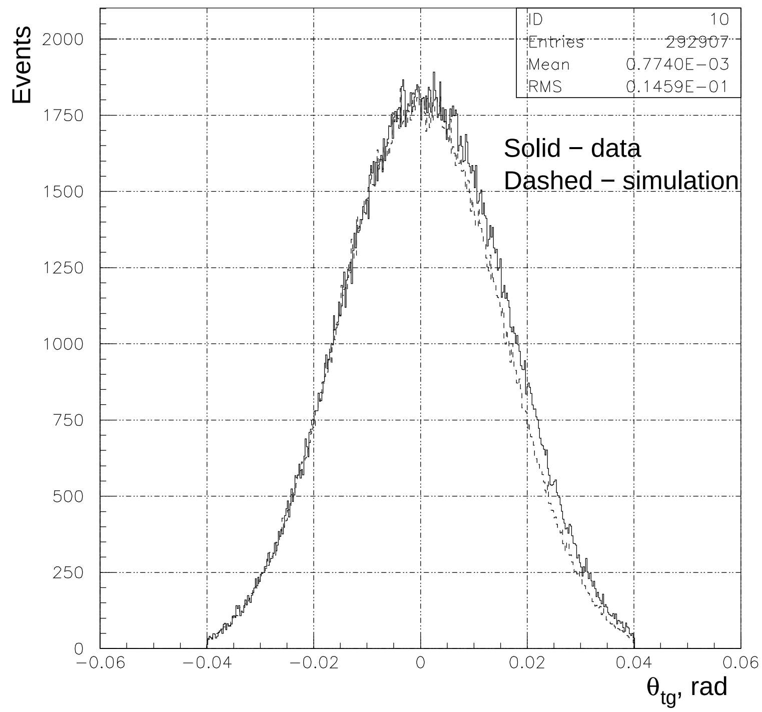

Figure 3-11: Distribution of θ_{tg} reconstructed with the 3966 MeV/c electron spectrometer optics database (solid), and that simulated with MCEEP (dashed), at kinematics 1, before a correction to θ_{tg}; see text for details.

the vertical and horizontal angles of the detected particles.

An offset of -1.23 mrad was later applied to θ_{tg} (the vertical angle) reconstructed by the 3966 MeV/c electron spectrometer optics database, to correct for an observed shift in the θ_{tg} reconstruction. The shift is illustrated in Fig. 3-11. Shown is the distribution of the electron spectrometer θ_{tg} for the data (solid) and simulation (dashed) at kinematics 1, with the "square" acceptance cuts applied to data and simulation: $|\phi_{tge}| < 20$ mrad, $|\theta_{tge}| < 40$ mrad, $|\delta_{tge}| < 3\%$, $|z_{labe}| < 3.5$ cm; an E_{miss} cut selecting the ^{3}He(e,e$'$p)D two-body breakup (2bbu) peak was also applied. With the unpolarized ^{3}He target, the ^{3}He(e,e$'$p) cross section is symmetric with respect to the out-of-plane angle. The slight shift in the θ_{tg} reconstruction was most probably caused by a ~ 1 mm vertical offset of the sieve slit during collection of the E91010 optics data.

3.3 Spectrometer mispointing

Each of the two high resolution spectrometers ideally would have just one spatial degree of freedom – rotational around the center of the hall, with the spectrometer central rays going through the hall center. In reality, although "pitch"(the angle between a horizontal plane and the Q1 optical axis) and "roll" (the rotational angle around the Q1 optical axis) displacements were negligible, a translational movement of the spectrometers caused the central rays to miss the hall center in the horizontal direction up to 3 mm and in the vertical direction up to 0.5 mm. These movements were not reproducible, i.e. at the same angular location at a different time each spectrometer could have had a different "horizontal pointing" (the horizontal distance between the spectrometer central ray and the hall center; the horizontal pointing is also known as the "spectrometer mispointing") and the vertical offset. Two reliable methods of measurement of these displacements were available:

1. A survey of the spectrometers, giving both the horizontal pointing and the vertical offset.

2. The calculation of the horizontal pointing from the position of the carbon foil along the beam reconstructed by a spectrometer (and a knowledge of the location of the carbon foil target; "pointing" runs with an unrastered beam and the carbon foil as the target were made at many kinematic settings).

The most precise information came from the surveys, which were performed several times during the experiment. In particular, the electron spectrometer location (which was fixed most of the time) at the 4.8 GeV and 1.2 GeV kinematics, as well as the location of the hadron spectrometer at several kinematic settings, was determined from the surveys. For the spectrometer settings for which the surveys were not available, the vertical offset was deduced from the closest in time and the spectrometer angle vertical offset given by the surveys; the horizontal pointing was calculated using the carbon "pointing" runs, as outlined below.

For a spectrometer central scattering angle θ_0 (determined from floor marks, > 0), the beam position centered at (0, 0) in the HCS[10], and the carbon foil offset along the beam z_{lab} (positive – downstream), the horizontal pointing Δl (positive – downstream) is given by

$$\Delta l = S \cdot y_{tg} + z_{lab} \sin(\theta_0), \tag{3.11}$$

where S is equal to 1 for the electron spectrometer and to -1 for the hadron spectrometer, and y_{tg} is the position of the carbon foil reconstructed by the spectrometer. This formula simply reflects the transformation between the target and the hall coordinate systems. The accuracy of the method was studied by a comparison with the horizontal pointings given by the surveys [49], and was found to be ~ 0.5 mm.

The horizontal pointing Δl gave an important correction $\Delta\theta_0$ to the central scattering angle of the spectrometers, through

$$\Delta\theta_0 = \Delta l / L, \tag{3.12}$$

where $L = 8.458$ m is the distance between the hall center and the floor marks designating the spectrometer angles. In general, the mispointing Δl was about 2 mm, corresponding to a ~ 0.2 mrad correction to the central scattering angle θ_0. In the analysis of systematic errors of the ^{3}He(e,e$'$p) measurements (Sec. 6.6), the uncertainty in the reconstructed horizontal angles of the detected particles, including the uncertainty in the determination of the central spectrometer angles, was estimated to be 0.3 mrad.

3.4 Computer and electronic deadtimes

The computer deadtime arises due to the inability of the DAQ system to record events occurring during a DAQ "dead time", when it is recording another event. Still, the total number of events of each type is counted by scalers, which allows one to correct for the number of events not recorded. For trigger type i, prescaled with an integer

[10] The Hall Coordinate System (Sec. 2.7).

prescale factor P_i (i.e. when the DAQ is set to record every P_ith event of type i), the computer deadtime $\epsilon_{cdt,i}$ for the E89044 trigger setup can be computed as [50]

$$\epsilon_{cdt,i} = 1 - N_i P_i / S'_i, \quad i = 1, ..., 5, \tag{3.13}$$

$$S'_i = S_i, \quad i = 2, 4, 5, \tag{3.14}$$

$$S'_i = S_i - S_5 - N_{14}, \quad i = 1, 3, \tag{3.15}$$

where S_i is the end-of-run scaler count for trigger type i, and N_i is the number of recorded events of type i. The subtraction of S_5 and N_{14} from S_1 and S_3 in formula (3.15) is necessary, since, in the trigger setup used, the S_1 and S_3 scalers overcounted the number of the singles triggers by the number of the coincidence triggers (S_5) and the number of triggers type 14 (N_{14}). The trigger type 14 occurred (very infrequently) when there was an overlap of 10 ns or less between different triggers at the trigger supervisor. The prescale factor for the coincidence trigger (P_5) was set to 1 in all measurements. In cross section measurements, the computer deadtime was kept below 20% by prescaling the singles triggers or an adjustment of the beam current.

The electronic deadtime arises due to non-zero time widths of digital signals in the front-end electronics. As a result, at high rates of data acquisition some of the signals merge, sometimes decreasing the numbers counted by the scalers. The electronic deadtime for the E89044 trigger setup was thoroughly studied by M. Jones and R. Michaels [50], during the E91011 ("N-delta") experiment in the summer of 2000. They introduced into the E91010 datastream artificial triggers, caused by a pulser sending scintillator-type signals to a linear OR with the paddle signals in both scintillator planes of both spectrometers, thus imitating the regular physics triggers occurring during the data acquisition. The ratio of the number of the recorded events of this type (discriminated from the rest of the data by a tag in a TDC channel), corrected for the computer deadtime and prescaling, to the number of issued pulser-type triggers (reliably counted by dedicated scalers), yielded the electronic deadtime. The electronic deadtime found with this procedure for the coincidence trigger, for a wide range of the sum of the strobe rates in the electron and hadron spectrometers, is plotted in Fig. 3-12. The following parametrization of the electronic deadtime for trigger types 1, 3 and 5 was obtained in [50]:

$$\epsilon_{edt,i} = (0.019 \cdot \mathrm{kHz}^{-1}) \cdot R_i^S, \qquad i = 1, 3, 5, \tag{3.16}$$

were $\epsilon_{edt,i}$ is the electronic deadtime of trigger type i, R_1^S (R_3^S) is the strobe rate in the electron (hadron) spectrometer, $R_5^S = R_1^S + R_3^S$ is the total strobe rate.

The strobe rates in the electron and hadron spectrometers can be found from the rates of signals in the scintillator paddles, as [50]

$$R_1^S = (0.613 \pm 0.001) \cdot \sum_{j,k} R_{j,k,1}, \quad j = 1, ..., 6, \quad k = 1, 2, \tag{3.17}$$

$$R_3^S = (0.620 \pm 0.0007) \cdot \sum_{j,k} R_{j,k,3} - (5.1 \pm 0.04) 10^{-5} \cdot (\sum_{j,k} R_{j,k,3})^2, \tag{3.18}$$

$$j = 1, ..., 6, \quad k = 1, 2,$$

where $R_{j,k,1}$ ($R_{j,k,3}$) is the rate of pulses in the right phototube of paddle j in scintillator plane k of the electron (hadron) spectrometer (in kHz). The errors given in (3.17) and (3.18) are systematic (a $\sim$ 0.2% relative error on the calculated strobe rates) [50]. The overall systematic error of the calculated electronic deadtime is a $\sim$ 25% relative error for the total strobe rates below 500 kHz, and a $\sim$ 10% relative error for the total strobe rates above 500 kHz [50].

The electronic and computer deadtimes are combined as

$$\epsilon_{dt} = 1 - (1 - \epsilon_{cdt})(1 - \epsilon_{edt}) \tag{3.19}$$

to yield the total deadtime ϵ_{dt} for each trigger type.

For the highest strobe rates in the ^{3}He(e,e$'$p) measurements, at kinematics 14, the electronic deadtime was $\sim$ 16%, with the sum of the strobe rates $\sim$ 830 kHz, and the absolute systematic error of $\sim$ 1.6% due to correcting for the electronic deadtime.

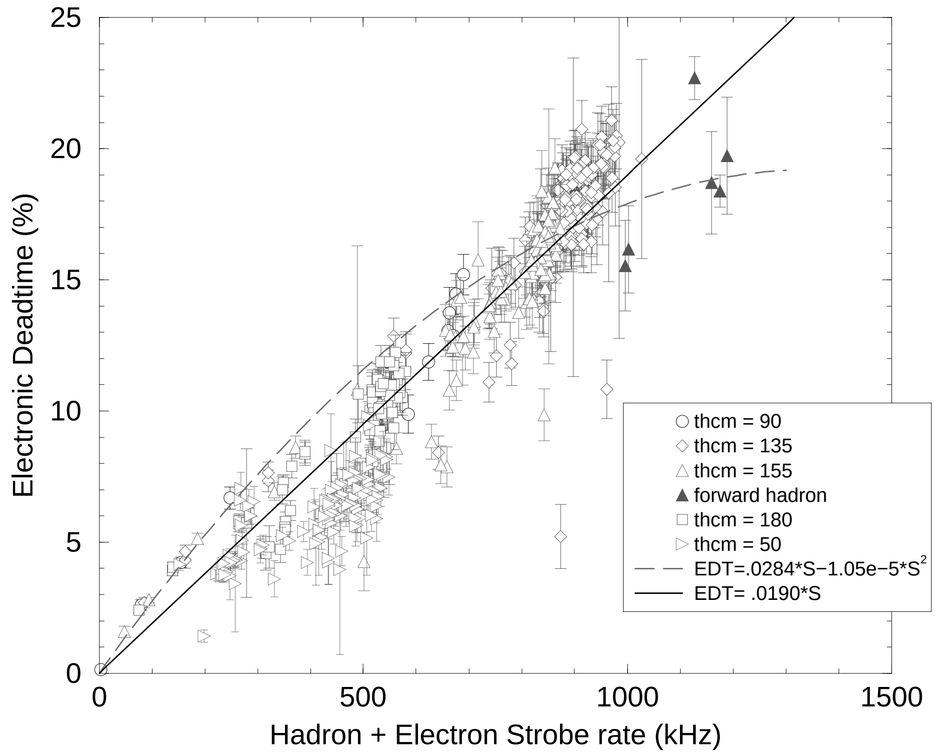

Figure 3-12: Electronic deadtime measured at different values of the sum of the strobe rates in the spectrometers. Figure courtesy of M. Jones [50].

At a majority of the spectrometer settings, however, the electronic deadtime and the systematic error associated with correcting for the deadtime were much smaller. The systematic error of the calculated computer deadtime is a $\sim 10\%$ relative error [40]. The influence of these errors on ^{3}He(e,e$'$p) analysis results is estimated in Sec. 6.6.

Chapter 4

Normalization of quasielastic data

4.1 Overview

The main objective of the experiment, the extraction of ^{3}He(e,e′p) cross sections, requires a knowledge of integrated luminosities during the ^{3}He(e,e′p) runs. If the integrated luminosity $\int Ldt$ is known for a run, the total cross section, σ, of scattering into a kinematic bin (uncorrected for radiation) is given simply by [51]

$$\sigma = \frac{N}{\epsilon_{eff}} \frac{1}{\int Ldt}, \tag{4.1}$$

where N is the number of events detected in the kinematic bin during the run, and ϵ_{eff} is a factor accounting for prescaling and the efficiency of particle detection.

For electrons of a total charge Q passing through the target of length l containing the ^{3}He gas of density ρ, the integrated luminosity is given by

$$\int Ldt = \frac{Q}{e} \frac{N_A \rho}{A_{^3He}} l, \tag{4.2}$$

where: $e = 1.602 \cdot 10^{-19}$ Coulomb is the electron charge, $A_{^3He} = 3.016$ g/mol is the atomic mass of ^{3}He, and $N_A = 6.022 \cdot 10^{23}$ mol^{-1} is Avogadro's number. For a given target nucleus and charge of incident particles, the integrated luminosity can also be expressed in units of [Coulomb·g/cm^2], with

$$\int L dt = Q \rho l.$$

The charge Q passing through the ^{3}He target during a run can be found with a high precision with BCMs (Sec. 2.3.2). The target length l of the ^{3}He "tuna can" target was measured to be 10.32 cm, or could be effectively set to a smaller value by a software cut on the reconstructed interaction point along the beam.

The density ρ of ^{3}He gas in the target can in principle be found by application of the ^{3}He equation of state to pressure and temperature readings from sensors located in the target. At a temperature of 6.3 K and pressures of 122 – 160 psi, as used in the experiment, however, the ^{3}He equation of state is not known with a high precision. Prof. Margaziotis from Cal State L. A. used the law of corresponding states (stating that for many gases equations of states, expressed in reduced temperatures, pressures and densities, are identical) and the accurately known ^{4}He equation of state to calculate the ^{3}He density for several values of temperature and pressure, close to those used in the experiment (Fig. 4-1). An estimate of the error of the calculation is not available, but is believed to be $\sim 7\%$.

A more precise approach to determination of the ^{3}He density in the target was based on "renormalization" of measured elastic ^{3}He(e,e) cross sections to world data. With this purpose, elastic ^{3}He(e,e) data was collected at each beam energy used, except for the beam energy of 4.8 GeV (explained below). In one analysis technique, described in Sec. 4.2, the ^{3}He(e,e) elastic yield was limited to a flat spectrometer acceptance region, and was compared to the yield in full MCEEP ^{3}He(e,e) simulation, after application of identical acceptance cuts. The ^{3}He(e,e) cross section model in the simulation was based on a fit of the ^{3}He elastic form factors to world ^{3}He(e,e) cross section data [52]. The density of ^{3}He in the simulation is adjusted to reproduce the measured yield in the elastic peak, after which both the ^{3}He density and the integrated luminosity for the analyzed elastic runs is known.

If the integrated luminosity is known for a run, it can be found for other runs

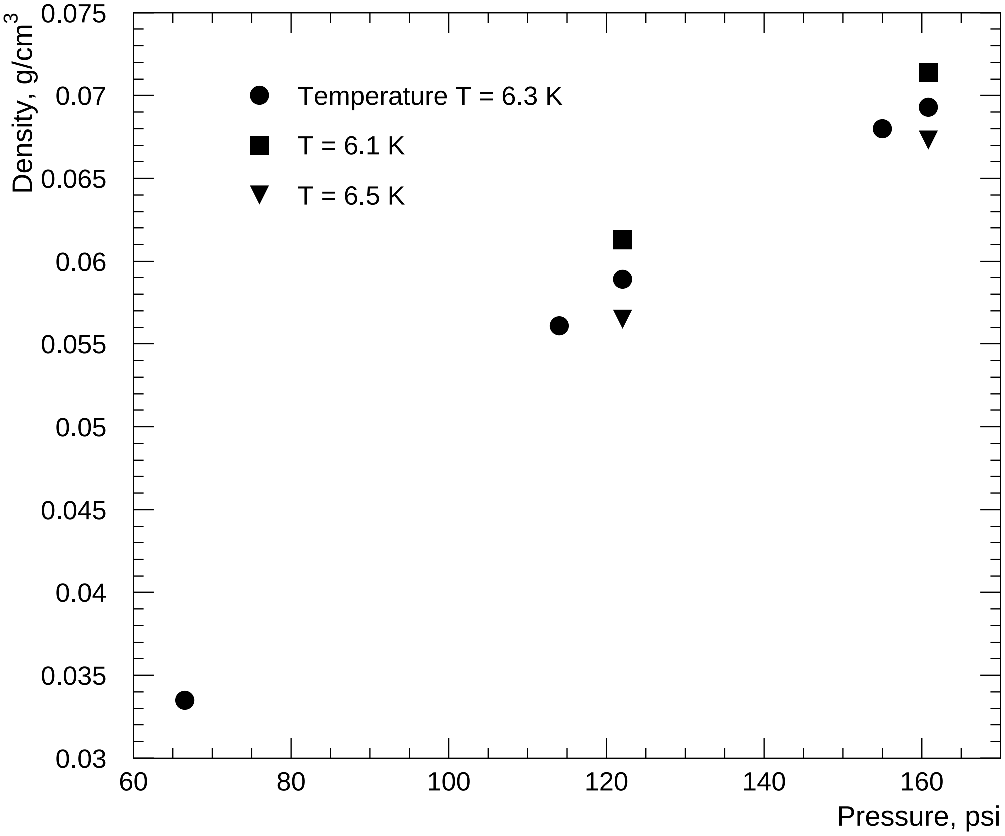

Figure 4-1: Density of ^{3}He gas at several values of temperature and pressure, calculated with the law of corresponding states and the ^{4}He equation of state (calculation provided by D. Margaziotis, Cal State L. A.). ^{3}He(e,e′p) data used in the cross section analysis was collected at ^{3}He temperature of 6.3 K and pressures 122 and 160 psi.

taken at the same beam energy with a procedure known as “luminosity monitoring” (described in Sec. 4.5). This technique is based on the fact that for a given beam energy and a spectrometer setting, the number of particles passing through a chosen spectrometer acceptance region in a given run is to a good approximation proportional to the integrated luminosity for that run. Hence, the integrated luminosity $\int Ldt$ for an “investigated” run can be determined from the known integrated luminosity $(\int Ldt)'$ during a “reference” run, with

$$\int Ldt = \frac{N}{\epsilon_{eff}} \frac{\epsilon'_{eff}}{N'} (\int Ldt)', \tag{4.3}$$

where N (N') is the number of events satisfying a fixed acceptance cut and detected in the investigated (reference) run, and ϵ_{eff} (ϵ'_{eff}) is the correction for efficiency of particle detection and prescaling in the investigated (reference) run.

Originally it was planned to determine the ^{3}He density (and the integrated luminosity) at each beam energy with elastic ^{3}He(e,e) scattering runs, with the electron spectrometer located closest to the beam dump angular position, $\approx 12.5°$ (and hence the lowest Q^2 for a beam energy, where the ^{3}He elastic form factors are known better), and then to monitor the luminosity in all other runs of the same beam energy with a spectrometer fixed during kinematics change. For beam energies of 2 – 4.8 GeV and the scattering angle of 12.5° ($5\ \mathrm{fm}^{-2} < Q^2 < 27\ \mathrm{fm}^{-2}$), the ^{3}He form factors are known with only 2 – 10% precision. It was therefore intended to improve the knowledge of the ^{3}He elastic form factors at Q^2 values corresponding to the elastic normalization runs, in a set of ^{3}He(e,e) measurements at a lower beam energy of 0.644 GeV.

This original plan of normalization of the ^{3}He(e,e$'$p) data was subsequently modified to include a single measurement of the ^{3}He density at the beam energy of 0.644 GeV, as the following circumstances became apparent:

- at the beam energy of 4.8 GeV the measurement of the elastic ^{3}He(e,e) cross section with a high statistical precision at low scattering angles was not feasible, since the central momentum of the electron spectrometer could not be set above 4 GeV/c;
- the ^{3}He density obtained from the ^{3}He(e,e) elastic measurements at the beam energy of 1.2 GeV and an electron scattering angle of 12.5° had a substantially higher systematic error than the density deduced from the ^{3}He(e,e) measurements at a beam energy of 0.644 GeV and an electron scattering angle of 30.8°, due to a higher sensitivity of the elastic cross sections to the scattering angle at lower scattering angles, and higher than expected error in determination of scattering angles;
- the density of ^{3}He in the target was observed to be stable to $\sim 0.5\%$ over periods of weeks; the stability of the ^{3}He target density could be further reliably

Time period, year 2000	Nominal beam energy, GeV	Measurements
Feb 7 – Feb 10	1.9	^{3}He(e,e$'$p)
Feb 11 – March 2	4.8	^{3}He(e,e$'$p)
March 3 – March 4	0.644	^{3}He(e,e)
March 6 – March 23	1.2	^{3}He(e,e$'$p)

Table 4.1: Time course of collection of ^{3}He quasielastic and elastic data analyzed in this thesis.

monitored by temperature and pressure sensors.

Table 4.1 presents the chronology of the measurements analyzed in this thesis. Quasielastic ^{3}He(e,e$'$p) measurements in perpendicular kinematics were done in succession with a set of ^{3}He(e,e) elastic measurements at a beam energy of 0.644 GeV, a subset of which could be used to determine the ^{3}He density with the highest precision achievable in the experiment. The density of ^{3}He in the target was not manipulated during all the beam energy changes and during the 0.644 GeV running[1], and its stability during these periods was further confirmed by consistent readings from pressure and temperature sensors in the target.

After analysis of errors associated with available methods of normalization of the ^{3}He(e,e$'$p) data, it was decided to use the following scheme:

1. Determine the ^{3}He density from the set of ^{3}He(e,e) measurements at the beam energy of 0.644 GeV.

2. Assume, taking into account the associated error, that the measured ^{3}He density at the beam energy of 0.644 GeV was equal to the ^{3}He density at the end of the 4.8 GeV and at the start of the 1.2 GeV ^{3}He(e,e$'$p) running, multiplied by appropriate boiling coefficients[2].

3. Monitor luminosity from the end of the 4.8 GeV running through the rest of 4.8 GeV kinematic settings by the fixed electron spectrometer.

[1]I.e., the amount of ^{3}He gas in the target loop was kept constant, and the ^{3}He temperature was fixed at 6.3 K by a feedback system.

[2]The boiling coefficients account for changes in the target density due to heating by the beam (Sec. 4.4).

4. Monitor luminosity from the start of the 1.2 GeV running through the rest of 1.2 GeV kinematic settings by the fixed electron spectrometer.

5. Assume, taking into account the associated error, that the ^{3}He density at the end of the 1.9 GeV running was equal to that at the start of the 4.8 GeV running, multiplied by the appropriate boiling coefficient.

6. Monitor luminosity through the rest of 1.9 GeV kinematic settings by the fixed electron spectrometer.

The rest of this chapter presents the extraction of the ^{3}He density from $E_{beam} =$ 0.644 MeV elastic ^{3}He(e,e) measurements (Sec. 4.2), the analysis of long-term target density stability (Sec. 4.3), the study of changes in ^{3}He gas density due to heating by the beam (Sec. 4.4), and the luminosity monitoring procedure (Sec. 4.5 and 4.6).

4.2 ^{3}He density and ^{3}He(e,e) elastic scattering

4.2.1 ^{12}C(e,e) measurements

"Pointing" runs with a carbon foil as the target and an unrastered beam were taken at almost all spectrometer settings to measure the mispointing of the spectrometers (Sec. 3.3). At the ^{3}He(e,e) elastic kinematics, electrons elastically scattered from the carbon foil fell within the HRSE acceptance. With the carbon foil thickness measured with a 1% precision and the cross section of elastic ^{12}C(e,e) scattering being well known, it was decided to check analysis techniques by extracting the ^{12}C(e,e) elastic cross sections from the pointing runs. The cross sections were extracted by comparing the yield in the elastic peak in a full MCEEP simulation of the pointing runs to that detected experimentally, as described below.

For relativistic electrons of momentum p_i, elastically scattering from a nucleus with mass M_A, momentum of the scattered electrons p depends on the scattering angle θ as [51]

$$p = \frac{p_i}{1 + \frac{p_i}{M_A}(1 - \cos\theta)}. \tag{4.4}$$

A more convenient variable representing the momentum of the scattered electrons, but independent of the scattering angle is the "kinematically corrected momentum" p_{kin}, defined as

$$p_{kin} = p\frac{1+\frac{p_i}{M_A}(1-\cos\theta)}{1+\frac{p_i}{M_A}(1-\cos\theta_0)}, \tag{4.5}$$

where θ_0 is the central scattering angle of the spectrometer. The independence of p_{kin} from θ is easily verified by substitution of (4.4) in (4.5): $p_{kin} = p_i/(1+\frac{p_i}{M_A}(1-\cos\theta_0))$.

Kinematically corrected relative momentum dp_{kin} is introduced as

$$dp_{kin} = \frac{p_{kin}-p_0}{p_0}, \tag{4.6}$$

where p_0 is the central momentum of the spectrometer.

Fig. 4-2 (a) shows the distribution of the kinematically corrected relative momentum dp_{kin} of electrons detected within the HRSE acceptance during the ^{12}C(e,e$'$) "pointing" run 2538 (beam energy $E_{beam} = 0.644$ GeV, central scattering angle $\theta_{scat} = 41.2°$, Q^2=5 fm^{-2}). The peak centered at $dp_{kin} = 0$ represents the elastically scattered electrons. The peak is shown in Fig 4-2 (b), together with a MCEEP simulation of the elastic ^{12}C(e,e) yield, after application of identical acceptance cuts to data and simulation: $|\phi_{tge}| < 0.02$ rad, $|\theta_{tge}| < 0.04$ rad, $-0.035 < \delta_{tge} < 0.03$, and a cut on dp_{kin} selecting the elastic peak. The simulation used the elastic ^{12}C(e,e) cross section model of Offermann et al [53], a simple form of Coulomb correction through the calculation of effective momentum transfer [14], and the standard MCEEP approach to simulation of radiation, energy losses and multiple scattering (Sec. 5.2). Spectrometer resolution was simulated by addition of Gaussian functions to generated transport variables ϕ_{tge}, θ_{tge}, y_{tge}, δ_{tge}.

A MCEEP simulation of yield requires an input of the integrated luminosity accumulated during the run. Instead, an "effective" integrated luminosity $(\int Ldt)_{eff}$, defined as the product of the integrated luminosity $\int Ldt$ and the efficiency of particle detection ϵ_{eff}[3], was used:

$$(\int Ldt)_{eff} = \epsilon_{eff} \int Ldt. \tag{4.7}$$

[3] ϵ_{eff} includes correction for prescaling of events with the prescale factor.

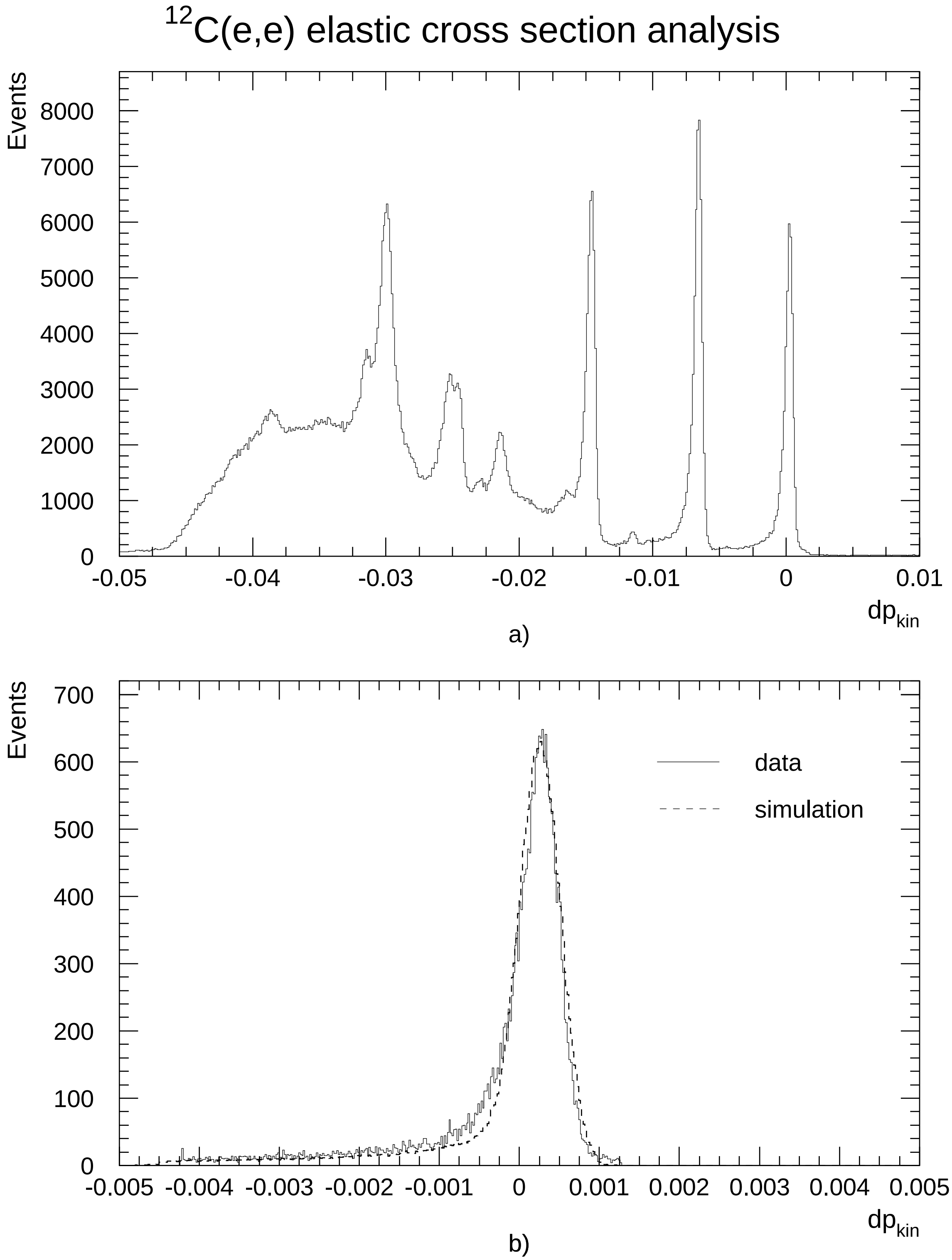

Figure 4-2: (a) dp_{kin} distribution for ^{12}C(e,e$'$) run 2538. The peak at $dp_{kin} \approx 0$ corresponds to elastic ^{12}C(e,e) scattering; other peaks correspond to inelastic ^{12}C(e,e$'$) scattering with the recoiling ^{12}C nucleus in a discrete excited state. (b) dp_{kin} yield in data and simulation after acceptance cuts and a cut selecting the elastic peak.

Thus, the simulated MCEEP yield contained ϵ_{eff} as a factor, and therefore the yield in the data and the simulation could be compared directly. $\int Ldt$ was determined with (4.2).

The ratio of the elastic peak yield experimentally detected to the simulated yield, after application of described above acceptance and dp_{kin} cuts, was found to be 1.02 $\pm$ 0.6%, where the error is statistical only. The efficiency of detection of electrons in this run (not including the prescale factor) was $\approx$ 73% (with main contributions from the computer deadtime, 15%, and the tracking efficiency, 86%).

Similar analysis of ^{12}C(e,e) elastic run 2603, taken at E_{beam} = 1.2 GeV, θ_{scat} = 20.6°, Q^2 = 5 fm^{-2}, was made. The ratio of the yield in the elastic peak in data to that in simulation, after application of similar acceptance cuts and a cut selecting the elastic peak, was found to be 0.99 $\pm$ 2.4%, where the error is statistical only. The efficiency of detection of electrons (not including the prescale factor) in this run was $\approx$ 73% (computer deadtime 9%, tracking efficiency 81%, electronic deadtime 0.8%, electron singles trigger prescale factor 28).

It was therefore concluded that the ^{12}C(e,e) elastic cross sections extracted in the measurements agreed with those in [53] within experimental errors, and that the technique of cross section extraction was performing well, at least for thin carbon targets.

4.2.2 ^{3}He(e,e) measurements

Fig. 4-3 (a) shows the dp_{kin} distribution for elastic ^{3}He(e,e) run 2528 (E_{beam} = 644 MeV, θ_{scat} = 41.2°, Q^2 = 5 fm^{-2}). The peak in the right part of the spectrum corresponds to electrons elastically scattered from ^{3}He. Analysis of this run was performed similarly to the ^{12}C(e,e) analysis described in the previous section, but was aimed at the extraction of the target density rather than the elastic cross section. The ^{3}He density in the MCEEP simulation was varied until an agreement in the elastic peak yield between the data and the simulation was obtained. Then, the density in the simulation was corrected by the factor $C = N_{data}/N_{sim}$, where N_{data} and N_{sim} are the number of counts in the elastic peak in the data and the simulation, respectively.

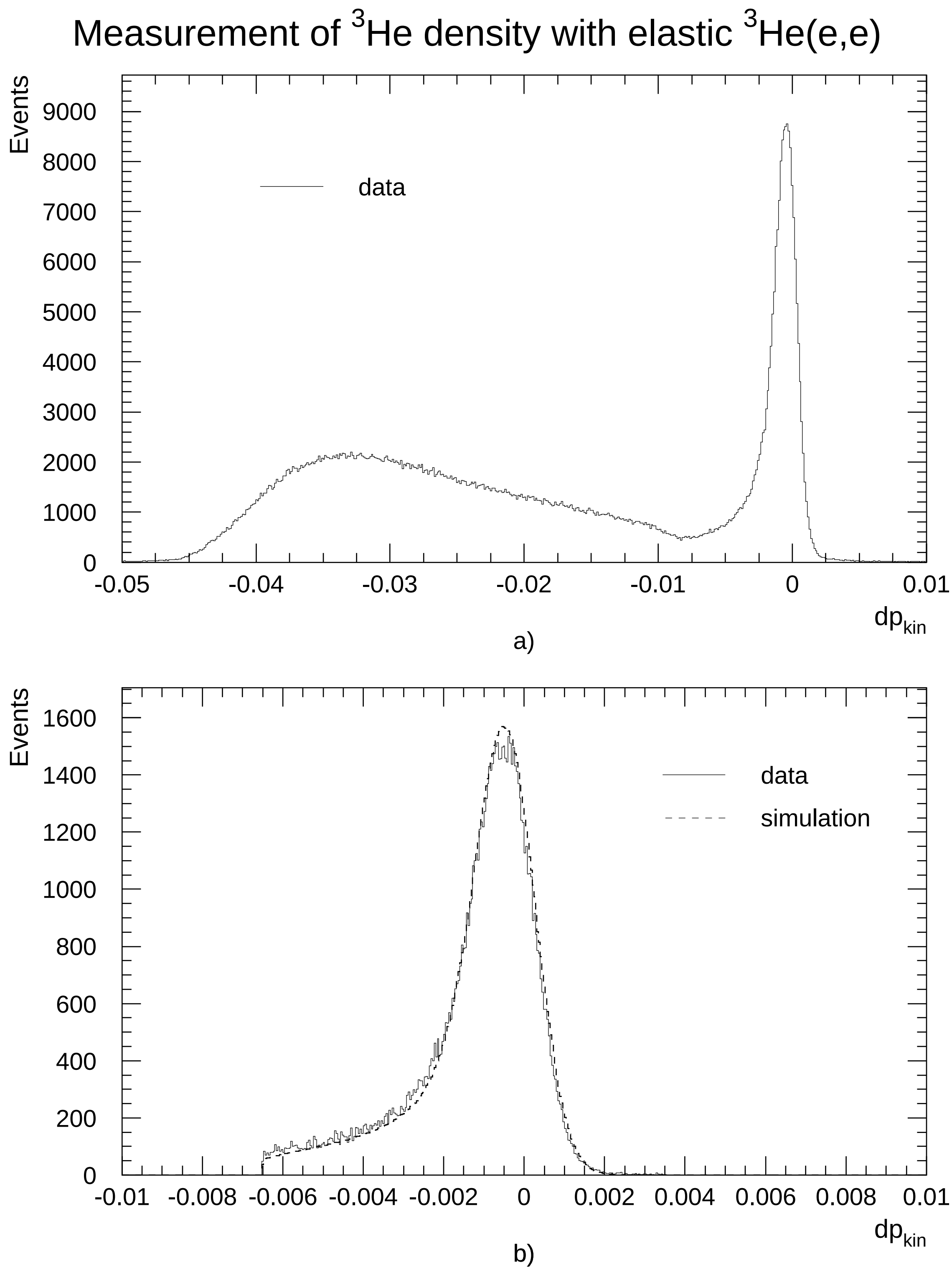

Figure 4-3: (a) dp_{kin} distribution for ^{3}He(e,e) run 2528. (b) dp_{kin} distribution in data and simulation after cuts (see text) and adjustment of the ^{3}He density in the simulation to 0.07197 g/cm^3.

The MCEEP simulation used the ^{3}He(e,e) elastic form factors from Amroun et al [52] fit to world ^{3}He elastic data, and a simple approximation to DWIA through the calculation of effective momentum transfer [14]. Acceptance cuts were: $|\phi_{tge}| < 20$ mrad, $|\theta_{tge}| < 40$ mrad, and $-0.035 < \delta_{tge} < 0.03$. A cut on the reconstructed interaction point along the beam, $|z_{labe}| < 3.5$ cm, removed contributions from the aluminum walls. A cut on dp_{kin}, $-0.0065 < dp_{kin} < 0.0035$, selected the ^{3}He(e,e) elastic peak. Spectrometer resolution was simulated by addition of Gaussian functions to ϕ_{tge}, θ_{tge}, δ_{tge} and y_{tge} reconstructed in the simulation. The parameters of the Gaussians were chosen in a manner similar to that used in the ^{3}He(e,e′p) analysis (Sec. 5.2.2), to as much as possible match the experimentally observed spectrometer resolution. The average ^{3}He gas density extracted from the run 2528 was 0.07197 g/cm^3$\pm$ 1% statistical error.

The ^{3}He density was also extracted with the technique described above for the ^{3}He(e,e) elastic run 2569 ($E_{beam} = 644$ MeV, $Q^2 = 2.91$ fm^{-2}). In this run the measured ^{3}He density was 0.0724 g/cm^3$\pm$ 0.5% statistical error. An analysis of systematic errors associated with this measurement is presented in Sec. 6.6. The value of the density extracted in this measurement (0.0724 g/cm^3) was used as a benchmark for normalization of the ^{3}He(e,e′p) data, due to lower statistical and systematic errors of the measurement compared to those of the other measurement. The disagreement between the two measurements of the ^{3}He density is $\sim$ 0.6%, within the statistical errors.

An independent extraction of the density from the E89044 set of ^{3}He(e,e) elastic measurements made at the beam energy of 644 MeV was performed by K. Aniol and his collaborators at Cal State L. A. They used radiative, computer deadtime and beam heating corrections; and PWBA calculation of the elastic cross sections, using the ^{3}He form factors from [54]. From the elastic scattering measurements at four angular settings of the electron spectrometer with 1.59 fm^{-2} $< Q^2 <$ 2.91 fm^{-2}, with the hadron spectrometer used as a luminosity monitor, they obtained the density of 0.0712 g/cm^3 $\pm$ 1.3% statistical error. Later, however, an error was found in this analysis; after reanalysis, which is currently pending, their estimate of the ^{3}He density is expected to increase by $\sim 4\%$.

4.3 Target density stability

^{3}He density in the target is proportional to the rate R, defined as

$$R = \frac{N}{\epsilon_{eff}} \frac{1}{Q}, \tag{4.8}$$

where N is the number of events detected in a chosen acceptance region of the fixed electron spectrometer, ϵ_{eff} is the correction for efficiency of particle detection and prescaling, Q is the accumulated beam charge. Therefore, one can study the stability of the ^{3}He density by observing the stability of the rate R over time.

The rate R was averaged over "good" runs of each ^{3}He(e,e$'$p) kinematic setting in the luminosity monitoring procedure (Sec. 4.5), and is presented in the third column of Table 4.2. In the fourth column of the table the values from the third column are normalized to 1 for kinematic settings during and between which the target density was not intentionally changed; an asterisk (*) denotes the start of a new normalization coefficient. As noted in the table, the target density was intentionally changed several times, either to increase luminosity, during maintenance periods or to investigate the effects of the target density on the resolution.

The deviation of values in the fourth column of Table 4.2 from 1 represents changes in the rate R due to the compound effect of:

1. Inherent instability of the target density, due to the target design.
2. Changes in the target density due to different boiling effects at different beam currents (Sec. 4.4).
3. Errors in the corrections ϵ_{eff} for prescaling and efficiency of particle detection.
4. Fluctuations in the beam position between kinematic settings.
5. Errors in the calculation of the accumulated beam charge.

Start date, year 2000	Kinematics number	Rate of detected in HRSE particles, Coul^{-1}	Relative change of the rate
2/11	1	$1.252 \cdot 10^8$	1*
2/12	4	$1.251 \cdot 10^8$	0.999
2/12	5	$1.247 \cdot 10^8$	0.996
2/12	8	$1.248 \cdot 10^8$	0.997
2/13	7	$1.249 \cdot 10^8$	0.998
Target density increase			
2/14	1	$1.507 \cdot 10^8$	1*
2/14	10	Electron quad. 2 off, luminosity monitoring N/A	
2/16	11	$1.502 \cdot 10^8$	0.997
2/17+2/26	14	$1.523 \cdot 10^8$	N/A (Target warmup 2/18 – 2/26)
2/17+2/27	13	$1.499 \cdot 10^8$	N/A (Target warmup 2/18 – 2/26)
3/1	28	$1.501 \cdot 10^8$	1*
3/1	29	$1.501 \cdot 10^8$	1.000
3/6	6	$4.764 \cdot 10^6$	N/A (Beam energy change)
3/7	3	$4.303 \cdot 10^6$	N/A (Target density varied)
3/9	9	$4.858 \cdot 10^6$	1*
3/7	12	$4.853 \cdot 10^6$	0.999
3/17	15	$4.867 \cdot 10^6$	1.002
3/22	12	$4.869 \cdot 10^6$	1.003

Table 4.2: Chronology of collection of the 1.2 GeV and 4.8 GeV ^{3}He(e,e′p) data and analysis of the ^{3}He target density stability (see text for details).

6. Statistical errors (less than $\sim 0.12\%$).

Still, the largest variation of the rate is $\sim 0.5\%$, even over periods of time as long as two weeks. Therefore, one can conclude that the target density is stable to at least $\sim 0.5\%$.

In the beginning of taking data at the ^{3}He(e,e′p) kinematics 10 ($E_{beam} = 4.8$ GeV, $P_{miss} = 425$ MeV/c, the proton is detected back of $\vec{q}$) a system for regulating current in the second quadrupole magnet of the electron spectrometer failed and started delivering current $\sim 2\%$ larger than a correct current value. The ensuing decrease in the electron spectrometer y_{tg} resolution was immediately noted, but it took 2 days to find and fix the source of the failure. As a result, the data collected at kinematics 10 had slightly different electron spectrometer optics than all other 4.8 GeV data (the change affected primarily the y_{tg} resolution, with the resolution of the ^{3}He(e,e$'$p)D peak unchanged), and the regular scheme of monitoring luminosity could not be applied. Data collected at this kinematics was normalized by assuming stability of the ^{3}He density between the start of the previous and the end of the next kinematic setting (kinematics 1 and 11 respectively), which was confirmed by consistent readings from pressure and temperature sensors located in the target.

4.4 Boiling study

A detailed analysis of changes in the ^{3}He density due to heating by the beam ("boiling") was made by K. Aniol and the Cal State L. A. group. They found that for the rastered 4×4 mm beam and the currents in the range of 1 – 140 μA, changes in the target density (measured as described in the previous section) were $\sim 2\%$. Such small "boiling" at the wide range of currents was probably due to the special target design, with a funneled gas entrance at the bottom of the "tuna can", that accelerated the gas to ~ 30 m/s and directed its flow perpendicularly to the electron beam.

The beam currents used at the end of the ^{3}He(e,e$'$p) kinematic settings at the beam energy of 4.8 GeV were about 110 μA, while the beam currents during the ^{3}He density measurement at the beam energy of 0.644 GeV were about 5 μA. Therefore, in the adopted scheme of normalization of the ^{3}He(e,e$'$p) data (Sec. 4.1), when assuming stability of the target density during the beam energy change from 4.8 to 0.644 GeV, one has to account for ^{3}He density "boiling" effects. This is done through calculation of a "boiling coefficient". The boiling coefficient is defined as the ratio of the ^{3}He density at one value of the beam current to that at another value of the beam current. The boiling coefficient for a current step from 5 to 110 μA was found by calculating the relative change in the target density (as described in the previous section) for several adjacent runs taken at the beam currents close to 5 and 110 μA. The coefficient was found to be $1.013 \pm 0.3\%$ statistical error.

4.5 Luminosity monitoring

The integrated luminosity for each run selected for the ^{3}He(e,e$'$p) cross section analysis was determined with the formula (4.3), which in an expanded form can be written as

$$\int Ldt = \left(\frac{N_1 P_1}{\epsilon_{cdt1}\epsilon_{edt1}\epsilon_{tr1}} + \frac{N_5 P_5}{\epsilon_{cdt5}\epsilon_{edt5}\epsilon_{tr5}} \right) \frac{(\int Ldt)'}{\frac{N_1' P_1'}{\epsilon_{cdt1}'\epsilon_{edt1}'\epsilon_{tr1}'} + \frac{N_5' P_5'}{\epsilon_{cdt5}'\epsilon_{edt5}'\epsilon_{tr5}'}}. \tag{4.9}$$

In this formula primed ($'$) quantities refer to the "reference" run for which the integrated luminosity is known, and unprimed quantities refer to the run for which the integrated luminosity is being measured. The notation in the formula is as follows: $\int Ldt$ is the integrated luminosity; N_i is the number of events of trigger type i passing the cut on the reconstructed reaction point along the beam, $|z_{labe}| < 3.5$ cm; P_i, ϵ_{cdti}, ϵ_{edti}, ϵ_{tri} are the prescale factor, computer livetime, electronic livetime and tracking efficiency, respectively, for trigger type i.

In the formula (4.9) HRSE singles events (trigger type 1) are summed with the coincidence events (trigger type 5)[4]. This addition is necessary since the HRSE singles trigger and the coincidence trigger are exclusive (Sec. 2.8.1). The HRSE trigger efficiency, measured to be stable during the whole experiment and equal to 99.9% (Sec. 3.1.1), is not included in the formula, since it is presumed to be the same during the reference and the investigated runs, and therefore correcting for it in the numerator and denominator of (4.9) would cancel out.

The integrated luminosities $(\int Ldt)_i$ determined with (4.9) for individual runs i taken at a ^{3}He(e,e$'$p) kinematic setting can be summed to give the total integrated luminosity $(\int Ldt)_{tot}$ for the kinematic setting, as

$$(\int Ldt)_{tot} = \sum_i (\int Ldt)_i. \tag{4.10}$$

The total integrated luminosity determined by (4.10) can be used in a "100% efficient" simulation of the ^{3}He(e,e$'$p) yield. Then, the simulated yield in a kinematic bin B can be directly compared to the number of detected events in the same bin B, if

[4]Before the addition, events of both types are corrected for the prescaling and efficiencies.

the detected events are corrected for prescaling and efficiencies. The correction for prescaling and efficiencies is made with the formula:

$$N_{tot,eff} = \sum_i \frac{N_i}{\epsilon_i}, \tag{4.11}$$

where N_i is the number of detected events in run i in the kinematic bin B, and ϵ_i is given by $\epsilon_i = \epsilon_{cdt5}\epsilon_{edt5}\epsilon_{tr5}/P_5$.

Alternatively, one can simulate the experiment with an "effective" (corrected for prescaling and efficiencies) integrated luminosity, defined as

$$(\textstyle\int Ldt)_{tot,eff} = \sum_i (\textstyle\int Ldt)_i \epsilon_i, \tag{4.12}$$

and then compare the yield simulated in a kinematic bin B to the number of experimentally detected in the same bin B events, uncorrected for prescaling and efficiencies:

$$N_{tot} = \sum_i N_i. \tag{4.13}$$

Let's show that both approaches are correct, but differ in weighting of the contribution of individual runs.

The number of counts N_i experimentally detected in a kinematic bin B in run i is related to the total cross section σ of scattering into the kinematic bin B, through:

$$N_i = \epsilon_i \sigma (\textstyle\int Ldt)_i, \quad \text{for all } i. \tag{4.14}$$

Dividing equations (4.14) by ϵ_i, summing over i and applying (4.10) and (4.11) yields:

$$N_{tot,eff} = \sigma (\textstyle\int Ldt)_{tot}. \tag{4.15}$$

This equation validates comparison of the yield simulated with the "true" integrated luminosity $(\int Ldt)_{tot}$, determined with (4.10), to the number of counts $N_{tot,eff}$ determined with (4.11).

Summing equations (4.14) over i and applying (4.12) and (4.13) yields:

$$N_{tot} = \sigma(\textstyle\int Ldt)_{tot,eff}. \tag{4.16}$$

This equation validates the comparison of the yield simulated with the effective integrated luminosity $(\int Ldt)_{tot,eff}$, determined with (4.12), to the total number of counts N_{tot} uncorrected for prescaling and efficiencies and given by (4.13).

In fact, it can be seen that the two methods are identical (up to an insignificant multiplicative coefficient), if prescaling and efficiencies are the same for all runs at a kinematic setting. If the correction factors ϵ_i differ between the runs and the first approach (given by (4.10), (4.11) and (4.15)) is used, runs with low ϵ_i (large prescaling or low efficiency) will contribute more to the corrected experimental yield, relative to runs with high ϵ_i. Since the cross sections in this thesis were extracted by an adjustment of the simulation cross section to match the detected and simulated yield in kinematic bins, the choice of the first or the second approach would slightly influence the final cross section results. (Without going into a detailed proof, this statement can be understood from the following example: for two runs ("1" and "2") and the total cross section $\sigma = 1$, the integrated luminosities $L_1 = 1000$, $L_2 = 1000$, the efficiencies of particle detection $\epsilon_1 = 0.5$, $\epsilon_2 = 0.25$, the expected number of counts is $N_1 = 500$, $N_2 = 250$. The cross section extracted with (4.15) would be $\sigma_1 = (500/0.5 + 250/0.25)/2000 = 1$. With (4.16) the cross section would be: $\sigma_2 = (500 + 250)/750 = 1$. However, if, for example, N_1 deviates by one standard deviation $\sqrt{500} \approx 20$ to 480, then $\sigma_1 = (480/0.5 + 250/0.25)/2000 = 0.98$, $\sigma_2 = (480 + 250)/750 = 0.973$. That is, the two methods of cross section extraction differ in sensitivity to fluctuations in N_1 and N_2).

In this experiment the coincidence trigger was not prescaled (the prescale factor P_5 equal to 1), and the efficiencies of particle detection were very similar for runs taken at the same kinematic setting. Hence, both methods of calculation for the integrated luminosities and comparison of data to simulation should have given identical cross section results.

In the analysis presented in this thesis, the second method of summation of integrated luminosities was used (given by formulas (4.9), (4.12) and (4.13)), i.e., integrated luminosity for each run, computed with (4.9), was corrected for efficiency of particle detection (computer and electronic deadtimes and tracking efficiency), summed over all "good" runs at a kinematic setting, and then used in the ^{3}He(e,e$'$p) simulation of the yield, which was compared to the (uncorrected for efficiencies) experimental yield, summed over the same runs at the kinematic setting[5].

4.6 Calculation procedure

From a practical perspective, the calculation of the "effective" integrated luminosities for ^{3}He(e,e$'$p) kinematic settings involved the following steps:

1. Determine the number of events of each trigger type passing the VDC tracking cuts (Sec. 3.1.2) in a run and the total number of recorded events of each trigger type, and apply formula (3.3) to obtain the tracking efficiencies for the run.

2. Find the average strobe rates in the electron and the hadron spectrometers from the scaler information (formulas (3.17) – (3.18)). Apply formula (3.16) to determine the electronic deadtimes for each trigger type.

3. Calculate the computer deadtime of each trigger type from the scaler information and the number of recorded events of each type (formulas (3.13) – (3.15)).

4. Find the number of electron singles and coincidence events passing the VDC tracking and acceptance cuts used for luminosity monitoring.

5. Apply formula (4.9) to obtain the total integrated luminosity for the run.

6. Repeat the above procedure for all "good" runs at a kinematic setting. Apply formula (4.12) to obtain the effective integrated luminosity for a kinematic setting.

[5]The corrections for scintillator efficiency, proton absorption and Gas Cherenkov efficiency were not described in this section. These corrections were applied as an overall multiplicative factor to the cross sections at a later stage.

7. Repeat the above procedure for each kinematic setting.

This enormous task (for 19 ^{3}He(e,e$'$p) kinematic settings analyzed in this thesis) was significantly simplified by the author's implementation of a MySQL database for the experiment[6]. The database contained all end-of-run scaler readouts for all E89044 runs, and therefore the calculation of the electronic deadtime and accumulated beam charge for each run was reduced to the execution of several SQL statements. Raw data files were analyzed with ESPACE on JLab's batch computer farm. After the execution of each job, a Perl program read ESPACE's summary file; extracted the number of events of each type recorded, the number of events of each type passing the VDC tracking cuts, and the number of events of each type passing the "luminosity monitoring" acceptance cuts; and through the network, entered this information in the MySQL database. After that, the calculation of the computer deadtimes and the tracking efficiencies of each event type for each run was also reduced to the execution of several SQL statements. Another SQL statement applied formula (4.9) to the tracking efficiencies, computer and electronic deadtimes and prescale factors to calculate the integrated luminosities for each run. These were then corrected for the efficiencies and summed, also by the execution of several SQL statements in the MySQL database, to yield the effective integrated luminosity for good runs of a kinematic setting.

Perl programming was also extensively used for submitting the analysis jobs to the computer batch farm, both in the elastic and the quasielastic analyses. An execution of a program with a kinematics number given as an argument located the appropriate header and database files, and submitted all jobs for the kinematic setting to the batch farm. Another Perl program was used for starting the MCEEP simulations for a kinematic setting, by reading ESPACE's header file for the kinematic setting, and reformatting the information into the MCEEP input file format.

Appendix B describes several of the most useful Perl programs written: a series of short programs that filled the MySQL database with the end-of-run scaler readouts.

[6] A copy of the database is available at Hall A web server at http://hallaweb.jlab.org/db, username "e89044", password "e89044" (read-only access).

Kinematics number	Σ	Nominal P_{miss}, MeV/c	Number of good runs	Total effective $\int Ldt$, Coul g/cm^2
1	$\Sigma_{1/2}$	0	8	0.3744
4	Σ_1	150	4	0.4855
7	Σ_1	300	15	2.2497
10	Σ_1	425	16	3.004
13	Σ_1	550	28	5.195
28	Σ_1	750	11	2.126
29	Σ_1	1000	13	2.003
5	Σ_2	150	4	0.3441
8	Σ_2	300	12	1.175
11	Σ_2	425	20	1.207
14	Σ_2	550	52	2.164
3	Σ_3	0	5	0.4245
6	Σ_3	150	11	1.767
9	Σ_3	300	31	6.031
12	Σ_3	425	31	11.57
15	Σ_3	550	53	14.15
33	$\Sigma_{4/5}$	0	2	0.1461
34	Σ_4	150	4	0.5034
35	Σ_5	150	4	0.403

Table 4.3: Number of runs used in the cross section analysis at each ^{3}He(e,e$'$p) kinematic setting, and calculated effective integrated luminosities.

Table 4.3 presents the effective integrated luminosities (for the coincidence trigger[7]) calculated for each ^{3}He(e,e$'$p) kinematic setting, along with the number of "good" runs used in the cross section analysis.

[7]The values in the table do not contain corrections for the scintillator efficiency, proton absorption, Gas Cherenkov efficiency, and a $\sim$ 1% correction to the reference value of the ^{3}He density used in the final analysis.

Chapter 5

Analysis of ^{3}He(e,e$'$p) data

5.1 Overview

Five-fold differential ^{3}He(e,e$'$p)D and six-fold differential ^{3}He(e,e$'$p)pn coincidence cross sections were extracted by adjustment of the ^{3}He(e,e$'$p) cross section model in a simulation to reproduce the experimentally detected yield. The following are preliminary steps:

1. Normalization of a spectrometer setting is calculated with the luminosity monitoring procedure, and is corrected for efficiencies (Chap. 4).

2. Coincidence events are reconstructed with ESPACE (Sec. 3.2), and the following cuts are applied:

    - VDC tracking cuts, to eliminate badly reconstructed events (Sec. 3.1.2);
    - R-function acceptance cuts, to limit events to flat acceptance regions of the spectrometers (Sec. 5.3);
    - cuts on the reconstructed reaction point along the beam, to remove contributions from the aluminum target walls (Sec. 5.4);
    - cut on difference between reaction points along the beam reconstructed by the two spectrometers, to remove some of accidental coincidences (Sec. 5.5);

- cut on sum of Gas Cherenkov ADC channels, to remove the contribution from the real coincident π^- (electron spectrometer only) (Sec. 3.1.3);
- cuts on corrected coincidence time between the spectrometers: a cut selecting the real (e,e$'$p) coincidence peak, and a cut on accidental coincidences. Created are two ntuples with event variables, one with real and one with accidental coincidences (Sec. 5.6);
- for all $P_{miss} \neq 0$ spectrometer settings, cut on reconstructed out-of-plane angle ϕ ($|\phi| < 20^\circ$ for forward of $\vec{q}$ spectrometer settings, and $|180^\circ - \phi| < 20^\circ$ for back of $\vec{q}$ spectrometer settings), to restrict events to coplanar kinematics;

3. Full MCEEP simulation of the spectrometer setting (including energy losses, internal and external radiation and multiple scattering in the target, and spectrometer resolutions) is made. Cuts identical to those imposed on data are applied to simulated events (except for cuts on Gas Cherenkov, coincidence time between spectrometers and VDC tracking cuts) (Sec. 5.2).

4. Events both in data (two ntuples, one with real and one with accidental coincidences) and in simulation are binned in missing momentum P_{miss}.

5. For Σ_1 and Σ_2 kinematic settings, position of the ^{3}He(e,e$'$p)D two body breakup (2bbu) peak reconstructed in data is finely adjusted to coincide with that in the simulation, separately for each P_{miss} bin (Sec. 5.7).

6. Events both in data (two ntuples, one with real and one with accidental coincidences) and in simulation are binned in missing energy E_{miss}.

7. Accidental coincidences are subtracted from each data bin (Sec. 5.6).

After these preliminary steps, a fitting procedure (described in Sec. 5.8 and listed in Appendix A.2) iteratively adjusted "vertex" (unradiated) ^{3}He(e,e$'$p) cross sections in "vertex" simulation bins until the number of "asymptotic" (radiated) counts in each bin in the simulation and the data agreed. After adjustment, the unradiated

^{3}He(e,e′p) cross sections at kinematic points corresponding to each bin (found by acceptance-weighted averaging of kinematic variables within the bin) in the adjusted simulation are the extracted radiatively corrected cross sections for the bins.

Two ^{3}He(e,e′p) cross section models were used in simulations: 1.) A factorization of the cc1 prescription for electron-nucleon cross section [25] with spectral functions fitted to data; 2.) A "flat" cross section (independent from all kinematic variables) within each bin (both models are described in Sec. 5.8.2). In the following, the cross section analysis, as well as extraction of distorted spectral functions, response functions and A_{TL} asymmetry, is discussed in detail.

5.2 Simulation of experiment

5.2.1 MCEEP

The experiment was simulated with a modified version of MCEEP[1] [55]. MCEEP simulates ^{3}He(e,e′p)D and ^{3}He(e,e′p)pn (three-body breakup, or 3bbu) processes separately, by 5-dimensional and 6-dimensional sampling of the phase space respectively. Ntuples simulated for the two processes are merged.

MCEEP calculates the average energy losses of electrons and protons with the Bethe-Bloch formula [56], with additional corrections for density and shell effects [56, 57]. Energy loss straggling is approximated by either Landau, Vavilov, or Gaussian distribution, depending on the ratio between mean energy loss and maximum energy loss in a single collision [55]. In a final stage of event simulation, the mean energy losses of electrons and protons are subtracted to allow comparison with data corrected for the mean energy losses.

Internal radiation of electrons is simulated in two passes. In one pass, an overall multiplicative weight equal to the Swinger correction [58] is applied to undisturbed event kinematics to simulate the emission of soft photons. In another pass, kinematics

[1] Written by P. Ulmer with contributions from others; for this experiment D. Higinbotham updated ^{3}He form factor calculation using the global fit of Amroun [52], and coded in an approximation to DWIA through calculation of effective momentum transfer [14].

of the generated events is affected by simulated emission of hard photons in the direction of either incident or scattered electron (peaking approximation), with the photon emission cross section calculated using the Borie and Drechsel prescription [59]. A multiphoton correction to the cross section is also applied [55, 60]. External radiation of electrons is simulated according to the distribution in Tsai [61]. Radiation of protons is neglected. Multiple scattering is accounted for by Gaussian approximation to the theory of Coulomb scattering of Moliere [56, 62].

MCEEP simulates spectrometer resolution by:

1. Transport of particles generated at the target to the focal plane, by application of spectrometer forward transfer functions [63].

2. Simulation of multiple scattering in the spectrometer exit window and air, by addition of Gaussian functions to particle transport coordinates.

3. Simulation of position resolution of VDCs.

4. Transport of particles back to target with reverse transfer functions.

Simulation by MCEEP of the FWHM (full width at half-maximum) of the ^{3}He(e,e$'$p)D missing energy peak, however, was observed to be substantially smaller than that reconstructed in data when physical values for multiple scattering and VDC resolution were used. This was probably due to the unaccounted resolution of the spectrometer optics databases in the simulation. In the analysis presented in this thesis, the spectrometer resolution was simulated by addition of Gaussian functions to particle coordinates reconstructed at the target, with parameters of the Gaussians chosen to match the experimentally observed spectrometer resolution (Sec. 5.2.2).

MCEEP simulates spectrometer acceptance by transport of particles to 5 internal spectrometer apertures, elimination of particles hitting the apertures, and reverse transport of particles to target. In the analysis of elastic scattering from ^{3}He (Sec. 4.2) it was found, however, that MCEEP's model of the spectrometer acceptance substantially differs from the experimentally reconstructed acceptance. Therefore, MCEEP's model of the spectrometer acceptance was not employed. Instead, in the ^{3}He(e,e$'$p) cross section analysis the acceptance was defined by software R-function cuts (Sec. 5.3)

Several MCEEP simulations of the same spectrometer setting were often started in parallel, with different starting seeds for MCEEP's random number generator. This allowed us to use many JLab batch farm computers for simulation of a single spectrometer setting, thus decreasing the time spent to achieve a large number of simulated events.

^{3}He(e,e$'$p) cross section models used in simulations are described in Sec. 5.8.2.

5.2.2 Spectrometer resolution

Momentum, angular and position resolution of both spectrometers was simulated by addition of Gaussian functions to reconstructed at the target δ_{tg}, θ_{tg}, ϕ_{tg} and y_{tg} coordinates of the particles, with FWHM:

- 2 mm for y_{tg};
- 2 mrad for ϕ_{tg};
- 6 mrad for θ_{tg};
- δ_{tg}: $(0.042 + 0.001 \cdot \delta_{tg}^2)\%$ for target density 0.060 g/cm^3, $(0.045 + 0.001 \cdot \delta_{tg}^2)\%$ for target density 0.072 g/cm^3,

where δ_{tg} is expressed in % deviation from the central momentum setting of the spectrometer.

The quadratic term for the FWHM of momentum resolution, $0.001 \cdot \delta_{tg}^2$, was obtained from a fit to the data [36] on the momentum resolution of the spectrometers across the focal planes. The constant offset (0.042% or 0.045%, depending on the value of the ^{3}He target density) was obtained by an adjustment to reproduce the reconstructed FWHM of the ^{3}He 2bbu peak. At the auxiliary Σ_4 and Σ_5 kinematic settings, the constant offset was adjusted to 0.074%. At these kinematic settings the momentum resolution of the spectrometers was lower, due to the optics databases that were not as good as those at the other kinematic settings.

The FWHM of 2 mm for the Gaussian approximating the y_{tg} resolution function was obtained by an adjustment to reproduce the FWHM of the distribution of the difference between the reaction points along the beam reconstructed by the two spectrometers. The FWHM of ϕ_{tg} and θ_{tg} resolution functions (2 mrad and 6 mrad respectively) were estimated from a sieve slit data taken at spectrometer settings close to those at the ^{3}He(e,e$'$p) kinematic settings. These values agree with those reported in [36, 26].

5.3 Spectrometer acceptance with R-functions

Acceptance cuts limiting events to a "flat" acceptance region of the spectrometers were placed using R-functions, or Rvachev's functions [64, 65, 66, 67]. This technique of placing cuts on data was invented, tested and first successfully applied by the author of this thesis during his analysis of the E89044 experiment. The technique is convenient and useful when dealing with complicated and/or multidimensional cuts: it allows one to easily construct these cuts using analytical expressions, and provides a parameter for varying the cuts uniformly across their boundaries. This section follows the discussion in [68, 69].

5.3.1 R-functions

An R-function is a function whose sign is completely determined by the signs of its arguments [64, 65, 66].

For example, the function $f = \min(x, y)$ is an R-function, because it is possible to predict its sign from a knowledge of signs of its arguments x and y. The function $f = \min(x, y) - 1$ is not an R-function, because it is not possible to predict its sign just from a knowledge of signs of its arguments. There are infinitely many R-functions acting on any number of arguments. Examples are [67]: $xyz, x + y + \sqrt{x^2 + y^2 + xy}, xy + z + |z - xy|$.

R-functions act on signs of their arguments in the same manner as the Boolean functions (the functions of the Boolean algebraic logic) act on the logical variables (considering the positive argument values as "true" or "1", and the negative values as "false" or "0") [64]. In fact, for every R-function $f(x_1, ..., x_n)$ there exists a Boolean function $F(X_1, ..., X_n)$ such that

$$S(f(x_1, ..., x_n)) = F(S(x_1), ..., S(x_n)), \qquad \text{for all } x_1, ..., x_n, \tag{5.1}$$

where $S(x)$ is a logical "step" function:

$$S(x) = \begin{cases} 0, \text{or "false"}, & \text{if } x < 0, \\ 1, \text{or "true"}, & \text{if } x > 0. \end{cases} \tag{5.2}$$

Such a Boolean function $F(X_1, ..., X_n)$ is said to be a companion to the R-function $f(x_1, ..., x_n)$ [64].

It turns out [64] that every Boolean function is a companion to infinitely many R-functions. For example, the Boolean "and" ($\wedge$) function is a companion to the R-functions $\min(x, y)$, $x+y-\sqrt{x^2+y^2}$, $(x+y)^3-|x-y|^3$ and many others. The Boolean "or" ($\vee$) function is a companion to $\max(x, y)$, $x+y+\sqrt{x^2+y^2}$, $(x+y)^3+|x-y|^3$ and many others. The Boolean "not" ($\neg$) function is a companion to $-x$, $-x^3$, $e^{-x} - e^x$ and many others.

Just as are Boolean functions, R-functions are closed under composition [64]. That is, an R-function acting on other R-functions yields another R-function. Any Boolean function F can be represented as a combination of the logical negation, conjunction and disjunction $(\neg, \vee, \wedge)$ acting on logical arguments. Using this representation, an R-function f corresponding to this arbitrary Boolean function F (i.e., an R-function f such that the Boolean function F is its companion) can be constructed by the formal substitution of the Boolean $\neg, \vee, \wedge$ by their corresponding R-functions and by substitution of the logical arguments by the real arguments.

These properties allow one to create functions describing complex geometrical objects, by:

1. Writing equations of the boundaries of an object.

2. Converting them to "greater than or equal to 0" inequalities describing the regions of space bounded by the boundaries.

3. Writing a Boolean expression combining these regions of space into the geometrical object.

4. Formally substituting the elementary Boolean functions in the Boolean expression by any of their corresponding R-functions, and the logical arguments by the corresponding[2] left-hand sides of the inequalities.

The constructed function is equal to 0 on the boundary of the object, greater than 0 inside the object, and less then 0 outside the object. Depending on the choice of R-functions, various differential properties of the constructed function can be obtained. Moreover, the absolute values of the constructed function, by choosing to use "normalized" R-functions and "normalized" inequalities (discussed below), can be made approximately equal to the distance to the nearest boundary of the object.

For example [66], the boundaries of the geometrical domain shown in Fig. 5-1 (a) can be described by the equations (step 1 of the procedure outlined above):

$$\omega_1 \equiv \frac{1}{10}(25 - x^2 - y^2) = 0, \quad \omega_2 \equiv x - 3 = 0, \quad \omega_3 \equiv \frac{1}{4}(4 - y^2) = 0. \tag{5.3}$$

The regions of space defined by the inequalities $\omega_1 \geq 0$, $\omega_2 \geq 0$ and $\omega_3 \geq 0$ (step 2), can be combined as $\Omega_1 \wedge \overline{(\Omega_2 \wedge \Omega_3)}$ to form the region inside the domain (step 3). Formally substituting the Boolean function $\wedge$ ("AND") by the corresponding R-function $x + y - \sqrt{x^2 + y^2}$, the Boolean negation $\neg$ by the corresponding R-function $-x$, and the Boolean arguments Ω_1, Ω_2, Ω_3 by the functions ω_1, ω_2, ω_3 (step 4), one obtains the function:

$$f(x, y) = \omega_1 + (-(\omega_2 + \omega_3 - \sqrt{\omega_2^2 + \omega_3^2})) - \sqrt{\omega_1^2 + (-(\omega_2 + \omega_3 - \sqrt{\omega_2^2 + \omega_3^2}))^2}, \tag{5.4}$$

plotted in Fig. 5-1 (b). This function is analytic everywhere except at the corner

[2]That is, a logical argument corresponding to a region of space should be substituted by the left-hand side of the inequality describing the region of space. An example is given below.

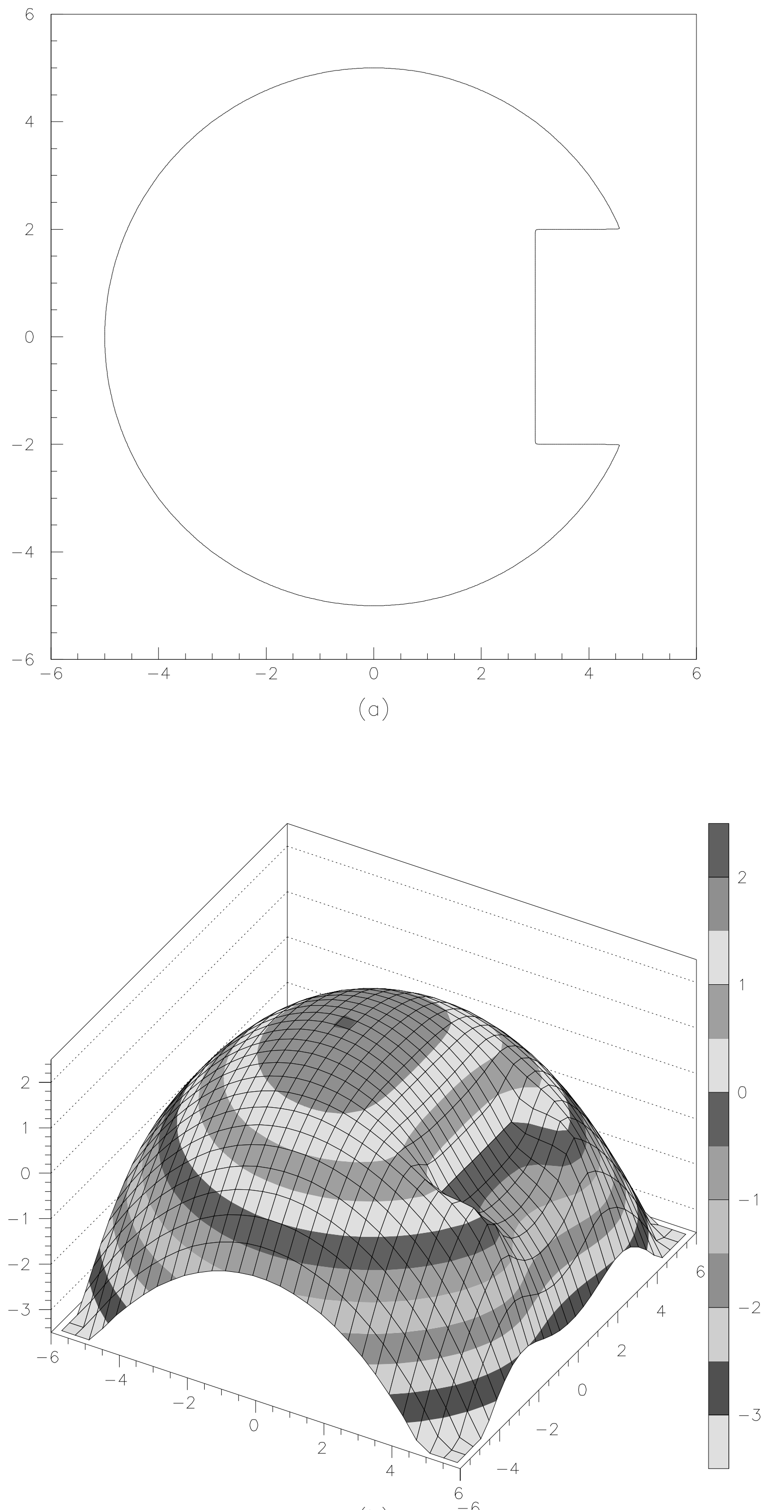

Figure 5-1: (a) A 2-dimensional domain and (b) the approximation (5.4) to the distance function to its boundary.

points, is equal to 0 on the boundary of the domain in Fig. 5-1 (a), is positive inside the domain, and is negative outside. It is also normalized on all regular points of the boundary, in the sense that

$$\frac{\partial f}{\partial \nu}|_{\partial\Omega} = 1, \tag{5.5}$$

where ν is the inner normal to the boundary $\partial\Omega$. In other words, $f(x, y)$ approximates the distance function to $\partial\Omega$ in the vicinity of non-corner points of the boundary.

In general, a function f is said to be normalized up to m-th order on a boundary $\partial\Omega$, if

$$f|_{\partial\Omega} = 0, \quad \tfrac{\partial f}{\partial \nu}|_{\partial\Omega} = 1, \quad \tfrac{\partial^k f}{\partial \nu^k}|_{\partial\Omega} = 0, \quad k = 2, 3, ..., m. \tag{5.6}$$

There are several techniques for constructing the normalized implicit functions, including a general method for recursively increasing the order of the normalization of any given function [64]. A simpler approach is based on the observation that many R-functions tend to preserve the normalization properties of their arguments. In the example above, the arguments to the R-functions, the functions ω_1, ω_2, ω_3, are normalized (at least to the first order), and the R-functions employed tend to preserve the normalization. Therefore, the constructed function (5.4) approximates the distance function to the boundary of the object.

R-functions translate changes in the sign and absolute magnitude of implicit functions describing a domain boundaries into changes of the sign and absolute magnitude of the constructed function, according to the Boolean and normalization properties of the employed R-functions, and a chosen combination of the R-functions. In many cases, the implicit functions describing the domain boundaries can be normalized by multiplication by a suitable coefficient. For example, it can be seen that the equation of a hyperplane $f = \sum_{i=1}^{N} a_i x_i = 0$ is normalized by multiplication by the coefficient

$$C_{norm} = \left(\sum_{i=1}^{N} a_i^2\right)^{-\frac{1}{2}}, \tag{5.7}$$

since the unit normal vector to the hyperplane is given by $\hat{n} = \{a_1, ..., a_N\}/\sqrt{(\sum_{i=1}^{N} a_i^2)}$,

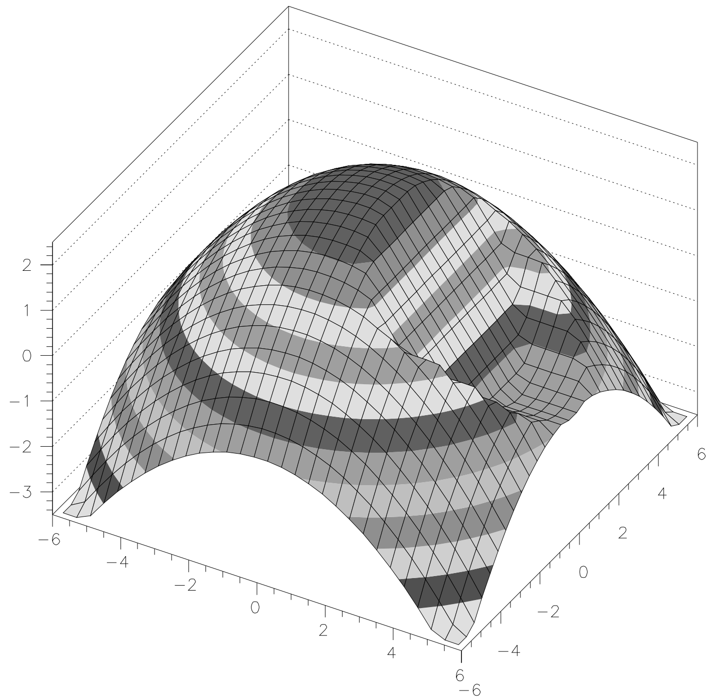

Figure 5-2: Approximation (5.9) to the distance function to the boundary of the geometrical domain in Fig. 5-1 (a).

and the derivative of f along the normal is then $\frac{\partial f}{\partial \hat{n}} = (\sum_{i=1}^{N} a_i^2)/\sqrt{(\sum_{i=1}^{N} a_i^2)} = \sqrt{(\sum_{i=1}^{N} a_i^2)}$, and therefore

$$\frac{\partial \left(C_{norm} f\right)}{\partial \hat{n}} = 1. \tag{5.8}$$

This property will be used in Sec. 5.3.4 to obtain a function describing the spectrometer acceptance.

If in the example considered above one used the R-function $\min(x, y)$ for the Boolean $\wedge$, one would obtain the function

$$f(x, y) = \min(\omega_1, [-\min(\omega_2, \omega_3)]), \tag{5.9}$$

plotted in Fig. 5-2. This function is easier to compute and is a better approximation to the distance function to the domain boundary, but does not possess as good differential properties as (5.4).

In general, if equations of boundaries of a multidimensional geometrical object are known, R-functions allow us to easily construct several functions that are equal to 0 on the boundary of the object, have different signs inside and outside the object, and in the absolute value approximate the distance to the nearest boundary of the object. Further information on the theory of R-functions and its applications is available in [64, 65, 67, 66].

5.3.2 Application to acceptance

Let's consider a charged particle entering a Hall A spectrometer. In a simple approximation, the trajectory of the particle inside the spectrometer is determined only by deflection of the particle in the spectrometer magnetic field, with a possibility of being terminated at an internal spectrometer aperture. Then, for every initial line of flight and momentum of the particle at the spectrometer entrance, there is a definite trajectory of the particle, which results in either the particle passing through the spectrometer to its focal plane, or the particle getting absorbed at an internal spectrometer aperture. It is clear that in this approximation the particles having exactly the same line of flight, momentum and charge at the spectrometer entrance will all pass through the spectrometer to its focal plane, or will all get absorbed at the apertures; and hence the spectrometer "acceptance function" defined in the space of the particle initial lines of flight and momenta, assumes values of either 0 or 1.

Although this approximation neglects many probabilistic effects, such as the multiple scattering, absorption in the spectrometer entrance and exit windows, particle rescattering, fluctuations of the magnetic field, and also the scintillator, tracking, trigger and other efficiencies, it does take into account the geometry of the (average) magnetic field in the spectrometer and the geometry of the spectrometer apertures. One can say that this approximation describes the geometrical aspect of the spectrometer acceptance.

In this approximation, the region where the acceptance function is equal to 1 (a "flat", or "good" acceptance region) can be described as a domain in the 5-dimensional space of the target variables x_{tg}, y_{tg}, ϕ_{tg}, θ_{tg} and δ_{tg} (the variables are defined in Sec. 2.7). This is so since x_{tg}, y_{tg}, ϕ_{tg} and θ_{tg} uniquely specify the initial line of flight of a particle in the 3-dimensional space and δ_{tg} specifies the particle momentum. For purposes of cross section extraction, software cuts are usually placed on the target variables, to select a region within the flat spectrometer acceptance region. Placing the cuts so that they define a large region but still lying within the flat acceptance region allows one to include more particles in the cross section analysis.

An accepted technique is to limit events to a flat spectrometer acceptance region by linear cuts in the target variables. For example, for the Hall A spectrometer acceptance and the unpolarized ^{3}He target a suitable set of cuts is $|\phi_{tg}| < 0.02$ rad, $|\theta_{tg}| < 0.04$ rad, $-0.035 < \delta_{tg} < 0.03$ (y_{tg} is limited by $|z_{lab}| < 0.035$ m). With the help of R-functions, much more complicated cuts, much better approximating the flat acceptance region, and including significantly more events in the cross section analysis, can be easily made. A significant advantage in using R-functions is that they provide a parameter for a continuous variation of the acceptance cut across its boundaries. Plotting the value of this parameter for data and simulation allows one to easily find a cutoff value, at which the cut starts to cross the boundary of the flat acceptance region. Then, the R-function cut is placed at this cutoff value, maximizing the accepted phase space.

5.3.3 Initial acceptance cut

The construction of an optimal function describing the 5-dimensional spectrometer acceptance requires an analytical model of the magnetic field lines and apertures of the spectrometers, and ray-tracing the particles through the spectrometers. Work along these lines has been made by John LeRose at JLab and Paul Ulmer at ODU. J. LeRose wrote a software package for generating the cut functions describing the acceptance based on his SNAKE model of the spectrometers, and P. Ulmer implemented the package in the simulation code MCEEP. In the analysis of data presented in this thesis, the author's original approach to constructing the function was used. The approach is based on the acceptance of the spectrometers reconstructed by the analysis

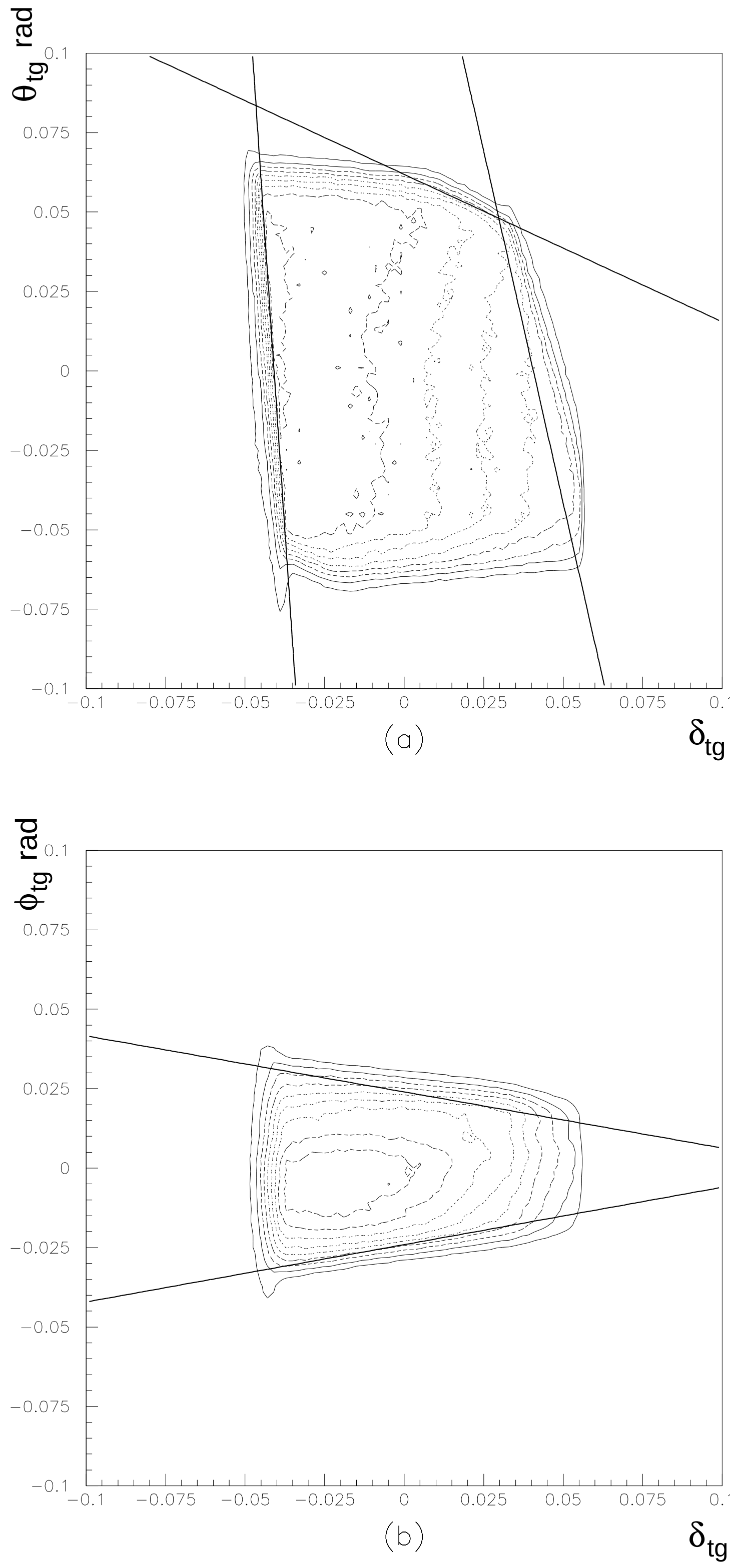

Figure 5-3: Contour plots of the proton singles distributions covering the hadron spectrometer acceptance: (a) θ_{tg} vs δ_{tg}, (b) ϕ_{tg} vs δ_{tg}. The solid lines indicate the edges of the initial cut placed on the acceptance.

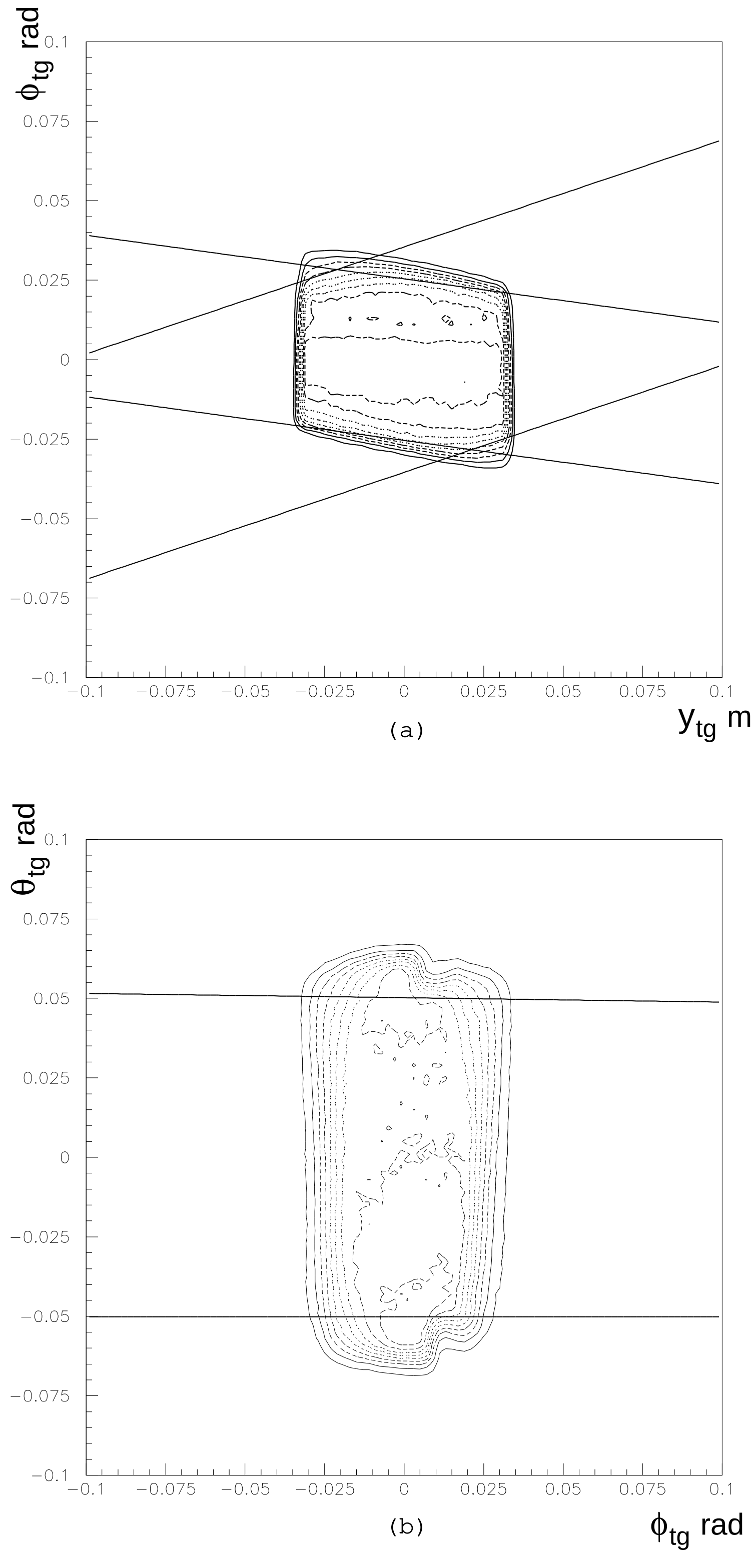

Figure 5-4: Contour plots of the proton singles distributions covering the hadron spectrometer acceptance: (a) ϕ_{tg} vs y_{tg}, (b) θ_{tg} vs ϕ_{tg}. The solid lines indicate the edges of the initial cut placed on the acceptance.

code ESPACE, and physical considerations. This approach is described below.

During the E89044, the x_{tg} coordinate of the detected particles was constrained to the interval (-4.5 mm, 4.5 mm) by the beam position, angular spectrometer settings, and the target geometry. With the constrained x_{tg}, the spectrometer acceptance can be treated as a 4-dimensional region of the variables $y_{tg}, \phi_{tg}, \theta_{tg}$ and δ_{tg}. The main features of this region can be seen at the distributions of the pairs of variables, $(\theta_{tg}, \delta_{tg})$, (ϕ_{tg}, δ_{tg}), (ϕ_{tg}, y_{tg}) and (θ_{tg}, ϕ_{tg}), for a singles data that covers the acceptance as much as possible (Figs. 5-3 and 5-4, proton singles in the hadron spectrometer, set at an angle of 48.3° and at a central momentum of 1480 MeV/c; kinematics 1, open collimators).

The spectrometer acceptance exhibits a number of features that can be explained from physical considerations:

- At the edges of δ_{tg} acceptance, the dependence of the accepted δ_{tg} on θ_{tg} (Fig. 5-3 (a)) is caused by the fact that the trajectories of the higher momentum particles have a lower curvature in the dipole magnet, and in order for them to "fit" into the spectrometer they have to have a lower θ_{tg} (negative θ_{tg} corresponds to upward flying particles in the laboratory coordinate system). For similar reasons the lower momentum particles (with a higher curvature in the dipole) have to have a higher θ_{tg} to reach the focal plane.

- The dipole magnet has a trapezoidal cross section and the higher momentum particles tend to fly closer to its shorter base (higher magnetic field) side, and this is why the accepted range of ϕ_{tg} decreases with an increasing δ_{tg} (Fig. 5-3 (b)).

- Increasing (decreasing) y_{tg} requires decreasing (increasing) ϕ_{tg} in order for the particles to enter the spectrometer through the entrance window (Fig. 5-4 (a)).

- The dependence of the accepted θ_{tg} on ϕ_{tg} at the edges of the θ_{tg} acceptance (Fig. 5-4 (b)) is (presumably) due to the internal apertures associated with NMR probes located in the dipole.

The 11 linear cuts shown as solid lines in Figs. 5-3 and 5-4 were placed on the $(\theta_{tg}, \delta_{tg})$, (ϕ_{tg}, δ_{tg}), (ϕ_{tg}, y_{tg}) and (θ_{tg}, ϕ_{tg}) distributions, and restricted the events to a domain that, judging from the figures, seems to be inside the flat acceptance region. The acceptances of the two spectrometers appear to be slightly different, but, for simplicity, the linear cuts were chosen so that they restricted events to the flat acceptance region of both spectrometers simultaneously (the electron spectrometer data is not shown). These 11 cuts, applied to each of the two spectrometers, define a domain in the 8-dimensional space of variables $y_{tge}, \phi_{tge}, \theta_{tge}, \delta_{tge}, y_{tgh}, \phi_{tgh}, \theta_{tgh}$ and δ_{tgh}. This domain is finite, is bounded by the 22 hyperplanes and forms the initial cut on the acceptance. In addition, a cut on the reaction point along the beam reconstructed by one of the two spectrometers removed the contributions from the particles originating in the target walls (Sec. 5.4). This cut effectively limited the y_{tg} range for both spectrometers.

5.3.4 Construction of cut function

Application of 22 cuts on 8 variables might seem to be a complicated task, but with the help of R-functions, all these cuts are transformed into a single cut ($f > 0$) on the value of the function $f(y_{tge}, \phi_{tge}, \theta_{tge}, \delta_{tge}, y_{tgh}, \phi_{tgh}, \theta_{tgh}, \delta_{tgh})$. As described in the previous sections, this function can be easily constructed in a number of different ways, from equations of the boundaries of the initial cut on the acceptance. The boundaries of the chosen initial cut are given by 22 linear equations. If these equations are normalized with the coefficient (5.7) (the coefficient $(a^2 + b^2)^{-1/2}$ for the equation $ax + by + c = 0$), and R-functions that are used in the construction tend to preserve the normalization (e.g., R-functions $\min(x, y)$, or $x + y - \sqrt{x^2 + y^2}$), then the modulus of the constructed function will approximate the distance from a point in the 8-dimensional "acceptance space" to the nearest boundary of the chosen initial domain. Then, cutting on a positive value of the constructed function ($f > f_0$, where $f_0 > 0$) will define new acceptance cuts, by "shrinking" the region of the initial cut approximately uniformly across all its boundaries by f_0. Cutting on a negative value of the function ($f > -f_0$, where $f_0 > 0$) will "unshrink" the region of the initial

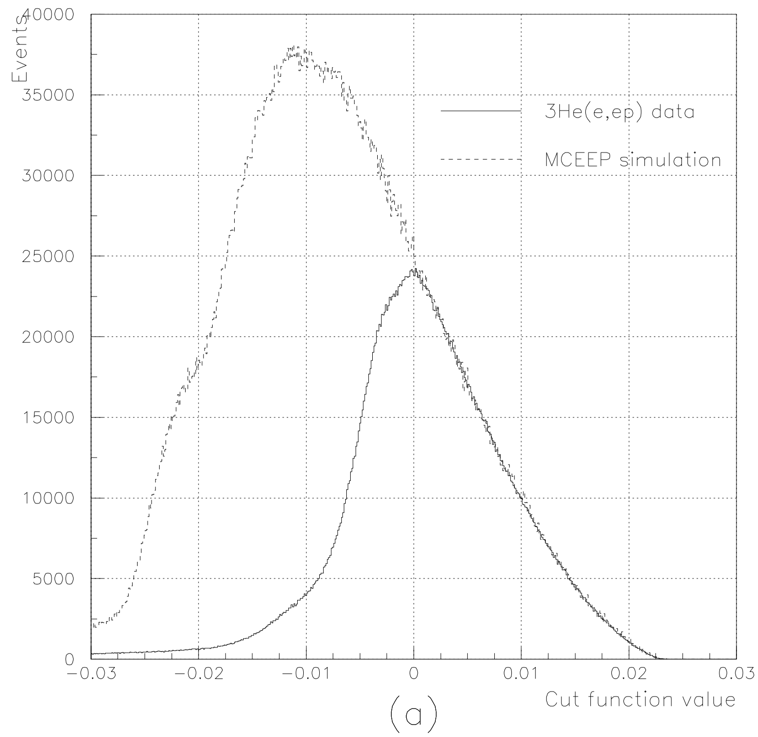

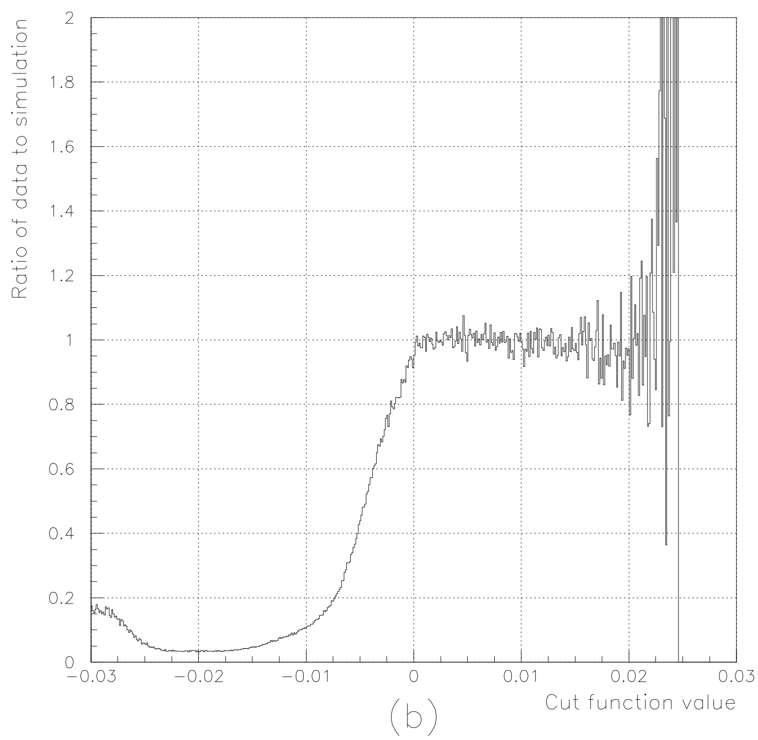

Figure 5-5: (a) The distributions of the cut function f_1 for data and simulation and (b) the ratio of the two distributions (the beam energy of 4.8 GeV, kinematics 1).

acceptance cut by f_0.

This is, in fact, how the function describing the acceptance, in the following referred to as the "cut function", was constructed. Equations of the linear cuts shown in Figs. 5-3 and 5-4 were normalized, and the R-function $\min(x, y)$ was used for the 21 Boolean ANDs required to define the intersection of the half-spaces bounded by the 22 hyperplanes (this is identical to the application of the R-function $\min(x_1, ..., x_{22})$ to the left hand sides of the 22 normalized equations). In the following, this function is denoted as f_1. f_1 is equal to 0 on the boundary of the 8-dimensional domain of the initial cut, increases toward the center of the domain, decreases in the opposite directions, and in the absolute value approximates the distance to the nearest boundary of the domain.

The solid line in Fig. 5-5 (a) shows the distribution of the value of this function for the ^{3}He(e,e$'$p) events detected at kinematics 1 [3]. The dashed line in the figure shows a similar distribution for events simulated at kinematics 1 with MCEEP, with no spectrometer apertures in the simulation. The ^{3}He(e,e$'$p) cross section model in the simulation was the factorization of the cc1 prescription for the off-shell electron-nucleon cross section with a spectral function fitted to data (Sec. 5.8.2).

The value of the function f_1 for a coincidence event characterizes how close is the event to the center of the combined electron/hadron spectrometer acceptance. Events with positive values of the function lie inside the region of the initial 8-dimensional acceptance cut; events with negative values of the function lie outside the region. From Fig. 5-5 (a) one can see that in the region closer to the center of the acceptance, the data and simulation agree, and as one departs from the center at a certain value of f_1 the yield in data starts to get cut by the spectrometer apertures. From Fig. 5-5 (b), which shows the ratio of the two curves in Fig. 5-5 (a), one can find that the cutoff value is, approximately, 0.001. That is, the cut restricting events to a flat acceptance region can be set at $f_1 > 0.001$.

The function f_1 is defined in terms of the target variables that are "tied" to the spectrometers. Therefore, changing the angular and momentum settings of the

[3] $E_{beam} = 4.8$ GeV, $P_{miss} = 0$.

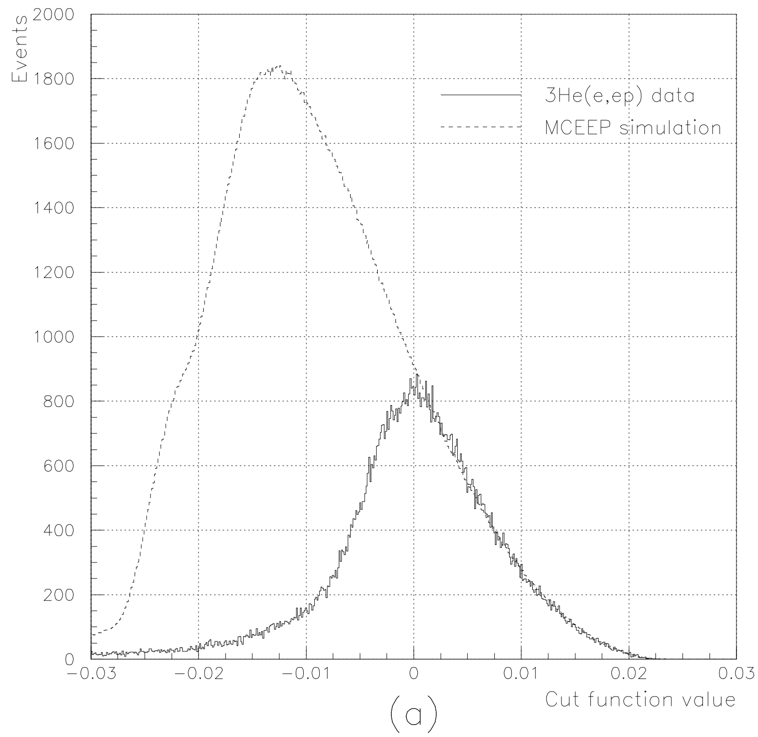

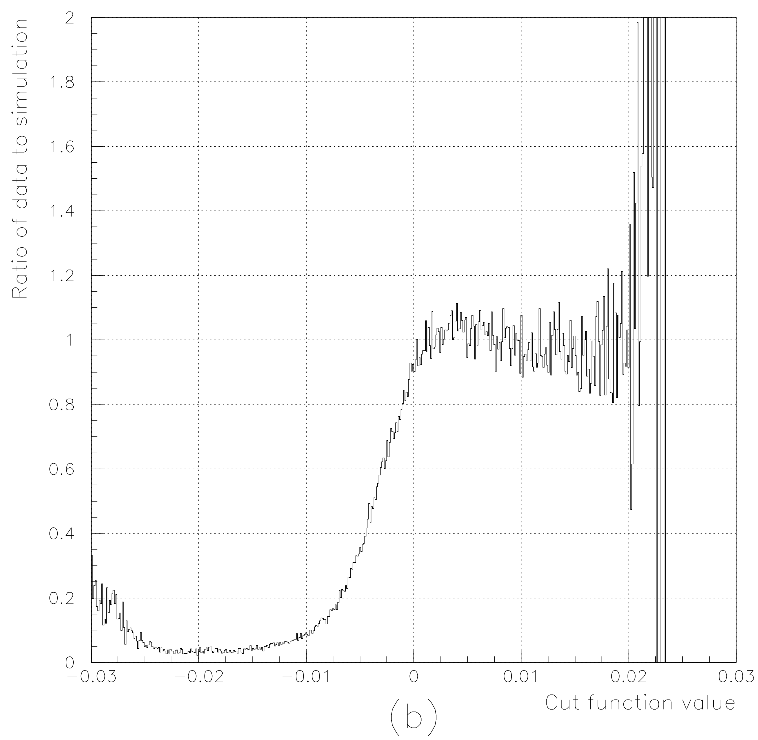

Figure 5-6: (a) The distributions of the cut function f_1 for data and simulation and (b) the ratio of the two distributions (the beam energy of 1.2 GeV, kinematics 3).

spectrometers should not change the form of the cut selecting the flat acceptance region. Fig. 5-6 (a) shows the value of f_1 plotted for the ^{3}He(e,e$'$p) data collected at kinematics 3 [4] (solid line) and the corresponding MCEEP simulation (dashed line), and Fig. 5-6 (b) shows the ratio of the two distributions. These plots exhibit the same general features as the plots in Fig. 5-5, with the optimal cutoff value at, approximately, 0.0014. The values of f_1 were also plotted for other ^{3}He(e,e$'$p) kinematic settings analyzed in this thesis, with a conclusion that the cut $f_1 > 0.002$ safely selects a flat acceptance region for the whole dataset. Therefore, in the final analysis, the cut $f_1 > 0.002$ was used as the acceptance-defining cut at all ^{3}He(e,e$'$p) kinematic settings. A definition of the function f_1 as the PAW function is given in Appendix A.1.

The acceptance region defined by the cut $f_1 > 0.002$ selects $\sim$ 52% of the ^{3}He(e,e$'$p) coincidence events collected at kinematics 1 (Fig. 5-5), and $\sim$ 44% of the coincidence events collected at kinematics 3 (Fig. 5-6) (after removing the contributions from the aluminum target walls by a cut on the reaction point along the beam reconstructed by one of the two spectrometers, Sec. 5.4). Regular linear acceptance cuts applied to the target variables (e.g., $|\phi_{tg}| < 0.02$ rad, $|\theta_{tg}| < 0.04$ rad, $-0.035 < \delta_{tg} < 0.03$, y_{tg} is limited by the cut on the reaction point along the beam) select $\sim$ 28% and $\sim$ 22% of the events at kinematics 1 and 3, respectively. That is, the cut $f_1 > 0.002$ is almost 2 times more effective than the regular "square" acceptance cuts. Another advantage in using the R-function cuts is that they allow one to see how well the yield in data agrees with that in a simulation in different regions of the acceptance, by plotting the value of the cut function for data and simulation.

Several other cut functions constructed from the 22 equations of the linear cuts are discussed in [68].

5.3.5 History of R-functions

R-functions were invented by Vladimir Logvinovich Rvachev, in Ukraine, in 1963. The original motivation for creating R-functions was in their application to the so-

[4] $E_{beam} = 1.2$ GeV, $P_{miss} = 0$.

lution of differential equations with boundary conditions specified on complicated domains. V. L. Rvachev intensively developed the subject, in the process analytically solving many otherwise analytically unsolvable problems of mathematical physics, and creating a full-fledged theory of R-functions and their applications [64, 65].

In one of his other areas of research, V. L. Rvachev discovered a new class of finite infinitely differentiable functions, called "atomic" functions, that rectify some deficiencies of the elementary and spline functions in approximations of arbitrary functions [70]. These functions, as well as R-functions, are actively used in various branches of computational and mathematical physics. In 1989, V. L. Rvachev turned his attention to developing a non-Archimedean algebra (algebra based on the notion of a "largest number") and its application to gravitation and cosmology [71].

V. L. Rvachev is an Academician of the Ukrainian National Academy of Sciences; he lives and actively works in Kharkov, Ukraine. His scientific works are reflected in several hundred publications, including 17 monographs. The author of this thesis is V. L. Rvachev's grandnephew.

5.4 Cut on target length

Fig. 5-7 shows the distribution of the reaction point along the beam (i.e. $\hat{z}$ coordinate of the reaction point in the laboratory coordinate system, denoted as z_{lab}) reconstructed by the hadron spectrometer at kinematics 29, after applying the VDC tracking cuts (Sec. 3.1.2) and the cut selecting the coincidence events. The two peaks in the figure correspond to the particles scattered from the aluminum target walls. The manufactured diameter of the tuna can target is 10.32 cm, while the distance between the peaks in Fig. 5-7 is 10.29 cm, signifying a good reconstruction of the reaction point by the hadron spectrometer.

The contributions from the aluminum target walls were removed by the cut $|z_{lab}| < 3.5$ cm, imposed on the reaction point along the beam reconstructed by the spectrometer positioned at a larger scattering angle. Still, a small fraction of particles originating in the walls satisfied the cut, and can be seen as a small back-

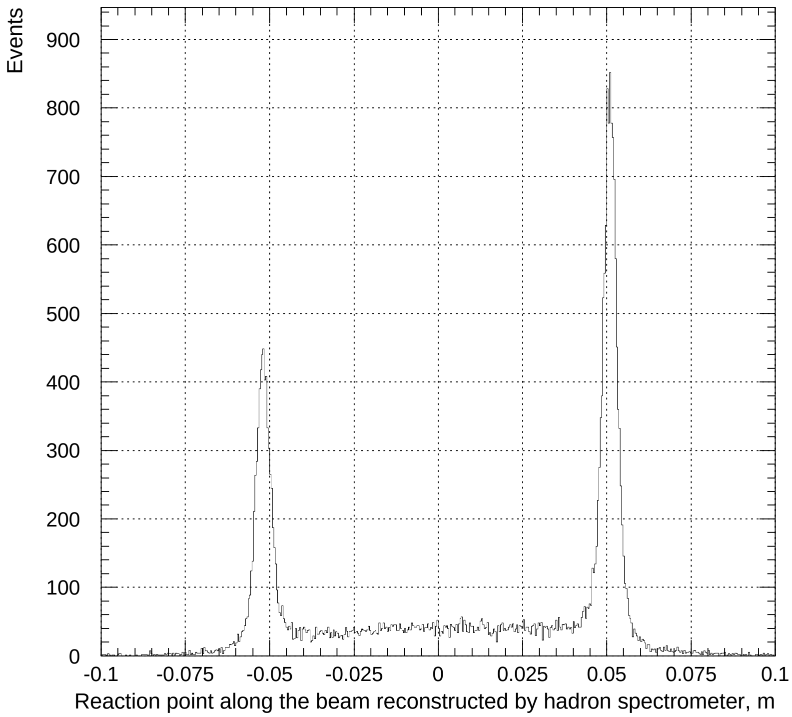

Figure 5-7: Reaction point along the beam reconstructed by the hadron spectrometer at kinematics 29, coincidence events.

ground at E_{miss} distributions in Figs. 5-21 through 5-39, for $E_{miss} < 5.5$ MeV [5]. In the cross section analysis, corrections for the background were applied individually at each kinematic setting. At all kinematic settings, the corrections were less than 1%.

The overall location of the target relative to the hall center, determined from the reconstructed position of the target walls in Fig. 5-7, is 0.9 mm upstream, while the location measured by surveying the target position during a target warmup is 0.1 mm upstream. The 0.8 mm difference could be due to the thermal deformation of the target system during the target warmup. The ^{3}He(e,e$'$p)D results obtained in this thesis are insensitive to small ($\sim$ 1 mm) uncertainties in the overall position of the target along the beam. This is so because the events originating close to the target walls are eliminated by the cut on the reconstructed reaction point along the beam.

[5]It has been verified that this small background is due to contributions from the target walls, and not due to the accidental coincidences.

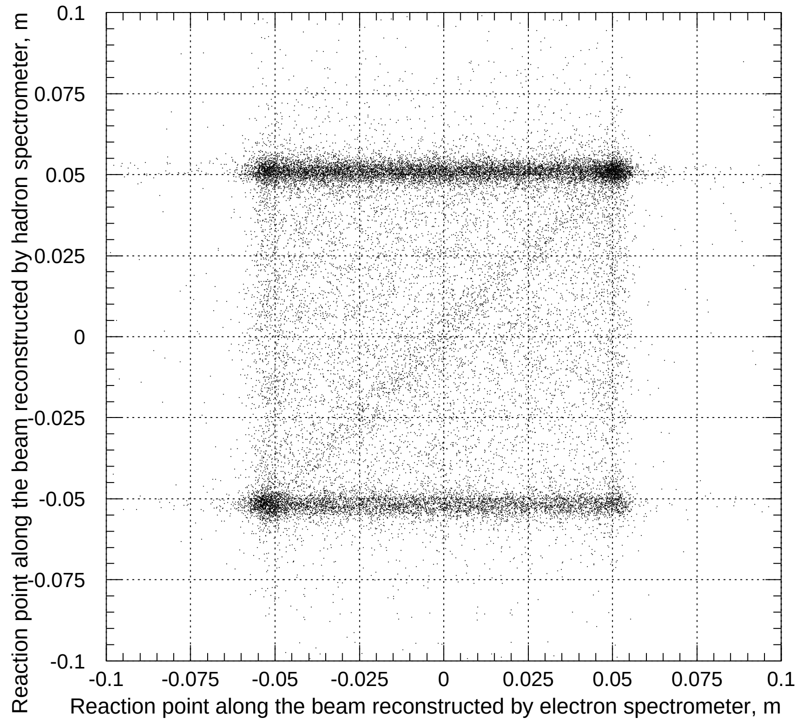

Figure 5-8: Reaction points along the beam reconstructed by the two spectrometers, kinematics 29, coincidence events. True ^{3}He(e,e′p) coincidences are contained in the diagonal band of events.

The influence of the uncertainties in the reconstruction of the reaction point along the beam on the ^{3}He(e,e′p) results is analyzed in Sec. 6.6.

It should be noted that the distribution in Fig. 5-7 was plotted without an E_{miss} cut on the ^{3}He 2bbu peak. The cut would substantially decrease the contribution of the events originating in the target walls relative to the contribution from ^{3}He.

5.5 Cut on difference between reaction points reconstructed by the electron spectrometer and the hadron spectrometer

Fig. 5-8 shows the distribution of the reaction point along the beam reconstructed

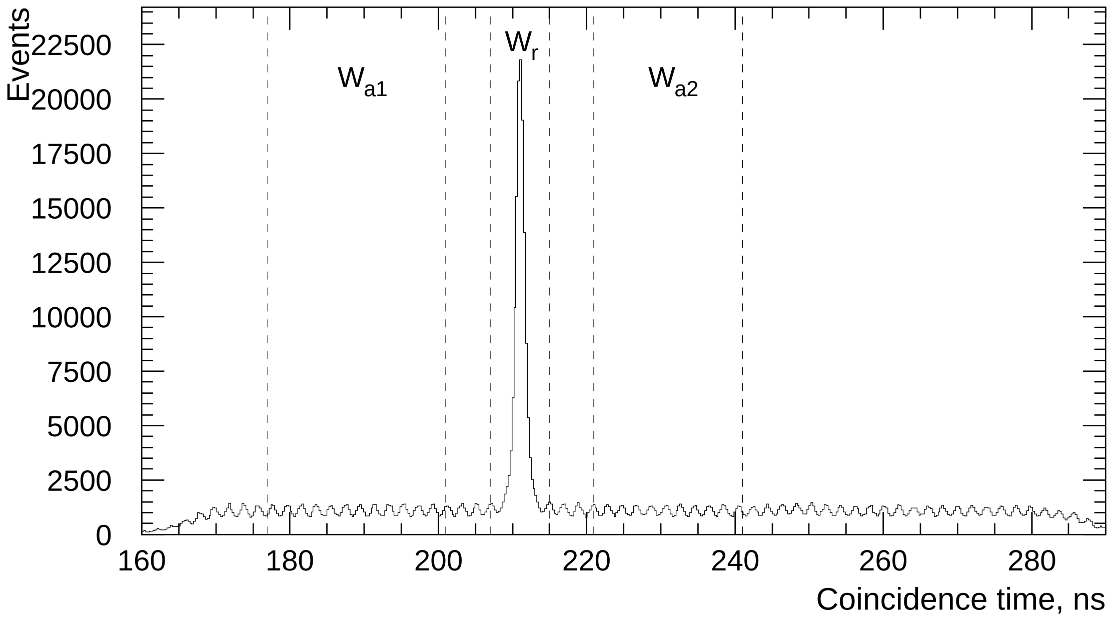

Figure 5-9: Coincidence time between particles detected in the two spectrometers, corrected for time of flight to the focal planes.

by the hadron spectrometer (z_{labh}) plotted versus the reaction point along the beam reconstructed by the electron spectrometer (z_{labe}), for coincidence events detected at kinematics 29, with the VDC tracking cuts applied. The real coincidence events are located along diagonal $z_{labh} = z_{labe}$. The cut on the difference between the reconstructed reaction points, $|z_{labh} - z_{labe}| < 2$ cm for Σ_1, Σ_2, Σ_4 and Σ_5 kinematic settings, and the cut $|z_{labh} - z_{labe}| < 2.5$ cm for Σ_3 kinematic settings, was used for rejection of most of the accidental coincidences.

5.6 Subtraction of accidental coincidences

Fig. 5-9 shows the distribution of coincidence time between particles detected in the electron and hadron spectrometers corrected for time of flight to the focal planes. The events are detected in kinematics 8 and all the cuts listed in Sec. 5.1 are applied, except for cuts on coincidence time. Vertical dashed lines in the figure indicate edges of real and accidental coincidence windows, with widths W_r and $W_{a1} + W_{a2}$ respectively. The oscillating character of the distribution is due to ~ 2 ns intervals between electron packets in the incoming electron beam.

For each kinematic bin, the number of true coincidence events N_t was determined with the formula

$$N_t = N_r - N_a \frac{W_r}{W_{a1} + W_{a2}}, \tag{5.10}$$

where N_r is the number of events within the bin reconstructing in the real coincidence window W_r, N_a is the number of events within the bin reconstructing in the accidental coincidence windows W_{a1} or W_{a2}. Statistical errors were propagated as

$$\delta N_t = \sqrt{N_r + N_a \left(\frac{W_r}{W_{a1} + W_{a2}} \right)^2}. \tag{5.11}$$

Widths of the windows varied between kinematic settings, with wider accidental and more narrow real coincidence windows at settings with a higher relative rate of accidental coincidence events. Multiplicative corrections for cut out real coincident events were made based on the shape of the coincidence peak in nominal $P_{miss} = 0$ kinematics at each beam energy. Care was taken to exclude real coincident (e,e$'\pi^+$), (e,e$'^2$H) and (e,e$'^3$H) events from the windows.

5.7 Corrections to missing energy spectra

The position of the ^{3}He(e,e$'$p)D peak in the E_{miss} spectra was observed to be in the range (2.5, 4) MeV, deviating from the position of the peak at ~ 5.5 MeV in the simulation. The dominant errors contributing to the incorrect reconstruction were found to be errors in the linear calibration coefficients of the central momentum of the spectrometers[6]. A $2 \cdot 10^{-4}$ (relative) correction to the linear calibration coefficient of the electron spectrometer, and a $-1.6 \cdot 10^{-3}$ (relative) correction to the linear

[6]Omitting higher order terms, the spectrometer central momentum P_0 is determined with the formula: $P_0 = kB$, where k is the linear calibration coefficient, B is the magnetic field measured by an NMR probe located in the dipole magnet. The nominal relative error of the coefficient k is 10^{-3} for both spectrometers.

calibration coefficient of the hadron spectrometer positioned the ^{3}He 2bbu peak close to 5.5 MeV at all kinematic settings simultaneously.

Still, at Σ_1 and Σ_2 kinematic settings (beam energy 4.8 GeV), the reconstructed location of the 2bbu peak varied by as much as ~ 1 MeV depending on values of the kinematic variables, most significantly as a function of P_{miss}. The origin of the variation was most definitely in the errors in the matrix elements of the electron spectrometer optics database. Reoptimization of the momentum part of the database, as well as artificial shifts to central scattering angles of the spectrometers, did not remove or reduce the variation.

While errors in the matrix elements of optics databases were within tolerances of the experiment and were ultimately taken into account in analysis of systematic errors, in the 2bbu cross section analysis it was important to place E_{miss} cuts on data and simulation at the same place relative to the 2bbu peak. This was accomplished by shifting the experimentally reconstructed E_{miss} spectrum for each P_{miss} bin individually[7]. The procedure of finding the amount of the shift for each P_{miss} bin is outlined below.

Figs. 5-10 and 5-11 show magnitude of deviation of the ^{3}He 2bbu peak reconstructed in data from that reconstructed in the simulation as a function of P_{miss} bin, for Σ_1 and Σ_2 kinematic settings. The magnitude of the deviation was determined with Kolmogorov test [72, 73] of similarity of two statistical distributions[8]. The following procedure was developed:

1. At each spectrometer setting, the R-function and other cuts described in Sec. 5.1 are applied to the data and to the simulation; data and simulation are binned in P_{miss}.

2. For each P_{miss} bin, finely binned histograms of the E_{miss} 2bbu peak are filled for data and for simulation; accidental coincidences are subtracted from data.

[7]At Σ_1 and Σ_2 kinematic settings only; at Σ_3, Σ_4 and Σ_5 kinematic settings, the ^{3}He(e,e′p)D peak position did not vary within spectrometer acceptance.

[8]Employed was PAW implementation (function "HDIFF") of the Kolmogorov test [72]; for unbinned statistical data Kolmogorov test is commonly regarded as superior to the chi-square test [72].

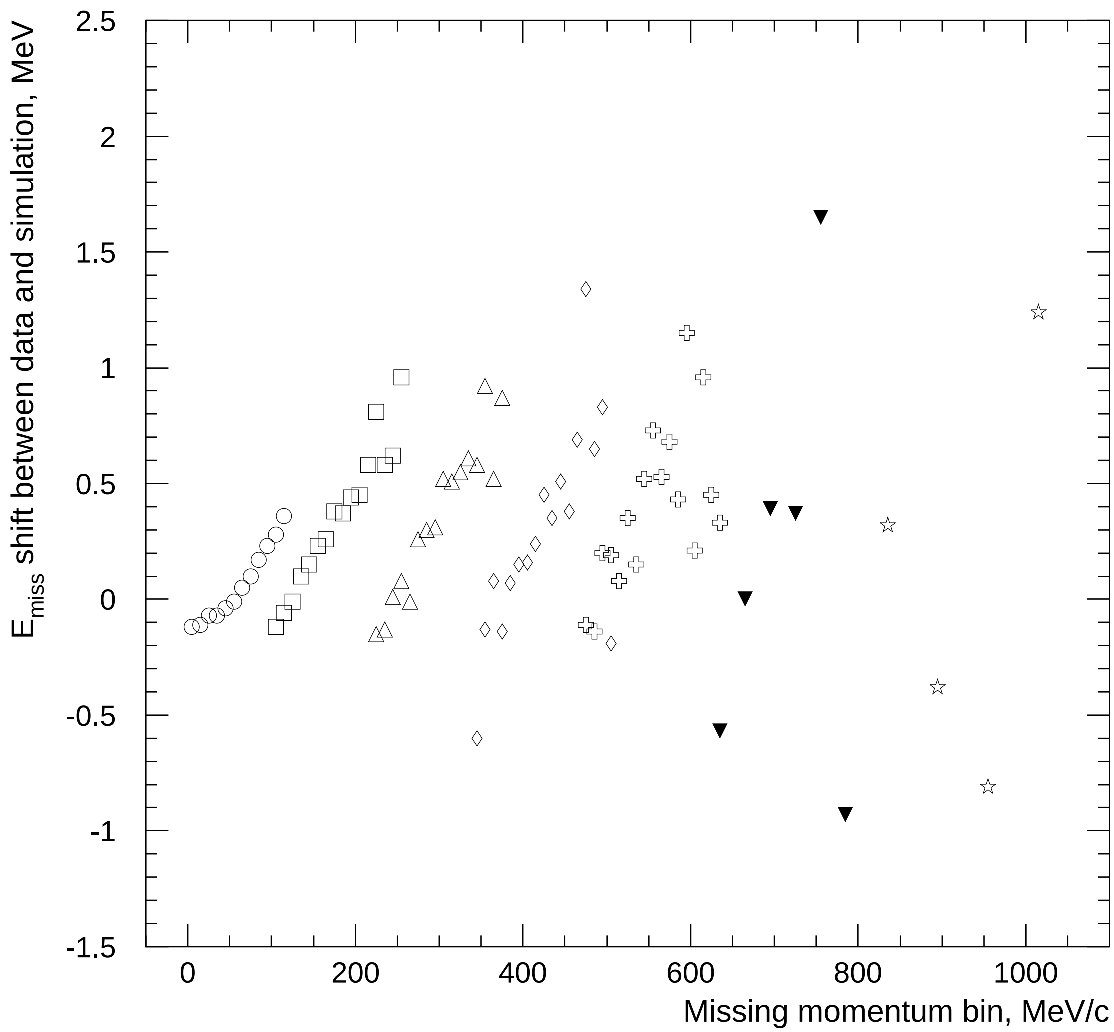

Figure 5-10: Offsets between missing energy ^{3}He(e,e′p)D peak in data and simulation, as determined by Kolmogorov algorithm, for missing momentum bins at Σ_1 kinematic settings. Different marker types correspond to different angular and momentum settings of the hadron spectrometer, while the setting of the electron spectrometer is fixed.

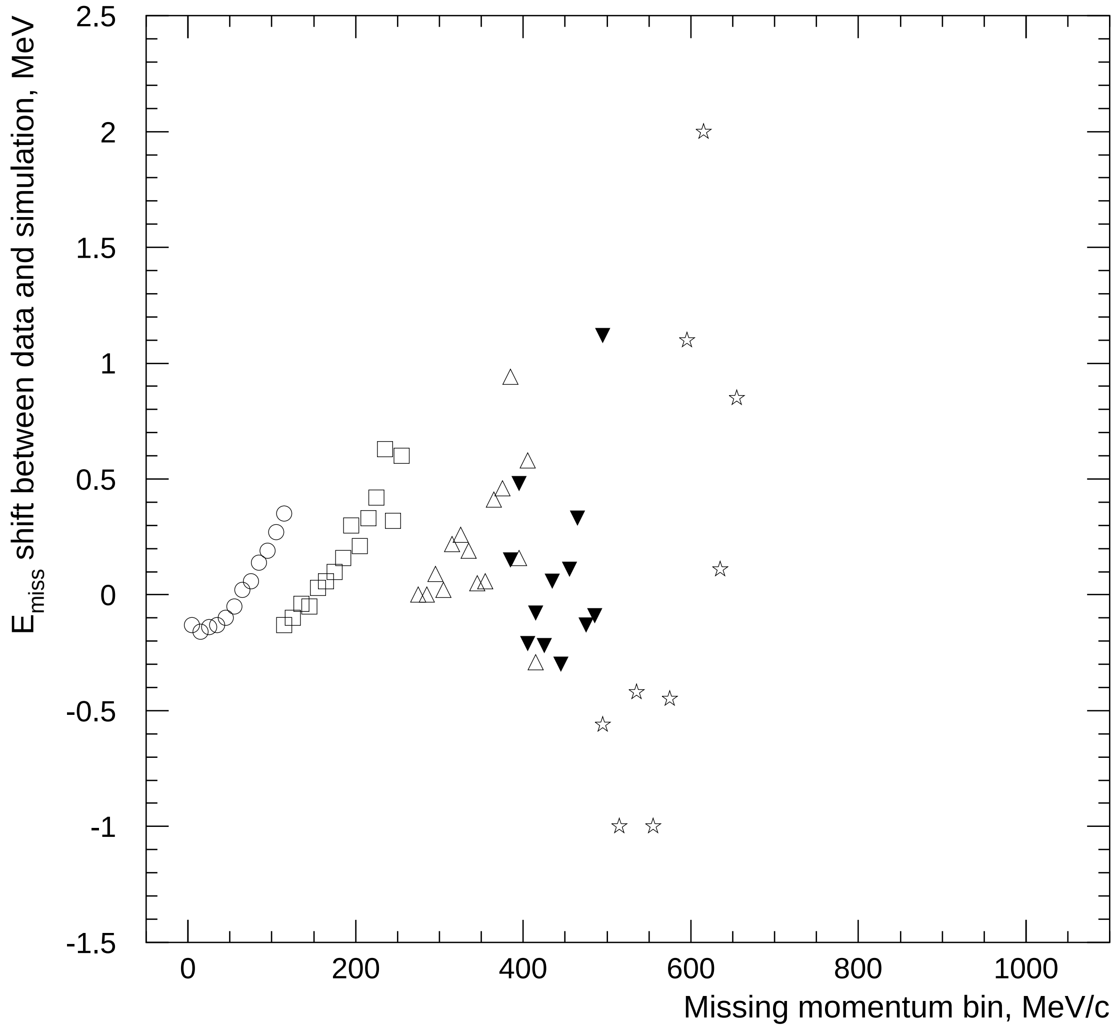

Figure 5-11: Offsets between missing energy ^{3}He(e,e$'$p)D peak in data and simulation, as determined by Kolmogorov algorithm, for missing momentum bins at Σ_2 kinematic settings. Different marker types correspond to different angular and momentum settings of the hadron spectrometer, while the setting of the electron spectrometer is fixed.

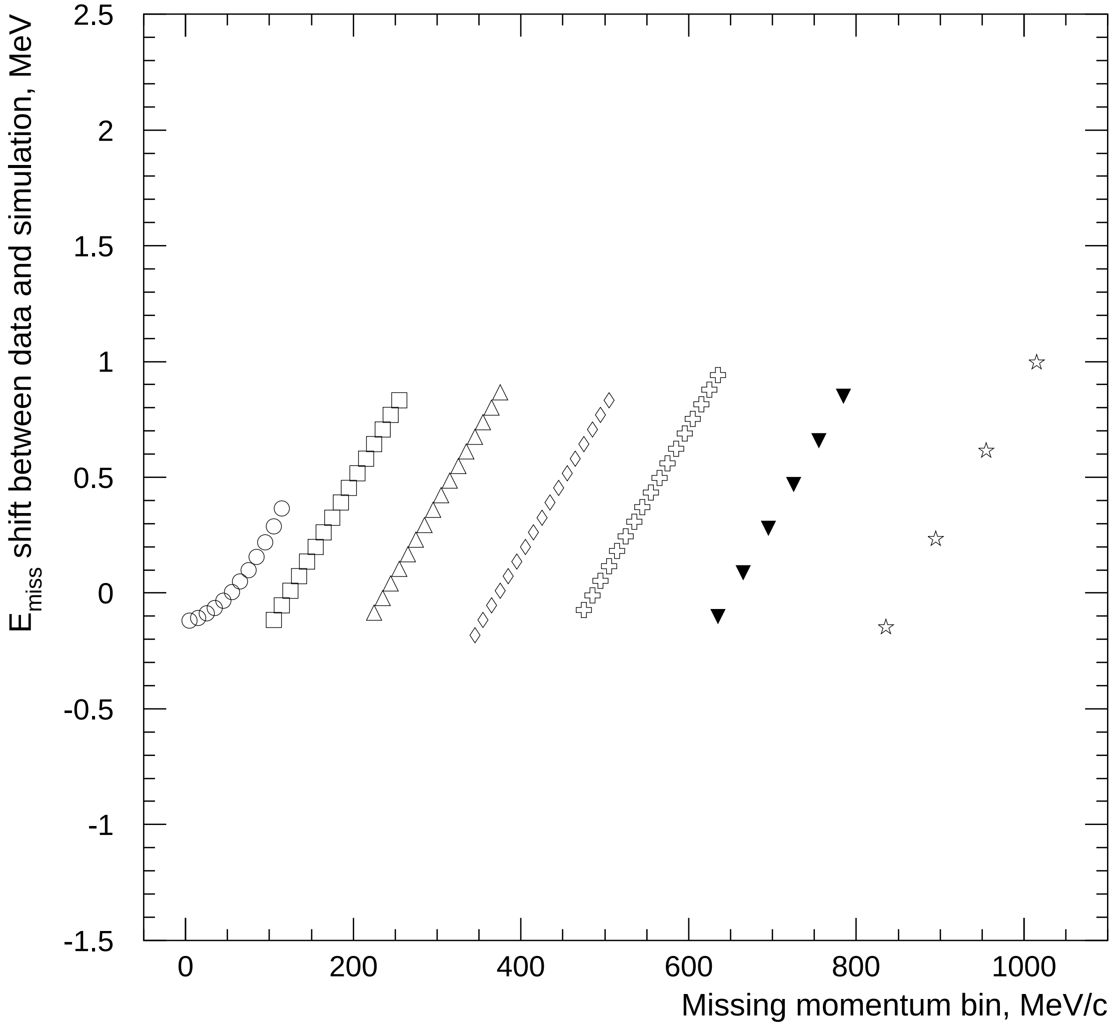

Figure 5-12: Offsets applied to reconstructed missing energy spectra at Σ_1 kinematic settings, as a function of missing momentum bin. Different marker types correspond to different angular and momentum settings of the hadron spectrometer, while the setting of the electron spectrometer is fixed.

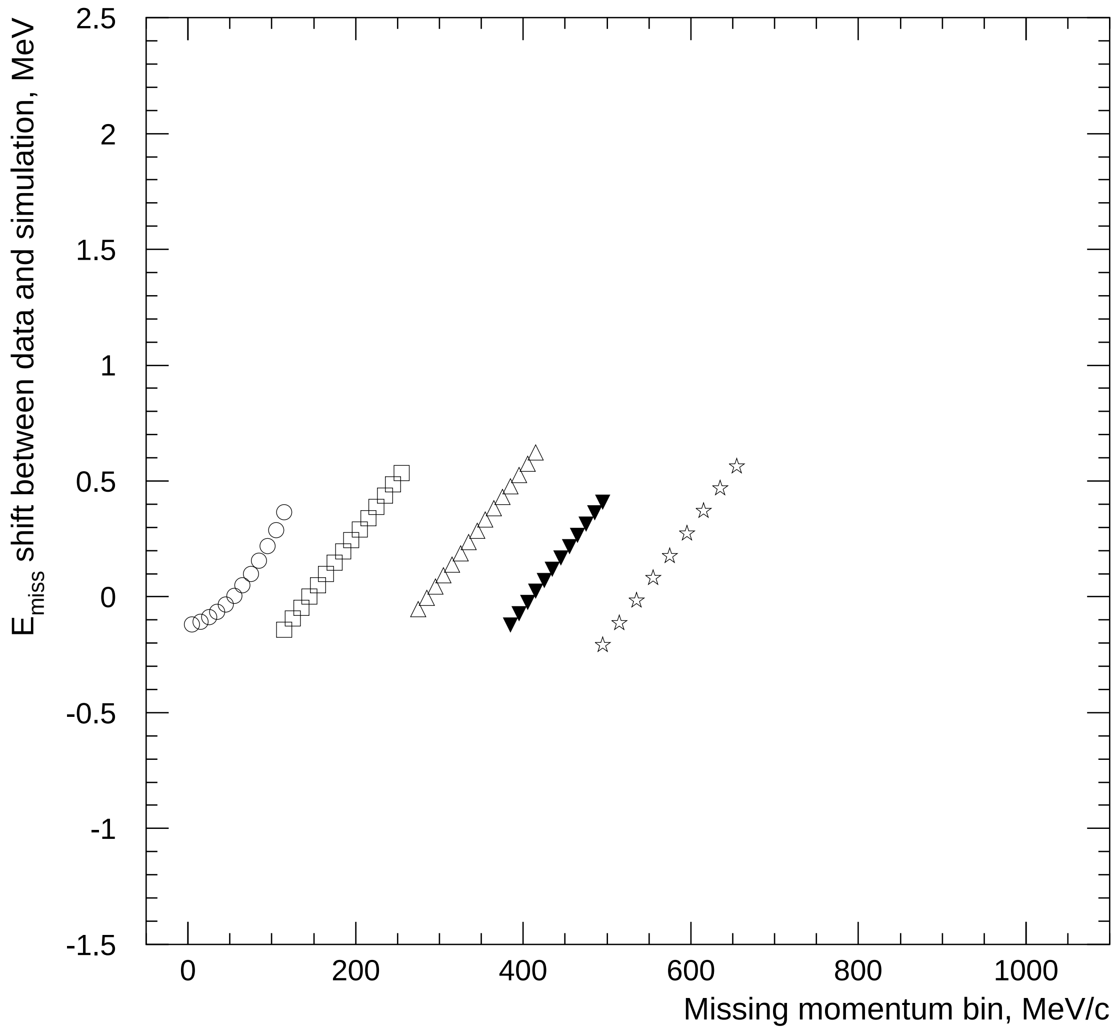

Figure 5-13: Offsets applied to reconstructed missing energy spectra at Σ_2 kinematic settings, as a function of missing momentum bin. Different marker types correspond to different angular and momentum settings of the hadron spectrometer, while the setting of the electron spectrometer is fixed.

3. Data E_{miss} histogram is shifted in 0.01 MeV increments, with Kolmogorov test between data and simulation histograms applied at each increment.

4. The shift returning highest similarity of the spectra is the magnitude of the deviation, plotted on vertical axis in Figs. 5-10 and 5-11.

The program executing the procedure is listed in Appendix A.2, as part of PAW program used for extraction of ^{3}He(e,e′p) cross sections (Sec. 5.8).

The vertical scatter of points in Figs. 5-10 and 5-11 is due to low statistics at the high missing momentum kinematics or at the edges of acceptance in low missing momentum kinematics, where the small number of events reconstructed in the 2bbu E_{miss} bin translated into a statistical scatter of the fitted position of the 2bbu peak. With the exception of kinematics 1 (nominal $P_{miss} = 0$), the dependence of the shift on missing momentum within each spectrometer setting is approximately linear, with a similar slope of the dependence.

For kinematics 1 (nominal $P_{miss} = 0$), the dependence was fitted with a second-order polynomial. For other Σ_1 and Σ_2 kinematic settings, slope of the dependence was found from fit to high statistics points in Figs. 5-10 and 5-11, and the offset along P_{miss} was found individually for each spectrometer setting. The resulting offsets are plotted in Figs. 5-12 and 5-13, and were applied to Σ_1 and Σ_2 data E_{miss} spectra before E_{miss} binning, both in the 2bbu and 3bbu analysis.

5.8 Extraction of cross sections

5.8.1 Extraction of ^{3}He(e,e′p)D cross sections

Preliminary steps in the ^{3}He(e,e′p) analysis are summarized in Sec. 5.1 and are described in more detail in previous sections. Here the fitting program that extracted the ^{3}He(e,e′p)D cross sections is described. The program is given in Appendix A.2. In these sections, it is assumed that the preliminary steps in the ^{3}He(e,e′p) analysis, summarized in Sec. 5.1, are completed, and that a P_{miss} bin is selected in data and simulation.

Full simulation of the experiment with MCEEP [55] provides two sets of kinematic variables (E_{miss}, P_{miss}, Q^2, ω and others) for each simulated ^{3}He(e,e$'$p) event. One set is the "asymptotic", or "radiated" kinematic variables. These variables are analogous to the experimentally reconstructed kinematic variables and are calculated based on:

- 4-momentum of the incident electron after subtraction of the mean energy losses before the interaction point.
- 4-momenta of the scattered electron and the proton after simulation of the energy losses[9], radiation, multiple scattering and spectrometer resolution.

Another set of MCEEP kinematic variables is named "vertex", or "unradiated" variables. The "vertex" variables are calculated on the ^{3}He(e,e$'$p) reaction vertex in the simulation. That is, these variables are calculated based on

- 4-momentum of the incident electron after simulation of the energy losses, radiation and multiple scattering.
- 4-momenta of the scattered electron and the proton before simulation of the energy losses, radiation, mulitple scattering and spectrometer resolution[10].

Internally MCEEP assigns each event a ^{3}He(e,e$'$p) cross section based on values of the "vertex" kinematic variables and a factorization of a spectral function with the cc1 prescription for electron-nucleon cross section. The assigned ^{3}He(e,e$'$p) cross section is referred to as the "vertex" (or "unradiated", or "simulation") cross section. Ideally, if the simulated yield was equal to the detected yield in the asymptotic kinematic bins, one could say that the vertex ^{3}He(e,e$'$p) cross section in the simulation is equal to the unradiated ^{3}He(e,e$'$p) cross section sampled in the experiment[11].

The philosophy of the fitting procedure is to adjust the vertex ^{3}He(e,e$'$p) cross section in the simulation until the yield simulated in the asymptotic kinematic bins is

[9] Also, the mean energy losses of the scattered electron and the proton after the interaction point are added, to mimic the algorithm of event reconstruction in the analysis code ESPACE.

[10] More details on the "asymptotic" and "vertex" notation, and on how MCEEP calculates these variables, can be found in MCEEP manual [55].

[11] Up to variation of the ^{3}He(e,e$'$p) cross section within kinematic bins, and intricacies related to the question of "physical existance" of an unradiated ^{3}He(e,e$'$p) cross section.

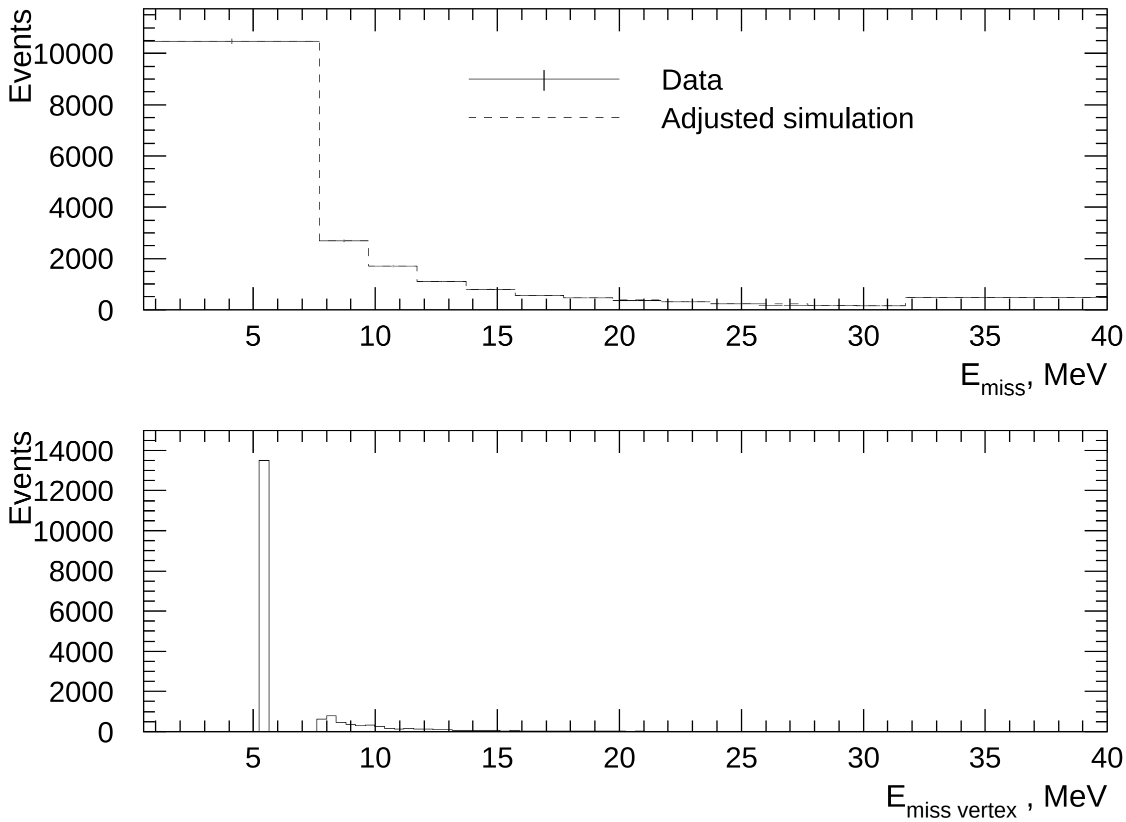

Figure 5-14: Top panel: asymptotic E_{miss} distribution, after binning and adjustment of the simulation with the fitting program. Lower panel: vertex E_{miss} distribution in simulation, after adjustment of simulation with the fitting program. Kinematics 4 (Σ_1), P_{miss} bin (110, 120) MeV/c.

equal to the yield detected experimentally in these bins. After adjustment, the vertex simulation ^{3}He(e,e$'$p) cross section is quoted as the extracted radiatively corrected cross section.

Results of the fitting for asymptotic P_{miss} bin (110, 120) MeV/c (kinematics 4) are illustrated in Figs. 5-14 and 5-15. The top panel of Fig. 5-14 shows the yield in data and the adjusted simulation, binned in asymptotic E_{miss}[12]. The bottom panel of the figure shows the distribution of vertex E_{miss} in the adjusted simulation, with delta

[12]The first E_{miss} bin is (0.5, 7.72) MeV, next 12 bins are 2 MeV wide, the last bin is (31.72, 40) MeV (Σ_1 and Σ_2 kinematic settings); at Σ_4 and Σ_5 kinematic settings, the first bin was set to (2.5, 7.72) MeV, with the rest of the bins the same; in Σ_3 analysis, first two E_{miss} bins were set to (2.5, 7.45, 9.72) MeV, with the rest of the bins the same.

function at $E_{miss} = 5.49$ MeV (^{3}He(e,e$'$p)D process), and the continuum ^{3}He(e,e$'$p)pn spectrum starting at $E_{miss} = 7.72$ MeV. One can see that $\sim 30\%$ of the 2bbu events are radiated from the first E_{miss} bin.

Fig. 5-15 shows how the adjusted simulated spectrum in the top panel of Fig. 5-14 was obtained. The simulated events are binned in vertex E_{miss}, with weight w_i assigned to each bin[13]. The total number of simulated events in asymptotic E_{miss} bin i is found with

$$N_i(S) = \sum_{j=1}^{n} N_{ji}(S) \cdot w_j, \tag{5.12}$$

where $N_{ji}(S)$ is contribution of vertex E_{miss} bin j to asymptotic E_{miss} bin i, and n is number of E_{miss} bins. The weights w_i are adjusted until

$$N_i(D) = N_i(S), \qquad \text{for all } i = 1, ..., n, \tag{5.13}$$

where $N_i(D)$ is the number of events detected in the asymptotic E_{miss} bin i, after the subtraction of accidental coincidences. After adjustment, the radiatively corrected ^{3}He(e,e$'$p)D cross section is found with

$$\frac{d^5\sigma}{dE_f d\Omega_e d\Omega_p} = \frac{d^5\sigma^{sim}}{dE_f d\Omega_e d\Omega_p}\left(\bar{E}_i, \bar{Q}^2, \bar{\omega}, \bar{P}_{miss}\right) \cdot w_1, \tag{5.14}$$

where $\frac{d^5\sigma^{sim}}{dE_f d\Omega_e d\Omega_p}(\bar{E}_i, \bar{Q}^2, \bar{\omega}, \bar{P}_{miss})$ is the ^{3}He(e,e$'$p)D cross section in the simulation cross section model (that is, the vertex cross section), at point $(\bar{E}_i, \bar{Q}^2, \bar{\omega}, \bar{P}_{miss})$, found as the acceptance-weighted average of vertex values of E_i, Q^2, ω and P_{miss} within the bin and coplanar proton kinematics, and w_1 is the adjusted weight for the 2bbu bin[14].

The relative statistical error for the extracted ^{3}He(e,e$'$p)D cross section $\frac{d^5\sigma}{dE_f d\Omega_e d\Omega_p}$

---

[13]Vertex E_{miss} binning was identical to binning in asymptotic E_{miss}; this is a good approximation, since asymptotic E_{miss} is corrected for mean energy losses of the particles.

[14]In another analysis technique, cross sections were "renormalized" to fixed Q^2 and ω (see p. 160). For purposes of finding average values of vertex variables, only events falling within the same vertex and asymptotic E_{miss} bin were considered.

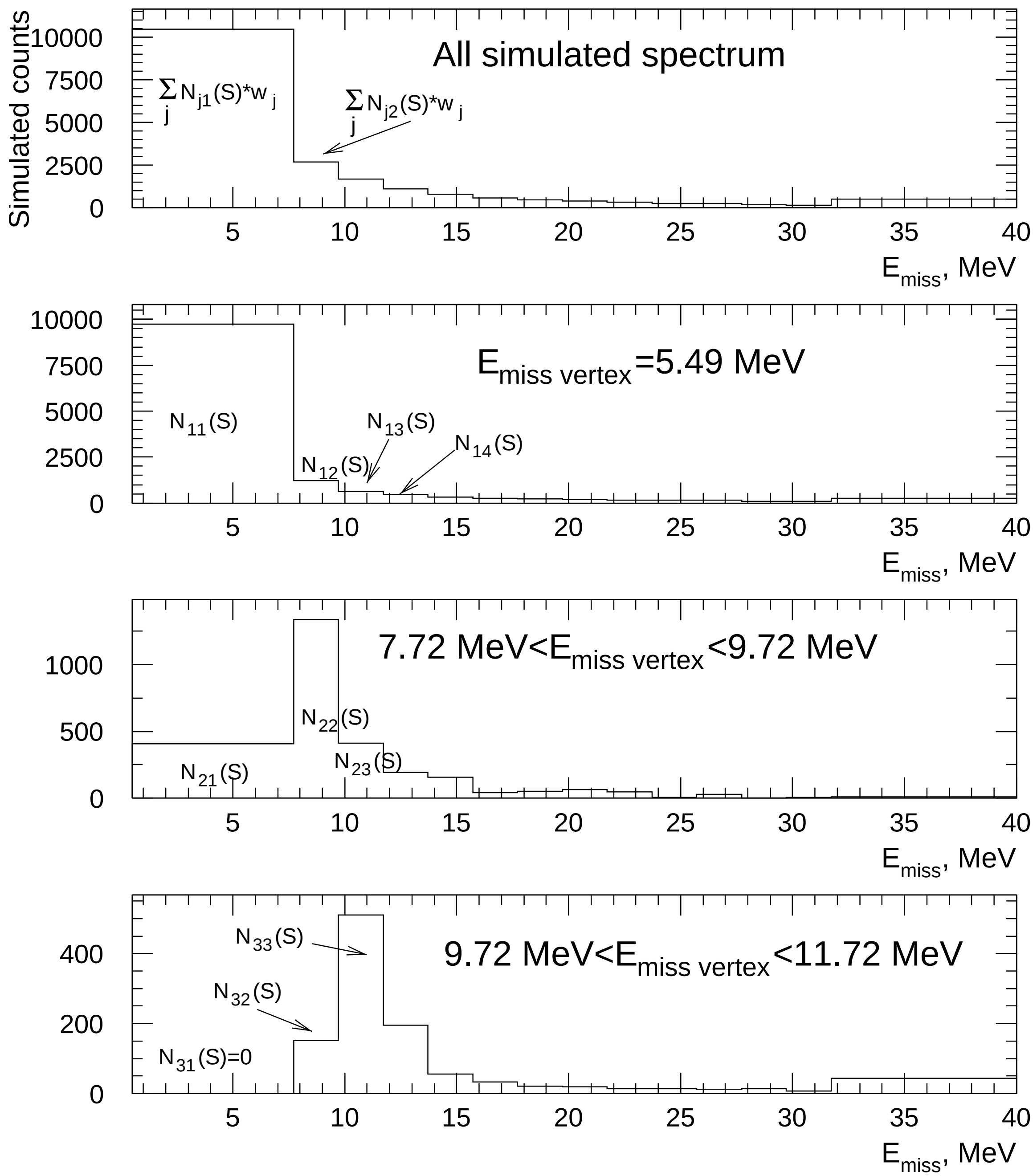

Figure 5-15: Plots illustrating operations on histograms of simulated yield in the procedure of extraction of ^{3}He(e,e′p)D cross sections: lower plots are multiplied by weights w_i and added to produce the top plot (formula (5.12)).

was calculated as[15]

$$\epsilon_{st} = \frac{\sqrt{\delta N_1(D)^2 + \sum_{j=2}^{n} \delta N_{j1}(S)^2 \cdot w_j^2}}{N_1(D) - \sum_{j=2}^{n} N_{j1}(S) \cdot w_j}, \tag{5.15}$$

where $\delta N_1(D)$ is the standard deviation of number of events detected in the ^{3}He(e,e$'$p)D bin, given by formula (5.11), and $\delta N_{ji}(S)$ is given by

$$\delta N_{ji}(S) = \sqrt{\sum_k W_{jik}^2}, \tag{5.16}$$

where the sum is over all weights W_{jik} of simulated events with vertex E_{miss} in bin j and asymptotic E_{miss} in bin i. The weights W_{jik} are those internally assigned in the MCEEP simulation of the yield to each simulated event [55]. In the formulas above, the simulated yield $N_{ji}(S)$ in the vertex E_{miss} bin j and asymptotic E_{miss} bin i was calculated with standard MCEEP procedure[16]:

$$N_{ji}(S) = \sum_k W_{jik}. \tag{5.17}$$

Essentially, the fitting procedure adjusted the strength of the vertex ^{3}He(e,e$'$p) cross section in the vertex E_{miss} bins to reproduce the detected yield in asymptotic E_{miss} bins, while accounting for the spread of events from the vertex E_{miss} bins to different asymptotic E_{miss} bins (due to radiation, energy losses and multiple scattering experienced by the particles, and due to the resolution of the spectrometers). Adjusted weights were found iteratively, with initial values set to 1. At each iteration step, new weights w_i were found from weights w_i' at the previous step with

$$w_i = \frac{N_i(D) - \sum_{j=1}^{\prime n} N_{ji}(S) \cdot w_j'}{N_{ii}(S)}, \tag{5.18}$$

where the sum excludes $i = j$ term.

[15] In fact, statistical errors were calculated using built-in PAW propagation of errors on histogram channels, and operations on histograms (see the program body in Appendix A.2). The calculation in PAW should be identical to given formulas.

[16] Except when extracting the cross sections with a "model independent" technique, see p. 161.

5.8.2 Cross section models used in simulations

In the first pass of analysis, the experiment was simulated with the ^{3}He(e,e$'$p) vertex cross section modeled as the factorization of the Salme spectral function $S^{Salme}(E_{miss}, P_{miss})$ with the cc1 prescription for electron-nucleon cross section:

$$\frac{d^5\sigma}{dE_f d\Omega_e d\Omega_p} = C_1 \sigma_{cc1} S^{Salme}(5.49 \text{ MeV}, P_{miss}), \tag{5.19}$$

for the 2bbu process, and

$$\frac{d^6\sigma}{dE_f dE_p d\Omega_e d\Omega_p} = C_2 \sigma_{cc1} S^{Salme}(E_{miss}, P_{miss}), \tag{5.20}$$

for the 3bbu process, where C_1 and C_2 are kinematic factors [2], and σ_{cc1} is the off-shell electron-nucleon cross section of de Forest [25]. This simulation, together with the fitting procedure described in the previous section, was used to extract ^{3}He(e,e$'$p)D experimental "distorted" spectral functions, as

$$S'^{\Sigma_n}(5.49 \text{ MeV}, \bar{P}_{miss}) = S^{Salme}(5.49 \text{ MeV}, \bar{P}_{miss}) \cdot w_1, \tag{5.21}$$

where Σ_n denotes kinematics of the setting[17], w_1 is the adjusted weight for the ^{3}He(e,e$'$p)D E_{miss} bin, and $\bar{P}_{miss}$ is the acceptance-weighted average of vertex values of P_{miss} within the E_{miss}/P_{miss} bin. The extracted ^{3}He(e,e$'$p)D spectral functions were fitted with continuous curves, tabulated on a MCEEP-compatible P_{miss} grid, to obtain "fitted-to-data" 2bbu spectral functions $S^{\Sigma_n}(5.49 \text{ MeV}, P_{miss})$ for each of the Σ_n, $n = 1, ..., 5$ kinematic settings. It was observed that the Salme spectral function, in the first approximation, correctly reproduces the relative strength of the 2bbu and 3bbu processes at each P_{miss} value, and therefore "fitted-to-data" 3bbu spectral functions were obtained as

$$S^{\Sigma_n}(E_{miss}, P_{miss}) = \frac{S^{\Sigma_n}(5.49 \text{ MeV}, P_{miss})}{S^{Salme}(5.49 \text{ MeV}, P_{miss})} S^{Salme}(E_{miss}, P_{miss}). \tag{5.22}$$

[17] Definition of Σ_n, $n = 1, ..., 5$ notation for kinematic settings is given in Sec. 1.6.

Then, the experiment was resimulated with ^{3}He(e,e$'$p) vertex cross section modeled as the factorization of σ_{cc1} with the "fitted-to-data" spectral functions $S^{\Sigma_n}(5.49\ \mathrm{MeV}, P_{miss})$ and $S^{\Sigma_n}(E_{miss}, P_{miss})$ for kinematic settings Σ_n, $n = 1, ..., 5$ [18]. The experimental ^{3}He(e,e$'$p)D spectral function was re-extracted, with the fitting procedure described in the previous section, as

$$S''^{\Sigma_n}(5.49\ \mathrm{MeV}, \bar{P}_{miss}) = S^{\Sigma_n}(5.49\ \mathrm{MeV}, \bar{P}_{miss}) \cdot w_1, \tag{5.23}$$

where w_1 is the new adjusted weight for the ^{3}He(e,e$'$p)D bin, and $\bar{P}_{miss}$ is the acceptance-weighted average of vertex values of P_{miss} within the bin. It was observed that the new extracted values of the 2bbu spectral functions were almost identical to those extracted with the Salme spectral function used in simulation, i.e.

$$S''^{\Sigma_n}(5.49\ \mathrm{MeV}, P_{miss}) \approx S'^{\Sigma_n}(5.49\ \mathrm{MeV}, P_{miss}), \tag{5.24}$$

for all P_{miss} values and Σ_n kinematics. Therefore, further adjustment of the "fitted-to-data" spectral functions $S^{\Sigma_n}(5.49\ \mathrm{MeV}, P_{miss})$ and $S^{\Sigma_n}(E_{miss}, P_{miss})$ was not necessary.

cc1 averaging within bins

As described above, in the final analysis the experiment was simulated with ^{3}He(e,e$'$p) cross section modeled as the factorization of σ_{cc1} with the "fitted-to-data" $S^{\Sigma_n}(5.49\ \mathrm{MeV}, P_{miss})$ and $S^{\Sigma_n}(E_{miss}, P_{miss})$ spectral functions for the ^{3}He(e,e$'$p)D and ^{3}He(e,e$'$p)pn processes respectively, where Σ_n denotes the kinematic setting at which the spectral function was extracted, and for which it was used in simulations.

^{3}He(e,e$'$p)D cross sections extracted with this simulation and with the fitting

[18] In fact, "fitted-to-data" spectral functions at Σ_3, Σ_4 and Σ_5 kinematic settings turned out to be almost identical to the "fitted-to-data" spectral functions at the Σ_1 kinematic setting (in the region of missing momentum overlap), and they were set equal to the Σ_1 spectral function.

Nominal E_{beam} GeV	$\bar{E}_i$ MeV	Q^2_{fixed} (GeV/c)^2	ω_{fixed} MeV	q_{fixed} MeV/c
1.2	1253.8	1.5503	836.5	1500.0
1.9	1953.0	1.5503	836.5	1500.0
4.8	4805.5	1.5244	822.6	1483.6

Table 5.1: Mean energy of incident electron $\bar{E}_i$ at the interaction vertex, and values of Q^2_{fixed} and ω_{fixed} used in "cc1-renormalization" of $\frac{d^5\sigma^{ren}}{dE_f d\Omega_e d\Omega_p}$ ^{3}He(e,e$'$p)D cross sections, at each nominal beam energy E_{beam}. Values of q_{fixed} in the table were obtained with $q_{fixed} = \sqrt{Q^2_{fixed} + \omega^2_{fixed}}$.

procedure described in Sec. 5.8.1, in the following are denoted as $\frac{d^5\sigma^{cc1}}{dE_f d\Omega_e d\Omega_p}$, i.e.

$$\frac{d^5\sigma^{cc1}}{dE_f d\Omega_e d\Omega_p} = \frac{d^5\sigma^{sim}}{dE_f d\Omega_e d\Omega_p}\left(\bar{E}_i, \bar{Q^2}, \bar{\omega}, \bar{P}_{miss}\right) \cdot w_1, \tag{5.25}$$

where $\frac{d^5\sigma^{sim}}{dE_f d\Omega_e d\Omega_p}(\bar{E}_i, \bar{Q^2}, \bar{\omega}, \bar{P}_{miss})$ is the vertex ^{3}He(e,e'p)D cross section[19] in the simulation cross section model at the point $(\bar{E}_i, \bar{Q^2}, \bar{\omega}, \bar{P}_{miss})$, found as the acceptance-weighted average of the vertex values of E_i, Q^2, ω and P_{miss} within the 2bbu bin and coplanar proton kinematics, and w_1 is the adjusted weight for the 2bbu bin.

With the E89044 acceptances, extracted $\frac{d^5\sigma^{cc1}}{dE_f d\Omega_e d\Omega_p}$ cross sections are not convenient quantities for observing the P_{miss} dependence of the ^{3}He(e,e$'$p)D reaction, since the systematic variation of the accepted Q^2 and ω with P_{miss} at each spectrometer setting introduced two hidden variables in the plots of the cross sections as a function of P_{miss}. For the sake of eliminating the Q^2 and the ω dependence, another set of ^{3}He(e,e$'$p)D cross sections, denoted as $\frac{d^5\sigma^{ren}}{dE_f d\Omega_e d\Omega_p}$, was obtained as

$$\frac{d^5\sigma^{ren}}{dE_f d\Omega_e d\Omega_p} = \frac{d^5\sigma^{sim}}{dE_f d\Omega_e d\Omega_p}\left(\bar{E}_i, Q^2_{fixed}, \omega_{fixed}, \bar{P}_{miss}\right) \cdot w_1, \tag{5.26}$$

where w_1 is the same value of adjusted weight as in formula (5.25), and $\frac{d^5\sigma^{sim}}{dE_f d\Omega_e d\Omega_p}(\bar{E}_i, Q^2_{fixed}, \omega_{fixed}, \bar{P}_{miss})$ is the vertex ^{3}He(e,e$'$p)D cross section in the simulation cross section model at point $(\bar{E}_i, Q^2_{fixed}, \omega_{fixed}, \bar{P}_{miss})$ and coplanar proton

[19] For convenience, vertex ^{3}He(e,e'p)D cross sections in simulations of all kinematic settings are designated with superscript *sim* instead of Σ_n.

kinematics. $\bar{E}_i$ and $\bar{P}_{miss}$ were found as the acceptance-weighted average of the vertex E_i and P_{miss} within the bin. Values of Q^2_{fixed} and ω_{fixed} were found as the acceptance-weighted average of the vertex Q^2 and ω for all ^{3}He(e,e$'$p)D data taken at a given beam energy. At each beam energy, the average energy of the incident electron at the reaction vertex, $\bar{E}_i$, was also the same. Values of $\bar{E}_i$, Q^2_{fixed} and ω_{fixed} at each beam energy are listed in Table 5.1.

The ^{3}He(e,e$'$p)D distorted spectral function was obtained as

$$S_{2bbu}(\bar{P}_{miss}) = S^{\Sigma_n}(5.49\text{ MeV}, \bar{P}_{miss}) \cdot w_1, \tag{5.27}$$

where w_1 is the same value of the adjusted weight as in formulas (5.25) and (5.26), and $S^{\Sigma_n}(5.49\text{ MeV}, \bar{P}_{miss})$ is the simulation ^{3}He(e,e$'$p)D spectral function at point $\bar{P}_{miss}$. $\bar{P}_{miss}$ was found as the acceptance-weighted average of the vertex P_{miss} within the 2bbu bin.

Since a single fit was made to obtain $\frac{d^5\sigma^{cc1}}{dE_f d\Omega_e d\Omega_p}$, $\frac{d^5\sigma^{ren}}{dE_f d\Omega_e d\Omega_p}$ and S_{2bbu}, their relative statistical errors, given by (5.15), are the same.

Model independent averaging within bins

In another analysis technique, unit vertex ^{3}He(e,e$'$p)D and ^{3}He(e,e$'$p)pn cross sections were assigned to each event simulated by MCEEP. This was accomplished by modifying the fitting program to weight each simulated event by weight

$$W^*_{jik} = \frac{W_{jik}}{\sigma_{jik}} \tag{5.28}$$

when calculating the number $N_{ji}(S)$ of simulated events in the vertex E_{miss} bin j and asymptotic E_{miss} bin i. That is, in the "model independent" analysis $N_{ji}(S)$ was computed as

$$N_{ji}(S) = \sum_k \frac{W_{jik}}{\sigma_{jik}}, \tag{5.29}$$

instead of formula (5.17). In the formulas above, W_{jik} is the internal MCEEP weight [55] assigned in the MCEEP simulation of yield to events simulated in the vertex E_{miss}

bin j and asymptotic E_{miss} bin i, and σ_{jik} is the corresponding vertex (^{3}He(e,e$'$p)D or ^{3}He(e,e$'$p)pn) cross section calculated within MCEEP[20]. The number of simulated events calculated with (5.29) is identical to that that would be obtained in a simulation of the yield with vertex ^{3}He(e,e$'$p) cross sections set to 1, since MCEEP weights W_{jik} contain the vertex cross sections σ_{jik} as a factor [55, 46]. Hence, the simulation of the experiment with the ^{3}He(e,e$'$p) cross section, modeled as the factorization of σ_{cc1} with the "fitted-to-data" spectral functions $S^{\Sigma_n}(5.49\text{ MeV}, P_{miss})$ and $S^{\Sigma_n}(E_{miss}, P_{miss})$, was re-weighted to emulate the simulation with unit model ^{3}He(e,e$'$p)D and ^{3}He(e,e$'$p)pn cross sections.

The rest of the procedure of adjustment of weights was identical to that described in Sec. 5.8.1. After adjustment, the weight w_1 assigned to the 2bbu E_{miss} bin is the extracted ^{3}He(e,e$'$p)D cross section. In the following it is denoted as $\frac{d^5\sigma^{ind}}{dE_f d\Omega_e d\Omega_p}$, i.e.

$$\frac{d^5\sigma^{ind}}{dE_f d\Omega_e d\Omega_p} = w_1. \tag{5.30}$$

Although absolute values of the adjusted weights w_i in the "model independent" analysis were very different from those obtained in the "cc1 averaging" analysis (equal to extracted cross sections in the former case, and close to 1 in the latter), the relative statistical error in the "model independent" procedure is computed with the same formula (5.15):

$$\epsilon_{st} = \frac{\sqrt{\delta N_1(D)^2 + \sum_{j=2}^{n} \delta N_{j1}(S)^2 \cdot w_j^2}}{N_1(D) - \sum_{j=2}^{n} N_{j1}(S) \cdot w_j}, \tag{5.31}$$

with the difference that $\delta N_{ji}(S)$ is calculated as

$$\delta N_{ji}(S) = \sqrt{\sum_k W_{jik}^{*2}} \tag{5.32}$$

(cf (5.16)). The number of experimentally detected events, $N_i(D)$, and the statistical errors, $\delta N_i(D)$, are identical both in the "model independent" and the "cc1 averaging"

[20]MCEEP was modified to output a variable equal to the vertex cross section assigned to each ^{3}He(e,e$'$p) event; the variable was saved in the simulation ntuple. Simulated ^{3}He(e,e$'$p)pn events with $\sigma_{jik} = 0$ were filtered out from the ntuple at a preliminary stage.

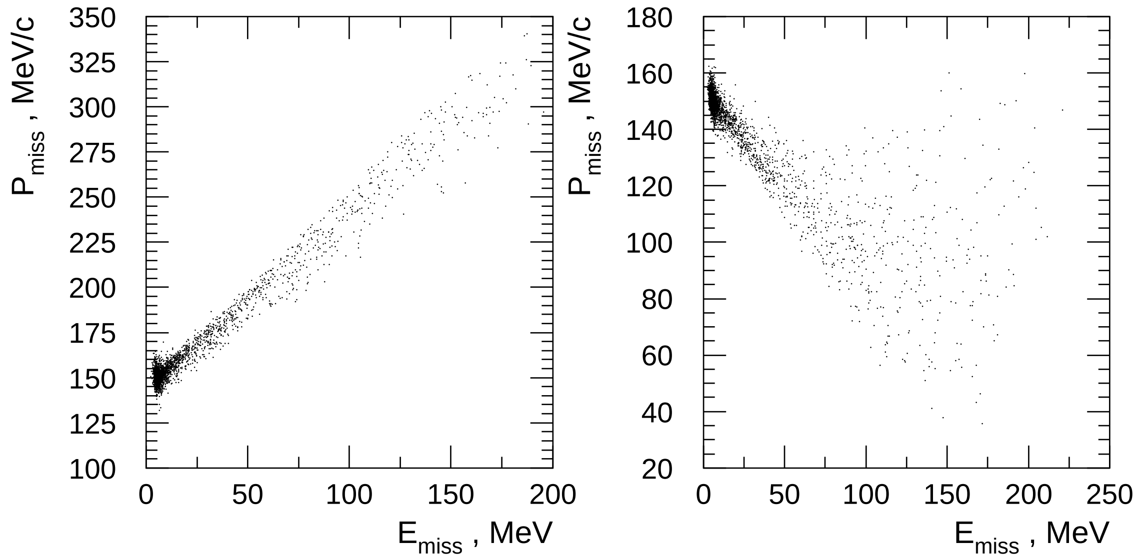

Figure 5-16: Propagation of ^{3}He(e,e$'$p)D radiative tail in the (E_{miss}, P_{miss}) space, simulated with MCEEP. A P_{miss} bin is selected in: kinematics 4 (left panel); kinematics 5 (right panel).

analyses, but differences between the two techniques can lead to slightly differing relative statistical errors of the extracted cross sections[21]. The fitting program used for the "model independent" extraction of ^{3}He(e,e$'$p)D cross sections is given in Appendix A.2.

5.8.3 Extraction of ^{3}He(e,e$'$p)pn cross sections

For the extraction of ^{3}He(e,e$'$p)pn cross sections a fitting procedure similar to the ^{3}He(e,e$'$p)D fitting procedure (Sec. 5.8.1) was written, but with vertex binning both in the E_{miss} and in the P_{miss} space, thus allowing for 2-dimensional propagation of radiative tails (Fig. 5-16). However, due to limited statistics and large radiative tails from the ^{3}He(e,e$'$p)D process, at each spectrometer setting the whole accepted P_{miss}

[21]The differences in the relative statistical errors stem from the different weighting of simulated events in the two methods. In general, the effect on the results is negligible, since in both techniques the statistical errors are dominated by the errors on the number of experimentally detected events.

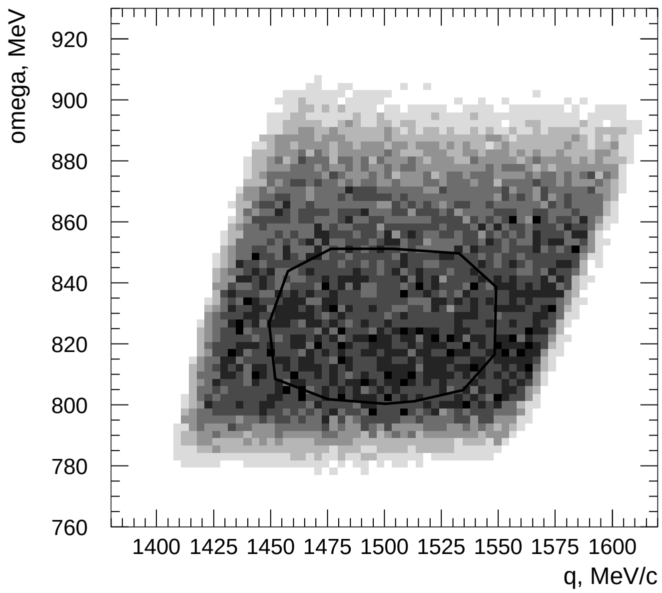

Figure 5-17: (ω, q) phase space covered in kinematics 4 by events in E_{miss} range from 7.72 MeV to 30 MeV (grayscale), and contour cut imposed in the ^{3}He(e,e$'$p)pn analysis.

range was treated as a single P_{miss} bin[22]. With the single P_{miss} bin covering the acceptance, in effect, the ^{3}He(e,e$'$p)pn fitting procedure was performing identically to the ^{3}He(e,e$'$p)D fitting procedure described above.

The systematic variation of Q^2 and ω with E_{miss} was removed by the contour cut imposed in (ω, q) space (Fig. 5-17). The ^{3}He(e,e$'$p)pn cross sections were extracted only with the "model independent" technique, i.e. MCEEP weighting factors W_{jik} were modified according to (5.28) to emulate simulation with unit vertex ^{3}He(e,e$'$p)D and ^{3}He(e,e$'$p)pn cross sections. After adjustment of the weights w_i, the extracted 6-differential ^{3}He(e,e$'$p)pn cross section for E_{miss} bin i, in the following denoted as $\frac{d^6\sigma^{ind}}{dE_f dE_p d\Omega_e d\Omega_p}$, was obtained as[23]

[22]In the ^{3}He(e,e$'$p)pn analysis boundaries of the E_{miss} bins were set at E_{miss} equal to 0.5, 7.72, 12, 16, 20, 24, 28, 32 and 40 MeV.

[23]MCEEP internally uses ^{3}He(e,e$'$p)pn cross sections differential in proton momentum. After adjustment of weights, they were multiplied by E_p/p_p to obtain cross sections differential in proton energy.

$$\frac{d^6\sigma^{ind}}{dE_f dE_p d\Omega_e d\Omega_p} = w_i, \tag{5.33}$$

where w_i is the adjusted weight for bin i.

The ^{3}He(e,e$'$p)pn spectral function, in the following denoted as $S_{3bbu}(E_{miss}, P_{miss})$, was obtained as

$$S_{3bbu}(\bar{E}_{miss}, \bar{P}_{miss}) = S^{\Sigma_n}(\bar{E}_{miss}, \bar{P}_{miss}) \times \tag{5.34}$$
$$\frac{d^6\sigma^{ind}}{dE_f dE_p d\Omega_e d\Omega_p} \left(\frac{d^6\sigma^{sim}}{dE_f dE_p d\Omega_e d\Omega_p} (\bar{E}_i, \bar{Q^2}, \bar{\omega}, \bar{E}_{miss}, \bar{P}_{miss}) \right)^{-1},$$

where S^{Σ_n} is the spectral function fitted to the data, and $\frac{d^6\sigma^{ind}}{dE_f dE_p d\Omega_e d\Omega_p}$ is the ^{3}He(e,e$'$p)pn cross section extracted with (5.33). $\frac{d^6\sigma^{sim}}{dE_f dE_p d\Omega_e d\Omega_p}$ is the vertex simulation ^{3}He(e,e$'$p)pn cross section (the factorization of S^{Σ_n} by σ_{cc1}), at point $\bar{E}_i$, $\bar{Q^2}$, $\bar{\omega}$, $\bar{E}_{miss}$, $\bar{P}_{miss}$, found as the acceptance-weighted average of the vertex E_i, Q^2, ω, E_{miss}, P_{miss} within the E_{miss} bin and coplanar proton kinematics[24]. In effect, (5.34) expresses division of the extracted cross section $\frac{d^6\sigma^{ind}}{dE_f dE_p d\Omega_e d\Omega_p}$ by MCEEP σ_{cc1} model and by corresponding kinematic factor.

The relative statistical error for the cross section $\frac{d^6\sigma^{ind}}{dE_f dE_p d\Omega_e d\Omega_p}$ and for the spectral function S_{3bbu} extracted in E_{miss} bin i was calculated as[25]

$$\epsilon_{st,i} = \frac{\sqrt{\delta N_i(D)^2 + \sum_{j=1}^{\prime n} \delta N_{ji}(S)^2 \cdot w_j^2}}{N_i(D) - \sum_{j=1}^{\prime n} N_{ji}(S) \cdot w_j}. \tag{5.35}$$

w_j is the adjusted weight assigned to the vertex E_{miss} bin j, $\delta N_i(D)$ is the standard deviation of the number of events $N_i(D)$ detected in asymptotic E_{miss} bin i ($\delta N_i(D)$ is given by (5.11), $N_i(D)$ is given by (5.10)), and $\delta N_{ji}(S)$ and $N_{ji}(S)$ are given by (5.32) and (5.29) respectively. The sums exclude $i = j$ terms.

To allow comparison with previous measurements, the extracted ^{3}He(e,e$'$p)pn

[24]For each E_{miss} bin, $\bar{E}_{miss}$ was very close to the middle of the E_{miss} bin. Therefore, $\bar{E}_{miss}$ was set equal to the central E_{miss} value of the E_{miss} bin. With a good approximation, $\bar{P}_{miss}$, $\bar{Q^2}$ and $\bar{\omega}$ was the same for all E_{miss} bins at a given spectrometer setting.

[25]For each E_{miss} bin, relative statistical error for the extracted cross section is the same as for the extracted spectral function, since both are obtained from the same fit.

spectral function was integrated in missing energy from 7.72 MeV to 20 MeV, as

$$\int_{7.72MeV}^{20MeV} S_{3bbu} dE_{miss} = \sum_{i=2}^{4} \Delta E_{miss,i} \cdot S_{3bbu}(\bar{E}_{miss,i}, \bar{P}_{miss}), \tag{5.36}$$

where $\Delta E_{miss,i}$ is the width of ith E_{miss} bin, and $S_{3bbu}(\bar{E}_{miss,i}, \bar{P}_{miss})$ is the extracted spectral function for the E_{miss} bin i. The sum is over the first three ^{3}He(e,e′p)pn E_{miss} bins with boundaries at E_{miss} equal to 7.72, 12, 16 and 20 MeV.

The statistical error of the integral was calculated as

$$\delta\left(\int_{7.72MeV}^{20MeV} S_{3bbu} dE_{miss}\right) = \sqrt{\sum_{i=2}^{4} \left(\Delta E_{miss,i} \cdot \delta S_{3bbu}(\bar{E}_{miss,i}, \bar{P}_{miss})\right)^2}, \tag{5.37}$$

where $\delta S_{3bbu}(\bar{E}_{miss,i}, \bar{P}_{miss})$ follows from the relative statistical error given by (5.35).

5.9 Extraction of A_{TL}

At the beam energy of 4.8 GeV, ^{3}He(e,e′p)D data was collected at both sides of $\vec{q}$ up to $P_{miss} \sim 650$ MeV/c. This data was used for the extraction of A_{TL}, defined as

$$A_{TL} = \frac{\sigma_2 - \sigma_1}{\sigma_2 + \sigma_1}, \tag{5.38}$$

where σ_1 and σ_2 are coplanar ^{3}He(e,e′p)D cross sections measured back and forward of $\vec{q}$ respectively.

Extraction of A_{TL} at kinematics 1 (nominal $P_{miss} = 0$) is described in Sec. 5.11. In this section, the extraction of A_{TL} at all other $E_{beam} = 4.8$ GeV kinematic settings is described.

A_{TL} extraction with bin-by-bin ω-q matching

In one analysis technique, for each P_{miss} bin selected both at Σ_1 and Σ_2 kinematic settings, a contour cut imposed in (ω, q) space restricted events to a common Q^2 and

ω region for both forward and back of $\vec{q}$ bin[26]. ^{3}He(e,e$'$p)D cross sections extracted with this technique at kinematic settings Σ_1 and Σ_2, denoted as σ_1 and σ_2 respectively, were combined as

$$A_{TL} = \frac{\sigma_2 - \sigma_1}{\sigma_2 + \sigma_1}, \tag{5.39}$$

to yield the A_{TL}, with statistical errors propagated as

$$\delta A_{TL} = \frac{2 \cdot \sqrt{(\sigma_2 \delta\sigma_1)^2 + (\sigma_1 \delta\sigma_2)^2}}{(\sigma_2 + \sigma_1)^2}, \tag{5.40}$$

where $\delta\sigma_1$ and $\delta\sigma_2$ are standard deviations of σ_1 and σ_2.

^{3}He(e,e$'$p)D cross sections σ_1 and σ_2 were extracted both with the "model independent" technique (Sec. 5.8.2), and with the "cc1 averaging" technique (Sec. 5.8.2), with and without renormalization to fixed Q^2 and ω, thus providing three sets of extracted A_{TL} that could be used for analysis of the model dependence of the methods of extraction.

A_{TL} extraction without ω-q matching

In another analysis technique, (ω, q) acceptances of forward of $\vec{q}$ and back of $\vec{q}$ P_{miss} bins were not matched. The ^{3}He(e,e$'$p)D cross sections were extracted using the "cc1 averaging" procedure with renormalization to fixed Q^2 and ω points (Sec. 5.8.2, the renormalization points are given in Table 5.1). Cross sections σ_1^{ren} and σ_2^{ren} extracted for the same P_{miss} bin back and forward of $\vec{q}$ respectively, were combined as

$$A_{TL}^{ren} = \frac{\sigma_2^{ren} - \sigma_1^{ren}}{\sigma_2^{ren} + \sigma_1^{ren}}, \tag{5.41}$$

to yield the A_{TL}, with statistical errors propagated as

$$\delta A_{TL}^{ren} = \frac{2 \cdot \sqrt{(\sigma_2^{ren} \delta\sigma_1^{ren})^2 + (\sigma_1^{ren} \delta\sigma_2^{ren})^2}}{(\sigma_2^{ren} + \sigma_1^{ren})^2}, \tag{5.42}$$

[26] The contour cut was imposed after a cut selecting the ^{3}He(e,e$'$p)D E_{miss} peak (and a cut selecting the P_{miss} bin). As mentioned in Sec. 5.1, all data analyzed in this thesis was restricted to coplanar kinematics by a cut on the out-of-plane angle, except for data taken at nominal $P_{miss} = 0$ kinematic settings.

where $\delta\sigma_1^{ren}$ and $\delta\sigma_2^{ren}$ are standard deviations of σ_1^{ren} and σ_2^{ren}. This technique allowed us to increase the P_{miss} range of the extracted A_{TL}, and to decrease statistical errors.

5.10 Separation of response functions

Original derivations of the decomposition of the coincidence (e,e′p) cross sections in terms of nuclear response functions in the one-photon-exchange approximation are available in [74, 75, 76]. Here we use the notation of Kelly [2].

In the one-photon-exchange approximation, with unpolarized incident electron and unobserved polarization of detected electron and proton, the ^{3}He(e,e′p)D cross section can be written in terms of four independent nuclear response functions R_L, R_T, R_{TL} and R_{TT}, as

$$\frac{d^5\sigma}{d\Omega_e d\Omega_p dE_f} = R\frac{E_p p_p}{(2\pi)^3}\sigma_M\left(V_L R_L + V_T R_T + V_{TL} R_{TL}\cos\phi + V_{TT} R_{TT}\cos 2\phi\right), \quad (5.43)$$

where R is recoil factor given by

$$R = \left|1 - \frac{E_p}{E_D}\frac{\vec{p}_p\cdot\vec{p}_D}{\vec{p}_p\cdot\vec{p}_p}\right|^{-1}. \quad (5.44)$$

V_L, V_T, V_{TL}, V_{TT} are kinematic factors given by

$$V_L = \frac{Q^4}{\vec{q}^4}, \quad (5.45)$$

$$V_T = \frac{Q^2}{2\vec{q}^2} + \tan^2(\theta_e/2), \quad (5.46)$$

$$V_{TL} = \frac{Q^2}{\vec{q}^2}\left(\frac{Q^2}{\vec{q}^2} + \tan^2(\theta_e/2)\right)^{\frac{1}{2}}, \quad (5.47)$$

$$V_{TT} = \frac{Q^2}{2\vec{q}^2}, \quad (5.48)$$

and σ_M is the Mott cross section,

$$\sigma_M = \frac{\alpha^2}{4E_i^2} \frac{\cos^2(\theta_e/2}{\sin^4(\theta_e/2)}, \tag{5.49}$$

where α is the fine structure constant, with E_p, $\vec{p}_p$, E_D, $\vec{p}_D$, Q^2, $\vec{q}$, θ_e and ϕ defined in Sec. 1.4.

As described in Sec. 1.6, the ^{3}He(e,e$'$p)D cross sections were measured in fixed Q^2 and ω coplanar kinematics, at both sides of $\vec{q}$ at beam energy 4.8 GeV (out-of-plane angle $\phi = 0°$ at Σ_2 kinematic setting, and $\phi = 180°$ at Σ_1 kinematic setting), and at one side of $\vec{q}$ at beam energy 1.2 GeV ($\phi = 180°$, Σ_3 kinematic setting). These measurements were used for separation of R_T and R_{TL} response functions, and of combination $R_L + V_{TT}/V_L R_{TT}$, as described below.

The ^{3}He(e,e$'$p)D cross sections extracted for separation of the ^{3}He(e,e$'$p)D response functions have to cover a common (ω, Q^2, P_{miss}) phase space. (ω, Q^2) acceptances were matched by imposition of two contour cuts shown in Fig. 5-18: the larger of the cuts matched (ω, Q^2) acceptances between all Σ_1 and Σ_2 spectrometer settings, the smaller of the cuts matched (ω, Q^2) acceptances between all Σ_1, Σ_2 and Σ_3 spectrometer settings. After imposition of either of these cuts, common P_{miss} range was selected by a cut in P_{miss}.

The ^{3}He(e,e$'$p)D cross sections extracted for the separation of R_T, R_{TL} and $R_L + V_{TT}/V_L R_{TT}$ response functions were obtained with the "model independent" technique only, described in Sec. 5.8.2.

5.10.1 R_{TL} separation

R_{TL} was calculated with

$$R_{TL} = \frac{\sigma_2 - \sigma_1}{2KV_{TL}}, \tag{5.50}$$

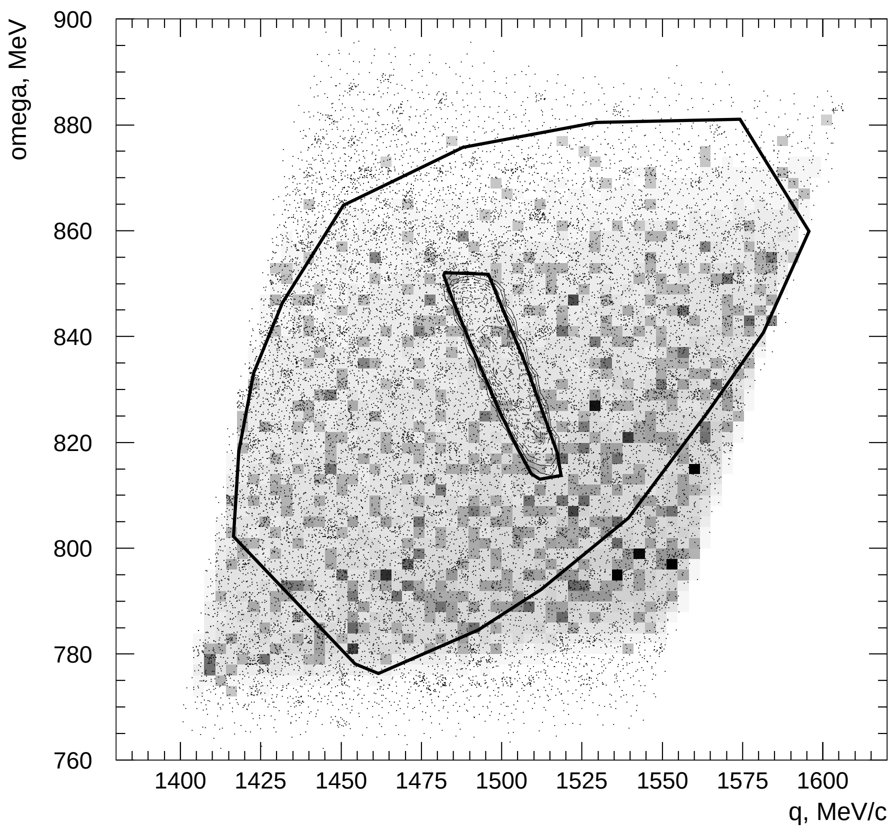

Figure 5-18: (ω, q) phase space covered in kinematics 4 (grayscale), 5 (scatter plot) and 6 (contour plot) by events in E_{miss} range from 2 MeV to 7.7 MeV, and contour cuts imposed in extraction of the response functions.

where σ_1 and σ_2 are ^{3}He(e,e′p)D cross sections extracted at Σ_1 and Σ_2 kinematic settings respectively, and K is given by

$$K = R\frac{E_p p_p}{(2\pi)^3}\sigma_M. \tag{5.51}$$

Formula (5.50) can be verified by direct substitution in (5.43). For central ^{3}He(e,e′p)D spectrometer settings analyzed in this thesis, the recoil factor R is within 0.7% from unity.

The statistical error was calculated as

$$\delta R_{TL} = \frac{\sqrt{(\delta\sigma_2)^2 + (\delta\sigma_1)^2}}{2KV_{TL}}, \tag{5.52}$$

where $\delta\sigma_1$ and $\delta\sigma_2$ are absolute statistical errors of cross sections σ_1 and σ_2.

5.10.2 R_T and $R_L + V_{TT}/V_L R_{TT}$ separation

From (5.43) one can obtain:

$$\frac{\sigma_1 + \sigma_2}{2K} = V_L R_L + V_T R_T + V_{TT} R_{TT} = S_1, \tag{5.53}$$

with V_L, V_T, V_{TL}, V_{TT} and K calculated according to (5.45) – (5.48) and (5.51), for Σ_1 and Σ_2 kinematic settings.

Using the ^{3}He(e,e′p)D cross section σ_3 measured at Σ_3 kinematic setting and R_{TL} extracted as described in the previous subsection, one can construct the linear combination

$$S_2 = \frac{\sigma_3}{K'} + V'_{TL} R_{TL} = V_L R_L + V'_T R_T + V_{TT} R_{TT}, \tag{5.54}$$

with V'_T, V'_{TL} and K' calculated for Σ_3 kinematic setting, and where the last equality follows from (5.43).

From (5.53) and (5.54) one can easily obtain

$$R_L + \frac{V_{TT}}{V_L} R_{TT} = \frac{V_T S_2 - V'_T S_1}{V_L(V_T - V'_T)}, \tag{5.55}$$

$$R_T = \frac{S_1 - S_2}{V_T - V_T'}, \tag{5.56}$$

with statistical errors propagated as

$$\delta(R_L + \frac{V_{TT}}{V_L} R_{TT}) = \frac{\sqrt{V_T^2(\delta S_2)^2 + V_T'^2(\delta S_1)^2}}{V_L |V_T - V_T'|}, \tag{5.57}$$

$$\delta R_T = \frac{\sqrt{(\delta S_1)^2 + (\delta S_2)^2}}{|V_T - V_T'|}, \tag{5.58}$$

where

$$\delta S_1 = \frac{\sqrt{(\delta\sigma_1)^2 + (\delta\sigma_2)^2}}{2K}, \tag{5.59}$$

$$\delta S_2 = \sqrt{\frac{(\delta\sigma_3)^2}{K'^2} + V_{TL}'^2(\delta R_{TL})^2}. \tag{5.60}$$

The ^{3}He(e,e$'$p)D cross sections extracted with similar techniques at Σ_4 and Σ_5 kinematic settings (nominal beam energy 1.9 GeV), and denoted as σ_4 and σ_5 respectively, can be combined as

$$\frac{\sigma_4 + \sigma_5}{2K''} = V_L R_L + V_T'' R_T + V_{TT} R_{TT} = S_3, \tag{5.61}$$

where K'' are V_T'' are calculated for Σ_4 and Σ_5 kinematic settings. Rearranging terms in the last equation, one obtains

$$\frac{S_3}{V_L} = (R_L + \frac{V_{TT}}{V_L} R_{TT}) + \frac{V_T''}{V_L} R_T. \tag{5.62}$$

Similarly, from (5.53) and (5.54) it follows that

$$\frac{S_1}{V_L} = (R_L + \frac{V_{TT}}{V_L} R_{TT}) + \frac{V_T}{V_L} R_T, \tag{5.63}$$

$$\frac{S_2}{V_L} = (R_L + \frac{V_{TT}}{V_L} R_{TT}) + \frac{V_T'}{V_L} R_T, \tag{5.64}$$

and therefore a straight line fit to plot of $\frac{S_n}{V_L}$ versus $\frac{V_T}{V_L}$ at each kinematic setting yields $R_L + \frac{V_{TT}}{V_L} R_{TT}$ as the intersect of the fitted line with the $\frac{S_n}{V_L}$ axis, and R_T as the tangent of the angle between the line and the $\frac{V_T}{V_L}$ axis.

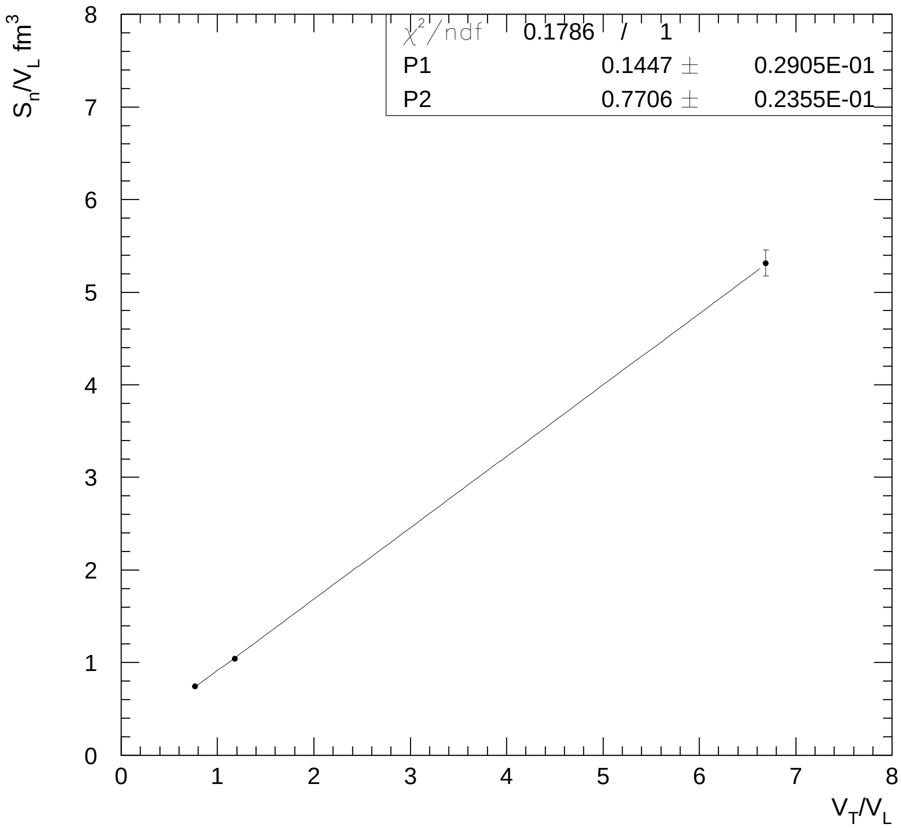

Figure 5-19: Rosenbluth plot ($\frac{S_n}{V_L}$ vs $\frac{V_T}{V_L}$) for $P_{miss} = 150$ MeV/c spectrometer settings, with a straight line fit.

Fig. 5-19 shows such a plot for the nominal $P_{miss} = 150$ MeV/c spectrometer settings at Σ_1, Σ_2, Σ_3, Σ_4 and Σ_5 kinematics (kinematic settings 4, 5, 6, 34, 35 respectively[27]), with (Q^2, ω, P_{miss}) matched between all kinematic settings. The fitted parameters P_1 and P_2, of the form $y = P_1 + x \cdot P_2$, are shown in the figure, indicating that at $P_{miss} = 156.2$ MeV/c, $R_L + \frac{V_{TT}}{V_L} R_{TT} = 0.1447 \pm 0.0291$ fm^3 and $R_T = 0.7706 \pm 0.0236$ fm^3, where the errors are statistical only. Values of $\frac{S_n}{V_L}$ and $\frac{V_T}{V_L}$ for the plotted points are given in Table 5.2.

[27]Definition of notation for the kinematic settings is given in Sec. 1.6.

$P_{miss} \pm \sigma_{Pm}$ MeV/c	E_{beam} GeV	$S_n/V_L \pm \epsilon_{st}$ fm^3	V_T/V_L	$Q^2 \pm \sigma_{Q^2}$ (GeV/c)^2	$\bar{\omega} \pm \sigma_\omega$ MeV
156.2±18.8	1.2	5.314e+00±1.403e-01	6.689e+00	1.5542±0.0359	834.9±9.3
	1.9	1.042e+00±2.939e-02	1.178e+00		
	4.8	7.413e-01±2.137e-02	7.679e-01		

Table 5.2: Values of $\frac{S_n}{V_L}$ and $\frac{V_T}{V_L}$ extracted for the ^{3}He(e,e$'$p)D reaction at $P_{miss} = 150$ MeV/c spectrometer settings, with (Q^2, ω, P_{miss}) phase space matching (the points are plotted in Fig. 5-19).

5.10.3 R_T and R_L separation

For separation of response functions at nominal $P_{miss} = 0$ spectrometer settings, events were restricted to the low P_{miss} region by the cut $P_{miss} < 25$ MeV/c. With this cut and E89044 acceptances, contributions of R_{TL} and R_{TT} response functions to measured ^{3}He(e,e$'$p)D cross sections, given by (5.43), were effectively eliminated by averaging over the out-of-plane angle ϕ. Hence, introducing S_1', S_2' and S_3' with

$$S_1' = \frac{\sigma_1}{K}, \qquad S_2' = \frac{\sigma_3}{K'}, \qquad S_3' = \frac{\sigma_4}{K''}, \tag{5.65}$$

where σ_1, σ_3, σ_4 are ^{3}He(e,e$'$p)D cross sections measured at beam energies of 4.8 GeV, 1.2 GeV and 1.9 GeV respectively, from (5.43) one obtains

$$\frac{S_1'}{V_L} = R_L + \frac{V_T}{V_L} R_T, \qquad \frac{S_2'}{V_L} = R_L + \frac{V_T'}{V_L} R_T, \qquad \frac{S_3'}{V_L} = R_L + \frac{V_T''}{V_L} R_T. \tag{5.66}$$

Therefore, a straight line fit to a plot of $\frac{S_n'}{V_L}$ versus $\frac{V_T}{V_L}$ at each beam energy provides separation of R_L and R_T response functions.

Fig. 5-20 shows such a plot for $P_{miss} = 0$ spectrometer settings at Σ_1, Σ_3 and Σ_4 kinematics (kinematic settings 1, 3, 33 respectively), with (Q^2, ω, P_{miss}) phase space matched between all kinematic settings. The plotted points were fitted with polynomial $y = P_1 + x \cdot P_2$. Fitted values of parameters P_1 and P_2, shown in the figure, indicate that at $P_{miss} = 19$ MeV/c, $R_L = 5.687 \pm 0.869$ fm^3 and $R_T = 32.74 \pm 0.71$ fm^3, where the errors are statistical only. Values of $\frac{S_n'}{V_L}$ and $\frac{V_T}{V_L}$ for the plotted points are given in Table 5.3.

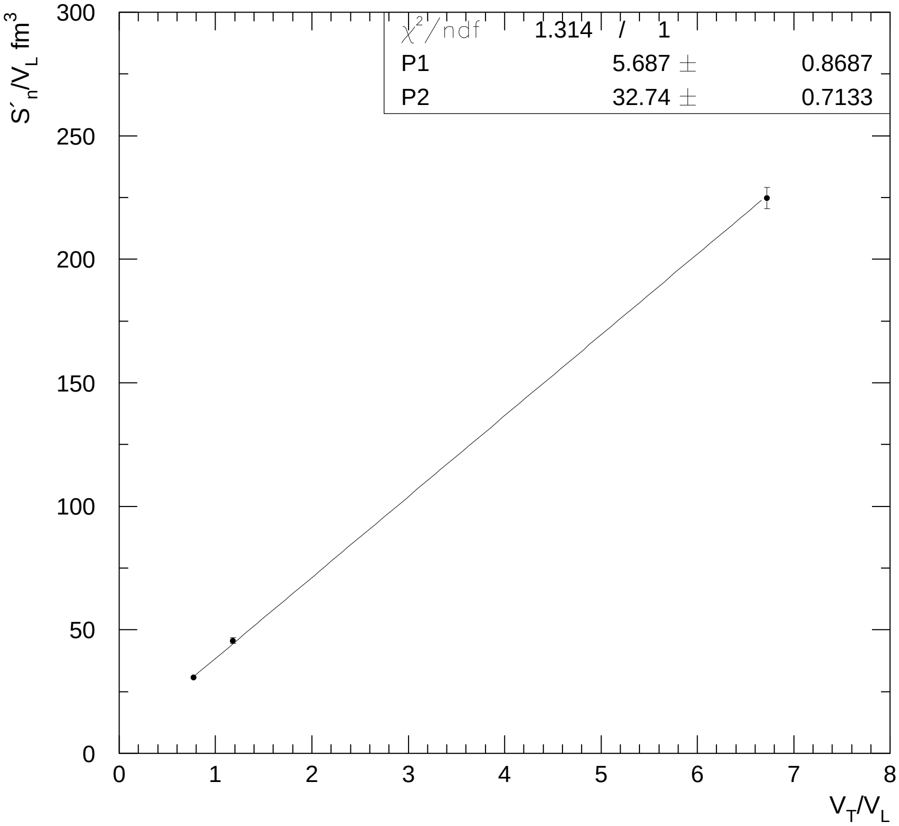

Figure 5-20: Rosenbluth plot ($\frac{S'_n}{V_L}$ vs $\frac{V_T}{V_L}$) for $P_{miss} = 0$ spectrometer settings, with a straight line fit.

$P_{miss} \pm \sigma_{Pm}$ MeV/c	E_{beam} GeV	$S_n/V_L \pm \epsilon_{st}$ fm^3	V_T/V_L	$Q^2 \pm \sigma_{Q^2}$ (GeV/c)^2	$\bar{\omega} \pm \sigma_\omega$ MeV
19±5.4	1.2	2.248e+02±4.260e+00	6.723e+00	1.5477±0.0225	836.7±6.1
	1.9	4.561e+01±1.231e+00	1.181e+00		
	4.8	3.060e+01±6.165e-01	7.698e-01		

Table 5.3: Values of $\frac{S_n}{V_L}$ and $\frac{V_T}{V_L}$ extracted for the ^{3}He(e,e$'$p)D reaction at $P_{miss} =$ 0 spectrometer settings, with (Q^2, ω, P_{miss}) phase space matching (the points are plotted in Fig. 5-20).

5.11 Binning in the out-of-plane angle at kinematics 1

As described in Sec. 5.1, ^{3}He(e,e$'$p) data collected at nominal $P_{miss} = 0$ spectrometer settings (kinematics 1, 3 and 33) was not restricted to coplanar proton kinematics. In the ^{3}He(e,e$'$p)D analysis at these settings, the collected data was "split" into forward of $\vec{q}$ and back of $\vec{q}$ parts, by a cut on the reconstructed out-of-plane angle ϕ. The condition $-90° < \phi < 90°$ selected forward of $\vec{q}$ events, while the condition $90° < \phi < 270°$ selected back of $\vec{q}$ events. These two parts were analyzed separately, with the ^{3}He(e,e$'$p)D cross sections extracted both with the "model independent" extraction procedure, and with the "cc1 averaging" procedure, with and without renormalization to fixed Q^2 and ω (Sec. 5.8).

In another approach, the ^{3}He(e,e$'$p) data collected at kinematics 1 (nominal $P_{miss} = 0$, beam energy 4.8 GeV) was restricted to perpendicular kinematics by the cut $80° < \theta_{Bq} < 100°$, where θ_{Bq} is the angle between the momentum of the unobserved recoil and $\vec{q}$, and binned both in P_{miss} and in the out-of-plane angle ϕ. For each P_{miss}/ϕ bin, the ^{3}He(e,e$'$p)D cross section, denoted as $\sigma(P_{miss}, \phi)$, was extracted with the "cc1 averaging" technique with renormalization to fixed Q^2 and ω (Sec. 5.8). For each P_{miss} value, the ϕ dependence of the extracted cross sections was fitted with the functional form

$$\sigma(P_{miss}, \phi) = P_1(1 + P_2 \cos\phi + P_3 \cos 2\phi), \tag{5.67}$$

where P_1, P_2 and P_3 are free parameters. Fitted values of parameters yielded A_{TL} and R_{TT}, with

$$A_{TL} = \frac{P_2}{1 + P_3}, \tag{5.68}$$

$$R_{TT} = \frac{P_1 P_3}{V_{TT} K}, \tag{5.69}$$

where V_{TT} and K are given by (5.48) and (5.51) respectively. Forward of $\vec{q}$ and back of $\vec{q}$ ^{3}He(e,e$'$p)D "in-plane" cross sections, denoted as σ_f and σ_b, were obtained as

$$\sigma_f = P_1(1 + P_2 + P_3), \qquad \sigma_b = P_1(1 - P_2 + P_3). \tag{5.70}$$

Statistical errors were calculated with

$$\delta A_{TL} = \frac{P_2}{1+P_3}\sqrt{\left(\frac{\delta P_2}{P_2}\right)^2 + \left(\frac{\delta P_3}{1+P_3}\right)^2}, \tag{5.71}$$

$$\delta R_{TT} = \frac{P_1 P_3}{V_{TT}K}\sqrt{\left(\frac{\delta P_1}{P_1}\right)^2 + \left(\frac{\delta P_3}{P_3}\right)^2}, \tag{5.72}$$

$$\delta\sigma_f = \sigma_f\sqrt{\frac{(\delta P_2)^2 + (\delta P_3)^2}{(1+P_2+P_3)^2} + \left(\frac{\delta P_1}{P_1}\right)^2}, \tag{5.73}$$

$$\delta\sigma_b = \sigma_b\sqrt{\frac{(\delta P_2)^2 + (\delta P_3)^2}{(1-P_2+P_3)^2} + \left(\frac{\delta P_1}{P_1}\right)^2}, \tag{5.74}$$

where absolute statistical errors of parameters, δP_1, δP_2 and δP_3, were calculated within the PAW routine that fitted the parameters.

5.12 Missing energy spectra

This section presents spectra of missing energy obtained at all 19 kinematic settings analyzed in this thesis (the notation for kinematic settings is introduced in Sec. 1.6).

Each of the figures presents E_{miss} spectra for one spectrometer setting and contains:

1. E_{miss} spectrum reconstructed from the data (solid line).
2. E_{miss} spectrum obtained in MCEEP simulation of the ^{3}He(e,e$'$p)D reaction (dotted line).
3. E_{miss} spectrum obtained in the MCEEP simulation of the ^{3}He(e,e$'$p)pn reaction (dashed-dotted line).
4. Sum of the two simulation E_{miss} spectra (dashed line).

The ^{3}He(e,e$'$p) cross section model used in the MCEEP simulation was the factorization of spectral functions fitted to the data with the cc1 prescription for the off-shell electron-nucleon cross section (Sec. 5.8). The following cuts were applied both to data and simulation spectra: R-function acceptance cuts (Sec. 5.3), target length cuts (Sec. 5.4), and the cut on the difference between reaction points reconstructed by the two spectrometers (Sec. 5.5). VDC tracking cuts (Sec. 3.1.2) and the cut on Gas Cherenkov ADCs (Sec. 3.1.3) were applied to data spectra. Accidental coincidences were subtracted from data. The cut on the out-of-plane angle ϕ (limiting events to coplanar kinematics, Sec. 5.1), was not applied.

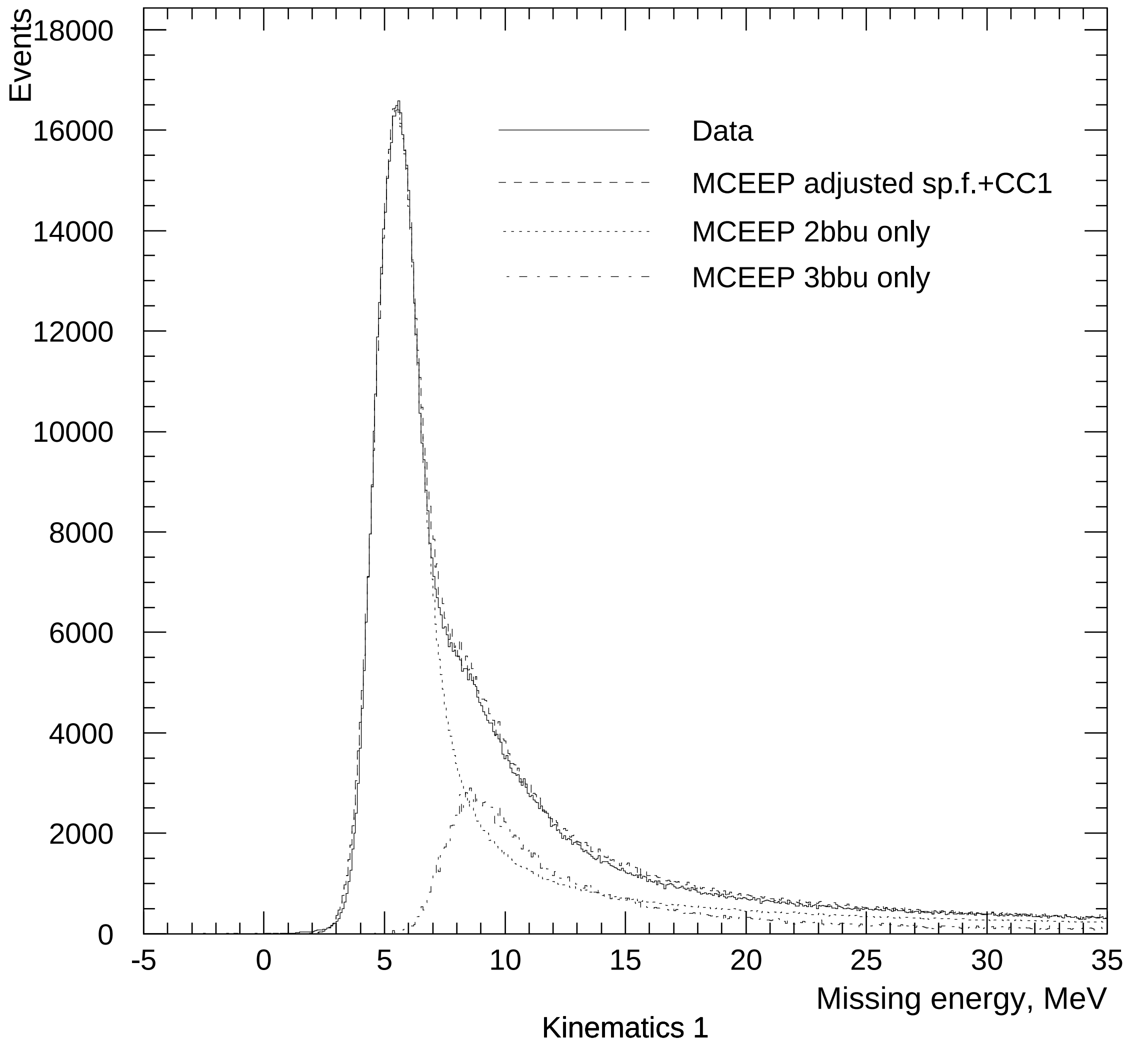

Figure 5-21: ^{3}He(e,e$'$p) missing energy distributions at kinematics 1, E_{beam} = 4.8 GeV, $P_{miss} = 0$.

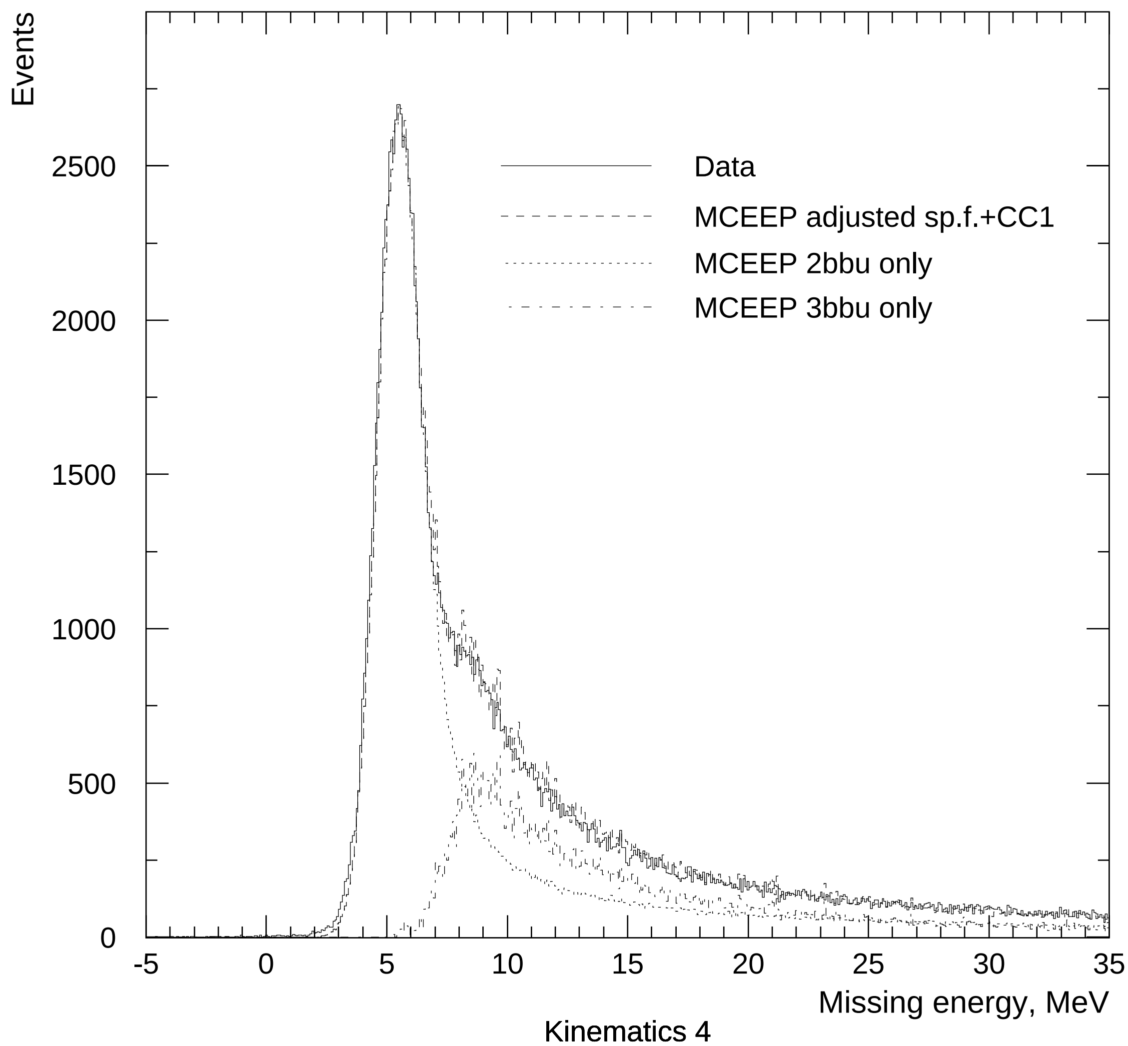

Figure 5-22: ^{3}He(e,e$'$p) missing energy distributions at kinematics 4, E_{beam} = 4.8 GeV, $P_{miss} = 150$ MeV/c, the detected proton is back of $\vec{q}$.

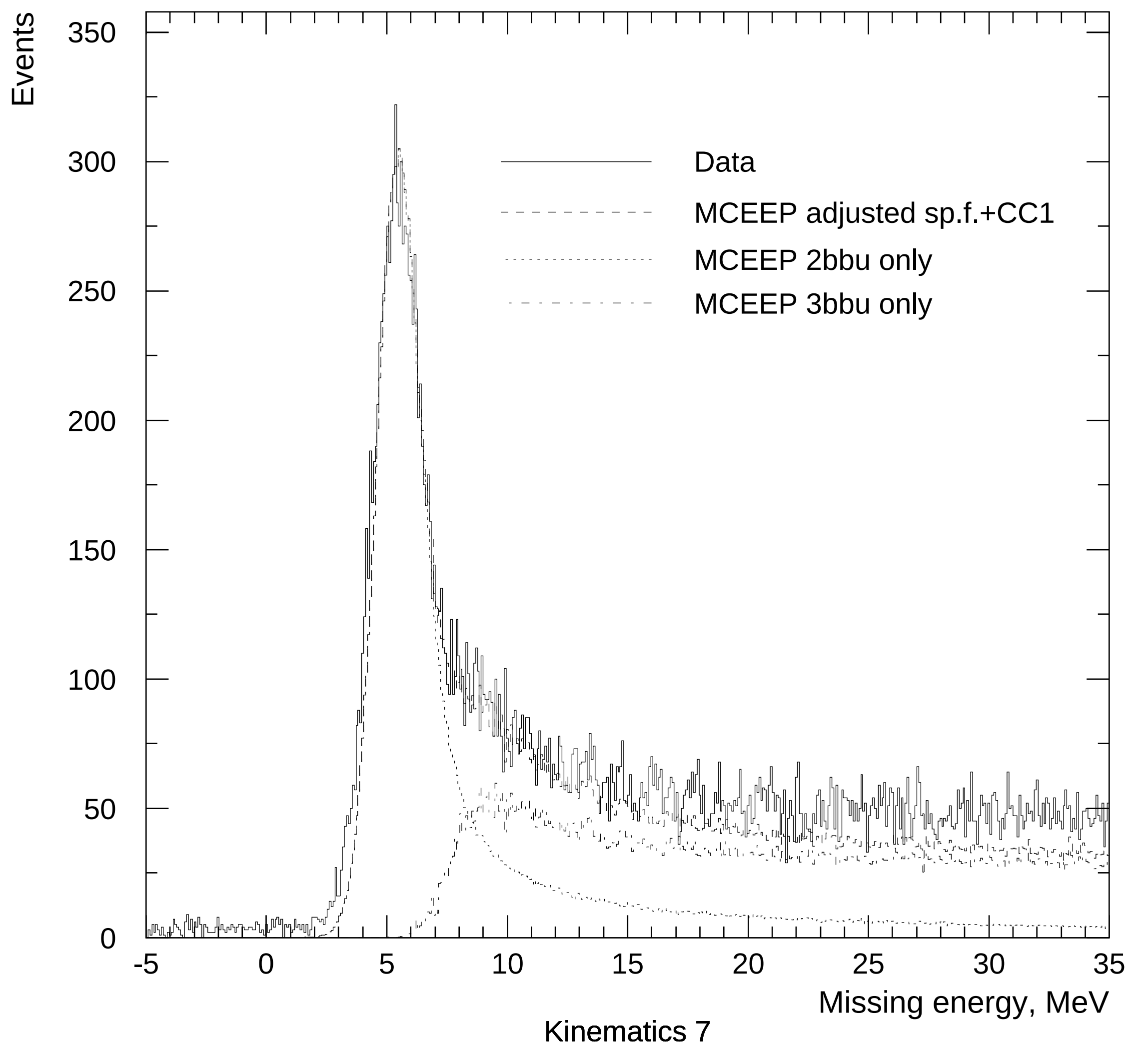

Figure 5-23: ^{3}He(e,e$'$p) missing energy distributions at kinematics 7, E_{beam} = 4.8 GeV, $P_{miss} = 300$ MeV/c, the detected proton is back of $\vec{q}$.

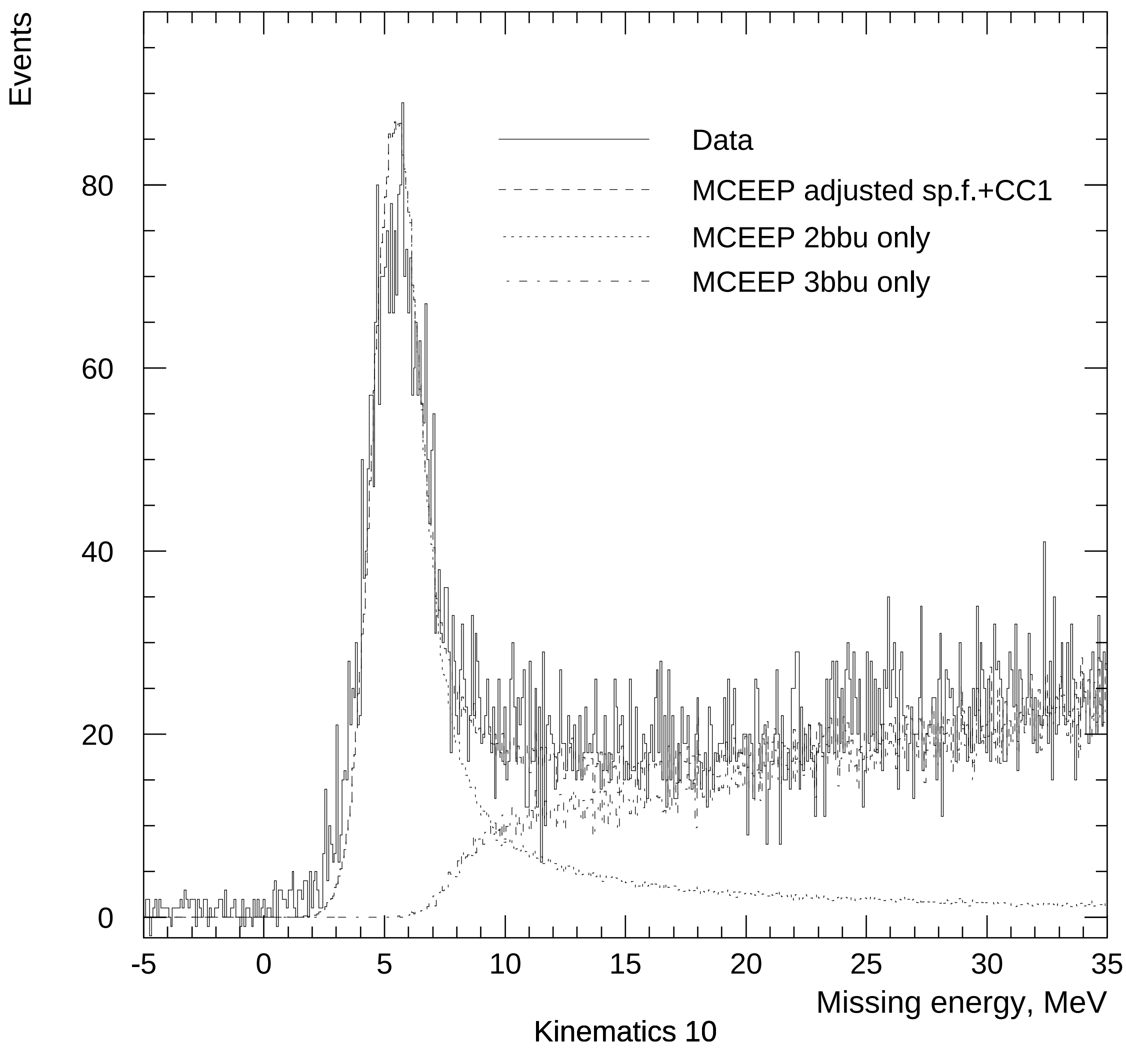

Figure 5-24: ^{3}He(e,e$'$p) missing energy distributions at kinematics 10, E_{beam} = 4.8 GeV, $P_{miss} = 425$ MeV/c, the detected proton is back of $\vec{q}$.

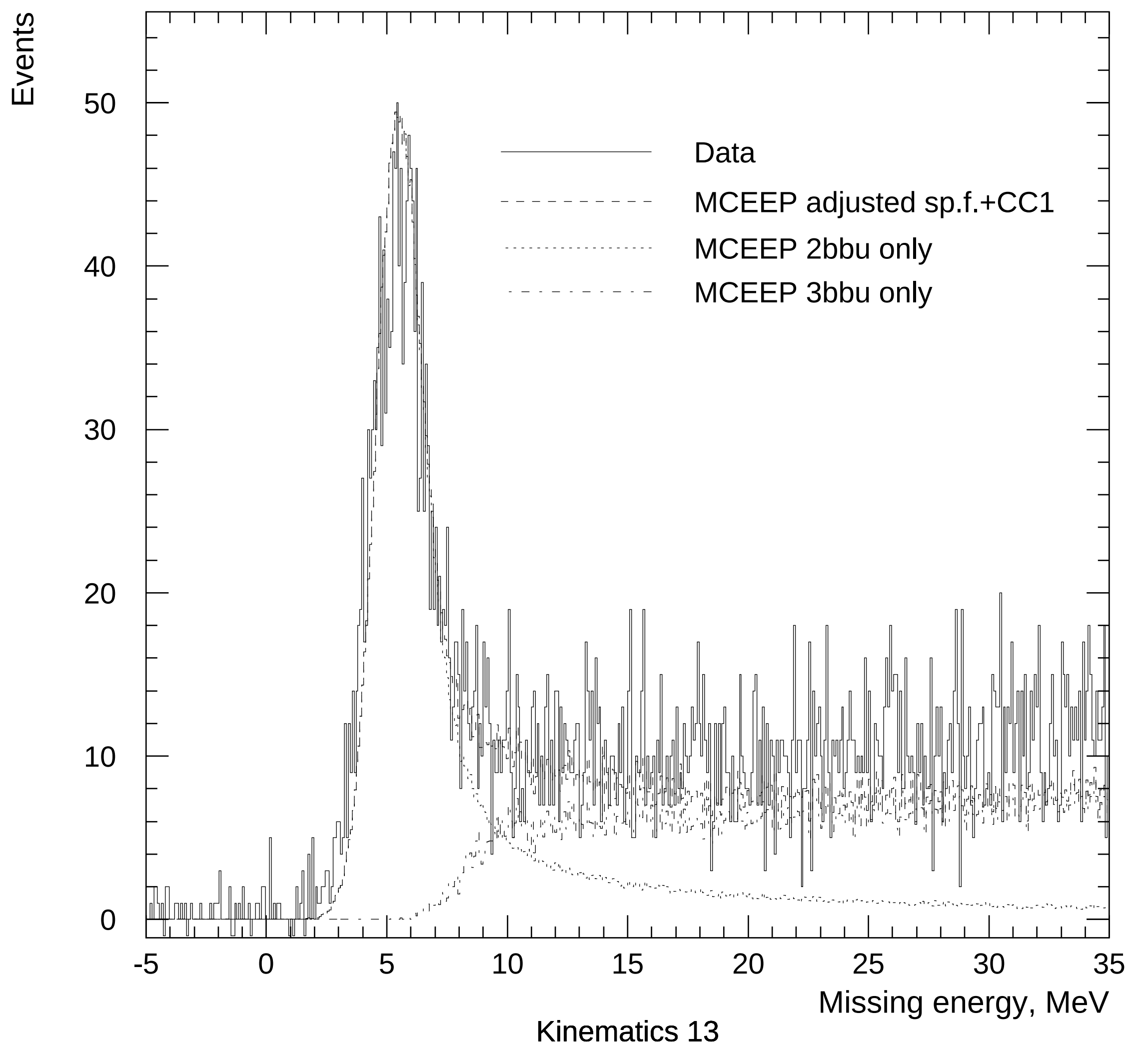

Figure 5-25: ^{3}He(e,e$'$p) missing energy distributions at kinematics 13, E_{beam} = 4.8 GeV, $P_{miss} = 550$ MeV/c, the detected proton is back of $\vec{q}$.

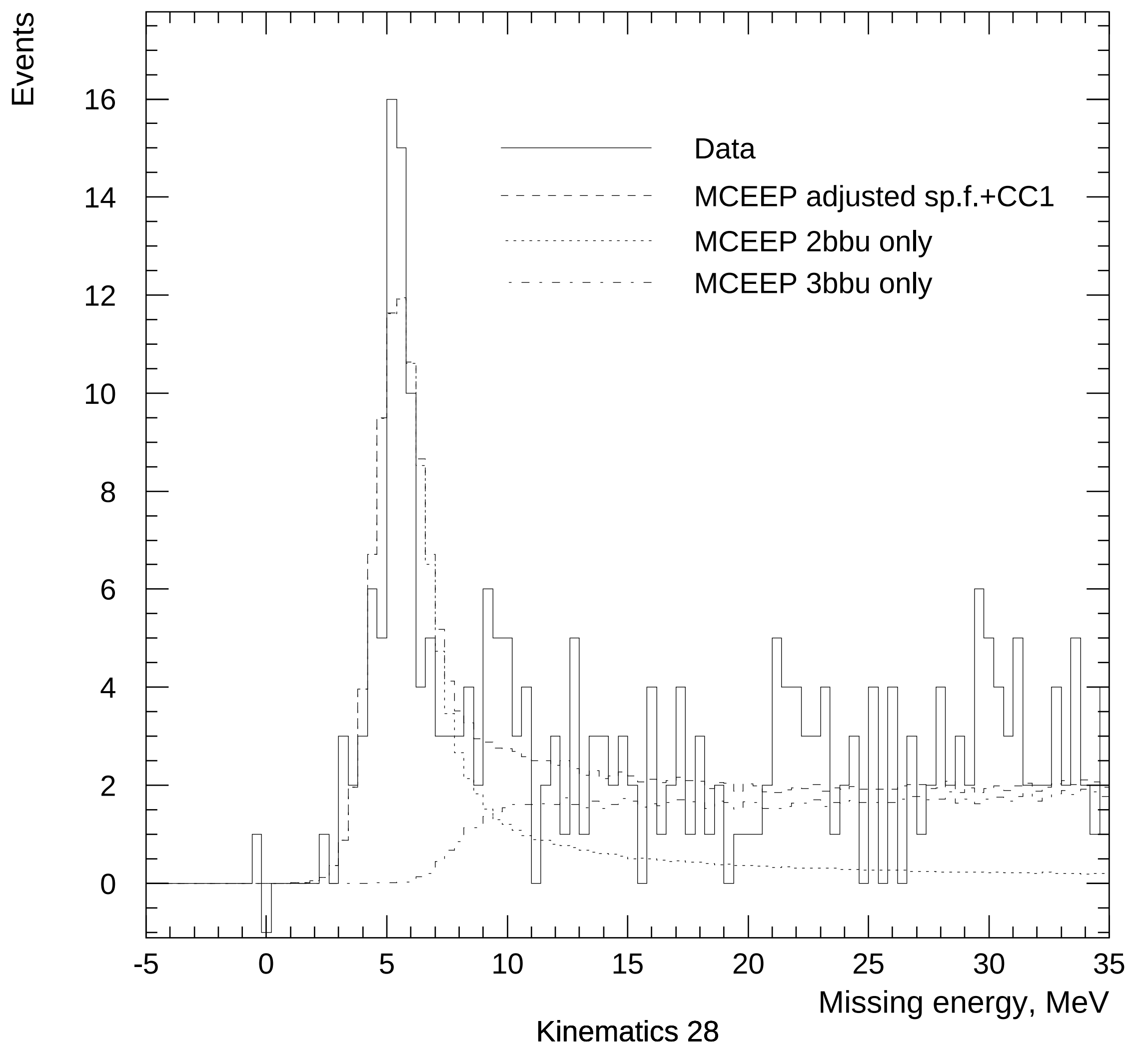

Figure 5-26: ^{3}He(e,e′p) missing energy distributions at kinematics 28, E_{beam} = 4.8 GeV, $P_{miss} = 750$ MeV/c, the detected proton is back of $\vec{q}$.

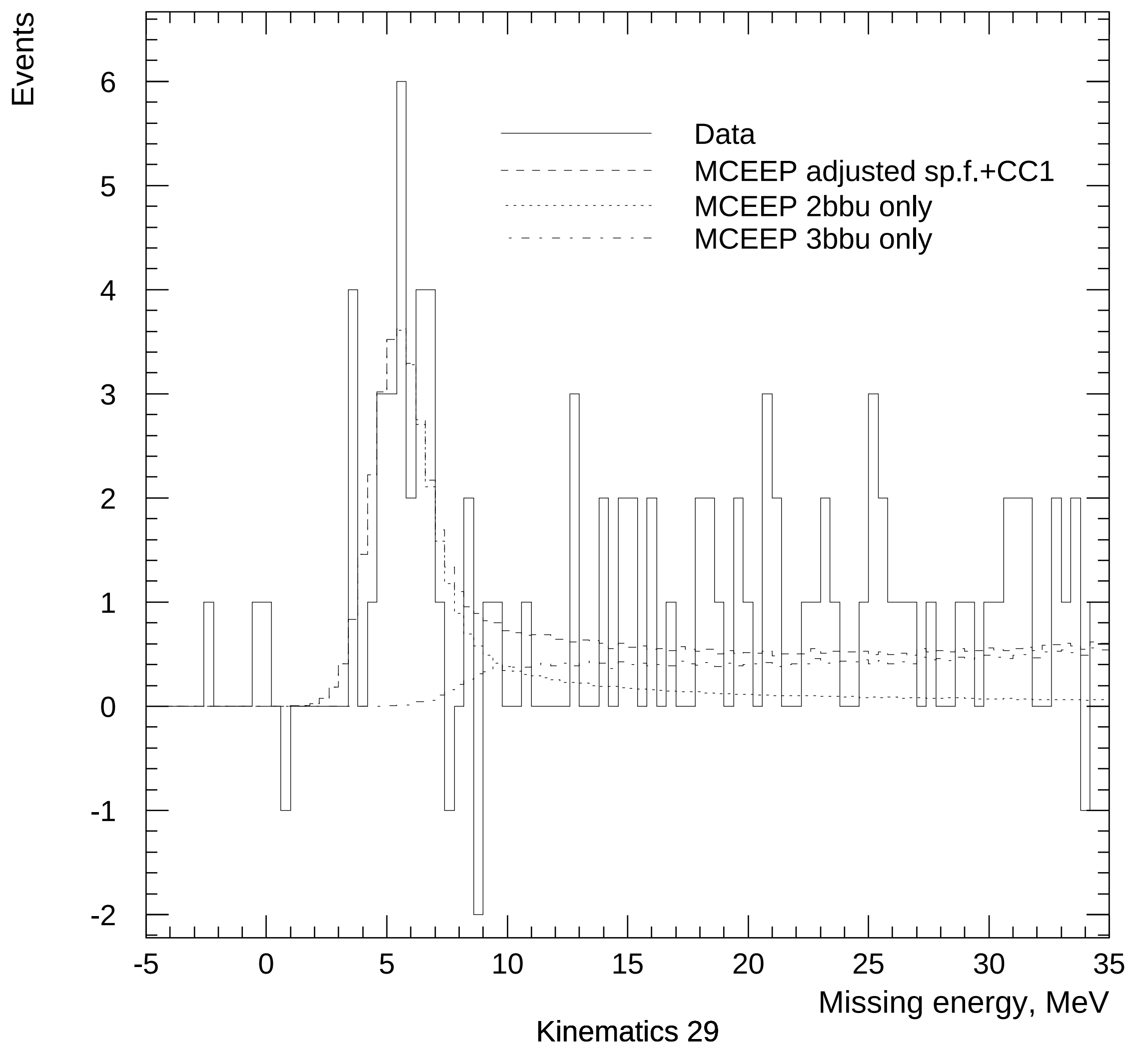

Figure 5-27: ^{3}He(e,e′p) missing energy distributions at kinematics 29, E_{beam} = 4.8 GeV, $P_{miss} = 1000$ MeV/c, the detected proton is back of $\vec{q}$.

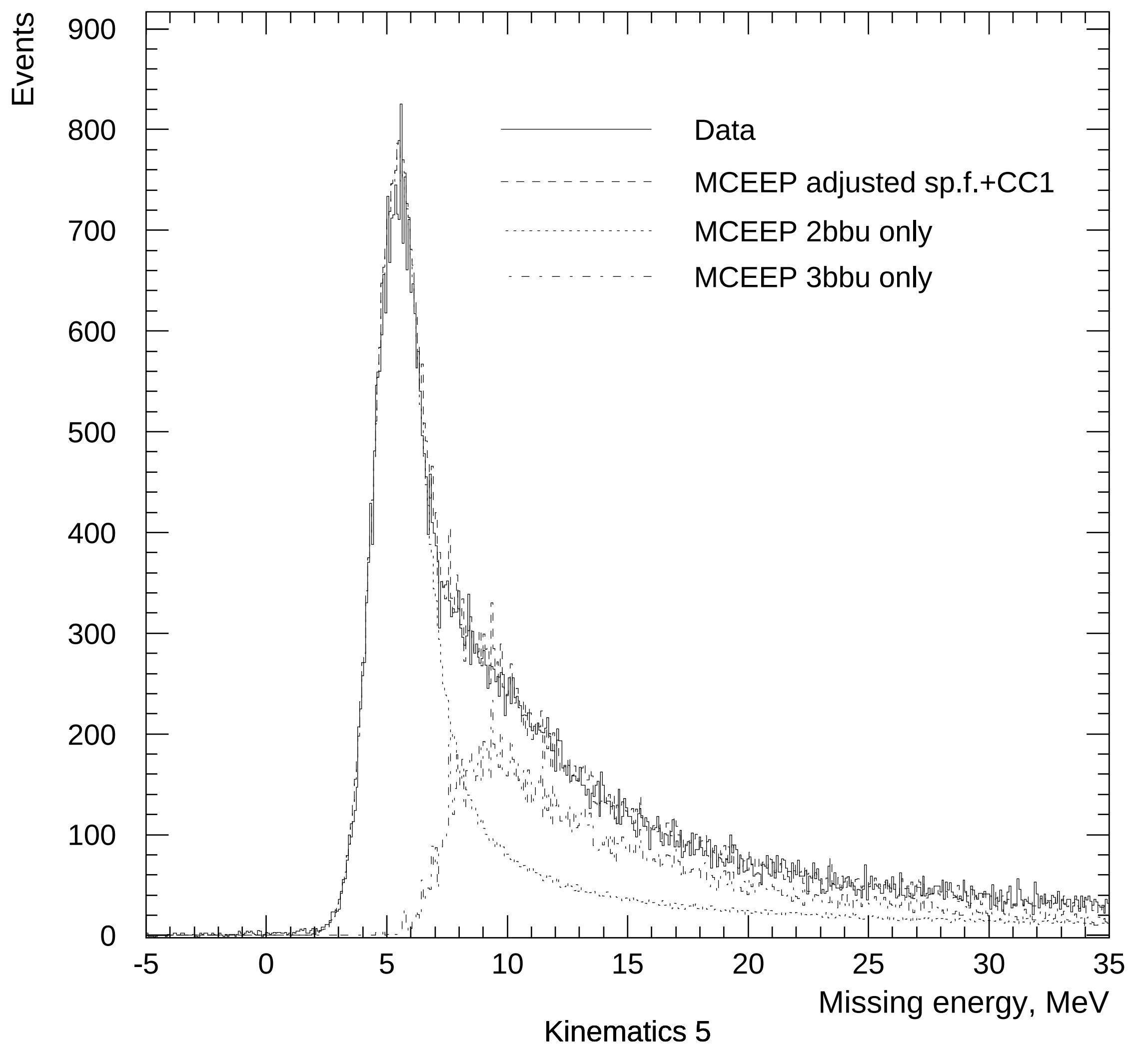

Figure 5-28: ^{3}He(e,e$'$p) missing energy distributions at kinematics 5, E_{beam} = 4.8 GeV, $P_{miss} = 150$ MeV/c, the detected proton is forward of $\vec{q}$.

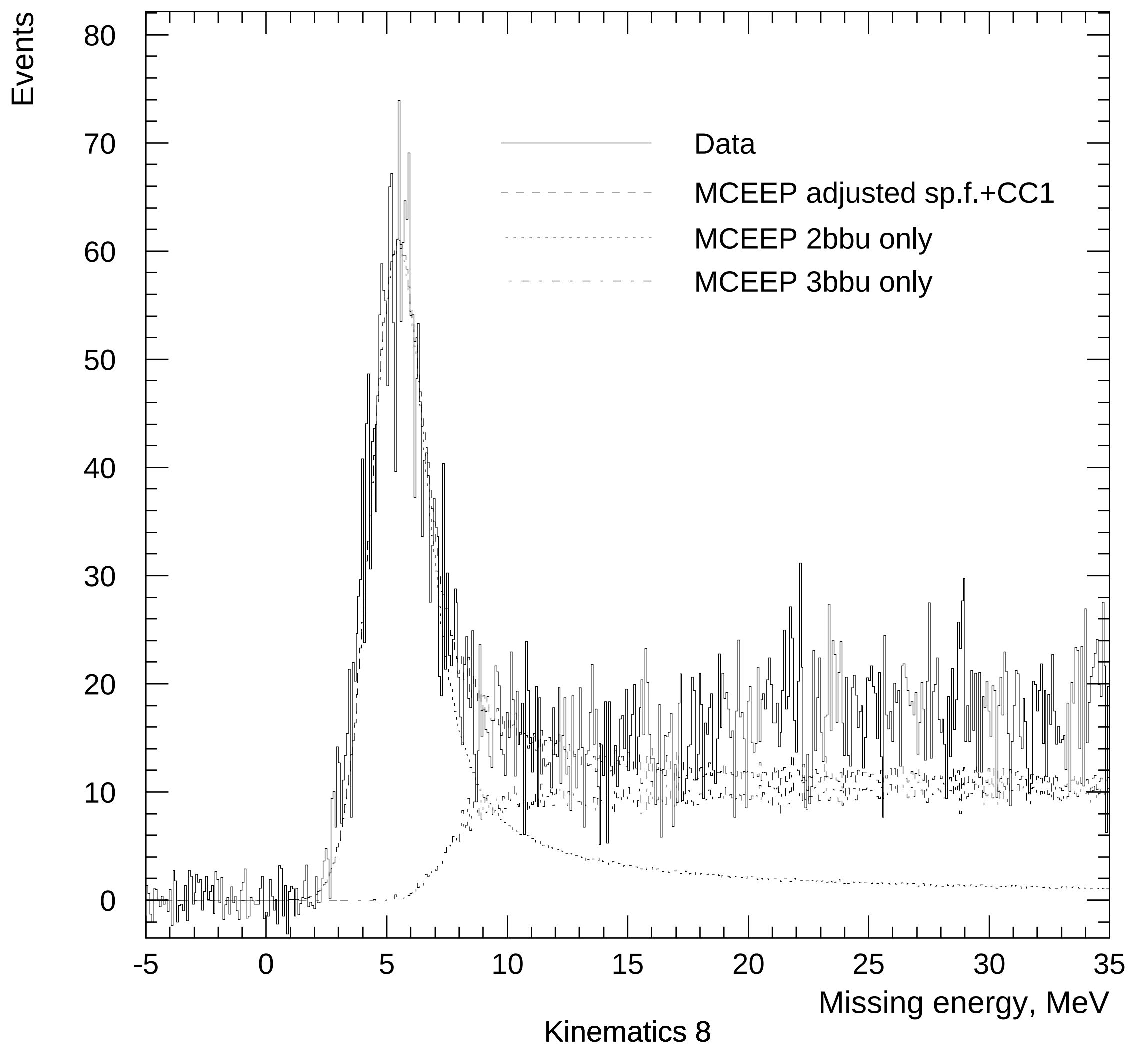

Figure 5-29: ^{3}He(e,e$'$p) missing energy distributions at kinematics 8, E_{beam} = 4.8 GeV, $P_{miss} = 300$ MeV/c, the detected proton is forward of $\vec{q}$.

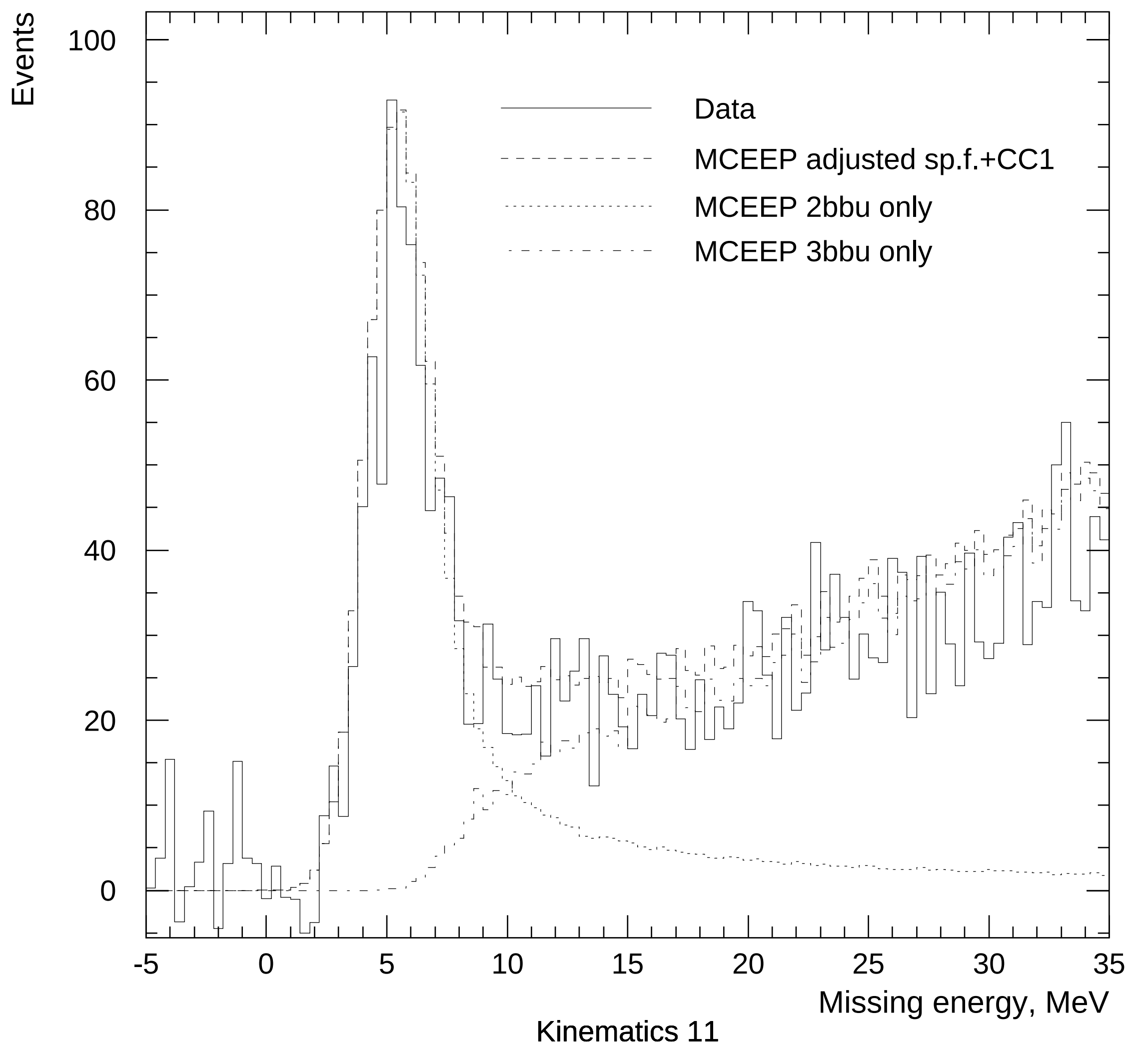

Figure 5-30: ^{3}He(e,e′p) missing energy distributions at kinematics 11, E_{beam} = 4.8 GeV, $P_{miss} = 425$ MeV/c, the detected proton is forward of $\vec{q}$.

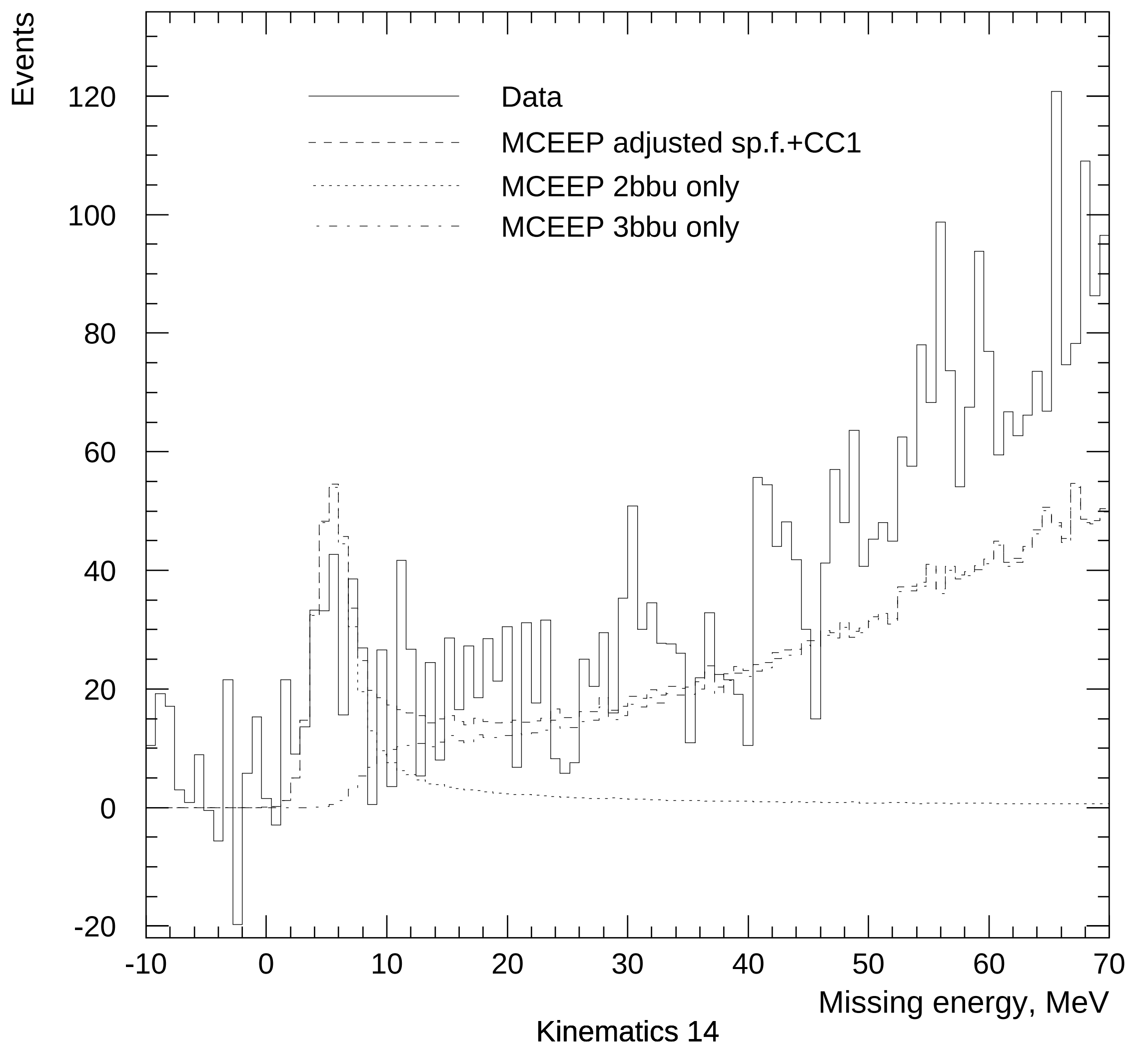

Figure 5-31: ^{3}He(e,e$'$p) missing energy distributions at kinematics 14, E_{beam} = 4.8 GeV, $P_{miss} = 550$ MeV/c, the detected proton is forward of $\vec{q}$.

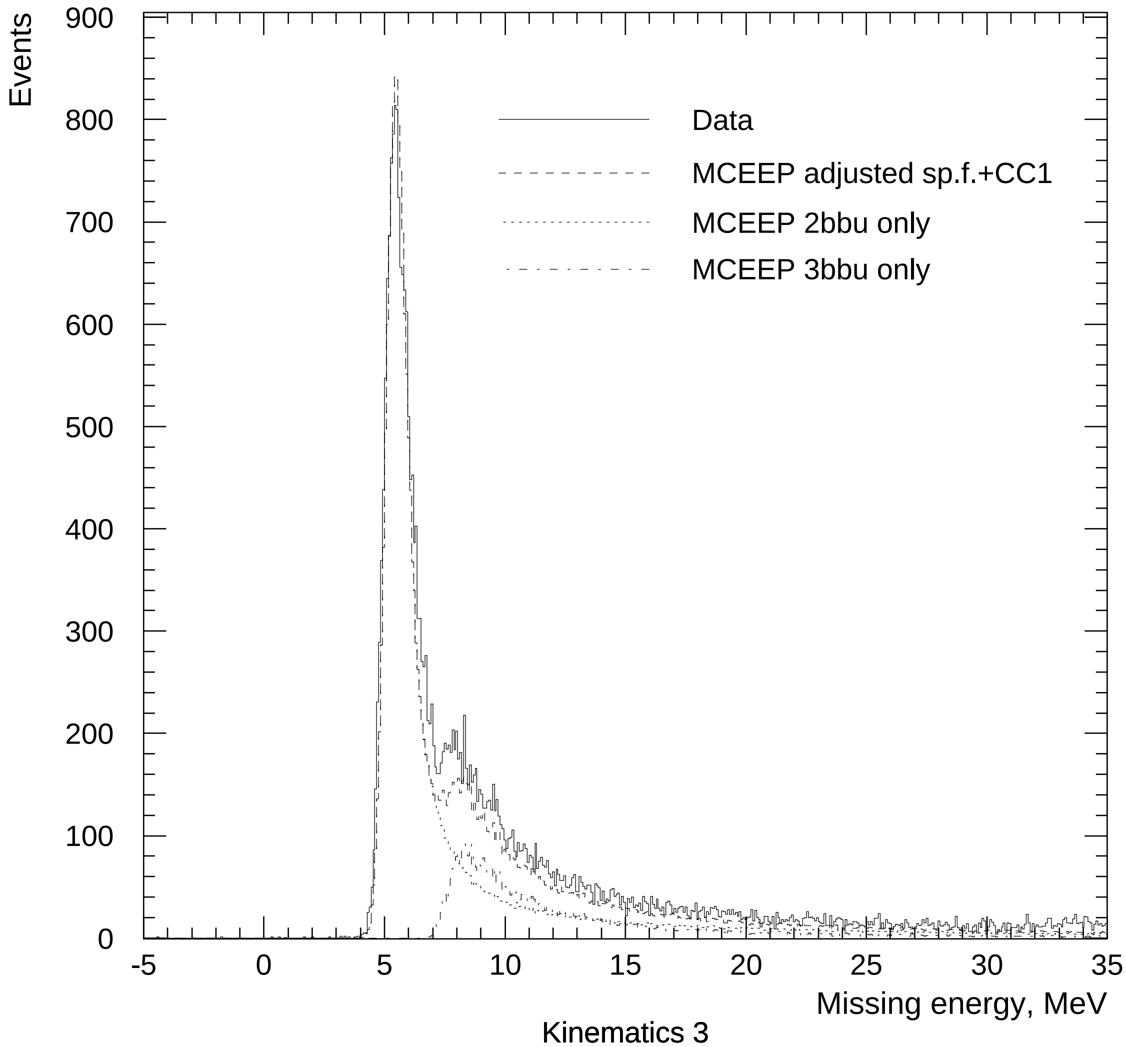

Figure 5-32: ^{3}He(e,e$'$p) missing energy distributions at kinematics 3, E_{beam} = 1.2 GeV, $P_{miss} = 0$.

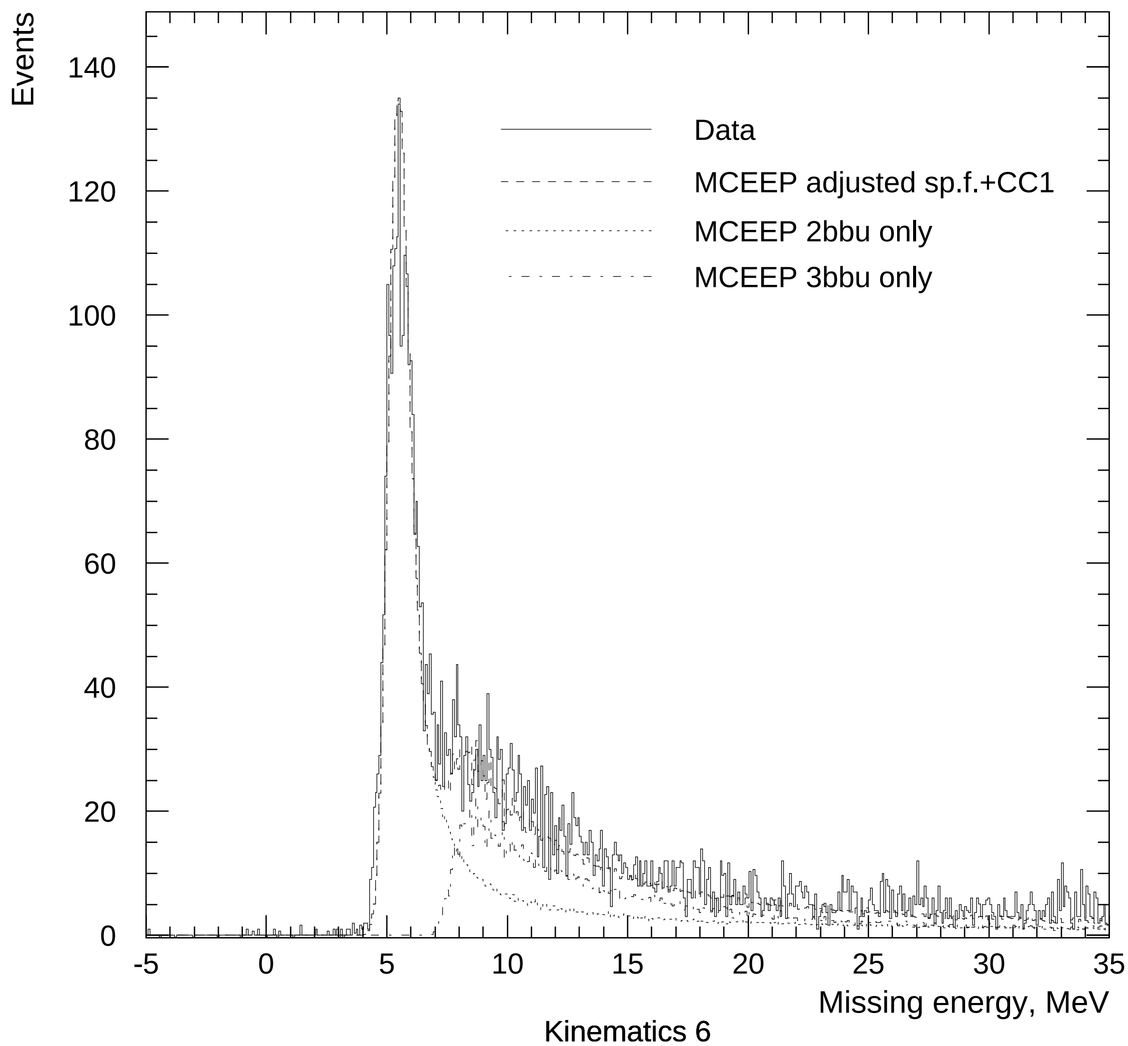

Figure 5-33: ^{3}He(e,e$'$p) missing energy distributions at kinematics 6, E_{beam} = 1.2 GeV, $P_{miss} = 150$ MeV/c, the detected proton is back of $\vec{q}$.

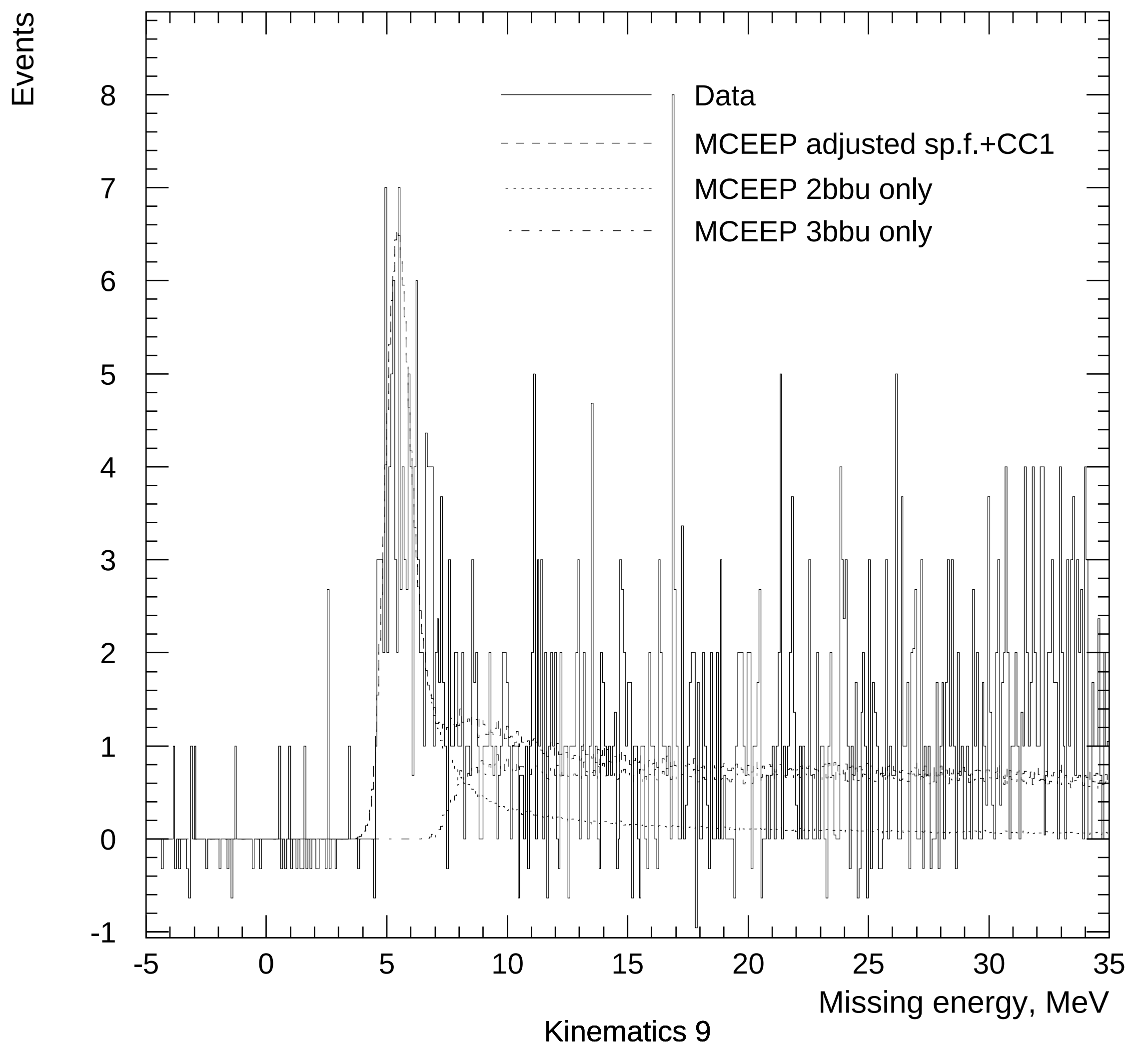

Figure 5-34: ^{3}He(e,e$'$p) missing energy distributions at kinematics 9, E_{beam} = 1.2 GeV, $P_{miss} = 300$ MeV/c, the detected proton is back of $\vec{q}$.

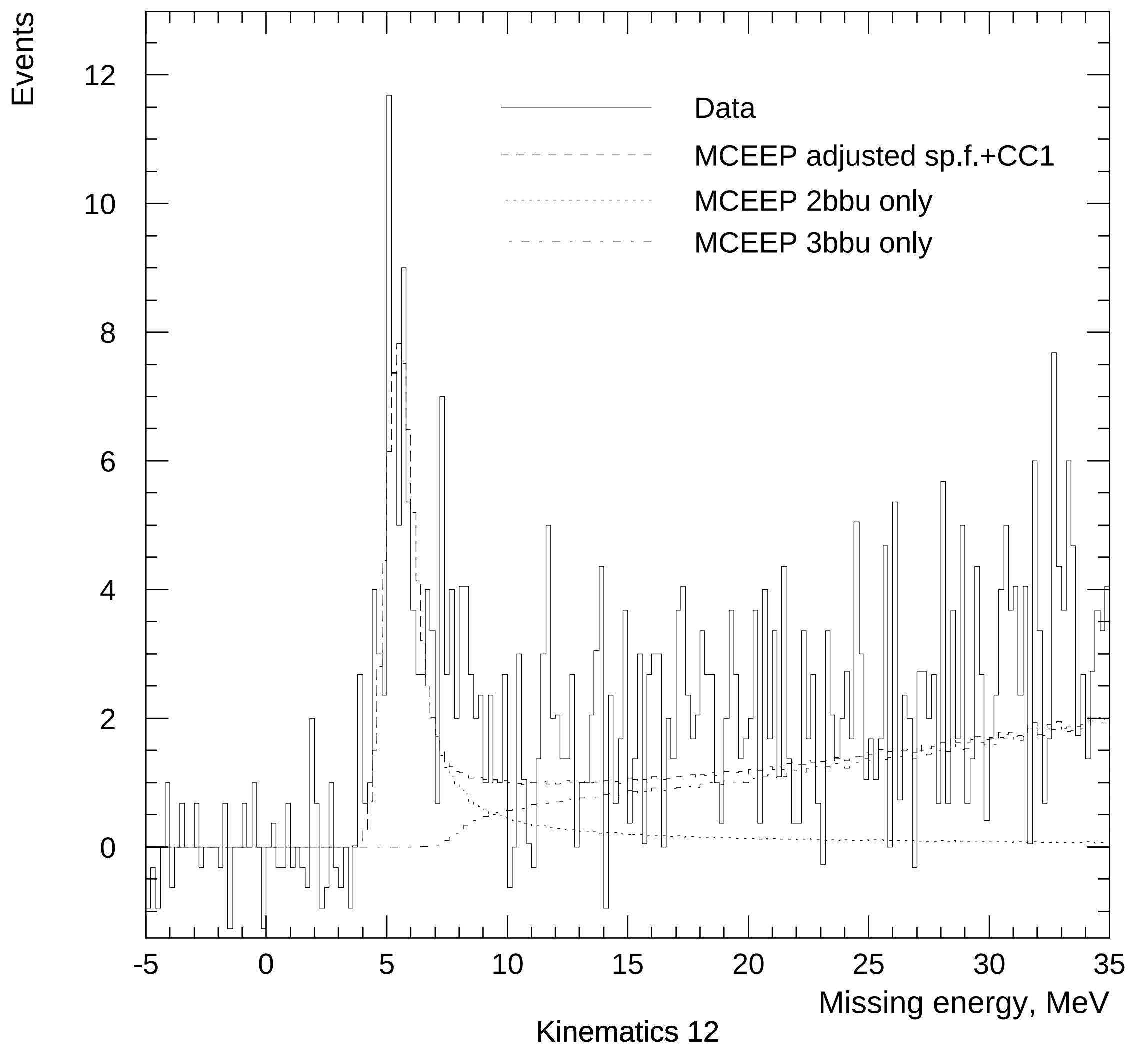

Figure 5-35: ^{3}He(e,e$'$p) missing energy distributions at kinematics 12, E_{beam} = 1.2 GeV, $P_{miss} = 425$ MeV/c, the detected proton is back of $\vec{q}$.

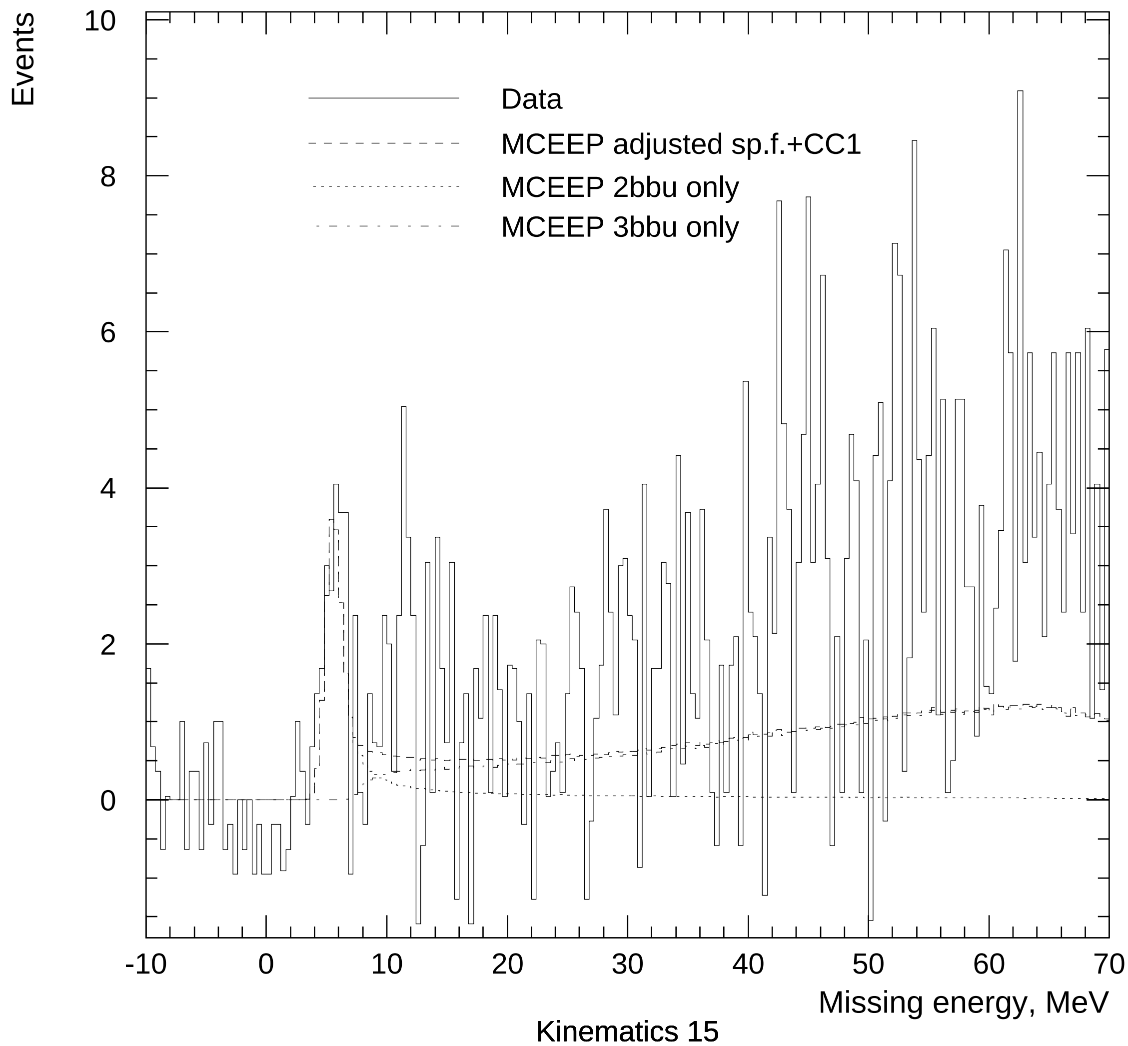

Figure 5-36: ^{3}He(e,e$'$p) missing energy distributions at kinematics 15, E_{beam} = 1.2 GeV, $P_{miss} = 550$ MeV/c, the detected proton is back of $\vec{q}$.

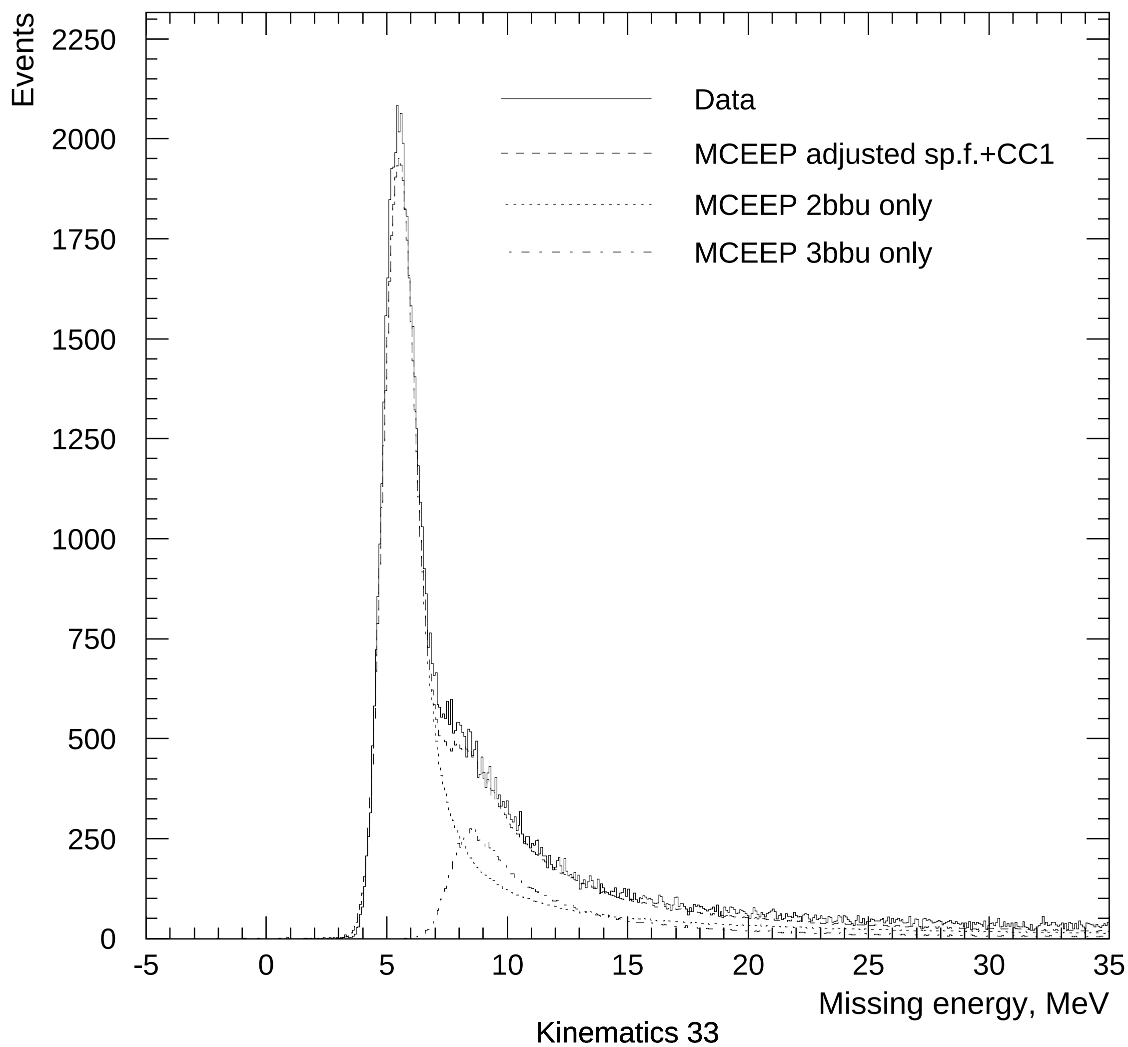

Figure 5-37: ^{3}He(e,e$'$p) missing energy distributions at kinematics 33, E_{beam} = 1.9 GeV, $P_{miss} = 0$.

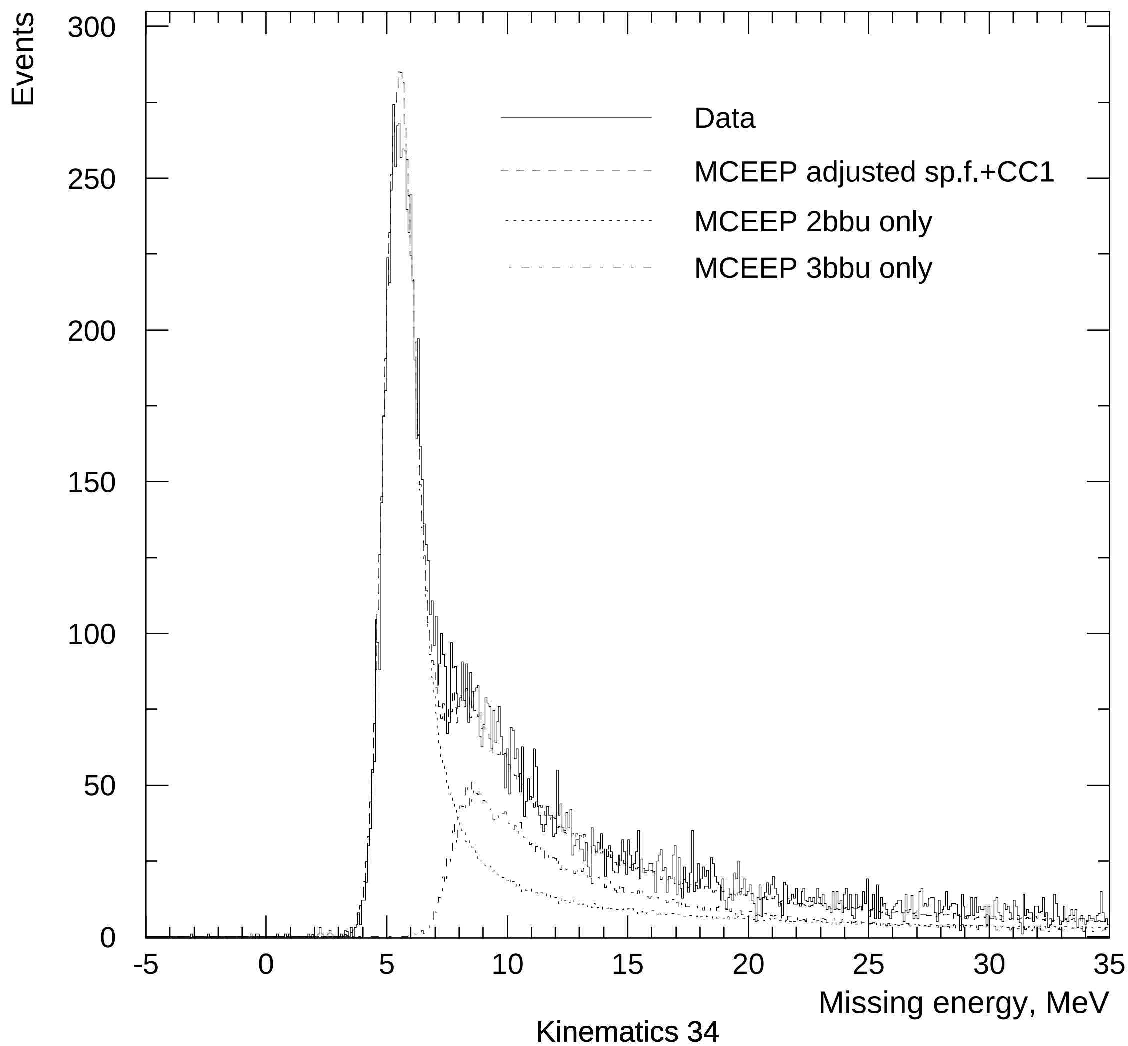

Figure 5-38: ^{3}He(e,e$'$p) missing energy distributions at kinematics 34, E_{beam} = 1.9 GeV, $P_{miss} = 150$ MeV/c, the detected proton is back of $\vec{q}$.

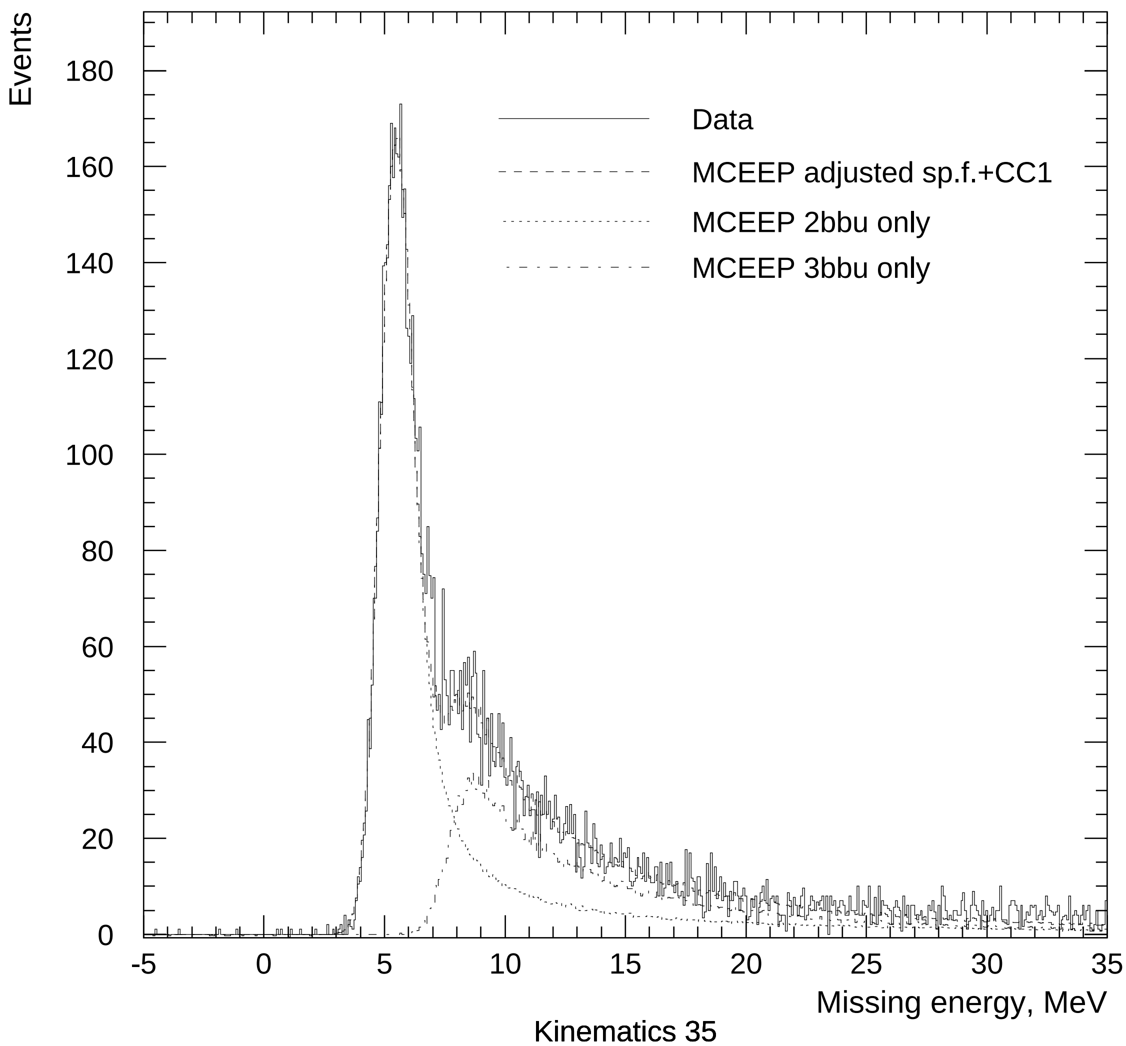

Figure 5-39: ^{3}He(e,e′p) missing energy distributions at kinematics 35, E_{beam} = 1.9 GeV, $P_{miss} = 150$ MeV/c, the detected proton is forward of $\vec{q}$.

Chapter 6

Results and discussion

This chapter presents results of the ^{3}He(e,e$'$p) analysis described in the previous chapters. Kinematic settings of the measurements are summarized in Sec. 1.6. R_T, R_L and $R_L + R_{TT}V_{TT}/V_L$ response functions extracted at several values of P_{miss} with the Rosenbluth technique were already presented in Sec. 5.10. Missing energy spectra are presented in Sec. 5.12.

The order of presentation in this chapter is as follows: ^{3}He(e,e$'$p)D cross sections and distorted spectral functions; ^{3}He(e,e$'$p)D A_{TL} asymmetry; results extracted at kinematics 1 [1] with binning both in P_{miss} and in the out-of-plane angle ϕ (^{3}He(e,e$'$p)D cross sections, distorted spectral functions, A_{TL} and R_{TT}); ^{3}He(e,e$'$p)D response functions; ^{3}He(e,e$'$p)pn cross sections and distorted spectral functions up to $E_{miss} = 30$ MeV. Quoted up to Sec. 6.6 errors are statistical only. Systematic errors are analyzed in Sec. 6.6. Results are compared to theoretical calculations.

6.1 ^{3}He(e,e$'$p)D cross sections and spectral functions

^{3}He(e,e$'$p)D cross sections extracted in the measurements are presented in Figs. 6-1 through 6-19 and Tables 6.1 through 6.18. As described in Sec. 1.6, the measure-

[1] $E_{beam} = 4.8$ GeV, nominal $P_{miss} = 0$.

ments were performed with ω and q fixed at 837 MeV and 1500 MeV/c respectively (quasielastic peak), at three beam energies of 1.2, 1.9 and 4.8 GeV, in perpendicular coplanar kinematics. Three sets of ^{3}He(e,e$'$p)D cross sections were obtained:

1. with "cc1-averaging" within kinematic bins, denoted as $\frac{d^5\sigma^{cc1}}{dE_f d\Omega_e d\Omega_p}$;
2. with "cc1-averaging" within kinematic bins and "cc1-renormalization" to fixed values of ω and Q^2 (the values are given in Table 5.1), denoted as $\frac{d^5\sigma^{ren}}{dE_f d\Omega_e d\Omega_p}$;
3. with a "model independent" technique (flat simulation cross section within each kinematic bin), denoted as $\frac{d^5\sigma^{ind}}{dE_f d\Omega_e d\Omega_p}$.

All three methods of extraction are described in Sec. 5.8. The "cc1-averaging" technique assumes that within each kinematic bin the variation of the ^{3}He(e,e$'$p) cross section can be described as the factorization (5.19) – (5.20) of the cc1 prescription for electron-nucleon cross section [25] with a "fitted-to-data" spectral function. Cross sections extracted with this technique are quoted at a coplanar kinematic point within the bins. Cross sections extracted with the "model independent" technique are averaged within the bins with a flat model for the ^{3}He(e,e$'$p) cross section, and are quoted for the whole bin. Therefore, if one is to compare the "model-independent" cross sections to theoretical calculations, one has to average the theory over the acceptance of the bins.

Use of the "cc1-averaging" technique with "cc1-renormalization" to fixed values of Q^2 and ω allowed one to remove the variation of the extracted ^{3}He(e,e$'$p)D cross sections due to systematic changes in the accepted range of Q^2 and ω at each spectrometer setting, and thus to isolate the cross section dependence with P_{miss} (Sec. 5.8). In doing so, the technique facilitated the comparison of the extracted cross sections with the theories. Q^2 and ω points of the "cc1-renormalization", as well as precise values of energy of incident electrons at the interaction vertex after corrections for the mean energy losses, are given in Table 5.1.

In the following, we compare cross sections extracted with the "cc1-averaging" technique with the "cc1-renormalization" to fixed values of Q^2 and ω to theoretical calculations, and then compare this set of extracted cross sections to those obtained with the other (mentioned above) techniques.

$E_{beam} = 4.8$ GeV, detected proton back of $\vec{q}$

The ^{3}He(e,e$'$p)D cross sections extracted at the nominal beam energy of 4.8 GeV with the detected proton back of $\vec{q}$ (Σ_1 kinematics), using the "cc1-averaging" technique with cc1-renormalization to fixed values of Q^2 and ω, are plotted in Fig. 6-1. Figs. 6-2 through 6-4 give enlarged views of Fig. 6-1. On these plots, different marker types correspond to different settings of the hadron spectrometer (the electron spectrometer is fixed in angle and momentum).

Also plotted are theoretical calculations:

1. Laget Plane Wave (PW) calculation, with the bound nucleon wave function corresponding to the solution of the three-body Faddeev equations with the Paris potential with 18 channels.

2. The PW calculation + lowest-order FSI amplitudes for nucleon-nucleon rescattering in the final state (Laget).

3. The PW + FSI calculation + lowest-order two-nucleon π and ρ meson exchange currents and intermediate Δ formation amplitudes (Laget; for simplification, this calculation is denoted as "MEC").

4. The PW + FSI + MEC calculation + three-nucleon π double scattering ("3 body") amplitudes (Laget's "full" calculation).

5. The variational Salme ^{3}He two-body breakup (2bbu) spectral function [77] factorized by the cc1 prescription for the off-shell electron-nucleon cross section [25], as implemented in MCEEP [55].

6. Ciofi degli Atti and Kaptari Plane Wave (PW) calculation, with a ^{3}He realistic wave function from the Pisa Group, corresponding to AV18 interaction.

7. Ciofi degli Atti and Kaptari PW + FSI calculation, with FSI taken into account in a Glauber-type calculation[2].

A detailed description of Laget's calculations is available in [6][3]. Laget's calculations use an updated ("high-energy") parametrization of the NN scattering amplitude [5]. Laget's PW+FSI, PW+FSI+MEC and the full PW+FSI+MEC+3 body calculations are almost indistinguishable for P_{miss} range from 0 to $\sim$ 260 MeV. Laget's PW+FSI+MEC and the full calculations are almost indistinguishable for P_{miss} range from 0 to $\sim$ 600 MeV. In the following, we compare the calculations to the measurements in different regions of missing momentum P_{miss} (Figs. 6-1 through 6-4).

P_{miss} **close to 0:** The Salme spectral function factorized by cc1 describes the data closely in this region. Laget's calculations are 19% (FSI calculations) – 26% (PW calculation) above the datapoints.

P_{miss} **from 100 to 320 MeV/c:** The calculations of Laget and of Ciofi degli Atti and Kaptari indicate a strong reduction of the cross sections due to NN rescattering in the final state. Ciofi degli Atti and Kaptari calculations seem to overpredict the magnitude of the rescattering, with the PW+FSI calculation by as much as a factor of two below the data. Laget's PW+FSI calculations are up to $\sim$ 25% above the data for P_{miss} from 100 to 195 MeV/c, but follow the data within statistical errors in the rest of the region; the calculations indicate the relative unimportance of MEC and intermediate Δ formation processes. Plane wave calculations by as much as the factor of two overpredict cross sections in this region.

P_{miss} **from 320 to 740 MeV/c:** Both Laget and Ciofi degli Atti and Kaptari calculations indicate a strong enhancement of the cross sections due to NN rescattering in the final state. Laget's PW+FSI calculation is up to $\sim$ 20% below the data. The PW+FSI+MEC calculation describes the data within statistical errors. The contribution of the three-nucleon MEC amplitudes ("3 body") is negligible. Inclusion of FSI in Ciofi degli Atti and Kaptari PW calculations in general reproduces

[2]Ciofi degli Atti and Kaptari calculations were made with $E_i = 4.8$ GeV, $q = 1.5$ GeV/c and $\omega = 0.837$ GeV, which is slightly different from the central kinematic values of the measurements (Table 5.1).

[3][6] describes Laget's calculations for ^{4}He and ^{3}H; ^{3}He calculations presented in this thesis use an analogous diagrammatic approach [78].

the character of the experimental curve, but is above the datapoints by up to $\sim 70\%$ in this region. All PW calculations are up to four-fold below the data.

P_{miss} **from 740 to 1035 MeV/c:** All available calculations grossly underpredict the measured cross sections in this region. Laget's calculations indicate increasing contributions from three-nucleon π double scattering ("3-body") processes at highest missing momenta, but still the full Laget's calculation significantly underpredicts the cross section, by as much as ~ 26 times at the highest P_{miss} datapoint.

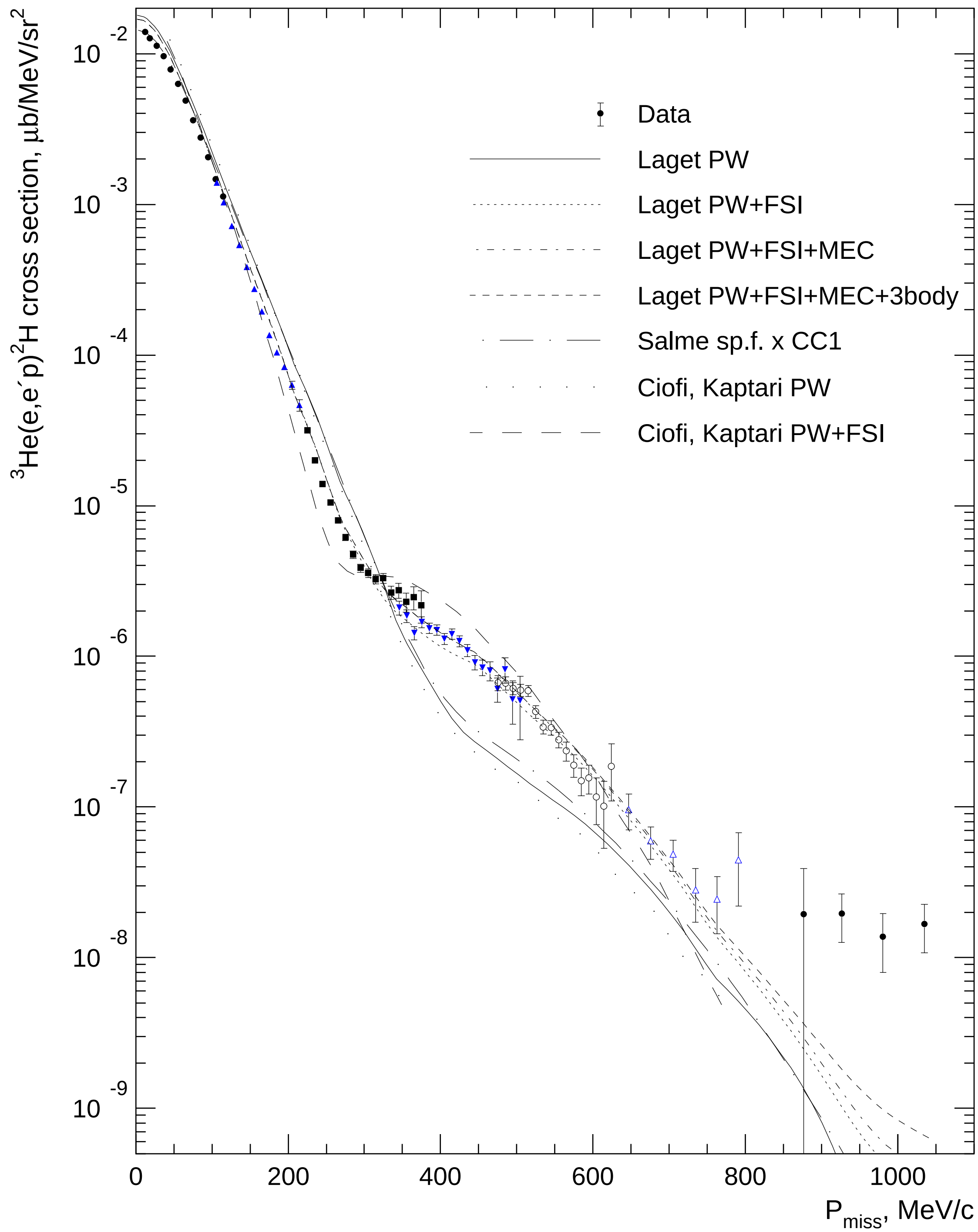

Figure 6-1: ^{3}He(e,e$'$p)D cross sections extracted at incident electron energy 4805.5 MeV. The detected proton is at angles back of $\vec{q}$.

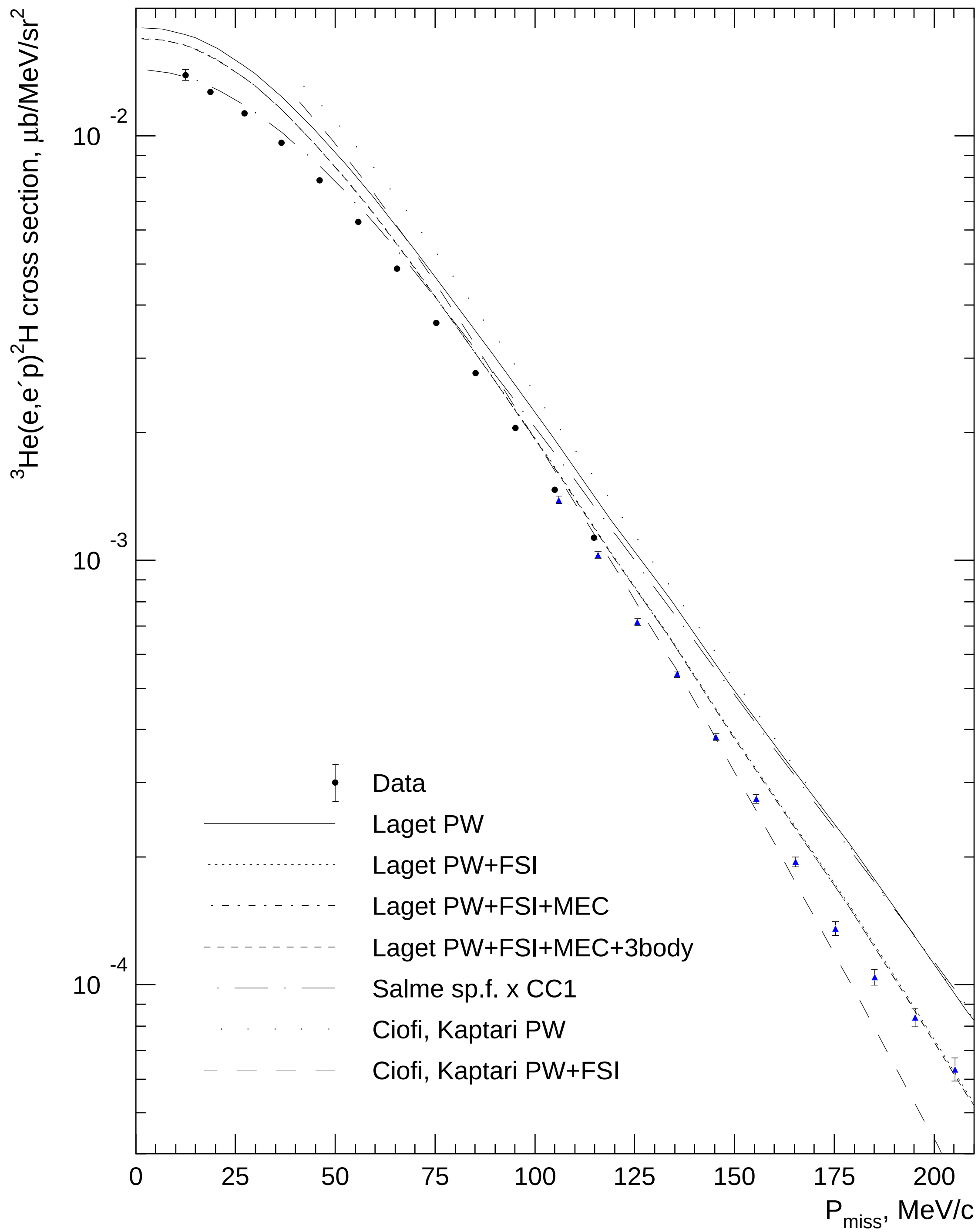

Figure 6-2: ^{3}He(e,e$'$p)D cross sections extracted at incident electron energy 4805.5 MeV. The detected proton is at angles back of $\vec{q}$.

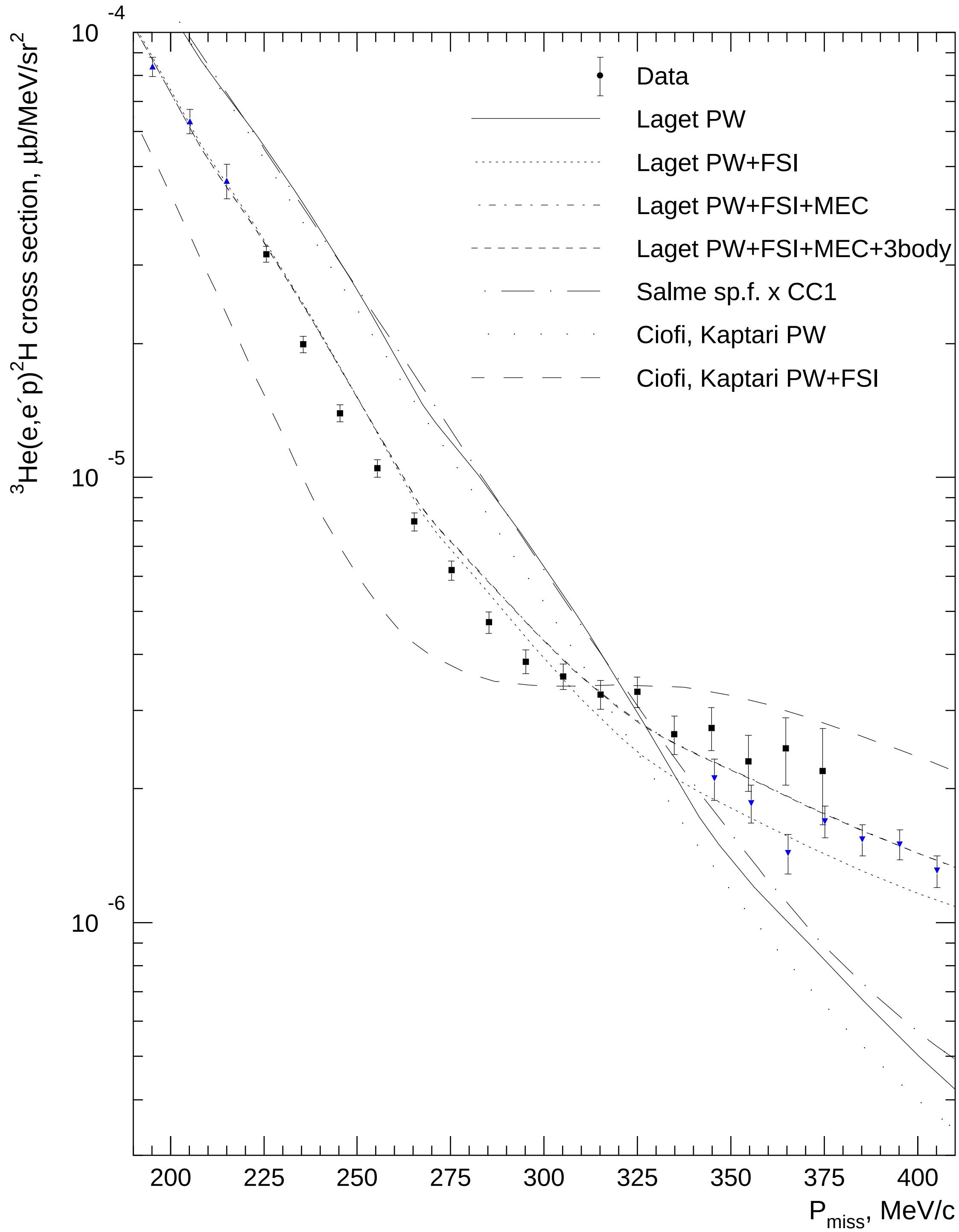

Figure 6-3: ^{3}He(e,e′p)D cross sections extracted at incident electron energy 4805.5 MeV. The detected proton is at angles back of $\vec{q}$.

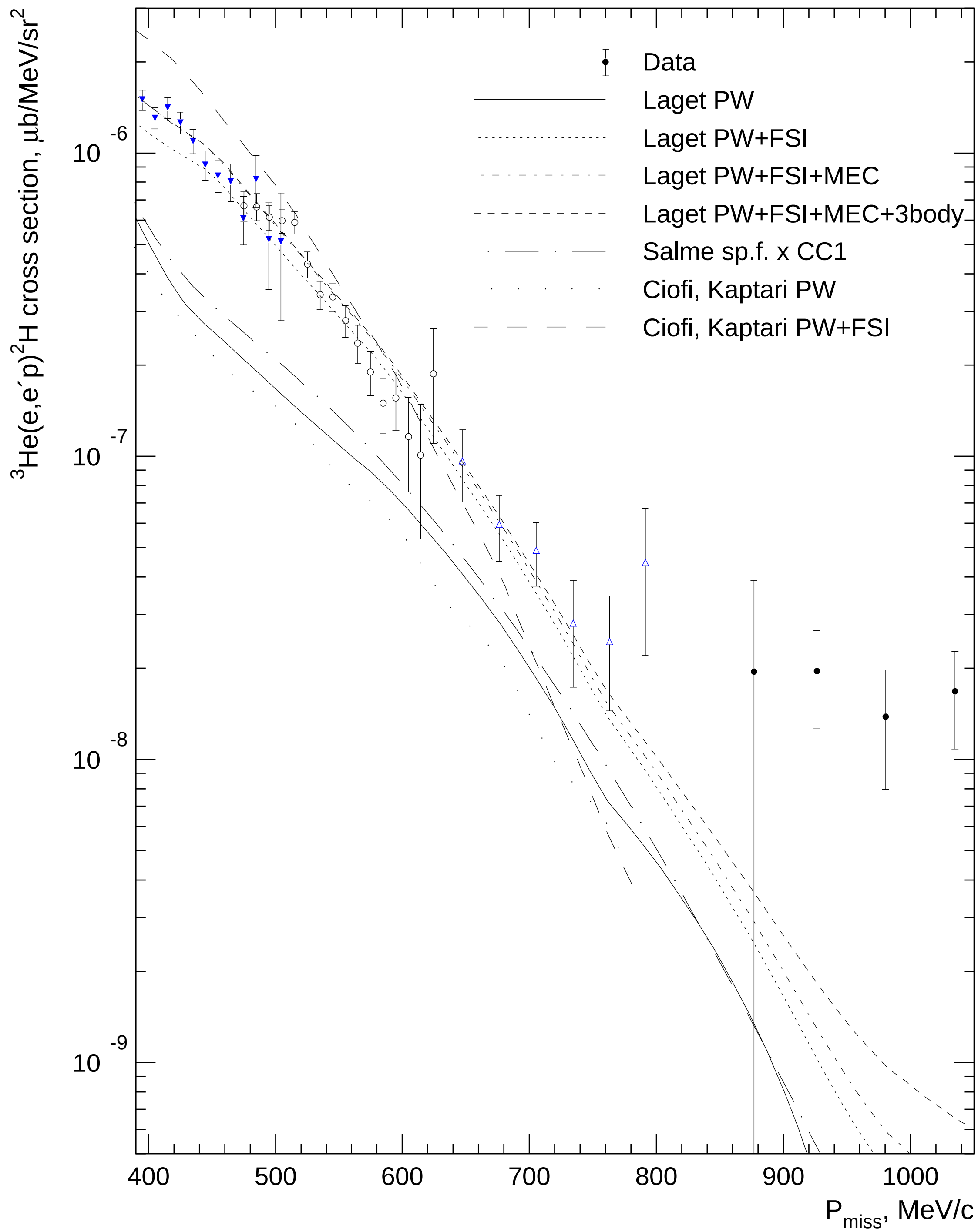

Figure 6-4: ^{3}He(e,e$'$p)D cross sections extracted at incident electron energy 4805.5 MeV. The detected proton is at angles back of $\vec{q}$.

$E_{beam} = 4.8$ GeV, detected proton forward of $\vec{q}$

The ^{3}He(e,e$'$p)D cross sections extracted at the nominal beam energy of 4.8 GeV with the detected proton forward of $\vec{q}$ (Σ_2 kinematics), using the "cc1-averaging" technique with cc1-renormalization to fixed values of Q^2 and ω, are plotted in Fig. 6-5. Figs. 6-6 through 6-8 give enlarged views of Fig. 6-5. Different marker types correspond to different settings of the hadron spectrometer, while the electron spectrometer is fixed in angle and momentum.

Also plotted are the theoretical calculations of Laget and Salme, described on p. 201. In the following, we compare the calculations to the measurements in different regions of missing momentum P_{miss}.

P_{miss} close to 0: This region is kinematically close to the Σ_1 low P_{miss} region discussed above, and results in similar conclusions. The Salme spectral function factorized by cc1 describes the data closely in this region. Laget's calculations are 19% (FSI calculations) – 26% (PW calculation) above the datapoints.

P_{miss} from 100 to 270 MeV/c: Laget's calculations indicate a strong reduction of the cross sections due to NN rescattering in the final state in this region, and a relative unimportance of MEC and intermediate Δ formation processes. Laget's PW+FSI calculation agrees with the data very well, following it within statistical errors. Both plane wave calculations are up to $\sim$ twice above the data.

P_{miss} from 270 to 655 MeV/c: Laget's calculations indicate a strong enhancement of the cross sections (starting at $P_{miss} \sim 290$ MeV/c) due to NN rescattering in the final state, and a smaller enhancement due to two-nucleon π and ρ MEC and intermediate Δ formation currents. Laget's full calculation reproduces well the general character of the experimental curve, but is about 30% below the data for P_{miss} from 270 to 450 MeV/c, with a fair agreement (within the large statistical errors) from 450 to 600 MeV/c. The next to the highest P_{miss} datapoint (640 MeV/c) is ~ 5.5 times above the full calculation, but the large statistical error of the datapoint does not allow to make a strong conclusion on the disagreement. Both PW calculations are up to 15-fold lower than the data in this region.

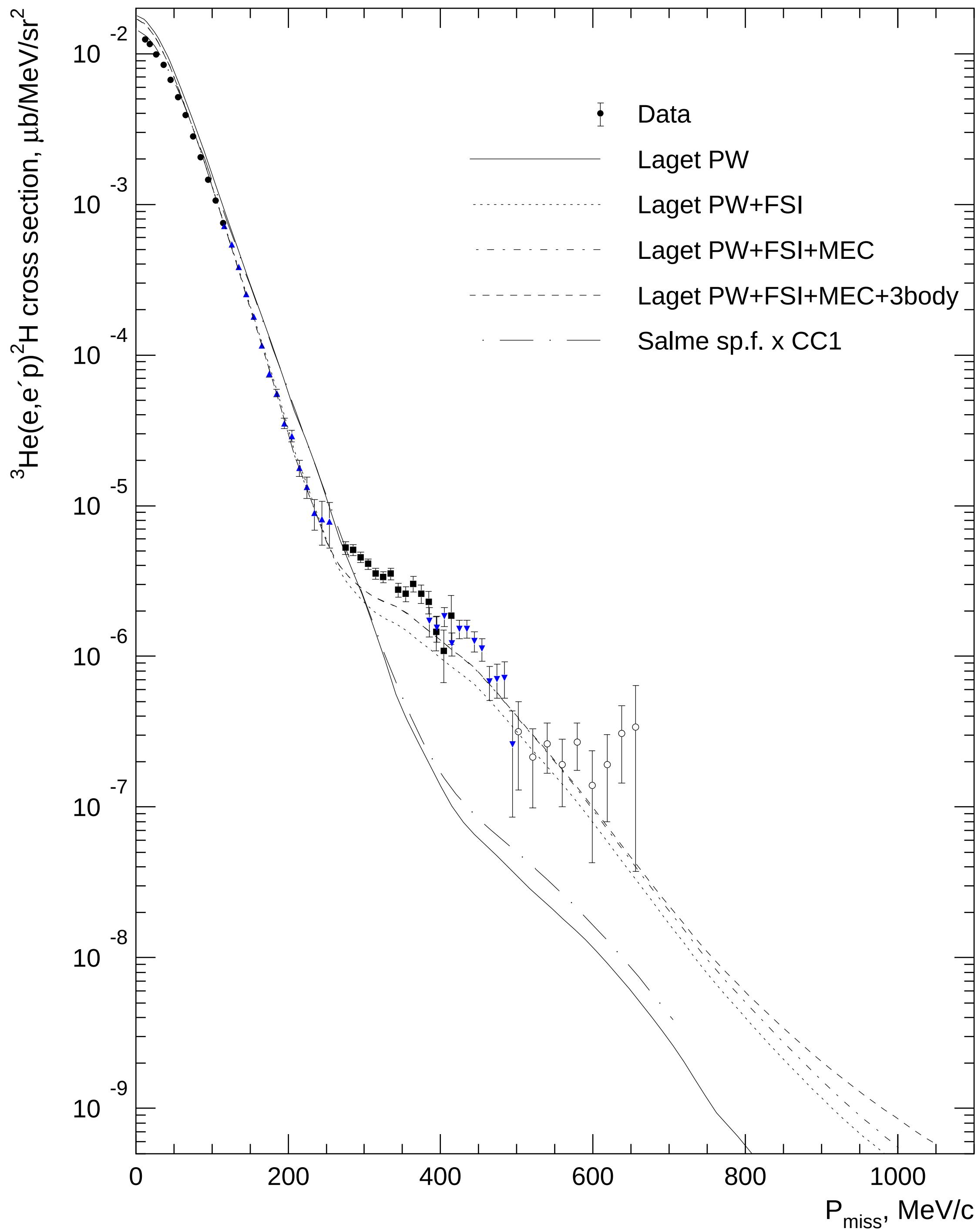

Figure 6-5: ^{3}He(e,e$'$p)D cross sections extracted at incident electron energy 4805.5 MeV. The detected proton is at angles forward of $\vec{q}$.

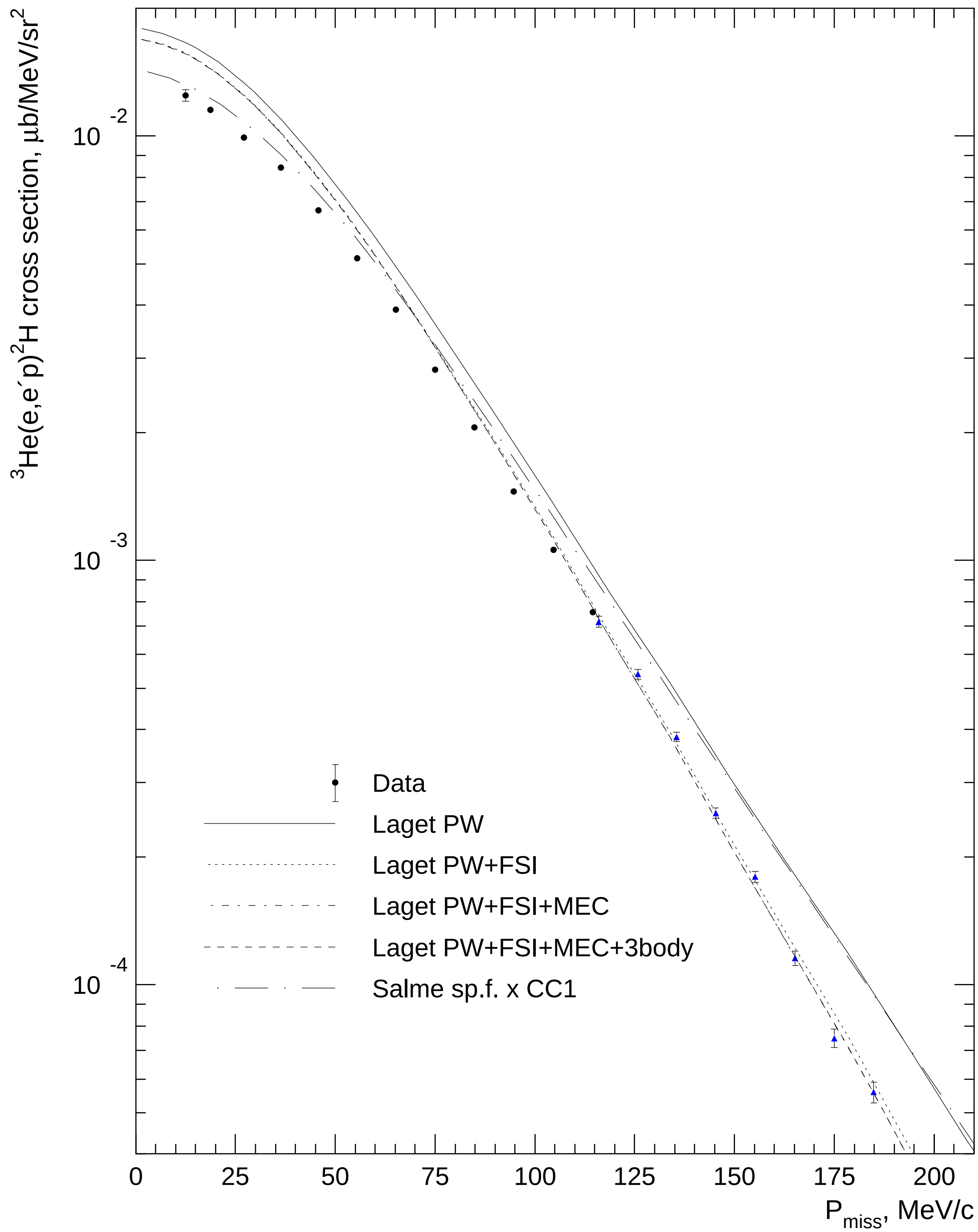

Figure 6-6: ^{3}He(e,e$'$p)D cross sections extracted at incident electron energy 4805.5 MeV. The detected proton is at angles forward of $\vec{q}$.

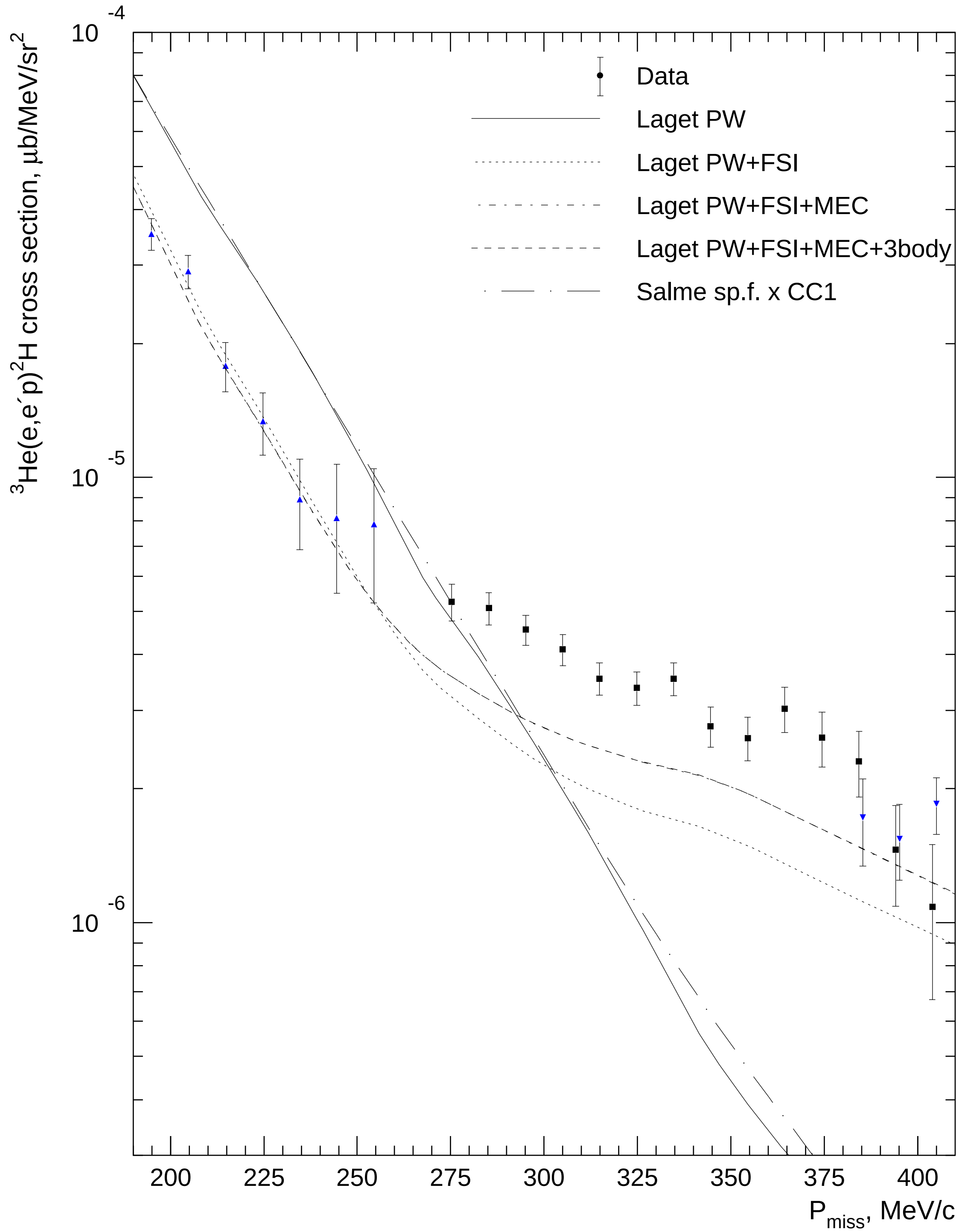

Figure 6-7: ^{3}He(e,e$'$p)D cross sections extracted at incident electron energy 4805.5 MeV. The detected proton is at angles forward of $\vec{q}$.

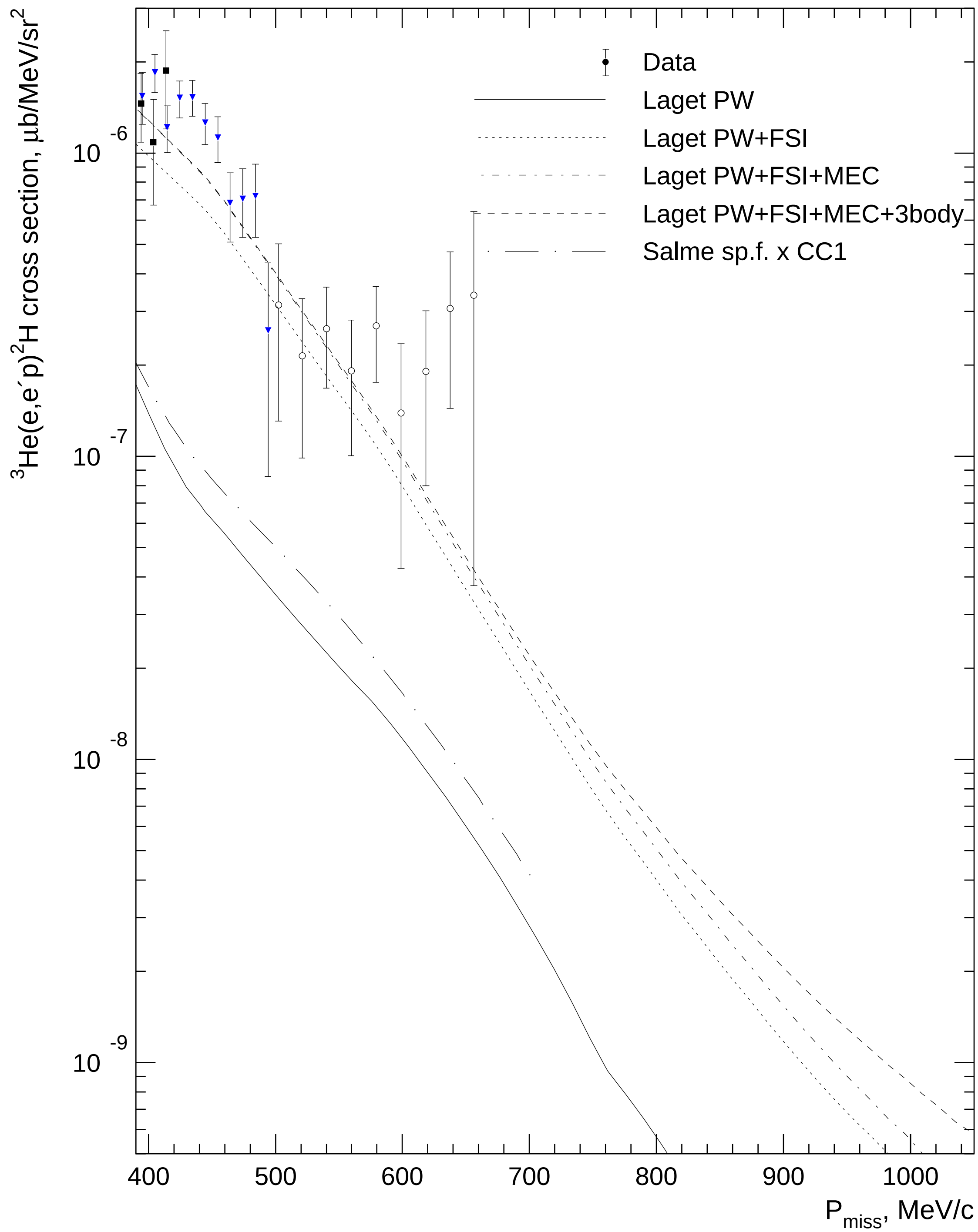

Figure 6-8: ^{3}He(e,e$'$p)D cross sections extracted at incident electron energy 4805.5 MeV. The detected proton is at angles forward of $\vec{q}$.

$E_{beam} = 1.2$ **GeV**

The ^{3}He(e,e$'$p)D cross sections extracted at the nominal beam energy of 1.2 GeV (Σ_3 kinematics), using the "cc1-averaging" technique with cc1-renormalization to fixed values of Q^2 and ω, are plotted in Fig. 6-9. Negative P_{miss} values in the figure correspond to the detected proton forward of $\vec{q}$ and perpendicular kinematics. Different marker types correspond to different settings of the hadron spectrometer, while the electron spectrometer is fixed in angle and momentum.

Also plotted are theoretical calculations of Laget and Salme, described on p. 201. In the following, we compare the calculations to the measurements in two regions of missing momentum P_{miss}.

P_{miss} **close to 0:** The Salme spectral function factorized by cc1 describes data better than Laget's calculations, but with larger disagreement than at Σ_1 and Σ_2 kinematic settings: the Salme prediction is about 13% above the data, Laget's predictions are 20% (FSI calculations) – 28% (PW calculation) above.

P_{miss} **from 60 to 570 MeV/c:** Laget's calculations indicate the dominance of FSI processes, with two-nucleon MEC and Δ formation amplitudes starting to be expressed at P_{miss} of $\sim$ 275 MeV/c. Laget's full calculation reproduces well the measured cross section, following it within statistical errors. Laget's PW+FSI+MEC calculation is not plotted in the figure, since it is very close to the full calculation in the shown P_{miss} region. PW calculations disagree with the data by up to $\sim$ 6 times in this region.

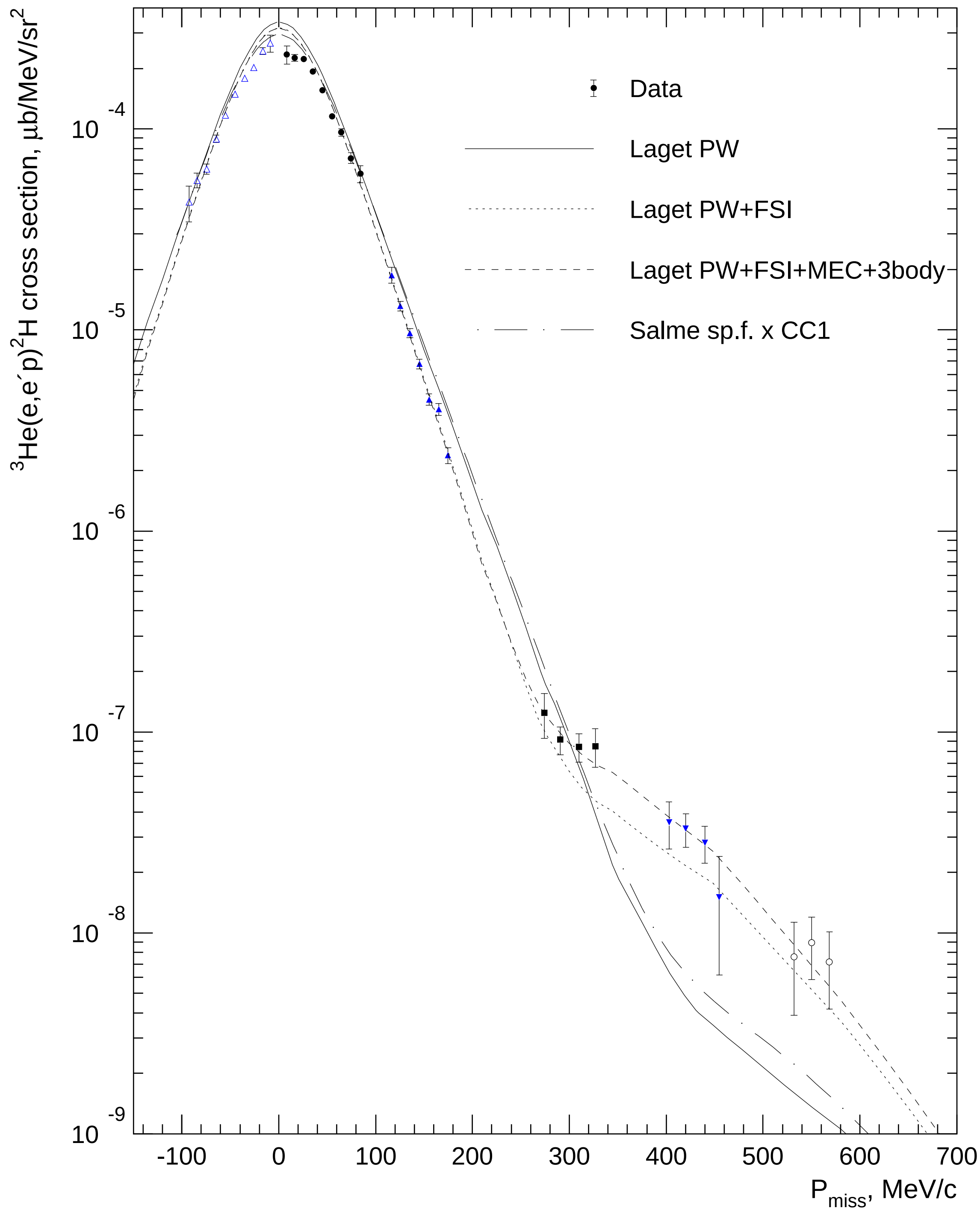

Figure 6-9: ^{3}He(e,e′p)D cross sections extracted at incident electron energy 1253.8 MeV. Negative P_{miss} values correspond to the detected proton forward of $\vec{q}$ and perpendicular kinematics.

$E_{beam} = 1.9$ **GeV**

The ^{3}He(e,e$'$p)D cross sections extracted at the nominal beam energy of 1.9 GeV (Σ_4 and Σ_5 kinematics), using the "cc1-averaging" technique with cc1-renormalization to fixed values of Q^2 and ω, are plotted in Fig. 6-10. Negative P_{miss} values in the figure correspond to the detected proton forward of $\vec{q}$ and perpendicular kinematics. Different marker types correspond to different settings of the hadron spectrometer, while the electron spectrometer is fixed in angle and momentum.

Also plotted are the theoretical calculations of Laget and Salme, described on p. 201. Σ_4 and Σ_5 kinematic settings were used for study of systematic errors in the procedure of separation of response functions (so called "3rd epsilon point" measurements), and therefore their P_{miss} range is rather limited (0 ± 200 MeV/c). Laget's PW+FSI+MEC calculation is not plotted in the figure, since it is very close to the full PW+FSI+MEC+3 body calculation. In the following, we compare the calculations to the measurements in two regions of missing momentum P_{miss}.

P_{miss} **close to 0:** As well as at the beam energy of 4.8 GeV, the Salme spectral function factorized by cc1 describes data very closely in this region. Laget's calculations are above the data by 17% (PW+FSI calculation) – 26% (PW calculation).

$|P_{miss}|$ **from 80 to 205 MeV/c:** Laget's calculations indicate a decrease of the cross sections due to NN rescattering in the final state, with a relative unimportance of MEC and intermediate Δ formation processes. Laget's calculations including FSI amplitudes reproduce the measured cross section within statistical errors in this region. Both PW calculations are up to $\sim$ twice above the data.

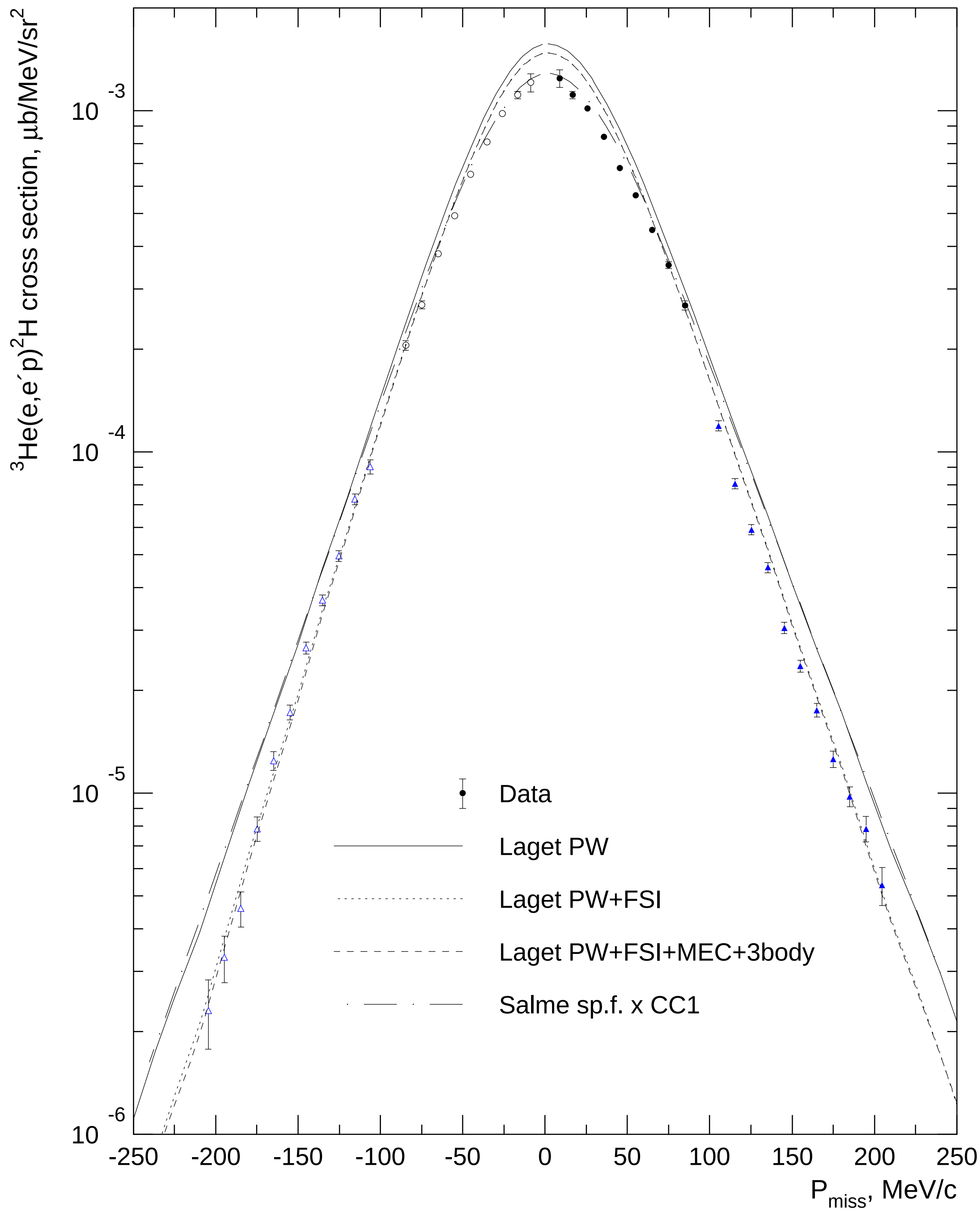

Figure 6-10: ^{3}He(e,e$'$p)D cross sections extracted at incident electron energy 1953.0 MeV. Negative P_{miss} values correspond to the detected proton forward of $\vec{q}$ and perpendicular kinematics.

Distorted ^{3}He(e,e′p)D spectral functions

Fig. 6-11 shows the ^{3}He(e,e′p)D distorted spectral functions obtained from the whole dataset analyzed in this thesis. The spectral functions were extracted by dividing the measured ^{3}He(e,e′p)D cross sections by the cc1 off-shell e-p cross section [25] and by appropriate kinematic factors [2]. The corresponding procedure is described in Sec. 5.8. Different marker types in the figure correspond to different values of energy of incident electron. Negative P_{miss} values correspond to the detected proton forward of $\vec{q}$ and perpendicular kinematics. For clarity, the available Salme spectral function is not plotted in the figure since its comparison with the data follows from figures presented above.

The distorted spectral functions extracted at different values of energy of incident electron show a good agreement with each other in common regions of P_{miss}. Notably, for the detected proton back of $\vec{q}$ and P_{miss} from 275 to 570 MeV/c, the 1.2 GeV spectral function is up to $\sim$ 1.6 times above the 4.8 GeV spectral function. This indicates that in this P_{miss} region the PWIA factorization with the cc1 is not describing well the dependence of the ^{3}He(e,e′p)D cross section on the polarization of the exchanged photon.

Comparison to previous measurements

Fig. 6-12 shows the ^{3}He(e,e′p)D distorted spectral functions extracted at the three beam energies, and the ^{3}He(e,e′p)D spectral function measured at Saclay by Jans et al [17]. The Saclay data was taken in perpendicular quasielastic kinematics at beam energies of 509 – 529 MeV, momentum transfers of 300 – 430 MeV/c and the detected proton back of $\vec{q}$ (Sec. 1.5). Therefore, in Fig. 6-12 it is compared to the E89044 data with the detected proton also back of $\vec{q}$ and in perpendicular quasielastic kinematics.

From the Fig. 6-12 one can see that the two experiments agree well, at least up to P_{miss} of $\sim$ 260 MeV/c. For P_{miss} above 260 MeV/c, the large statistical errors of the Saclay datapoints do not allow one to make a conclusion on the disagreement.

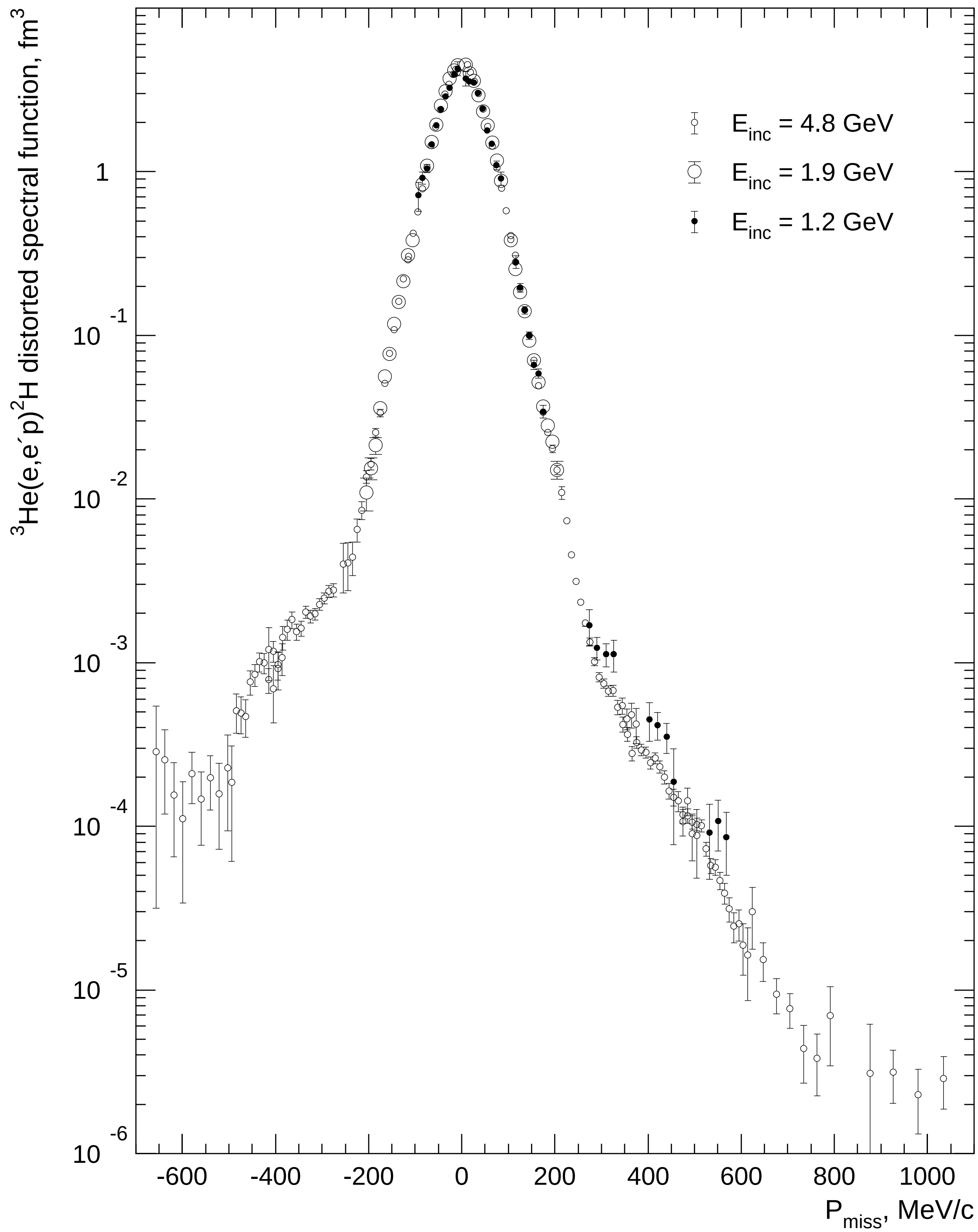

Figure 6-11: ^{3}He(e,e$'$p)D distorted spectral functions extracted in the experiment. Negative P_{miss} values correspond to the detected proton forward of $\vec{q}$. Quasielastic perpendicular coplanar kinematics.

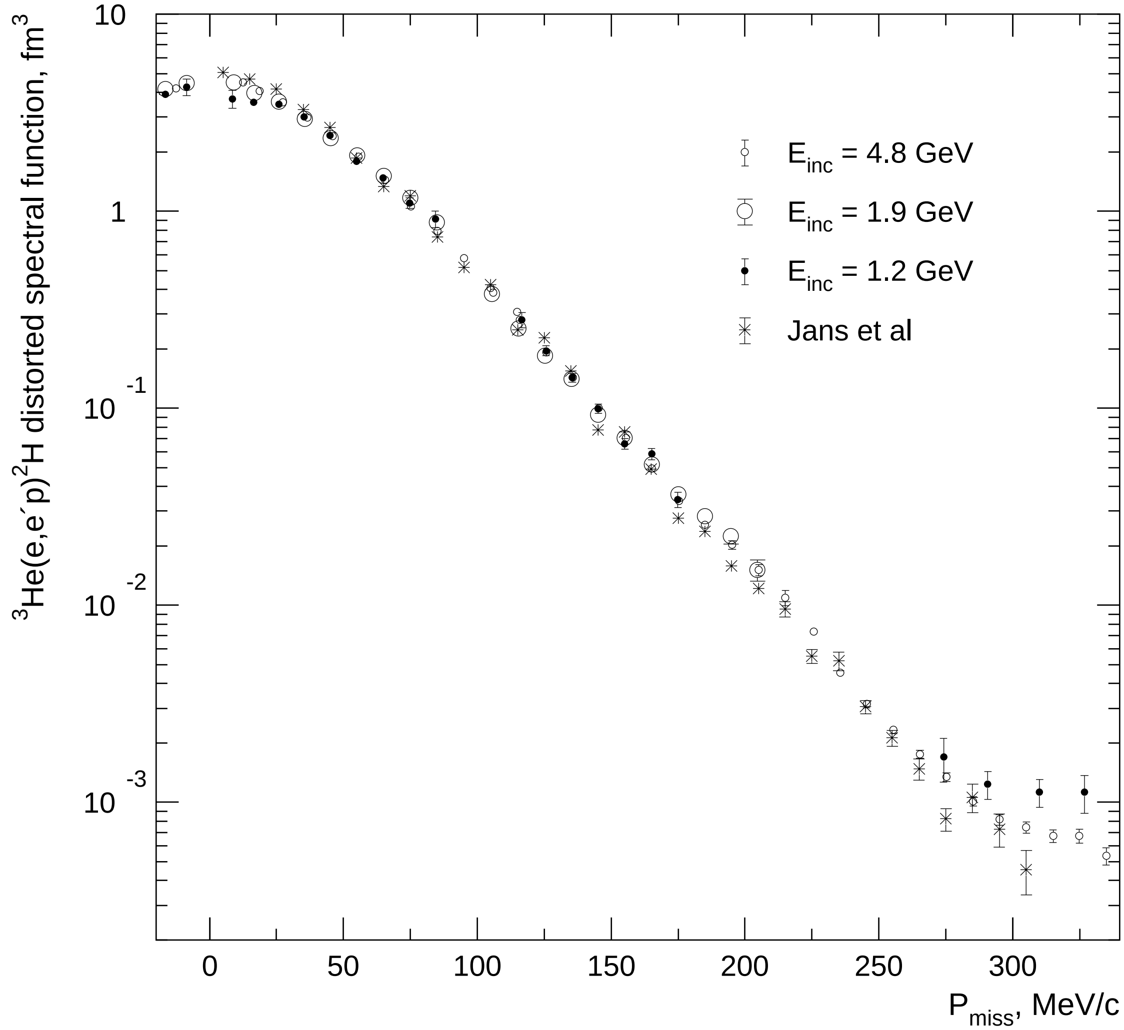

Figure 6-12: The ^{3}He(e,e$'$p)D distorted spectral functions extracted in the E89044 experiment (filled and empty circles), and the ^{3}He(e,e$'$p)D spectral function of Jans et al [17]. Quasielastic perpendicular coplanar kinematics. Negative P_{miss} values correspond to the detected proton forward of $\vec{q}$.

Comparison of techniques of extraction of ^{3}He(e,e′p)D cross section

Figs. 6-13 though 6-16 show the ^{3}He(e,e′p)D cross sections extracted both with the "model independent" technique, and with the "cc1-averaging" technique using "cc1-renormalization" to the fixed values of Q^2 and ω (both methods are described in Sec. 5.8). The difference between the techniques arises from the ^{3}He(e,e′p) cross section model used in the simulation (a flat cross section within each bin in the former case, and a "fitted-to-data" spectral function factorized by the cc1 in the latter case). Also, as mentioned above, the "cc1-averaged" cross sections are "renormalized", using cc1, to a coplanar kinematics with fixed values of Q^2 and ω (the values are given in Table 5.1).

This renormalization is necessary to remove the variation of the cross sections caused by systematic changes in accepted ranges of Q^2 and ω with P_{miss} at each spectrometer setting, and thus to simplify the interpretation of the P_{miss} dependence of the cross sections. From the figures it can be seen that for the cross sections extracted with the model independent technique, these Q^2 and ω-based variations lead to the general features:

- for the detected proton back of $\vec{q}$:

  a decrease in the cross section at lower missing momenta for each spectrometer setting,

  an increase in the cross section at higher missing momenta for each spectrometer setting;

- for the detected proton forward of $\vec{q}$:

  an increase in the cross section at lower missing momenta for each spectrometer setting,

  a decrease in the cross section at higher missing momenta for each spectrometer setting.

The averages and widths of the distributions of Q^2 and ω for each kinematic bin are given in the tables at the end of this section. The lowest variation in Q^2 and ω is observed for the 1.2 GeV dataset, which has relatively small Q^2 and ω acceptances.

The largest discrepancy between the ^{3}He(e,e$'$p)D cross sections extracted with the two techniques is $\sim$ 1.5-fold at the high P_{miss} edge of kinematics 14 [4] (Fig. 6-14). Despite this large disagreement, one can see that the "cc1-renormalization" to fixed values of Q^2 and ω simply removes discontinuities between cross sections measured at different spectrometer settings. In some cases it might be preferable to use the cross sections extracted with the "model independent" technique. However, when comparing this set of cross sections to theoretical calculations, one has to correctly average the theories over the acceptance of each P_{miss} bin. The definition of the spectrometer acceptances used for the cross section extraction is given in Appendix A.1.

Figs. 6-17 through 6-20 show the ratio of the ^{3}He(e,e$'$p)D cross sections extracted with the "model independent" technique to those extracted with the "cc1-averaging" technique, without the "renormalization" to fixed values of Q^2 and ω. The agreement between these two sets of cross sections is much closer, since both contain similar Q^2 and ω-based variations. Up to $\sim$ 5 % offset between the cross sections is due to the differences in the averaging within the kinematic bins.

The only significant disagreement between the two sets is observed for the detected proton forward of $\vec{q}$ at nominal $P_{miss} = 0$ spectrometer settings (kinematics 1, 3 and 33). As described in Sec. 5.11, at these spectrometer settings events were not restricted to an in-plane kinematics by a cut on the out-of-plane angle. The acceptance of the spectrometers is such, that at the large P_{miss} edge of these spectrometer settings, detected ^{3}He(e,e$'$p) events were close to 90° out-of-plane. Since the "cc1-averaged" cross sections are "cc1-renormalized" to an in-plane kinematic point (Sec. 5.8) and the A_{TL} is negative in this P_{miss} region (Fig. 6-21), this procedure of "cc1-renormalization" to an in-plane kinematic point decreased the "cc1-averaged" cross sections relative to the "model-independent" cross sections. Therefore, formally there is no disagreement between the two sets of cross sections: when one compares the model-independent set of cross sections to theories one has to properly average

[4] $E_{beam} = 4.8$ GeV, $P_{miss} = 550$ MeV/c, the detected proton forward of $\vec{q}$.

over the (possibly out-of-plane) acceptance of the bins; the "cc1-averaged" set of cross sections should be compared to theoretical calculations in coplanar kinematics.

Similar effects can be seen for the detected proton back of $\vec{q}$ at $P_{miss} = 0$ spectrometer settings, but, as expected, in this case the "cc1-renormalization" of the cross sections to in-plane leads to an increase in the "cc1-averaged" cross sections relative to the "model-independent" set; the disagreement here is smaller, since it is partially compensated for by changes in the distribution of accepted Q^2 and ω with P_{miss} [5].

All results presented in this section, as well as the averages and the standard deviations of the Q^2 and ω distributions for each kinematic bin, are presented in Tables 6.1 through 6.18.

[5] For example, at the beam energy of 4.8 GeV and $P_{miss} = 0$ kinematics (kinematics 1, Tables 6.1 and 6.7), the mean of the accepted Q^2 distribution increases by $\sim 7\%$ for P_{miss} from 0 to 115 MeV/c and the detected proton forward of $\vec{q}$, while for the same P_{miss} range and the detected proton back of $\vec{q}$ the mean of the Q^2 distribution decreases by $\sim 4.5\%$. Therefore, the Q^2 acceptances sampled for the detected proton forward and back of $\vec{q}$ are quite different, and effects of averaging over the Q^2 acceptances can contribute differently to the bins forward and back of $\vec{q}$.

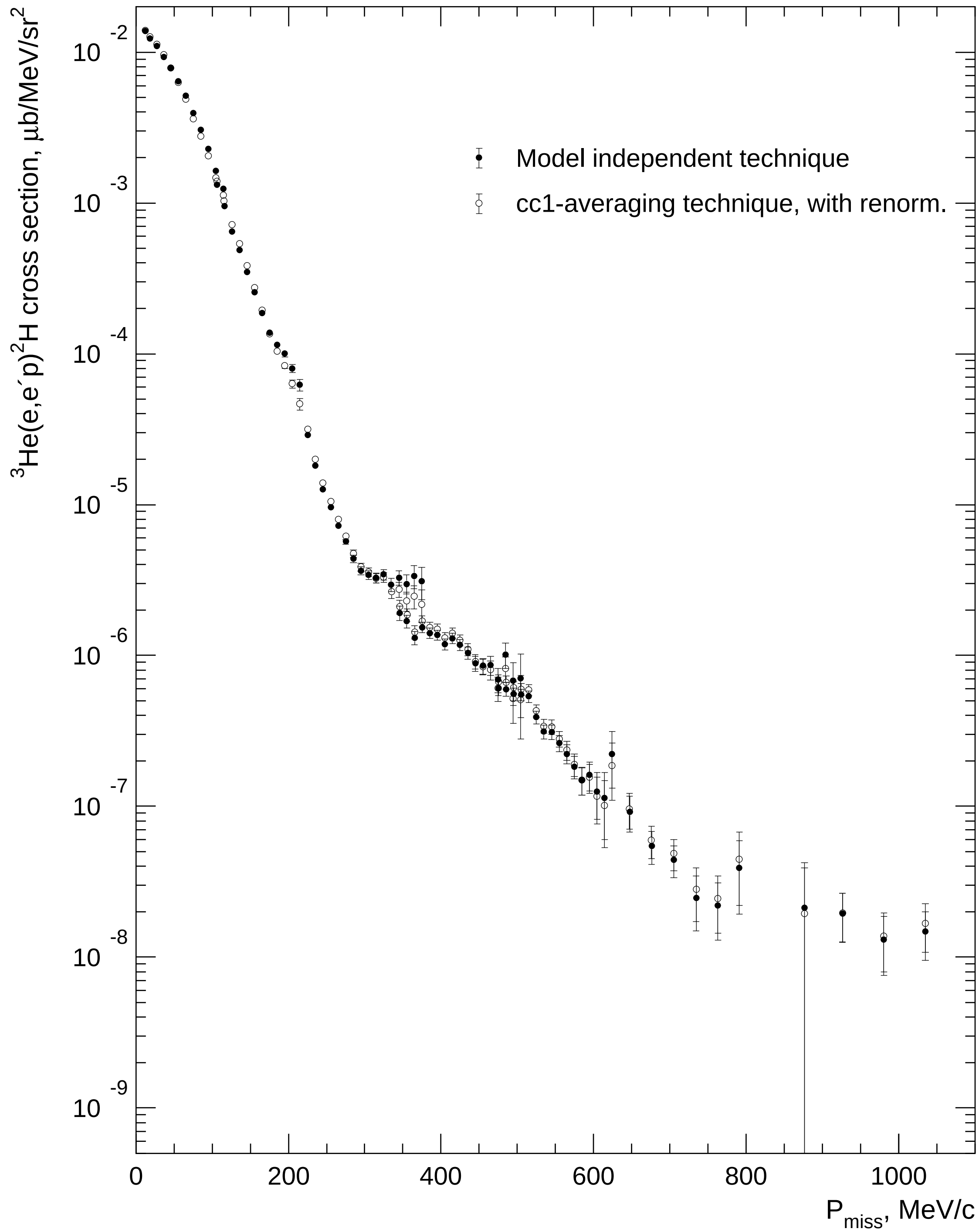

Figure 6-13: ^{3}He(e,e′p)D cross sections extracted with the "model independent" technique, and with the "cc1-averaging" technique with "cc1-renormalization" to fixed values of Q^2 and ω, at beam energy 4.8 GeV. The detected proton is at angles back of $\vec{q}$.

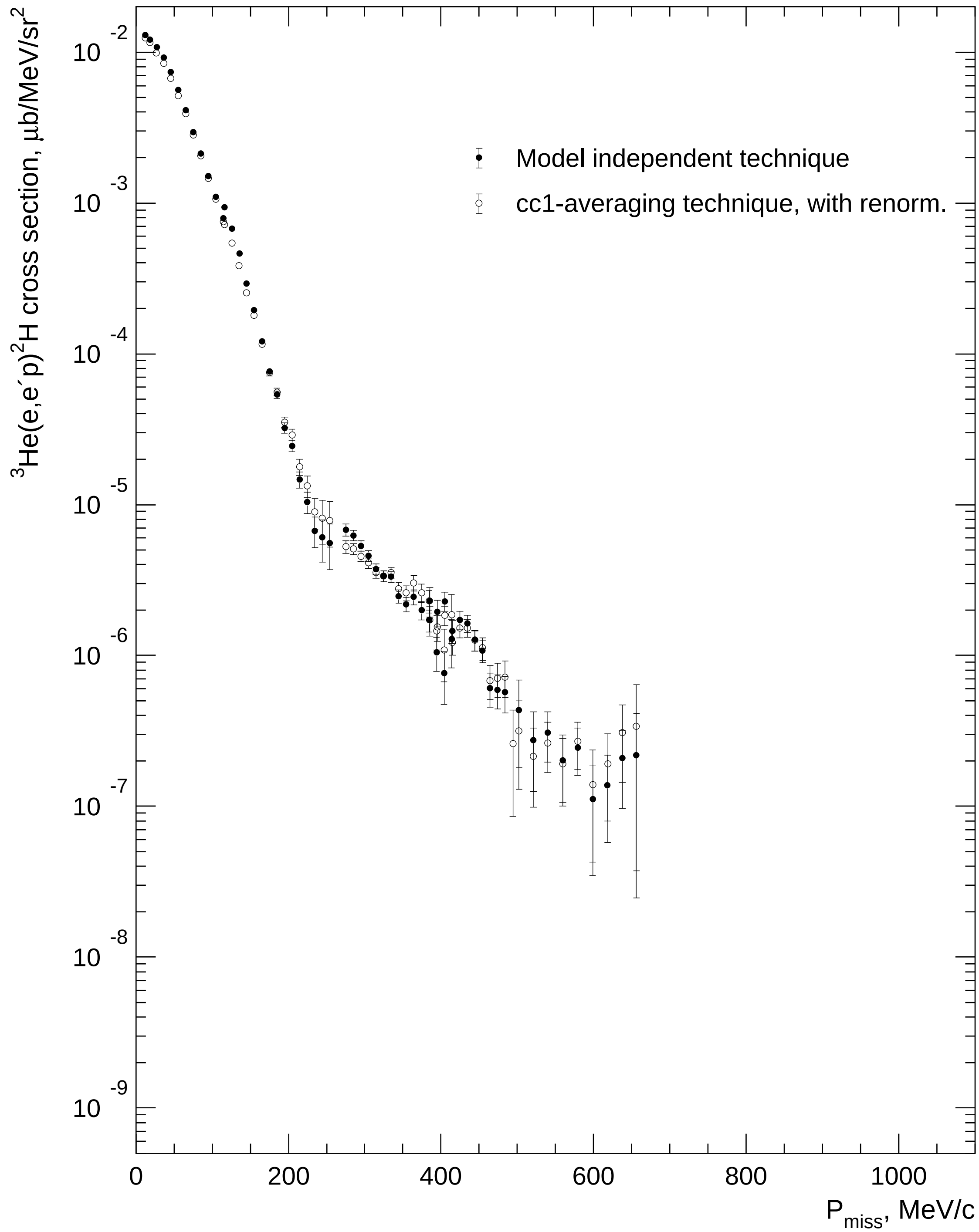

Figure 6-14: ^{3}He(e,e$'$p)D cross sections extracted with the "model independent" technique, and with the "cc1-averaging" technique with "cc1-renormalization" to fixed values of Q^2 and ω, at beam energy 4.8 GeV. The detected proton is at angles forward of $\vec{q}$.

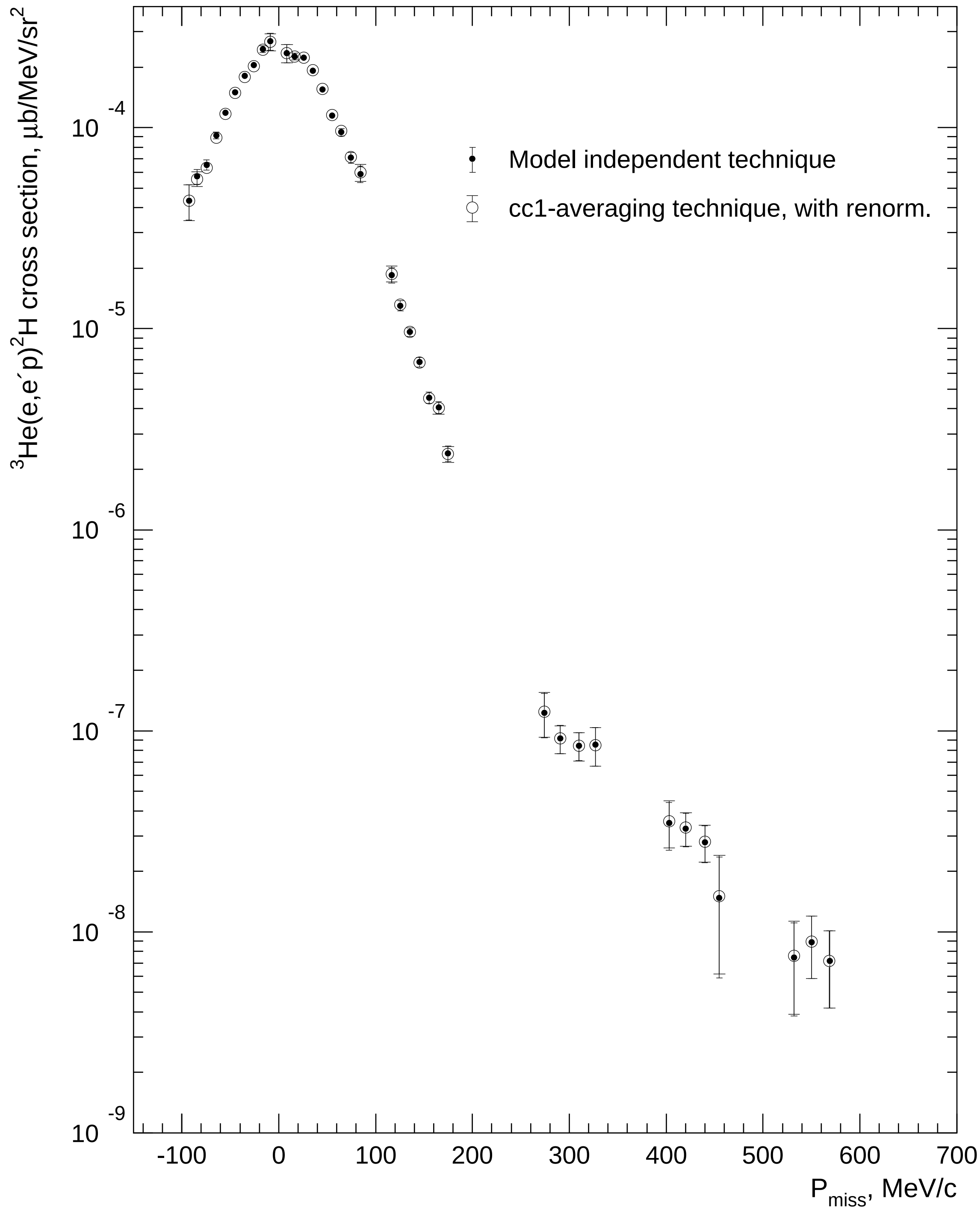

Figure 6-15: ^{3}He(e,e$'$p)D cross sections extracted with the "model independent" technique, and with the "cc1-averaging" technique with "cc1-renormalization" to fixed values of Q^2 and ω, at beam energy 1.2 GeV. Negative P_{miss} correspond to the detected proton forward of $\vec{q}$ and perpendicular kinematics.

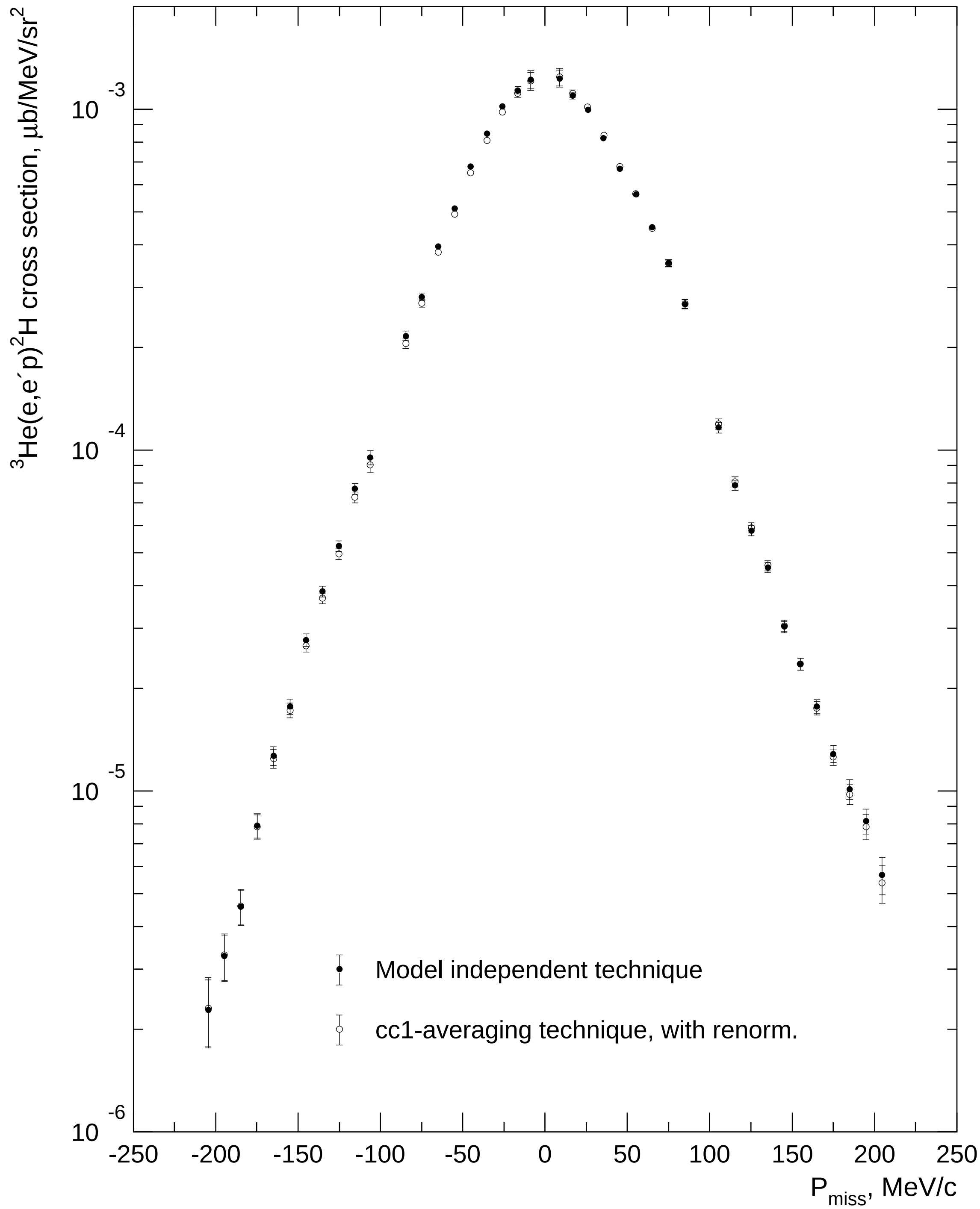

Figure 6-16: ^{3}He(e,e$'$p)D cross sections extracted with the "model independent" technique, and with the "cc1-averaging" technique with "cc1-renormalization" to fixed values of Q^2 and ω, at beam energy 1.9 GeV. Negative P_{miss} correspond to the detected proton forward of $\vec{q}$ and perpendicular kinematics.

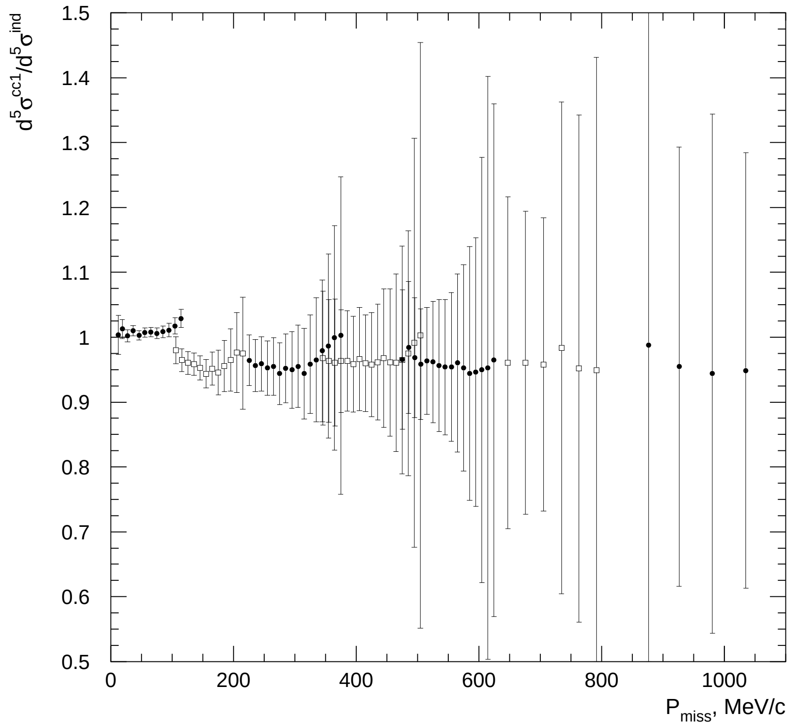

Figure 6-17: Ratio of ^{3}He(e,e$'$p)D cross sections extracted with the cc1-averaging technique without renormalization to fixed values of Q^2 and ω, to those extracted with the model-independent technique; Σ_1 kinematics; shown are statistical errors.

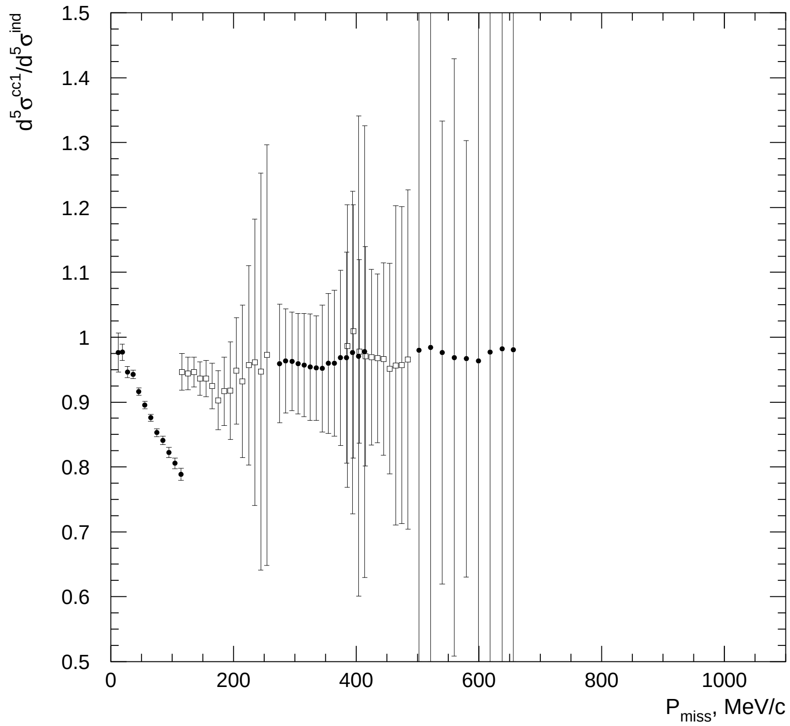

Figure 6-18: Ratio of ^{3}He(e,e′p)D cross sections extracted with the cc1-averaging technique without renormalization to fixed values of Q^2 and ω, to those extracted with the model-independent technique; Σ_2 kinematics; shown are statistical errors.

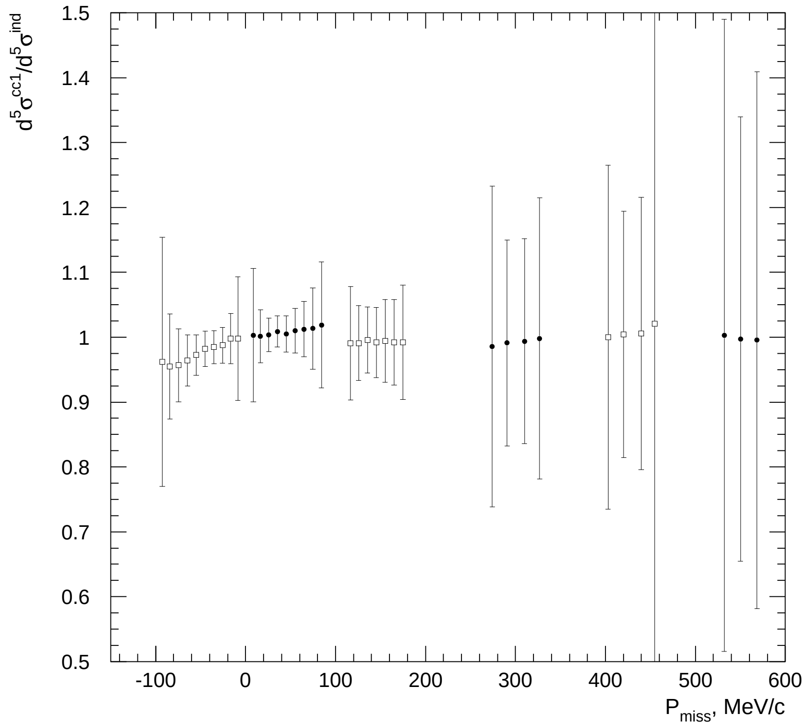

Figure 6-19: Ratio of ^{3}He(e,e$'$p)D cross sections extracted with the cc1-averaging technique without renormalization to fixed values of Q^2 and ω, to those extracted with the model-independent technique; Σ_3 kinematics; shown are statistical errors.

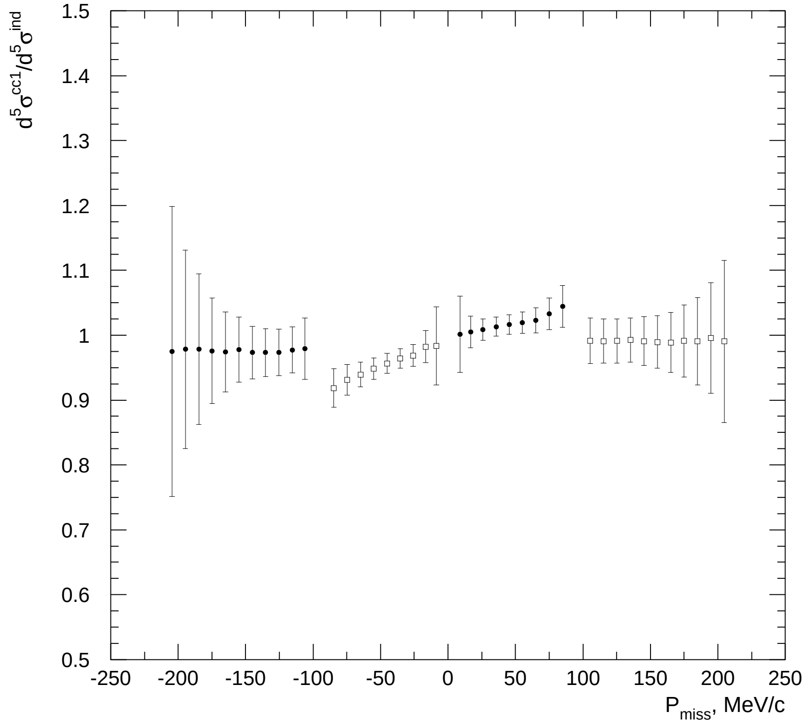

Figure 6-20: Ratio of ^{3}He(e,e$'$p)D cross sections extracted with the cc1-averaging technique without renormalization to fixed values of Q^2 and ω, to those extracted with the model-independent technique; Σ_4 and Σ_5 kinematics; shown are statistical errors.

P_{miss} MeV/c	$\frac{d^5\sigma^{ren}}{dE_f d\Omega_e d\Omega_p} \pm \epsilon_{st}$ μb MeV^{-1}sr^{-2}	$S_{2bbu}(P_{miss})$ fm^3	$\frac{d^5\sigma^{cc1}}{dE_f d\Omega_e d\Omega_p}$ μb MeV^{-1}sr^{-2}	$\frac{d^5\sigma^{ind}}{dE_f d\Omega_e d\Omega_p} \pm \epsilon_{st}$ μb MeV^{-1}sr^{-2}	$\bar{Q}^2 \pm \sigma_{Q^2}$ (GeV/c)^2	$\bar{\omega} \pm \sigma_\omega$ MeV
12.5	1.370e-02±3.0%	4.435e+00	1.362e-02	1.358e-02±3.0%	1.5262±0.0529	824.4±26.0
18.7	1.249e-02±1.5%	4.003e+00	1.226e-02	1.211e-02±1.3%	1.5309±0.0587	828.0±24.9
27.3	1.112e-02±0.9%	3.512e+00	1.081e-02	1.078e-02±0.9%	1.5340±0.0712	832.1±24.2
36.5	9.476e-03±0.8%	2.946e+00	9.262e-03	9.167e-03±0.7%	1.5301±0.0859	834.9±23.8
46.0	7.741e-03±0.7%	2.369e+00	7.758e-03	7.736e-03±0.7%	1.5176±0.0979	836.3±23.2
55.7	6.171e-03±0.7%	1.858e+00	6.373e-03	6.328e-03±0.7%	1.5030±0.1060	837.3±22.2
65.5	4.783e-03±0.7%	1.417e+00	5.083e-03	5.044e-03±0.7%	1.4888±0.1090	838.8±21.3
75.3	3.563e-03±0.8%	1.038e+00	3.894e-03	3.871e-03±0.8%	1.4750±0.1073	840.5±20.7
85.2	2.721e-03±0.9%	7.803e-01	3.032e-03	3.006e-03±0.8%	1.4657±0.1073	842.0±20.5
95.1	2.020e-03±1.0%	5.700e-01	2.271e-03	2.245e-03±1.0%	1.4612±0.1082	843.8±20.5
104.9	1.443e-03±1.2%	4.007e-01	1.633e-03	1.605e-03±1.1%	1.4578±0.1094	845.3±20.6
114.8	1.111e-03±1.4%	3.040e-01	1.257e-03	1.221e-03±1.3%	1.4587±0.1110	846.4±20.8

Table 6.1: ^{3}He(e,e$'$p)D cross sections and distorted spectral function extracted at kinematics 1; the detected proton is back of $\vec{q}$; incident electron energy 4805.5 MeV.

P_{miss} MeV/c	$\frac{d^5\sigma^{ren}}{dE_f d\Omega_e d\Omega_p} \pm \epsilon_{st}$ μb MeV^{-1}sr^{-2}	$S_{2bbu}(P_{miss})$ fm^3	$\frac{d^5\sigma^{cc1}}{dE_f d\Omega_e d\Omega_p}$ μb MeV^{-1}sr^{-2}	$\frac{d^5\sigma^{ind}}{dE_f d\Omega_e d\Omega_p} \pm \epsilon_{st}$ μb MeV^{-1}sr^{-2}	$\bar{Q}^2 \pm \sigma_{Q^2}$ (GeV/c)^2	$\bar{\omega} \pm \sigma_\omega$ MeV
106.0	1.365e-03±2.1%	3.786e-01	1.272e-03	1.298e-03±2.1%	1.5623±0.0960	792.5±14.3
115.8	1.012e-03±1.8%	2.762e-01	9.030e-04	9.360e-04±1.8%	1.5796±0.1089	798.6±17.3
125.7	7.047e-04±1.8%	1.894e-01	6.082e-04	6.333e-04±1.8%	1.5930±0.1174	804.3±20.4
135.6	5.307e-04±1.8%	1.404e-01	4.578e-04	4.776e-04±1.8%	1.5923±0.1218	809.7±22.9
145.4	3.775e-04±2.0%	9.844e-02	3.256e-04	3.418e-04±1.9%	1.5909±0.1258	816.9±23.8
155.4	2.699e-04±2.3%	6.927e-02	2.367e-04	2.509e-04±2.2%	1.5815±0.1311	824.7±22.9
165.3	1.917e-04±2.7%	4.848e-02	1.746e-04	1.834e-04±2.7%	1.5625±0.1327	834.0±20.4
175.3	1.335e-04±3.7%	3.326e-02	1.287e-04	1.361e-04±3.5%	1.5346±0.1293	841.7±18.7
185.1	1.025e-04±4.1%	2.517e-02	1.073e-04	1.123e-04±4.0%	1.4960±0.1182	846.9±17.8
195.2	8.246e-05±5.0%	1.995e-02	9.509e-05	9.854e-05±4.9%	1.4523±0.0945	850.7±16.6
205.2	6.219e-05±6.3%	1.484e-02	7.697e-05	7.884e-05±6.2%	1.4199±0.0731	854.9±14.8
215.1	4.568e-05±8.9%	1.075e-02	5.962e-05	6.114e-05±8.6%	1.3956±0.0587	859.2±13.4

Table 6.2: ^{3}He(e,e$'$p)D cross sections and distorted spectral function extracted at kinematics 4; the detected proton is back of $\vec{q}$; incident electron energy 4805.5 MeV.

P_{miss} MeV/c	$\frac{d^5\sigma^{ren}}{dE_f d\Omega_e d\Omega_p} \pm \epsilon_{st}$ μb MeV^{-1}sr^{-2}	$S_{2bbu}(P_{miss})$ fm^3	$\frac{d^5\sigma^{cc1}}{dE_f d\Omega_e d\Omega_p}$ μb MeV^{-1}sr^{-2}	$\frac{d^5\sigma^{ind}}{dE_f d\Omega_e d\Omega_p} \pm \epsilon_{st}$ μb MeV^{-1}sr^{-2}	$\bar{Q}^2 \pm \sigma_{Q^2}$ (GeV/c)^2	$\bar{\omega} \pm \sigma_\omega$ MeV
225.6	3.122e-05±4.1%	7.237e-03	2.758e-05	2.860e-05±4.0%	1.5885±0.1075	767.8±10.1
235.5	1.958e-05±4.2%	4.478e-03	1.712e-05	1.791e-05±4.2%	1.5918±0.1136	773.8±12.7
245.4	1.371e-05±4.4%	3.094e-03	1.193e-05	1.244e-05±4.4%	1.5929±0.1166	780.0±15.1
255.4	1.032e-05±4.4%	2.296e-03	8.995e-06	9.444e-06±4.4%	1.5909±0.1185	785.5±17.6
265.3	7.827e-06±4.6%	1.720e-03	6.821e-06	7.143e-06±4.6%	1.5902±0.1204	791.3±19.8
275.2	6.082e-06±5.0%	1.320e-03	5.321e-06	5.637e-06±5.0%	1.5871±0.1239	798.4±21.1
285.2	4.648e-06±5.6%	9.952e-04	4.093e-06	4.300e-06±5.6%	1.5824±0.1272	807.3±20.9
295.1	3.795e-06±6.2%	8.030e-04	3.395e-06	3.575e-06±6.2%	1.5737±0.1289	816.4±19.5
305.1	3.514e-06±6.6%	7.344e-04	3.215e-06	3.365e-06±6.6%	1.5622±0.1311	824.8±18.0
315.1	3.202e-06±7.4%	6.613e-04	3.042e-06	3.223e-06±7.3%	1.5441±0.1319	832.2±16.2
324.9	3.246e-06±7.9%	6.626e-04	3.243e-06	3.385e-06±7.9%	1.5208±0.1298	839.1±14.8
334.9	2.603e-06±9.9%	5.253e-04	2.799e-06	2.900e-06±9.9%	1.4883±0.1219	845.0±13.8
344.8	2.692e-06±11.1%	5.370e-04	3.162e-06	3.230e-06±11.2%	1.4497±0.1041	850.3±12.6
354.7	2.262e-06±14.4%	4.465e-04	2.896e-06	2.936e-06±14.4%	1.4132±0.0803	854.7±11.4
364.7	2.420e-06±17.3%	4.724e-04	3.301e-06	3.303e-06±17.3%	1.3863±0.0604	859.4±10.0
374.6	2.155e-06±24.4%	4.162e-04	3.056e-06	3.048e-06±24.4%	1.3695±0.0478	864.6±8.6
384.5	4.679e-07±95.8%	8.948e-05	6.948e-07	6.548e-07±100.6%	1.3502±0.0374	869.5±7.2
394.5	6.616e-07±140.7%	1.253e-04	1.012e-06	6.934e-07±212.0%	1.3376±0.0294	874.8±6.2

Table 6.3: ^{3}He(e,e$'$p)D cross sections and distorted spectral function extracted at kinematics 7; the detected proton is back of $\vec{q}$; incident electron energy 4805.5 MeV.

P_{miss} MeV/c	$\frac{d^5\sigma^{ren}}{dE_f d\Omega_e d\Omega_p} \pm \epsilon_{st}$ μb MeV^{-1}sr^{-2}	$S_{2bbu}(P_{miss})$ fm^3	$\frac{d^5\sigma^{cc1}}{dE_f d\Omega_e d\Omega_p}$ μb MeV^{-1}sr^{-2}	$\frac{d^5\sigma^{ind}}{dE_f d\Omega_e d\Omega_p} \pm \epsilon_{st}$ μb MeV^{-1}sr^{-2}	$\bar{Q}^2 \pm \sigma_{Q^2}$ (GeV/c)^2	$\bar{\omega} \pm \sigma_\omega$ MeV
345.6	2.071e-06±10.6%	4.128e-04	1.823e-06	1.884e-06±10.6%	1.5881±0.1117	763.6±9.9
355.4	1.824e-06±9.8%	3.597e-04	1.596e-06	1.657e-06±9.8%	1.5897±0.1154	769.4±12.0
365.3	1.409e-06±10.2%	2.749e-04	1.237e-06	1.288e-06±10.1%	1.5872±0.1169	775.5±14.0
375.2	1.662e-06±8.2%	3.209e-04	1.459e-06	1.514e-06±8.2%	1.5864±0.1192	781.4±16.1
385.2	1.511e-06±8.0%	2.886e-04	1.333e-06	1.384e-06±8.1%	1.5834±0.1219	787.4±18.0
395.2	1.473e-06±7.7%	2.786e-04	1.289e-06	1.345e-06±7.7%	1.5856±0.1240	794.3±19.3
405.2	1.284e-06±8.2%	2.406e-04	1.128e-06	1.167e-06±8.3%	1.5827±0.1277	803.0±19.4
415.2	1.386e-06±7.8%	2.571e-04	1.225e-06	1.276e-06±7.8%	1.5781±0.1292	812.4±18.9
425.0	1.238e-06±8.4%	2.276e-04	1.112e-06	1.161e-06±8.4%	1.5702±0.1323	820.6±17.9
435.0	1.076e-06±9.3%	1.960e-04	9.817e-07	1.021e-06±9.4%	1.5619±0.1341	829.0±16.5
444.9	8.978e-07±11.0%	1.621e-04	8.437e-07	8.716e-07±11.2%	1.5481±0.1355	836.6±14.9
454.9	8.276e-07±11.8%	1.481e-04	8.062e-07	8.390e-07±11.9%	1.5316±0.1380	843.7±13.5
464.8	7.908e-07±14.2%	1.403e-04	8.156e-07	8.488e-07±14.3%	1.5067±0.1331	850.1±12.2
474.7	5.975e-07±18.2%	1.052e-04	6.574e-07	6.813e-07±18.2%	1.4789±0.1261	856.2±11.2
484.7	8.073e-07±19.4%	1.410e-04	9.718e-07	9.962e-07±19.4%	1.4414±0.1125	861.3±10.2
494.7	5.108e-07±31.8%	8.858e-05	6.650e-07	6.708e-07±31.7%	1.4092±0.0915	866.4±8.9
504.5	5.009e-07±45.0%	8.623e-05	6.970e-07	6.949e-07±45.0%	1.3820±0.0638	871.7±7.7

Table 6.4: ^{3}He(e,e$'$p)D cross sections and distorted spectral function extracted at kinematics 10; the detected proton is back of $\vec{q}$; incident electron energy 4805.5 MeV.

P_{miss} MeV/c	$\frac{d^5\sigma^{ren}}{dE_f d\Omega_e d\Omega_p} \pm \epsilon_{st}$ μb MeV^{-1}sr^{-2}	$S_{2bbu}(P_{miss})$ fm^3	$\frac{d^5\sigma^{cc1}}{dE_f d\Omega_e d\Omega_p}$ μb MeV^{-1}sr^{-2}	$\frac{d^5\sigma^{ind}}{dE_f d\Omega_e d\Omega_p} \pm \epsilon_{st}$ μb MeV^{-1}sr^{-2}	$\bar{Q}^2 \pm \sigma_{Q^2}$ (GeV/c)^2	$\bar{\omega} \pm \sigma_\omega$ MeV
475.2	6.572e-07±11.1%	1.157e-04	5.784e-07	5.988e-07±11.1%	1.5846±0.1151	765.0±11.3
485.3	6.539e-07±10.3%	1.142e-04	5.794e-07	5.888e-07±10.6%	1.5809±0.1169	771.2±13.2
495.1	6.021e-07±9.5%	1.043e-04	5.284e-07	5.456e-07±9.6%	1.5842±0.1196	777.0±14.9
505.1	5.867e-07±8.9%	1.010e-04	5.178e-07	5.402e-07±8.9%	1.5811±0.1223	783.5±16.4
515.1	5.799e-07±8.6%	9.913e-05	5.067e-07	5.259e-07±8.6%	1.5845±0.1234	790.0±17.9
525.1	4.222e-07±9.7%	7.163e-05	3.693e-07	3.839e-07±9.8%	1.5830±0.1265	798.5±18.2
535.0	3.348e-07±10.6%	5.644e-05	2.943e-07	3.077e-07±10.6%	1.5798±0.1292	807.4±18.3
545.0	3.301e-07±11.0%	5.531e-05	2.913e-07	3.055e-07±11.0%	1.5773±0.1320	815.8±17.8
555.0	2.752e-07±12.0%	4.582e-05	2.459e-07	2.577e-07±12.1%	1.5709±0.1348	824.8±16.8
564.9	2.321e-07±14.3%	3.842e-05	2.105e-07	2.192e-07±14.5%	1.5638±0.1367	832.9±15.5
574.8	1.866e-07±16.7%	3.072e-05	1.714e-07	1.799e-07±16.8%	1.5575±0.1403	840.5±14.0
584.7	1.470e-07±20.7%	2.409e-05	1.387e-07	1.468e-07±20.7%	1.5460±0.1424	847.9±12.5
594.8	1.531e-07±21.9%	2.495e-05	1.502e-07	1.586e-07±21.9%	1.5288±0.1432	855.1±11.2
604.6	1.143e-07±34.5%	1.854e-05	1.166e-07	1.228e-07±34.6%	1.5117±0.1447	861.1±10.6
614.5	9.923e-08±47.2%	1.602e-05	1.063e-07	1.116e-07±47.2%	1.4911±0.1422	867.3±8.9
624.3	1.835e-07±41.0%	2.952e-05	2.107e-07	2.184e-07±40.8%	1.4630±0.1318	872.9±8.1
634.4	6.279e-08±100.0%	1.006e-05	7.825e-08	8.037e-08±100.0%	1.4298±0.1219	879.0±7.1

Table 6.5: ^{3}He(e,e$'$p)D cross sections and distorted spectral function extracted at kinematics 13; the detected proton is back of $\vec{q}$; incident electron energy 4805.5 MeV.

P_{miss} MeV/c	$\frac{d^5\sigma^{ren}}{dE_f d\Omega_e d\Omega_p} \pm \epsilon_{st}$ μb MeV^{-1}sr^{-2}	$S_{2bbu}(P_{miss})$ fm^3	$\frac{d^5\sigma^{cc1}}{dE_f d\Omega_e d\Omega_p}$ μb MeV^{-1}sr^{-2}	$\frac{d^5\sigma^{ind}}{dE_f d\Omega_e d\Omega_p} \pm \epsilon_{st}$ μb MeV^{-1}sr^{-2}	$\bar{Q}^2 \pm \sigma_{Q^2}$ (GeV/c)^2	$\bar{\omega} \pm \sigma_\omega$ MeV
647.2	9.481e-08±26.6%	1.512e-05	8.663e-08	9.020e-08±26.6%	1.5635±0.1043	740.0±11.5
676.0	5.851e-08±24.3%	9.247e-06	5.157e-08	5.368e-08±24.3%	1.5774±0.1138	757.9±15.4
705.1	4.795e-08±23.6%	7.527e-06	4.149e-08	4.331e-08±23.6%	1.5844±0.1225	779.2±18.5
734.4	2.762e-08±38.5%	4.316e-06	2.389e-08	2.429e-08±39.7%	1.5842±0.1303	803.6±18.6
763.1	2.408e-08±41.1%	3.755e-06	2.059e-08	2.164e-08±41.1%	1.5889±0.1379	826.2±16.0
791.2	4.388e-08±50.8%	6.844e-06	3.656e-08	3.851e-08±50.8%	1.6000±0.1456	845.5±12.8
876.6	1.916e-08±100.0%	3.031e-06	2.057e-08	2.082e-08±100.0%	1.4857±0.0619	737.0±8.9
926.2	1.925e-08±35.5%	3.100e-06	1.828e-08	1.916e-08±35.5%	1.5369±0.1064	768.2±15.6
980.5	1.359e-08±42.4%	2.253e-06	1.216e-08	1.287e-08±42.4%	1.5673±0.1281	808.2±20.7
1035.0	1.645e-08±35.4%	2.834e-06	1.378e-08	1.453e-08±35.4%	1.6036±0.1346	851.5±18.9

Table 6.6: ^{3}He(e,e$'$p)D cross sections and distorted spectral function extracted at kinematics 28 (top) and 29 (bottom); the detected proton is back of $\vec{q}$; incident electron energy 4805.5 MeV.

P_{miss} MeV/c	$\frac{d^5\sigma^{ren}}{dE_f d\Omega_e d\Omega_p} \pm \epsilon_{st}$ μb MeV^{-1}sr^{-2}	$S_{2bbu}(P_{miss})$ fm^3	$\frac{d^5\sigma^{cc1}}{dE_f d\Omega_e d\Omega_p}$ μb MeV^{-1}sr^{-2}	$\frac{d^5\sigma^{ind}}{dE_f d\Omega_e d\Omega_p} \pm \epsilon_{st}$ μb MeV^{-1}sr^{-2}	$\bar{Q}^2 \pm \sigma_{Q^2}$ (GeV/c)^2	$\bar{\omega} \pm \sigma_\omega$ MeV
12.5	1.225e-02±3.1%	4.142e+00	1.247e-02	1.277e-02±3.1%	1.5175±0.0531	819.2±26.9
18.7	1.134e-02±1.3%	3.874e+00	1.162e-02	1.190e-02±1.2%	1.5148±0.0585	817.7±25.9
27.1	9.748e-03±0.9%	3.380e+00	1.007e-02	1.064e-02±0.8%	1.5124±0.0694	815.3±24.8
36.4	8.288e-03±0.7%	2.921e+00	8.539e-03	9.057e-03±0.6%	1.5141±0.0821	813.7±24.0
45.8	6.579e-03±0.6%	2.356e+00	6.665e-03	7.273e-03±0.6%	1.5225±0.0952	812.6±23.8
55.5	5.071e-03±0.6%	1.847e+00	4.926e-03	5.501e-03±0.6%	1.5428±0.1045	812.9±24.4
65.2	3.839e-03±0.7%	1.422e+00	3.545e-03	4.048e-03±0.6%	1.5683±0.1089	813.6±24.7
75.0	2.770e-03±0.7%	1.044e+00	2.464e-03	2.889e-03±0.7%	1.5878±0.1114	813.6±24.4
84.9	2.024e-03±0.8%	7.759e-01	1.754e-03	2.086e-03±0.7%	1.6018±0.1123	812.9±23.9
94.7	1.429e-03±0.9%	5.575e-01	1.216e-03	1.478e-03±0.9%	1.6126±0.1133	812.2±23.4
104.6	1.041e-03±1.0%	4.133e-01	8.721e-04	1.083e-03±1.0%	1.6212±0.1146	811.5±23.2
114.5	7.416e-04±1.2%	2.995e-01	6.139e-04	7.785e-04±1.1%	1.6276±0.1159	811.0±23.3

Table 6.7: ^{3}He(e,e$'$p)D cross sections and distorted spectral function extracted at kinematics 1; the detected proton is forward of $\vec{q}$; incident electron energy 4805.5 MeV.

P_{miss} MeV/c	$\frac{d^5\sigma^{ren}}{dE_f d\Omega_e d\Omega_p} \pm \epsilon_{st}$ μb MeV^{-1}sr^{-2}	$S_{2bbu}(P_{miss})$ fm^3	$\frac{d^5\sigma^{cc1}}{dE_f d\Omega_e d\Omega_p}$ μb MeV^{-1}sr^{-2}	$\frac{d^5\sigma^{ind}}{dE_f d\Omega_e d\Omega_p} \pm \epsilon_{st}$ μb MeV^{-1}sr^{-2}	$\bar{Q}^2 \pm \sigma_{Q^2}$ (GeV/c)^2	$\bar{\omega} \pm \sigma_\omega$ MeV
116.0	7.046e-04±3.0%	2.852e-01	8.738e-04	9.231e-04±2.7%	1.4248±0.0706	844.2±17.2
125.8	5.309e-04±2.6%	2.186e-01	6.269e-04	6.641e-04±2.4%	1.4451±0.0801	839.1±20.8
135.5	3.778e-04±2.4%	1.582e-01	4.310e-04	4.555e-04±2.3%	1.4606±0.0895	834.4±23.5
145.3	2.499e-04±2.8%	1.064e-01	2.695e-04	2.878e-04±2.6%	1.4868±0.0977	829.2±24.4
155.2	1.768e-04±3.0%	7.661e-02	1.801e-04	1.923e-04±2.9%	1.5150±0.1043	824.8±24.9
165.2	1.137e-04±3.8%	5.008e-02	1.097e-04	1.186e-04±3.7%	1.5423±0.1101	821.3±25.2
175.0	7.367e-05±5.0%	3.301e-02	6.768e-05	7.499e-05±4.7%	1.5680±0.1125	818.5±25.0
184.9	5.490e-05±5.7%	2.502e-02	4.824e-05	5.262e-05±5.5%	1.5924±0.1120	815.7±24.6
194.9	3.469e-05±8.2%	1.608e-02	2.911e-05	3.173e-05±7.9%	1.6181±0.1053	813.0±23.4
204.7	2.857e-05±8.6%	1.346e-02	2.289e-05	2.414e-05±8.6%	1.6447±0.0949	810.8±21.9
214.7	1.753e-05±12.6%	8.399e-03	1.345e-05	1.445e-05±12.2%	1.6703±0.0829	808.6±19.9
224.7	1.314e-05±16.1%	6.400e-03	9.789e-06	1.023e-05±15.9%	1.6895±0.0726	805.6±17.7
234.6	8.784e-06±23.0%	4.349e-03	6.348e-06	6.603e-06±22.8%	1.7087±0.0621	803.5±15.5
244.5	7.972e-06±32.3%	4.010e-03	5.634e-06	5.950e-06±31.3%	1.7235±0.0526	801.2±13.5
254.4	7.718e-06±33.3%	3.946e-03	5.322e-06	5.474e-06±33.3%	1.7394±0.0433	799.6±11.7

Table 6.8: ^{3}He(e,e$'$p)D cross sections and distorted spectral function extracted at kinematics 5; the detected proton is forward of $\vec{q}$; incident electron energy 4805.5 MeV.

P_{miss} MeV/c	$\frac{d^5\sigma^{ren}}{dE_f d\Omega_e d\Omega_p} \pm \epsilon_{st}$ μb MeV^{-1}sr^{-2}	$S_{2bbu}(P_{miss})$ fm^3	$\frac{d^5\sigma^{cc1}}{dE_f d\Omega_e d\Omega_p}$ μb MeV^{-1}sr^{-2}	$\frac{d^5\sigma^{ind}}{dE_f d\Omega_e d\Omega_p} \pm \epsilon_{st}$ μb MeV^{-1}sr^{-2}	$\bar{Q}^2 \pm \sigma_{Q^2}$ (GeV/c)^2	$\bar{\omega} \pm \sigma_\omega$ MeV
275.3	5.168e-06±9.5%	2.732e-03	6.415e-06	6.686e-06±9.4%	1.4219±0.0579	826.6±19.5
285.2	5.006e-06±8.3%	2.687e-03	5.928e-06	6.152e-06±8.3%	1.4444±0.0667	822.3±21.6
295.1	4.474e-06±7.9%	2.439e-03	5.044e-06	5.238e-06±7.9%	1.4685±0.0757	818.4±23.5
305.0	4.041e-06±8.1%	2.236e-03	4.319e-06	4.503e-06±8.0%	1.4949±0.0844	815.7±24.4
314.8	3.474e-06±8.3%	1.951e-03	3.508e-06	3.666e-06±8.3%	1.5234±0.0935	813.7±25.0
324.8	3.311e-06±8.6%	1.888e-03	3.149e-06	3.301e-06±8.6%	1.5541±0.1004	812.4±25.4
334.7	3.473e-06±8.5%	2.010e-03	3.125e-06	3.281e-06±8.4%	1.5831±0.1039	811.4±25.5
344.6	2.716e-06±10.3%	1.594e-03	2.309e-06	2.426e-06±10.2%	1.6135±0.1018	810.6±25.0
354.5	2.555e-06±11.2%	1.521e-03	2.065e-06	2.152e-06±11.2%	1.6414±0.0955	809.5±23.9
364.4	2.977e-06±11.7%	1.798e-03	2.303e-06	2.400e-06±11.6%	1.6665±0.0865	807.5±22.4
374.4	2.559e-06±14.0%	1.568e-03	1.905e-06	1.968e-06±13.9%	1.6892±0.0762	805.9±20.7
384.3	2.262e-06±16.8%	1.404e-03	1.632e-06	1.685e-06±16.7%	1.7081±0.0670	804.1±18.7
394.1	1.434e-06±25.5%	9.023e-04	1.008e-06	1.033e-06±25.5%	1.7240±0.0579	802.4±16.4
403.9	1.067e-06±38.1%	6.803e-04	7.312e-07	7.532e-07±37.9%	1.7400±0.0491	801.1±14.3
413.9	1.835e-06±35.6%	1.185e-03	1.230e-06	1.259e-06±35.6%	1.7535±0.0418	799.6±12.3

Table 6.9: ^{3}He(e,e$'$p)D cross sections and distorted spectral function extracted at kinematics 8; the detected proton is forward of $\vec{q}$; incident electron energy 4805.5 MeV.

P_{miss}	$\frac{d^5\sigma^{ren}}{dE_f d\Omega_e d\Omega_p} \pm \epsilon_{st}$	$S_{2bbu}(P_{miss})$	$\frac{d^5\sigma^{cc1}}{dE_f d\Omega_e d\Omega_p}$	$\frac{d^5\sigma^{ind}}{dE_f d\Omega_e d\Omega_p} \pm \epsilon_{st}$	$\bar{Q}^2 \pm \sigma_{Q^2}$	$\bar{\omega} \pm \sigma_\omega$
MeV/c	μb MeV^{-1}sr^{-2}	fm^3	μb MeV^{-1}sr^{-2}	μb MeV^{-1}sr^{-2}	(GeV/c)^2	MeV
385.3	1.691e-06±22.1%	1.052e-03	2.232e-06	2.263e-06±22.1%	1.3925±0.0385	827.0±16.1
395.1	1.516e-06±19.3%	9.554e-04	1.924e-06	1.906e-06±19.9%	1.4113±0.0479	823.4±19.3
405.0	1.815e-06±14.5%	1.158e-03	2.202e-06	2.251e-06±14.5%	1.4328±0.0572	819.8±21.5
414.8	1.196e-06±17.4%	7.732e-04	1.384e-06	1.426e-06±17.3%	1.4558±0.0653	816.7±23.1
424.7	1.493e-06±14.0%	9.777e-04	1.636e-06	1.689e-06±14.0%	1.4821±0.0740	815.1±24.0
434.6	1.502e-06±13.4%	9.962e-04	1.555e-06	1.607e-06±13.5%	1.5103±0.0838	814.1±24.5
444.5	1.238e-06±15.4%	8.316e-04	1.206e-06	1.248e-06±15.5%	1.5410±0.0922	813.7±25.3
454.5	1.103e-06±17.0%	7.506e-04	1.009e-06	1.060e-06±16.9%	1.5734±0.0971	813.6±25.1
464.4	6.719e-07±25.7%	4.625e-04	5.733e-07	5.993e-07±25.7%	1.6089±0.0980	814.9±25.1
474.3	6.938e-07±25.6%	4.833e-04	5.578e-07	5.828e-07±25.5%	1.6409±0.0921	814.6±24.6
484.2	7.091e-07±27.1%	4.998e-04	5.422e-07	5.615e-07±27.1%	1.6685±0.0840	814.4±23.5
494.1	2.556e-07±67.0%	1.822e-04	1.878e-07	1.969e-06±69.3%	1.6909±0.0767	813.2±21.8

Table 6.10: ^{3}He(e,e$'$p)D cross sections and distorted spectral function extracted at kinematics 11; the detected proton is forward of $\vec{q}$; incident electron energy 4805.5 MeV.

P_{miss} MeV/c	$\frac{d^5\sigma^{ren}}{dE_f d\Omega_e d\Omega_p} \pm \epsilon_{st}$ μb MeV^{-1}sr^{-2}	$S_{2bbu}(P_{miss})$ fm^3	$\frac{d^5\sigma^{cc1}}{dE_f d\Omega_e d\Omega_p}$ μb MeV^{-1}sr^{-2}	$\frac{d^5\sigma^{ind}}{dE_f d\Omega_e d\Omega_p} \pm \epsilon_{st}$ μb MeV^{-1}sr^{-2}	$\bar{Q}^2 \pm \sigma_{Q^2}$ (GeV/c)^2	$\bar{\omega} \pm \sigma_\omega$ MeV
502.4	3.103e-07±58.7%	2.233e-04	4.196e-07	4.282e-07±58.2%	1.3819±0.0319	824.5±15.1
521.0	2.110e-07±54.1%	1.551e-04	2.651e-07	2.693e-07±54.2%	1.4172±0.0473	817.6±20.7
540.0	2.593e-07±36.6%	1.946e-04	2.966e-07	3.039e-07±36.6%	1.4621±0.0633	813.8±23.4
559.6	1.875e-07±47.5%	1.437e-04	1.914e-07	1.975e-07±47.4%	1.5173±0.0800	813.3±24.5
579.2	2.642e-07±34.8%	2.065e-04	2.335e-07	2.415e-07±34.8%	1.5886±0.0893	816.5±24.9
598.9	1.367e-07±69.3%	1.090e-04	1.056e-07	1.097e-07±68.7%	1.6584±0.0827	819.2±24.0
618.4	1.874e-07±58.1%	1.522e-04	1.323e-07	1.354e-07±58.1%	1.7076±0.0664	819.1±21.8
637.6	3.022e-07±53.2%	2.500e-04	2.009e-07	2.046e-07±53.2%	1.7410±0.0498	817.2±17.7
656.2	3.341e-07±89.0%	2.813e-04	2.112e-07	2.155e-07±88.7%	1.7692±0.0357	816.0±13.3

Table 6.11: ^{3}He(e,e$'$p)D cross sections and distorted spectral function extracted at kinematics 14; the detected proton is forward of $\vec{q}$; incident electron energy 4805.5 MeV.

P_{miss} MeV/c	$\frac{d^5\sigma^{ren}}{dE_f d\Omega_e d\Omega_p} \pm \epsilon_{st}$ μb MeV^{-1}sr^{-2}	$S_{2bbu}(P_{miss})$ fm^3	$\frac{d^5\sigma^{cc1}}{dE_f d\Omega_e d\Omega_p}$ μb MeV^{-1}sr^{-2}	$\frac{d^5\sigma^{ind}}{dE_f d\Omega_e d\Omega_p} \pm \epsilon_{st}$ μb MeV^{-1}sr^{-2}	$\bar{Q}^2 \pm \sigma_{Q^2}$ (GeV/c)^2	$\bar{\omega} \pm \sigma_{\omega}$ MeV
8.5	2.305e-04±10.3%	3.659e+00	2.312e-04	2.305e-04±10.3%	1.5485±0.0097	836.6±3.3
16.5	2.219e-04±4.1%	3.509e+00	2.226e-04	2.224e-04±4.0%	1.5480±0.0194	836.8±5.4
25.8	2.188e-04±2.6%	3.443e+00	2.197e-04	2.189e-04±2.6%	1.5477±0.0289	836.8±7.6
35.3	1.899e-04±2.4%	2.973e+00	1.902e-04	1.885e-04±2.3%	1.5490±0.0362	836.7±9.2
45.0	1.532e-04±2.8%	2.387e+00	1.533e-04	1.526e-04±2.7%	1.5497±0.0381	836.6±9.7
55.0	1.139e-04±3.4%	1.763e+00	1.140e-04	1.128e-04±3.4%	1.5495±0.0370	836.6±9.5
64.8	9.446e-05±4.2%	1.455e+00	9.454e-05	9.338e-05±4.2%	1.5498±0.0376	836.5±9.6
74.7	7.047e-05±6.2%	1.080e+00	7.054e-05	6.962e-05±6.1%	1.5494±0.0379	836.7±9.7
84.3	5.886e-05±9.5%	8.968e-01	5.886e-05	5.778e-05±9.5%	1.5503±0.0385	836.5±9.8
92.6	2.498e-05±37.5%	3.787e-01	2.474e-05	2.562e-05±33.6%	1.5577±0.0454	835.0±11.7

Table 6.12: ^{3}He(e,e$'$p)D cross sections and distorted spectral function extracted at kinematics 3; the detected proton is back of $\vec{q}$; incident electron energy 1253.8 MeV.

P_{miss} MeV/c	$\frac{d^5\sigma^{ren}}{dE_f d\Omega_e d\Omega_p} \pm \epsilon_{st}$ μb MeV^{-1}sr^{-2}	$S_{2bbu}(P_{miss})$ fm^3	$\frac{d^5\sigma^{cc1}}{dE_f d\Omega_e d\Omega_p}$ μb MeV^{-1}sr^{-2}	$\frac{d^5\sigma^{ind}}{dE_f d\Omega_e d\Omega_p} \pm \epsilon_{st}$ μb MeV^{-1}sr^{-2}	$\bar{Q}^2 \pm \sigma_{Q^2}$ (GeV/c)^2	$\bar{\omega} \pm \sigma_\omega$ MeV
116.7	1.847e-05±8.8%	2.760e-01	1.796e-05	1.812e-05±8.8%	1.5851±0.0233	824.6±5.2
125.7	1.293e-05±5.8%	1.924e-01	1.269e-05	1.280e-05±5.8%	1.5728±0.0304	829.1±6.9
135.4	9.483e-06±5.1%	1.402e-01	9.424e-06	9.467e-06±5.1%	1.5592±0.0352	833.2±8.6
145.2	6.662e-06±5.4%	9.794e-02	6.655e-06	6.709e-06±5.4%	1.5532±0.0361	835.1±9.2
155.1	4.441e-06±6.4%	6.492e-02	4.435e-06	4.462e-06±6.4%	1.5534±0.0359	835.1±9.3
165.1	3.959e-06±6.6%	5.752e-02	3.954e-06	3.986e-06±6.6%	1.5533±0.0361	835.1±9.3
174.9	2.337e-06±8.9%	3.374e-02	2.337e-06	2.355e-06±8.8%	1.5511±0.0364	836.0±9.1
274.2	1.221e-07±25.1%	1.663e-03	1.191e-07	1.208e-07±25.0%	1.5788±0.0292	826.9±6.7
290.7	8.993e-08±16.0%	1.214e-03	8.935e-08	9.016e-08±16.0%	1.5585±0.0351	833.5±8.8
310.0	8.280e-08±15.9%	1.104e-03	8.256e-08	8.308e-08±15.9%	1.5546±0.0357	834.8±9.2
326.8	8.355e-08±21.7%	1.104e-03	8.354e-08	8.370e-08±21.7%	1.5483±0.0350	837.7±8.8
403.0	3.487e-08±26.5%	4.435e-04	3.418e-08	3.418e-08±26.5%	1.5721±0.0325	828.9±7.6
420.3	3.239e-08±18.9%	4.088e-04	3.222e-08	3.208e-08±19.0%	1.5568±0.0353	834.1±9.0
439.8	2.768e-08±20.9%	3.464e-04	2.761e-08	2.745e-08±21.0%	1.5537±0.0360	835.1±9.2
454.9	1.483e-08±59.0%	1.845e-04	1.480e-08	1.450e-08±60.1%	1.5472±0.0331	839.0±8.3
532.0	7.463e-09±48.6%	9.038e-05	7.348e-09	7.328e-09±48.7%	1.5661±0.0341	830.9±8.2
550.1	8.785e-09±34.4%	1.058e-04	8.737e-09	8.763e-09±34.4%	1.5560±0.0354	834.4±9.1
568.6	7.032e-09±41.6%	8.438e-05	7.003e-09	7.033e-09±41.6%	1.5534±0.0359	835.7±9.2

Table 6.13: ^{3}He(e,e$'$p)D cross sections and distorted spectral function extracted at kinematics 6, 9, 12 and 15; the detected proton is back of $\vec{q}$; incident electron energy 1253.8 MeV.

P_{miss} MeV/c	$\frac{d^5\sigma^{ren}}{dE_f d\Omega_e d\Omega_p} \pm \epsilon_{st}$ μb MeV^{-1}sr^{-2}	$S_{2bbu}(P_{miss})$ fm^3	$\frac{d^5\sigma^{cc1}}{dE_f d\Omega_e d\Omega_p}$ μb MeV^{-1}sr^{-2}	$\frac{d^5\sigma^{ind}}{dE_f d\Omega_e d\Omega_p} \pm \epsilon_{st}$ μb MeV^{-1}sr^{-2}	$\bar{Q}^2 \pm \sigma_{Q^2}$ (GeV/c)^2	$\bar{\omega} \pm \sigma_\omega$ MeV
8.6	2.624e-04±9.6%	4.201e+00	2.632e-04	2.639e-04±9.6%	1.5487±0.0104	836.4±3.1
16.5	2.403e-04±3.9%	3.865e+00	2.411e-04	2.417e-04±3.9%	1.5484±0.0191	836.6±5.3
25.6	1.988e-04±2.8%	3.210e+00	1.995e-04	2.020e-04±2.8%	1.5493±0.0296	835.9±7.6
35.1	1.756e-04±2.6%	2.849e+00	1.750e-04	1.776e-04±2.6%	1.5582±0.0356	833.3±8.8
45.0	1.462e-04±2.8%	2.383e+00	1.445e-04	1.471e-04±2.8%	1.5658±0.0365	831.5±9.2
54.9	1.153e-04±3.2%	1.886e+00	1.138e-04	1.170e-04±3.2%	1.5665±0.0376	831.2±9.5
64.6	8.789e-05±4.1%	1.445e+00	8.669e-05	8.991e-05±4.1%	1.5673±0.0379	831.0±9.6
74.5	6.225e-05±5.9%	1.028e+00	6.139e-05	6.417e-05±5.8%	1.5674±0.0382	831.0±9.7
84.2	5.466e-05±8.5%	9.059e-01	5.371e-05	5.625e-05±8.5%	1.5711±0.0379	830.0±9.6
92.6	4.245e-05±20.0%	7.061e-01	4.099e-05	4.260e-05±20.0%	1.5897±0.0363	825.0±8.9

Table 6.14: ^{3}He(e,e$'$p)D cross sections and distorted spectral function extracted at kinematics 3; the detected proton is forward of $\vec{q}$; incident electron energy 1253.8 MeV.

P_{miss} MeV/c	$\frac{d^5\sigma^{ren}}{dE_f d\Omega_e d\Omega_p} \pm \epsilon_{st}$ μb MeV^{-1}sr^{-2}	$S_{2bbu}(P_{miss})$ fm^3	$\frac{d^5\sigma^{cc1}}{dE_f d\Omega_e d\Omega_p}$ μb MeV^{-1}sr^{-2}	$\frac{d^5\sigma^{ind}}{dE_f d\Omega_e d\Omega_p} \pm \epsilon_{st}$ μb MeV^{-1}sr^{-2}	$\bar{Q}^2 \pm \sigma_{Q^2}$ (GeV/c)^2	$\bar{\omega} \pm \sigma_\omega$ MeV
8.9	1.223e-03±5.9%	4.432e+00	1.214e-03	1.212e-03±5.9%	1.5528±0.0248	838.5±13.4
16.7	1.093e-03±2.4%	3.918e+00	1.085e-03	1.079e-03±2.4%	1.5523±0.0275	838.6±14.3
25.9	9.972e-04±1.6%	3.532e+00	9.864e-04	9.784e-04±1.6%	1.5520±0.0332	840.7±15.2
35.6	8.258e-04±1.5%	2.886e+00	8.178e-04	8.073e-04±1.4%	1.5485±0.0406	844.0±16.0
45.3	6.676e-04±1.5%	2.304e+00	6.691e-04	6.583e-04±1.5%	1.5385±0.0457	848.5±16.7
55.2	5.547e-04±1.6%	1.889e+00	5.645e-04	5.539e-04±1.6%	1.5269±0.0476	852.7±16.7
65.1	4.402e-04±1.9%	1.480e+00	4.537e-04	4.434e-04±1.9%	1.5182±0.0495	855.5±16.6
75.0	3.466e-04±2.3%	1.150e+00	3.600e-04	3.486e-04±2.3%	1.5138±0.0513	856.4±16.9
84.9	2.640e-04±3.1%	8.648e-01	2.748e-04	2.632e-04±3.1%	1.5135±0.0525	856.2±17.0

Table 6.15: ^{3}He(e,e$'$p)D cross sections and distorted spectral function extracted at kinematics 33; the detected proton is back of $\vec{q}$; incident electron energy 1953.0 MeV.

P_{miss} MeV/c	$\frac{d^5\sigma^{ren}}{dE_f d\Omega_e d\Omega_p} \pm \epsilon_{st}$ μb MeV^{-1}sr^{-2}	$S_{2bbu}(P_{miss})$ fm^3	$\frac{d^5\sigma^{cc1}}{dE_f d\Omega_e d\Omega_p}$ μb MeV^{-1}sr^{-2}	$\frac{d^5\sigma^{ind}}{dE_f d\Omega_e d\Omega_p} \pm \epsilon_{st}$ μb MeV^{-1}sr^{-2}	$\bar{Q}^2 \pm \sigma_{Q^2}$ (GeV/c)^2	$\bar{\omega} \pm \sigma_\omega$ MeV
105.4	1.174e-04±3.5%	3.746e-01	1.134e-04	1.145e-04±3.5%	1.5876±0.0383	806.3±10.1
115.3	7.935e-05±3.5%	2.498e-01	7.680e-05	7.749e-05±3.4%	1.5832±0.0403	811.9±12.3
125.2	5.826e-05±3.4%	1.811e-01	5.666e-05	5.718e-05±3.4%	1.5776±0.0421	816.8±14.5
135.2	4.510e-05±3.4%	1.384e-01	4.414e-05	4.447e-05±3.4%	1.5716±0.0442	821.4±16.6
145.2	3.003e-05±3.8%	9.103e-02	2.955e-05	2.982e-05±3.8%	1.5659±0.0463	825.9±18.4
155.1	2.319e-05±4.1%	6.940e-02	2.295e-05	2.320e-05±4.1%	1.5582±0.0481	832.5±18.9
165.1	1.722e-05±4.7%	5.090e-02	1.722e-05	1.742e-05±4.7%	1.5469±0.0487	841.0±17.8
175.0	1.236e-05±5.6%	3.608e-02	1.252e-05	1.263e-05±5.6%	1.5344±0.0483	849.2±15.7
185.0	9.619e-06±6.8%	2.774e-02	9.854e-06	9.942e-06±6.8%	1.5243±0.0478	855.4±12.8
194.8	7.738e-06±8.5%	2.205e-02	7.994e-06	8.028e-06±8.5%	1.5158±0.0461	860.9±9.8
204.7	5.276e-06±12.6%	1.486e-02	5.522e-06	5.575e-06±12.6%	1.5057±0.0446	866.1±7.1

Table 6.16: ^{3}He(e,e$'$p)D cross sections and distorted spectral function extracted at kinematics 34; the detected proton is back of $\vec{q}$; incident electron energy 1953.0 MeV.

P_{miss} MeV/c	$\frac{d^5\sigma^{ren}}{dE_f d\Omega_e d\Omega_p} \pm \epsilon_{st}$ μb MeV^{-1}sr^{-2}	$S_{2bbu}(P_{miss})$ fm^3	$\frac{d^5\sigma^{cc1}}{dE_f d\Omega_e d\Omega_p}$ μb MeV^{-1}sr^{-2}	$\frac{d^5\sigma^{ind}}{dE_f d\Omega_e d\Omega_p} \pm \epsilon_{st}$ μb MeV^{-1}sr^{-2}	$\bar{Q}^2 \pm \sigma_{Q^2}$ (GeV/c)^2	$\bar{\omega} \pm \sigma_\omega$ MeV
8.7	1.191e-03±6.1%	4.414e+00	1.182e-03	1.202e-03±6.0%	1.5525±0.0245	838.2±12.8
16.6	1.093e-03±2.5%	4.095e+00	1.097e-03	1.116e-03±2.5%	1.5495±0.0276	835.4±12.7
25.8	9.629e-04±1.7%	3.651e+00	9.717e-04	1.003e-03±1.7%	1.5496±0.0339	832.0±13.5
35.4	7.973e-04±1.6%	3.062e+00	8.029e-04	8.329e-04±1.5%	1.5547±0.0400	827.6±14.8
45.1	6.414e-04±1.6%	2.495e+00	6.381e-04	6.671e-04±1.6%	1.5660±0.0415	822.5±15.5
55.0	4.849e-04±1.8%	1.912e+00	4.772e-04	5.031e-04±1.7%	1.5763±0.0420	818.1±15.9
64.9	3.748e-04±2.0%	1.497e+00	3.661e-04	3.898e-04±2.0%	1.5828±0.0429	815.4±16.3
74.7	2.654e-04±2.5%	1.073e+00	2.581e-04	2.771e-04±2.5%	1.5866±0.0439	813.9±16.8
84.6	2.017e-04±3.2%	8.262e-01	1.954e-04	2.127e-04±3.2%	1.5884±0.0449	813.7±17.2

Table 6.17: ^{3}He(e,e$'$p)D cross sections and distorted spectral function extracted at kinematics 33; the detected proton is forward of $\vec{q}$; incident electron energy 1953.0 MeV.

P_{miss} MeV/c	$\frac{d^5\sigma^{ren}}{dE_f d\Omega_e d\Omega_p} \pm \epsilon_{st}$ μb MeV^{-1}sr^{-2}	$S_{2bbu}(P_{miss})$ fm^3	$\frac{d^5\sigma^{cc1}}{dE_f d\Omega_e d\Omega_p}$ μb MeV^{-1}sr^{-2}	$\frac{d^5\sigma^{ind}}{dE_f d\Omega_e d\Omega_p} \pm \epsilon_{st}$ μb MeV^{-1}sr^{-2}	$\bar{Q}^2 \pm \sigma_{Q^2}$ (GeV/c)^2	$\bar{\omega} \pm \sigma_\omega$ MeV
106.1	8.901e-05±4.8%	3.748e-01	9.153e-05	9.345e-05±4.8%	1.5140±0.0421	866.3±7.2
115.4	7.146e-05±3.6%	3.045e-01	7.398e-05	7.569e-05±3.6%	1.5155±0.0446	859.2±10.8
125.3	4.876e-05±3.7%	2.104e-01	5.008e-05	5.144e-05±3.6%	1.5235±0.0454	853.5±14.0
135.2	3.613e-05±3.8%	1.578e-01	3.684e-05	3.785e-05±3.8%	1.5303±0.0467	849.0±16.6
145.0	2.618e-05±4.2%	1.157e-01	2.652e-05	2.725e-05±4.1%	1.5376±0.0479	843.8±18.2
154.9	1.696e-05±5.2%	7.590e-02	1.701e-05	1.741e-05±5.1%	1.5494±0.0466	835.6±18.0
164.9	1.222e-05±6.3%	5.538e-02	1.214e-05	1.245e-05±6.3%	1.5619±0.0446	827.6±17.0
174.8	7.732e-06±8.3%	3.543e-02	7.606e-06	7.794e-06±8.3%	1.5718±0.0427	821.6±15.5
184.7	4.511e-06±11.9%	2.092e-02	4.408e-06	4.503e-06±11.8%	1.5796±0.0402	817.0±13.3
194.7	3.244e-06±15.6%	1.522e-02	3.150e-06	3.220e-06±15.6%	1.5868±0.0374	812.8±10.8
204.5	2.265e-06±22.9%	1.075e-02	2.183e-06	2.239e-06±22.7%	1.5945±0.0348	808.7±8.7

Table 6.18: ^{3}He(e,e$'$p)D cross sections and distorted spectral function extracted at kinematics 35; the detected proton is forward of $\vec{q}$; incident electron energy 1953.0 MeV.

6.2 A_{TL} asymmetry

A_{TL} extraction without bin-by-bin ω-q phase space matching

Fig. 6-21 shows the ^{3}He(e,e′p)D A_{TL} asymmetry extracted at the beam energy of 4.8 GeV, with the "cc1-averaging" technique with the "cc1-renormalization" to fixed values of Q^2 and ω, without ω-q phase space matching between back and forward of $\vec{q}$ bins[6]. This technique of A_{TL} extraction is described in Sec. 5.9. In the figure, the A_{TL} points below P_{miss} of 115 MeV/c were obtained with a fit to the out-of-plane ^{3}He(e,e′p)D cross section dependence, as described in Sec. 5.11 and Sec. 6.3.

Also plotted are theoretical calculations of Laget, Salme and very preliminary calculations of Udias and Vignote. The calculations of Laget and Salme are described on p. 201. Laget's PW+FSI+MEC calculation is not plotted, since it is very close to the full PW+FSI+MEC+3 body calculation in the shown P_{miss} region.

The preliminary results of Udias and Vignote use the relativistic mean field calculation of the bound state wave function [79, 9], with both bound and scattered nucleon wave functions described as Dirac solutions with scalar and vector potentials, and a relativistic form of nucleon current operator[7]. In the relativistic plane wave impulse approximation (RPWIA), FSI between the outgoing nucleon and the residual nucleus is neglected, while it is taken into account in the relativistic distorted wave impulse approximation (RDWIA). A detailed description of the calculations can be found in [9].

In the following, we compare the calculations to the measurements in different regions of missing momentum P_{miss}.

P_{miss} **from 0 to 220 MeV/c:** All available calculations give close predictions in this region. The data agrees fairly well with the calculations, with a notable

[6]As explained in Sec. 5.9, this (not strictly justified) technique allowed to increase the range of extracted A_{TL} and to decrease statistical errors; A_{TL} obtained with ω-q phase space matching and the model independent technique is described next. A comparison between A_{TL} obtained with the two techniques is given in Fig. 6-23.

[7]Although mean-field calculation of the wave function is clearly not appropriate for the ^{3}He nucleus, these very preliminary results present interest, since the A_{TL} observable downplays the significance of the ground state wave function (by virtue of the ratio involved in the A_{TL} definition, Sec. 5.9, [2]).

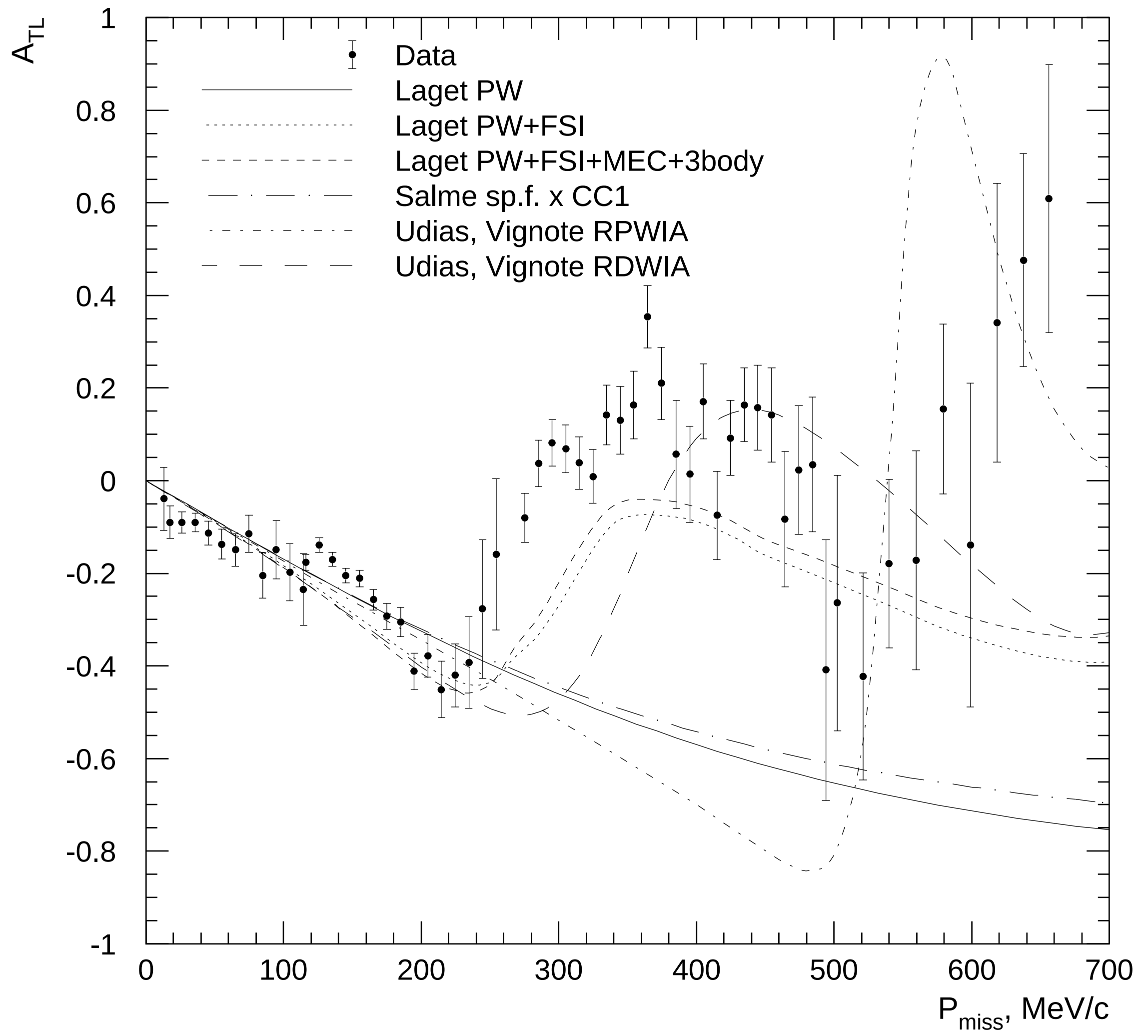

Figure 6-21: A_{TL} extracted at incident electron energy 4805.5 MeV, without ω-q phase space matching.

deviation at $P_{miss} \sim 140$ MeV/c. As described in Sec. 6.6, systematic errors of the measurements are in large part determined by errors in the reconstructed P_{miss}, and are largest where the ^{3}He(e,e$'$p)D cross section varies sharply with P_{miss}, i.e. for P_{miss} from 110 to 230 MeV/c ($\sim 8\%$ systematic error on the extracted ^{3}He(e,e$'$p)D cross sections at kinematics 4 and 5 (Sec. 6.6)).

P_{miss} **from 220 to 375 MeV/c:** The measured A_{TL} increases from its minimum of about -0.43 at $P_{miss} \sim 220$ MeV/c to a maximum of ~ 0.18 at $P_{miss} \sim 375$ MeV/c, in contrast with the decreasing character at $P_{miss} < 220$ MeV/c. The increasing character of the A_{TL} is reproduced in all calculations including FSI. Laget's PW+FSI and the full calculation seem to very well reproduce the P_{miss} position of the A_{TL} minimum and maximum, but at the maximum the A_{TL} in the calculations is still negative, at about -0.04 in the full calculation. The PW+FSI calculation of Udias and Vignote, on the other hand, seems to better reproduce the magnitude of the A_{TL} at the minimum and the maximum, but somewhat misses the P_{miss} position of the extrema. All PW calculations disagree with the data and show a monotonic A_{TL} decrease with P_{miss} in this region, although the A_{TL} in the RPWIA calculation changes the decreasing character to an increasing one at $P_{miss} \sim 480$ MeV/c.

P_{miss} **from 375 to 655 MeV/c:** The measured A_{TL} decreases from ~ 0.18 at $P_{miss} \sim 375$ MeV/c to ~ -0.3 at $P_{miss} \sim 510$ MeV/c, and then sharply increases to ~ 0.6 at $P_{miss} \sim 655$ MeV/c. It should be noted that the statistical errors of the datapoints were extracted in quadrature (formula (5.42)), which might be not a very good treatment for a few highest P_{miss} datapoints, where the extracted cross sections forward of $\vec{q}$ had very large statistical errors. Qualitatively, the decreasing character is reproduced in all calculation including FSI, whereas the "second ascent" of the A_{TL} is reproduced only in the PW and PW+FSI calculations of Udias and Vignote, but outside of the shown P_{miss} region. The non-relativistic PW calculations monotonically decrease and do not exhibit A_{TL} oscillations.

A_{TL} extraction with bin-by-bin ω-q phase space matching

Fig. 6-22 shows the ^{3}He(e,e$'$p)D A_{TL} asymmetry obtained at the beam energy of 4.8 GeV, with the "model independent" technique, with bin-by-bin ω-q phase space matching between back and forward of $\vec{q}$ P_{miss} bins. This technique of A_{TL} extraction is described in Sec. 5.9. Thus extracted A_{TL} shows a good agreement, in regions of P_{miss} overlap, with the A_{TL} extracted without ω-q phase space matching, and with the "cc1-averaging" technique with the "cc1-renormalization" to fixed values of Q^2 and ω (both are plotted in Fig. 6-23). Therefore, a comparison with available theories is quite similar to the comparison given above, except that a limited P_{miss} range of the "model-independent" A_{TL} does not allow one to make conclusions as to its behavior at $P_{miss} > 580$ MeV/c, and for larger ambiguity in the A_{TL} behavior at $P_{miss} < 580$ MeV/c, due to larger statistical errors.

To summarize, all available calculations indicate the importance of the rescattering in the final state on the A_{TL} behavior above $P_{miss} \sim 220$ MeV/c. However, FSI alone in Laget's calculations is not able to reproduce the full range of the observed A_{TL} oscillation in the P_{miss} region from 220 MeV/c to 520 MeV/c; based on the character of Udias's and Vignote's curves, the "missing positivity" of the A_{TL} in this region might be explained by relativistic ingredients of their calculations, such as the dynamical relativistic effects. Further refinements in the calculations are necessary to pinpoint the nature of the processes in this P_{miss} region.

The "second ascent" of the measured A_{TL} in the P_{miss} region from 520 to 655 MeV/c further hints on relativistic or other effects expressed in this region, but the large statistical errors and a mismatch in ω-q phase space covered by back and forward of $\vec{q}$ cross section measurements do not allow this data to strictly present requirements for theories in this region.

The A_{TL} extracted with both techniques are tabulated in Tables 6.19 though 6.21.

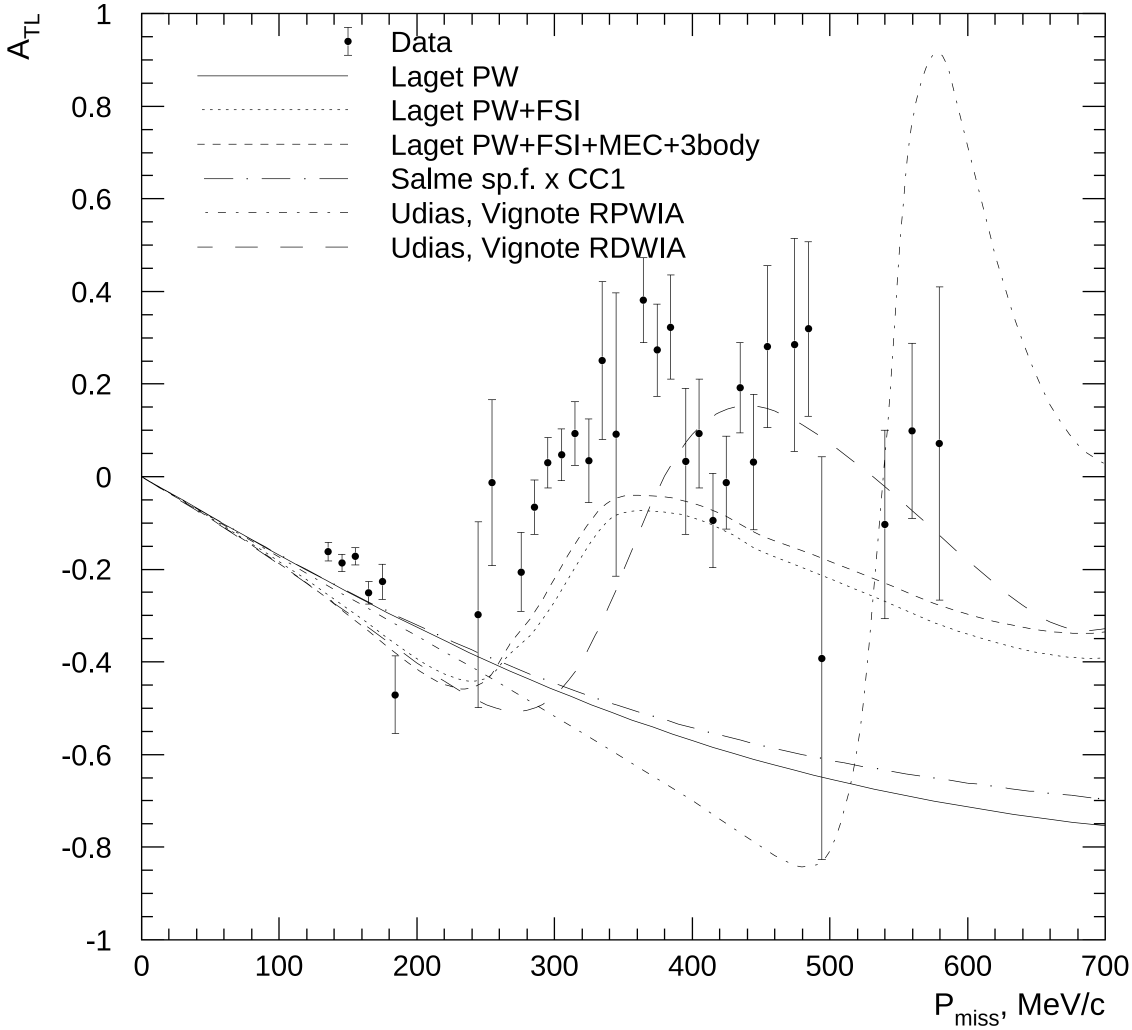

Figure 6-22: A_{TL} extracted at incident electron energy 4805.5 MeV, with ω-q phase space matching and flat simulation cross section.

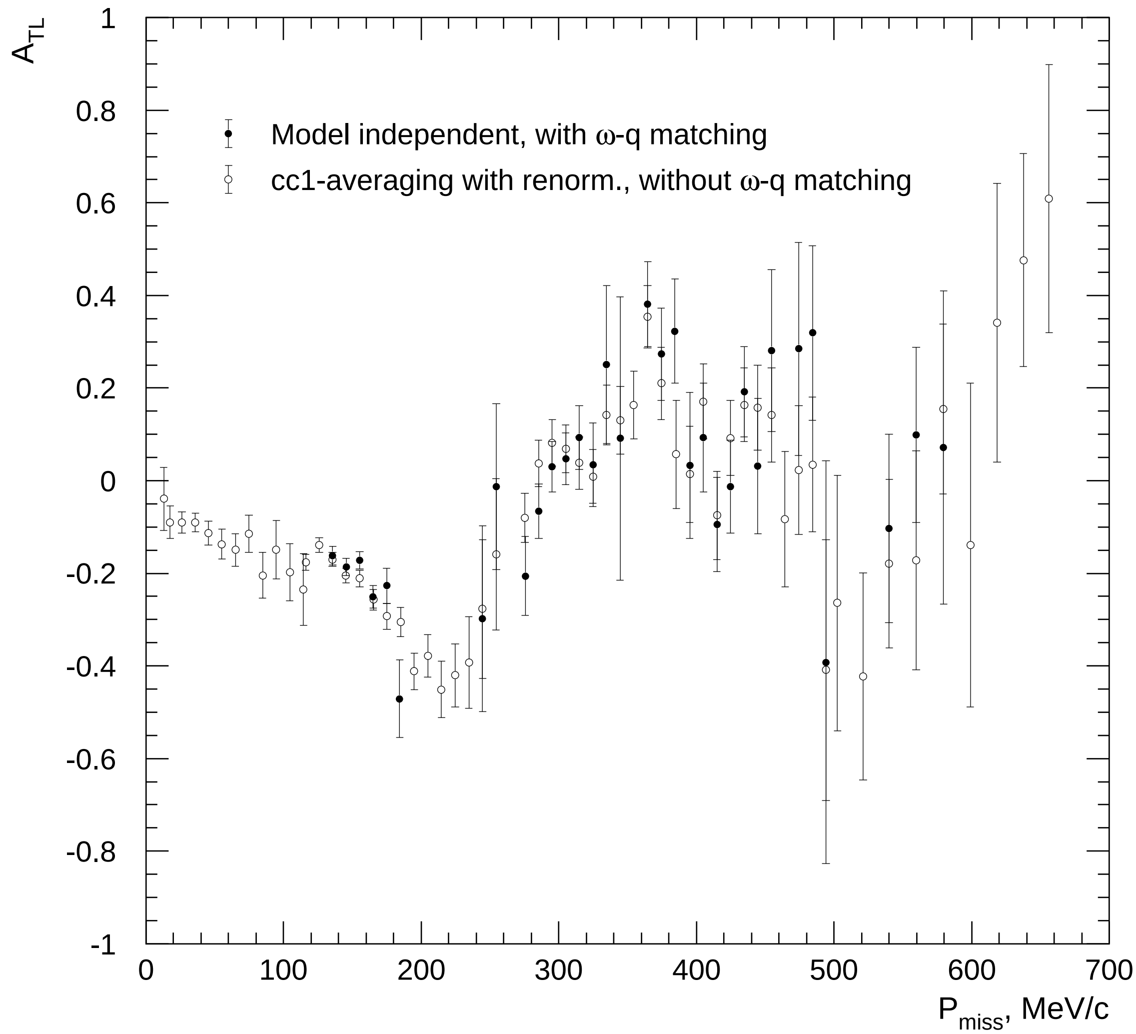

Figure 6-23: A_{TL} extracted at incident electron energy 4805.5 MeV, both with and without ω-q phase space matching.

P_{miss} MeV/c	$A_{TL}^{ren} \pm \epsilon_{st}$	Forward of $\vec{q}$ bin $Q^2 \pm \sigma_{Q^2}$ (GeV/c)^2	Forward of $\vec{q}$ bin $\bar{\omega} \pm \sigma_\omega$ MeV	Back of $\vec{q}$ bin $Q^2 \pm \sigma_{Q^2}$ (GeV/c)^2	Back of $\vec{q}$ bin $\bar{\omega} \pm \sigma_\omega$ MeV
116.0	-0.176±0.017	1.4248±0.0706	844.2±17.2	1.5796±0.1089	798.6±17.3
125.8	-0.139±0.016	1.4451±0.0801	839.1±20.8	1.5930±0.1174	804.3±20.4
135.5	-0.170±0.015	1.4606±0.0895	834.4±23.5	1.5923±0.1218	809.7±22.9
145.3	-0.205±0.016	1.4868±0.0977	829.2±24.4	1.5909±0.1258	816.9±23.8
155.2	-0.211±0.018	1.5150±0.1043	824.8±24.9	1.5815±0.1311	824.7±22.9
165.2	-0.257±0.022	1.5423±0.1101	821.3±25.2	1.5625±0.1327	834.0±20.4
175.0	-0.293±0.028	1.5680±0.1125	818.5±25.0	1.5346±0.1293	841.7±18.7
184.9	-0.305±0.032	1.5924±0.1120	815.7±24.6	1.4960±0.1182	846.9±17.8
194.9	-0.412±0.040	1.6181±0.1053	813.0±23.4	1.4523±0.0945	850.7±16.6
204.7	-0.378±0.046	1.6447±0.0949	810.8±21.9	1.4199±0.0731	854.9±14.8
214.7	-0.451±0.061	1.6703±0.0829	808.6±19.9	1.3956±0.0587	859.2±13.4
224.7	-0.420±0.068	1.6895±0.0726	805.6±17.7	1.5885±0.1075	767.8±10.1
234.6	-0.393±0.099	1.7087±0.0621	803.5±15.5	1.5918±0.1136	773.8±12.7
244.5	-0.277±0.150	1.7235±0.0526	801.2±13.5	1.5929±0.1166	780.0±15.1
254.4	-0.159±0.164	1.7394±0.0433	799.6±11.7	1.5909±0.1185	785.5±17.6
275.3	-0.080±0.053	1.4219±0.0579	826.6±19.5	1.5871±0.1239	798.4±21.1
285.2	0.037±0.050	1.4444±0.0667	822.3±21.6	1.5824±0.1272	807.3±20.9
295.1	0.082±0.050	1.4685±0.0757	818.4±23.5	1.5737±0.1289	816.4±19.5
305.0	0.069±0.052	1.4949±0.0844	815.7±24.4	1.5622±0.1311	824.8±18.0
314.8	0.038±0.056	1.5234±0.0935	813.7±25.0	1.5441±0.1319	832.2±16.2
324.8	0.009±0.058	1.5541±0.1004	812.4±25.4	1.5208±0.1298	839.1±14.8
334.7	0.142±0.064	1.5831±0.1039	811.4±25.5	1.4883±0.1219	845.0±13.8
344.6	0.130±0.073	1.6135±0.1018	810.6±25.0	1.5881±0.1117	763.6±9.9
354.5	0.163±0.073	1.6414±0.0955	809.5±23.9	1.5897±0.1154	769.4±12.0
364.4	0.354±0.068	1.6665±0.0865	807.5±22.4	1.5872±0.1169	775.5±14.0
374.4	0.210±0.078	1.6892±0.0762	805.9±20.7	1.5864±0.1192	781.4±16.1
385.3	0.057±0.117	1.3925±0.0385	827.0±16.1	1.5834±0.1219	787.4±18.0
395.1	0.014±0.104	1.4113±0.0479	823.4±19.3	1.5856±0.1240	794.3±19.3
405.0	0.171±0.081	1.4328±0.0572	819.8±21.5	1.5827±0.1277	803.0±19.4
414.8	-0.075±0.095	1.4558±0.0653	816.7±23.1	1.5781±0.1292	812.4±18.9
424.7	0.092±0.081	1.4821±0.0740	815.1±24.0	1.5702±0.1323	820.6±17.9
434.6	0.164±0.079	1.5103±0.0838	814.1±24.5	1.5619±0.1341	829.0±16.5
444.5	0.158±0.092	1.5410±0.0922	813.7±25.3	1.5481±0.1355	836.6±14.9
454.5	0.142±0.102	1.5734±0.0971	813.6±25.1	1.5316±0.1380	843.7±13.5
464.4	-0.083±0.146	1.6089±0.0980	814.9±25.1	1.5067±0.1331	850.1±12.2
474.3	0.023±0.139	1.6409±0.0921	814.6±24.6	1.5846±0.1151	765.0±11.3
484.2	0.035±0.145	1.6685±0.0840	814.4±23.5	1.5809±0.1169	771.2±13.2
494.1	-0.409±0.282	1.6909±0.0767	813.2±21.8	1.5842±0.1196	777.0±14.9

Table 6.19: ^{3}He(e,e$'$p)D A_{TL} extracted without ω-q phase space matching, with the "cc1-averaging" technique with cc1-renormalization of cross sections to $\omega = 822.6$ MeV, $q = 1483.6$ MeV/c (continued in Table 6.20).

P_{miss} MeV/c	$A_{TL}^{ren} \pm \epsilon_{st}$	Forward of $\vec{q}$ bin		Back of $\vec{q}$ bin	
		$Q^2 \pm \sigma_{Q^2}$ (GeV/c)^2	$\bar{\omega} \pm \sigma_\omega$ MeV	$Q^2 \pm \sigma_{Q^2}$ (GeV/c)^2	$\bar{\omega} \pm \sigma_\omega$ MeV
502.4	-0.264±0.276	1.3819±0.0319	824.5±15.1	1.5854±0.1187	775.5±14.8
521.0	-0.423±0.224	1.4172±0.0473	817.6±20.7	1.5862±0.1225	787.7±17.9
540.0	-0.179±0.182	1.4621±0.0633	813.8±23.4	1.5835±0.1281	803.5±19.5
559.6	-0.172±0.236	1.5173±0.0800	813.3±24.5	1.5765±0.1337	819.6±19.5
579.2	0.155±0.183	1.5886±0.0893	816.5±24.9	1.5655±0.1394	834.9±18.1
598.9	-0.139±0.349	1.6584±0.0827	819.2±24.0	1.5442±0.1435	849.0±16.1
618.4	0.341±0.301	1.7076±0.0664	819.1±21.8	1.5255±0.1475	860.4±13.9
637.6	0.476±0.230	1.7410±0.0498	817.2±17.7	1.5635±0.1043	740.0±11.5
656.2	0.609±0.290	1.7692±0.0357	816.0±13.3	1.5746±0.1113	751.6±14.1

Table 6.20: ^{3}He(e,e′p)D A_{TL} extracted without ω-q phase space matching, with the "cc1-averaging" technique with cc1-renormalization of cross sections to $\omega = 822.6$ MeV, $q = 1483.6$ MeV/c (continued from Table 6.19).

P_{miss} MeV/c	$A_{TL}^{ind} \pm \epsilon_{st}$	$A_{TL}^{cc1} \pm \epsilon_{st}$	$Q^2 \pm \sigma_{Q^2}$ MeV	$\bar{\omega} \pm \sigma_{\omega}$ (GeV/c)^2	$A_{TL}^{ren} \pm \epsilon_{st}$
135.6	-0.162±0.020	-0.185±0.021	1.4769±0.0809	819.6±19.6	-0.183±0.021
145.4	-0.186±0.019	-0.213±0.019	1.4985±0.0935	823.0±22.9	-0.211±0.019
155.2	-0.172±0.019	-0.204±0.019	1.5189±0.1035	826.3±23.3	-0.203±0.019
165.1	-0.251±0.024	-0.270±0.024	1.5507±0.1161	829.6±20.6	-0.272±0.024
174.9	-0.227±0.038	-0.230±0.040	1.5950±0.1252	836.3±18.9	-0.236±0.040
184.3	-0.471±0.084	-0.464±0.094	1.6448±0.1236	847.0±19.6	-0.473±0.093
244.6	-0.298±0.200	-0.324±0.209	1.7132±0.0494	795.8±8.5	-0.367±0.202
254.5	-0.013±0.179	-0.020±0.179	1.7390±0.0403	798.4±10.3	-0.075±0.178
275.5	-0.206±0.085	-0.219±0.085	1.4207±0.0465	809.2±13.3	-0.208±0.085
285.3	-0.066±0.059	-0.092±0.059	1.4470±0.0628	813.1±18.3	-0.083±0.059
295.1	0.030±0.054	0.002±0.055	1.4717±0.0756	817.6±20.8	0.009±0.055
304.9	0.047±0.056	0.028±0.056	1.4991±0.0854	821.3±19.8	0.031±0.056
314.8	0.093±0.069	0.085±0.069	1.5418±0.0971	826.5±17.3	0.082±0.069
324.7	0.034±0.090	0.050±0.090	1.5992±0.1005	835.7±14.3	0.039±0.091
334.7	0.251±0.171	0.297±0.171	1.6632±0.0827	845.6±9.9	0.278±0.173
344.5	0.091±0.306	0.107±0.306	1.7148±0.0550	857.7±6.0	0.079±0.308
364.5	0.381±0.092	0.387±0.092	1.6235±0.0777	789.4±9.1	0.362±0.094
374.4	0.273±0.099	0.292±0.098	1.6681±0.0725	794.6±11.4	0.256±0.100
384.3	0.323±0.112	0.334±0.111	1.6987±0.0634	798.4±13.3	0.294±0.114
395.1	0.033±0.158	0.031±0.155	1.4100±0.0372	804.7±12.1	0.048±0.155
405.1	0.093±0.118	0.067±0.119	1.4297±0.0508	809.2±16.9	0.082±0.118
414.8	-0.095±0.102	-0.123±0.102	1.4527±0.0624	812.9±19.2	-0.112±0.102
424.6	-0.013±0.100	-0.030±0.100	1.4863±0.0727	819.4±18.8	-0.024±0.100
434.6	0.192±0.098	0.162±0.099	1.5239±0.0814	823.6±17.5	0.162±0.099
444.6	0.032±0.146	0.036±0.140	1.5769±0.0885	831.7±15.5	0.028±0.141
454.6	0.281±0.175	0.268±0.178	1.6447±0.0789	841.4±11.5	0.249±0.179
474.1	0.285±0.230	0.278±0.231	1.5753±0.0731	783.6±4.8	0.260±0.234
484.3	0.319±0.188	0.322±0.187	1.6143±0.0721	789.6±6.7	0.297±0.190
494.1	-0.392±0.435	-0.388±0.433	1.6613±0.0701	794.4±7.8	-0.420±0.420
539.9	-0.103±0.204	-0.127±0.204	1.4632±0.0623	816.1±19.7	-0.116±0.204
559.6	0.099±0.189	0.076±0.190	1.5359±0.0748	823.9±17.4	0.074±0.190
579.6	0.072±0.338	0.053±0.339	1.6418±0.0715	838.8±13.3	0.032±0.340

Table 6.21: ^{3}He(e,e′p)D A_{TL} extracted with bin-by-bin ω-q phase space matching, with the three techniques.

6.3 Binning in the out-of-plane angle at kinematics 1

Figs. 6-24 and 6-25 show the ^{3}He(e,e$'$p)D cross sections extracted at kinematics 1 (E_{beam} = 4.8 GeV, nominal P_{miss} = 0) with binning both in P_{miss} and in the out-of-plane angle ϕ. Events are restricted to perpendicular kinematics by the cut on the angle between $\vec{P}_{miss}$ and $\vec{q}$: $80^\circ < \theta_{Bq} < 100^\circ$. The subscript "B" here denotes the undetected residual system, as in the generic reaction, A(e,e$'$p)B. The cross sections were extracted with the "cc1-averaging" technique, and with the "cc1-renormalization" to fixed values of Q^2 and ω (given in Table 5.1).

The decomposition of the ^{3}He(e,e$'$p)D cross sections in terms of response functions in one-photon exchange approximation (Sec. 5.10) allowed us to obtain the A_{TL} asymmetry, R_{TT} response function, and forward and back of $\vec{q}$ in-plane ^{3}He(e,e$'$p)D cross sections. They were obtained from a fit of the functional form 5.67 to the ^{3}He(e,e$'$p)D cross sections extracted at the same values of P_{miss}, but at different values of the out-of-plane angle ϕ. The fitted functions and parameters are shown in Figs. 6-24 and 6-25. The analysis presented is this section is described in Sec. 5.11.

Fig. 6-26 shows the ^{3}He(e,e$'$p)D A_{TL} asymmetry obtained from the fitted parameters, together with the A_{TL} corresponding to the factorization (5.19) – (5.20) of the Salme spectral function by cc1. These datapoints are also plotted in Figs. 6-21 and 6-23. As discussed in the previous section, the datapoints are in a good agreement with all available A_{TL} calculations.

Fig. 6-27 shows the ^{3}He(e,e$'$p)D R_{TT} response function obtained from the fitted parameters, together with the R_{TT} corresponding to the factorization of the Salme spectral function by cc1. The extracted R_{TT} is consistent both with the theory and with 0 within statistical errors.

Figs. 6-28 and 6-29 show the in-plane ^{3}He(e,e$'$p)D cross sections forward and back of $\vec{q}$ obtained from the fitted parameters. For comparison, also plotted are the ^{3}He(e,e$'$p)D cross sections obtained with the "cc1-averaging" procedure with the renormalization to fixed values of Q^2 and ω, without restricting events to in-plane or to perpendicular kinematics (empty points in Figs. 6-28 and 6-28; these datapoints are also plotted in Figs. 6-1, 6-2, 6-5 and 6-6). As described in Sec. 6.6, the largest systematic error at kinematics 1 was at its high P_{miss} edge, where accepted events were close to 90° out-of-plane. Excluding a possible disagreement for $P_{miss} > 90$ MeV/c, both techniques of extraction agree well.

All results presented in this section are tabulated in Table 6.22.

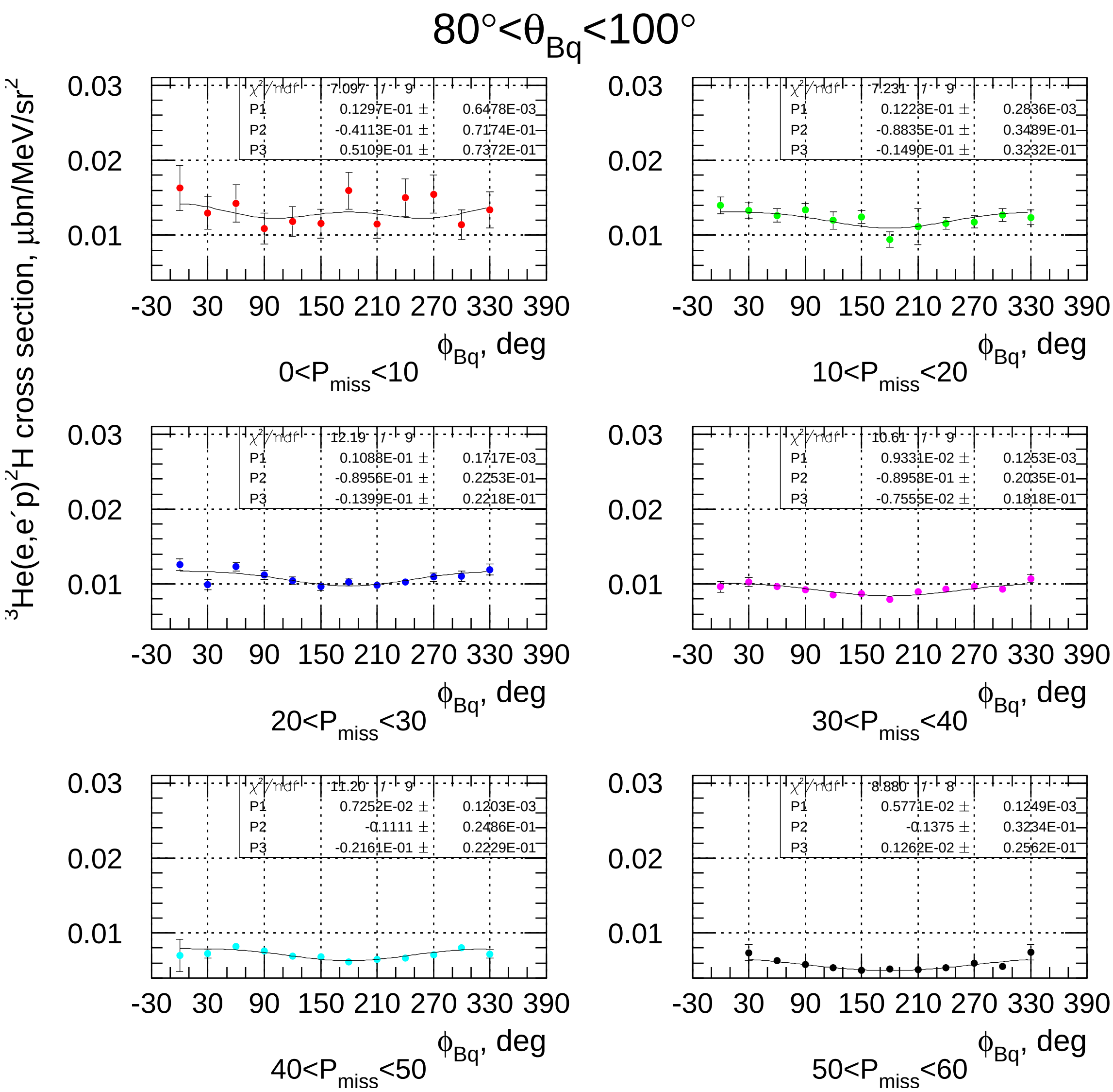

Figure 6-24: ^{3}He(e,e′p)D cross sections extracted at kinematics 1 with events restricted to perpendicular kinematics by the cut $80^\circ < \theta_{Bq} < 100^\circ$, and binning both in P_{miss} and in the out-of-plane angle ϕ. Shown lines are fits to the datapoints with the form $P_1(1 - P_2 \cos\phi_{Bq} + P_3 \cos 2\phi_{Bq})$, where $\phi_{Bq} = 180^\circ + \phi$. Insets show fitted values of the parameters P_1, P_2 and P_3, and statistical errors.

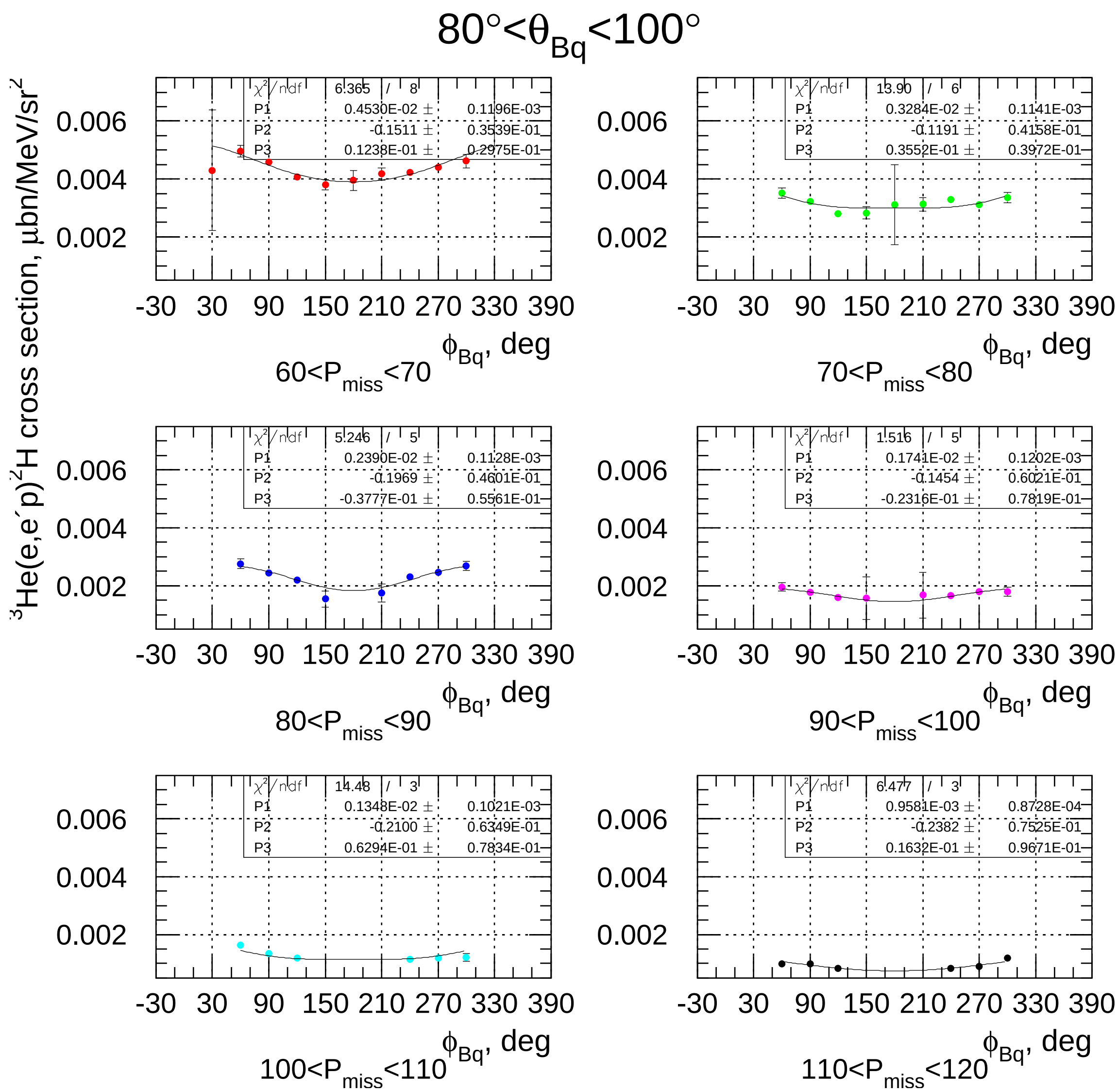

Figure 6-25: ^{3}He(e,e′p)D cross sections extracted at kinematics 1 with events restricted to perpendicular kinematics by the cut $80^\circ < \theta_{Bq} < 100^\circ$, and binning both in P_{miss} and in the out-of-plane angle ϕ. Shown lines are fits to the datapoints with the form $P_1(1 - P_2 \cos\phi_{Bq} + P_3 \cos 2\phi_{Bq})$, where $\phi_{Bq} = 180^\circ + \phi$. Insets show fitted values of the parameters P_1, P_2 and P_3, and statistical errors.

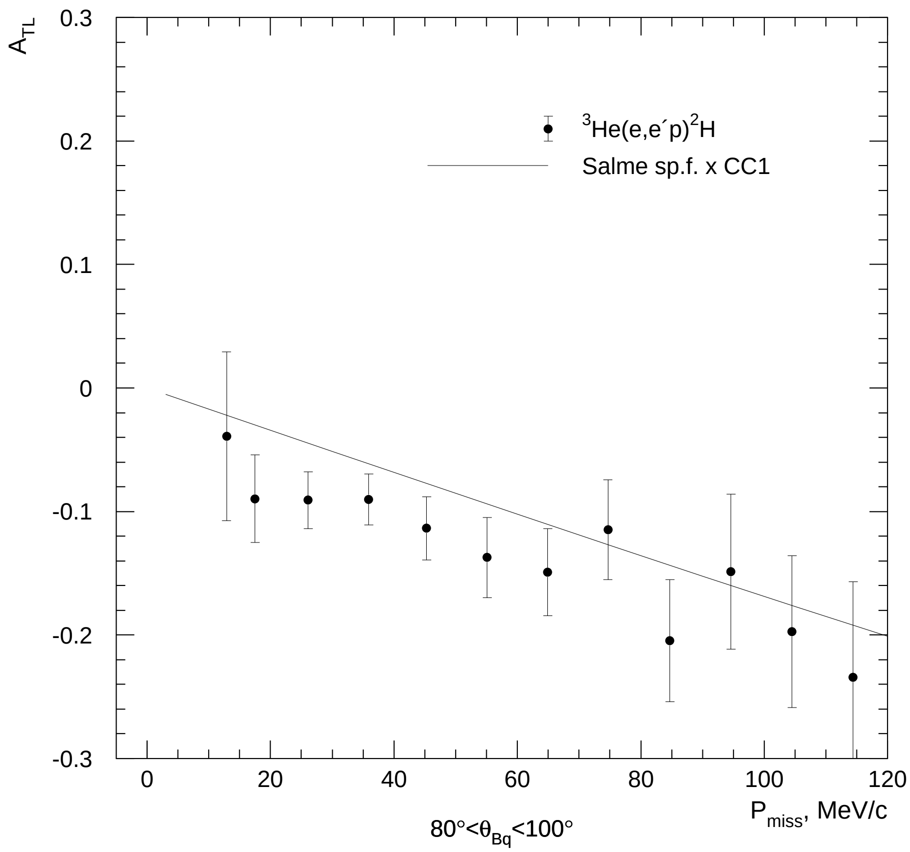

Figure 6-26: A_{TL} obtained from a fit to the out-of-plane dependence of the ^{3}He(e,e$'$p)D cross sections with events restricted to perpendicular kinematics by the cut $80^\circ < \theta_{Bq} < 100^\circ$. Shown curve is the factorization of the Salme ^{3}He(e,e$'$p)D spectral function with cc1.

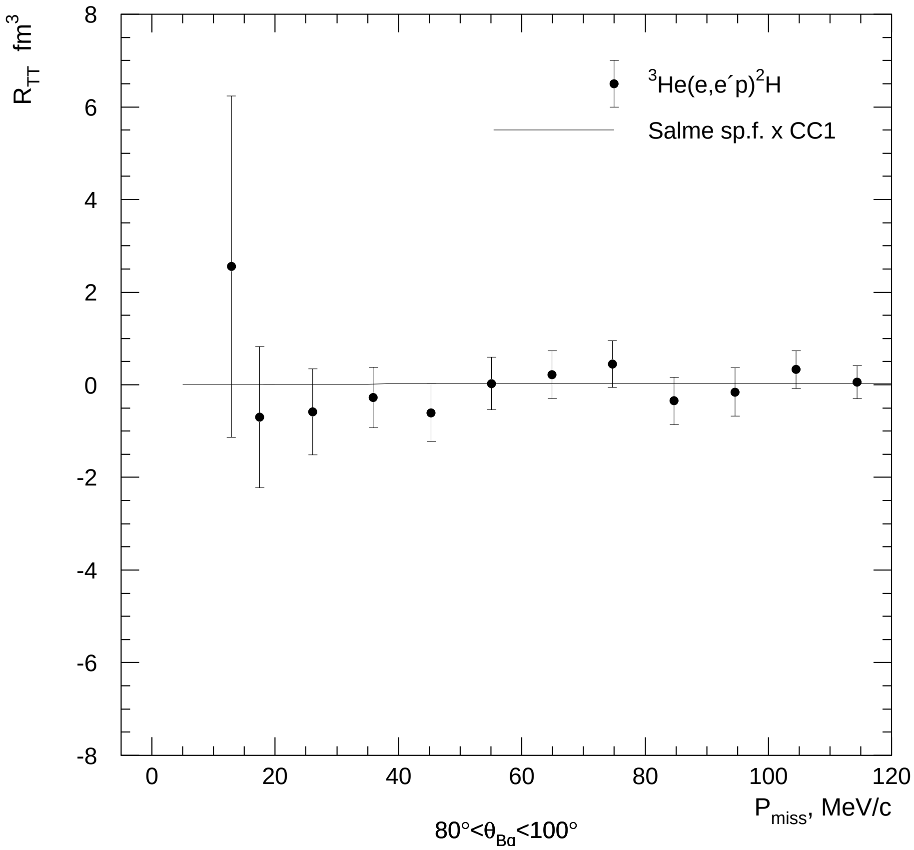

Figure 6-27: R_{TT} obtained from a fit to the out-of-plane dependence of the ^{3}He(e,e′p)D cross sections, with events restricted to perpendicular kinematics by the cut $80^\circ < \theta_{Bq} < 100^\circ$. Shown curve is the factorization of the Salme ^{3}He(e,e′p)D spectral function with cc1.

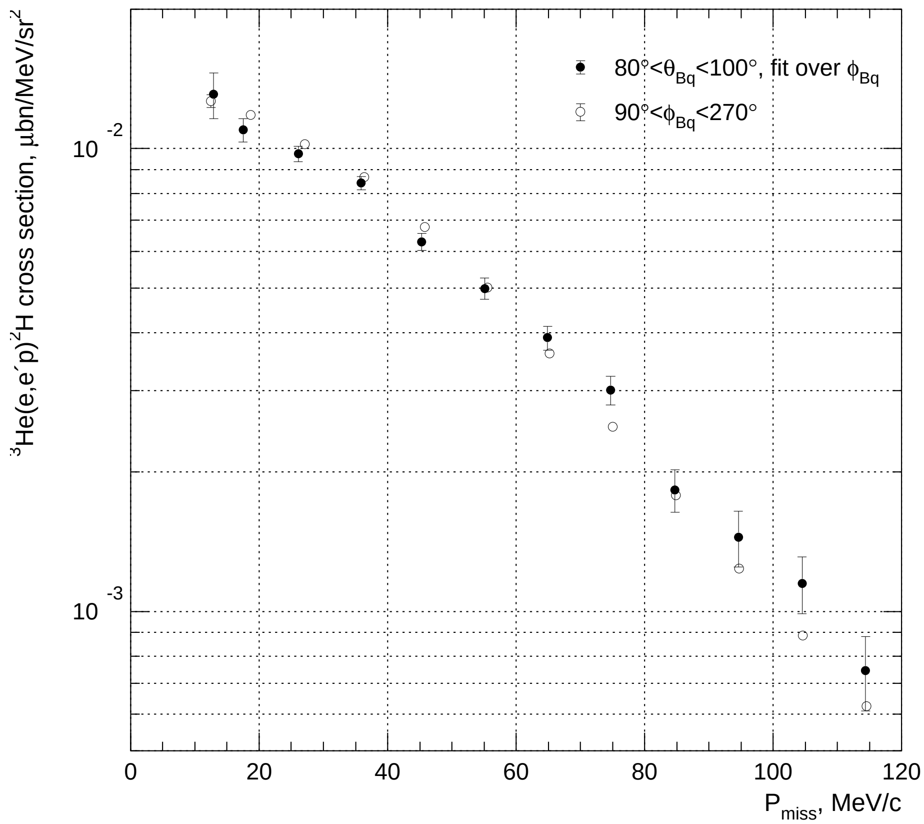

Figure 6-28: The ^{3}He(e,e$'$p)D in-plane cross sections forward of $\vec{q}$ obtained from a fit to the out-of-plane dependence of the ^{3}He(e,e$'$p)D cross sections, with events restricted to perpendicular kinematics by the cut $80^\circ < \theta_{Bq} < 100^\circ$ (solid points). Empty datapoints are described in the text.

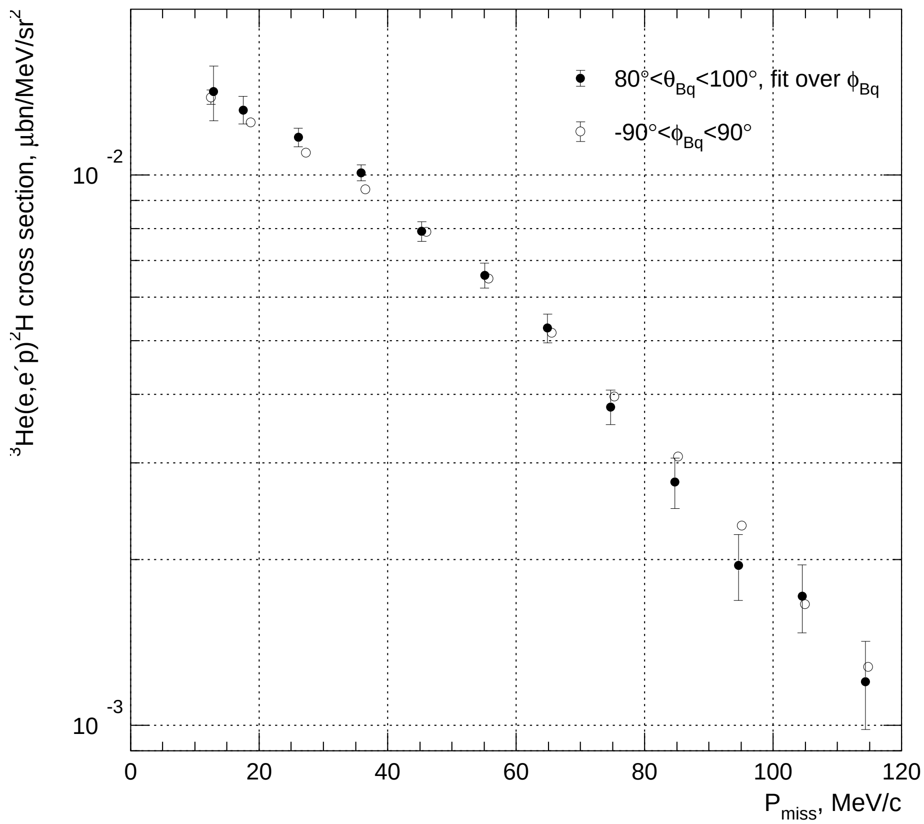

Figure 6-29: ^{3}He(e,e′p)D in-plane cross sections back of $\vec{q}$ obtained from a fit to the out-of-plane dependence of the ^{3}He(e,e′p)D cross sections, with events restricted to perpendicular kinematics by the cut $80° < \theta_{Bq} < 100°$ (solid points). Empty datapoints are described in the text.

P_{miss} MeV/c	A_{TL}	R_{TT} fm^3	$\frac{d^5\sigma^{ren}}{dE_f d\Omega_e d\Omega_p} \pm \epsilon_{st}$, μb MeV^{-1}sr^{-2}	
			Forward of $\vec{q}$, in plane	Back of $\vec{q}$, in plane
12.9	-0.3913e-01±0.6831e-01	2.512e+00±3.627e+00	1.288e-02±1.461e-03	1.394e-02±1.580e-03
17.5	-0.8968e-01±0.3554e-01	-6.909e-01±1.499e+00	1.079e-02±6.243e-04	1.291e-02±7.473e-04
26.1	-0.9083e-01±0.2294e-01	-5.768e-01±9.147e-01	9.591e-03±3.706e-04	1.151e-02±4.446e-04
35.9	-0.9026e-01±0.2057e-01	-2.671e-01±6.430e-01	8.285e-03±2.740e-04	9.933e-03±3.284e-04
45.3	-0.1136±0.2554e-01	-5.939e-01±6.128e-01	6.185e-03±2.593e-04	7.770e-03±3.258e-04
55.1	-0.1373±0.3249e-01	2.761e-02±5.604e-01	4.902e-03±2.571e-04	6.462e-03±3.389e-04
64.9	-0.1492±0.3523e-01	2.125e-01±5.108e-01	3.837e-03±2.295e-04	5.184e-03±3.101e-04
74.7	-0.1150±0.4040e-01	4.420e-01±4.946e-01	2.959e-03±2.122e-04	3.728e-03±2.674e-04
84.7	-0.2047±0.4926e-01	-3.420e-01±5.040e-01	1.799e-03±1.897e-04	2.724e-03±2.874e-04
94.6	-0.1489±0.6278e-01	-1.527e-01±5.160e-01	1.423e-03±1.954e-04	1.922e-03±2.638e-04
104.5	-0.1975±0.6148e-01	3.216e-01±4.009e-01	1.131e-03±1.587e-04	1.688e-03±2.369e-04
114.4	-0.2344±0.7733e-01	5.925e-02±3.513e-01	7.331e-04±1.334e-04	1.182e-03±2.151e-04

Table 6.22: A_{TL}, R_{TT} and ^{3}He(e,e′p)D cross sections extracted in kinematics 1 with $80° < \theta_{Bq} < 100°$ cut and fit to out-of-plane cross section dependence.

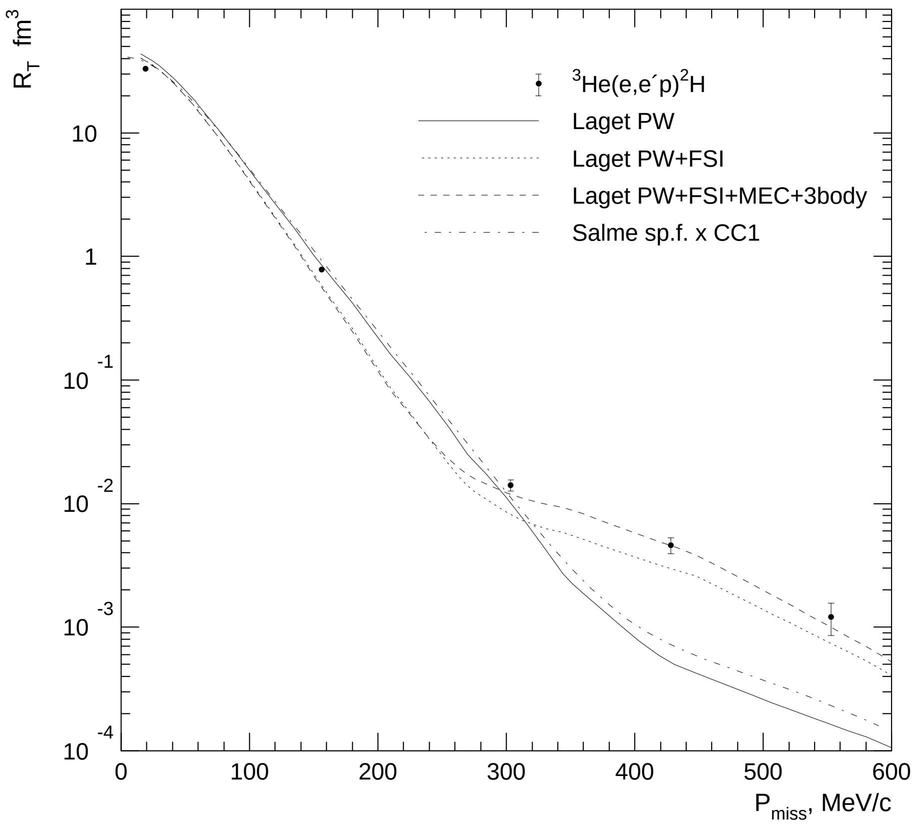

Figure 6-30: Separated ^{3}He(e,e′p)D R_T response function, with (ω, q, P_{miss}) phase space matching between Σ_1, Σ_2 and Σ_3 kinematics.

6.4 ^{3}He(e,e′p)D response functions

Figs. 6-30 through 6-32 show the ^{3}He(e,e′p)D R_T and R_{TL} response functions, and the combination of response functions $R_L + V_{TT}R_{TT}/V_L$, extracted in the measurements. The corresponding analysis is described in Sec. 5.10. The response functions were separated with the model independent technique only. The R_T and $R_L + V_{TT}R_{TT}/V_L$ were separated with the (ω, q, P_{miss}) phase space matching between Σ_1, Σ_2 and Σ_3 kinematics, while the R_{TL} was separated with the (ω, q, P_{miss}) phase space matching between Σ_1 and Σ_2 kinematics only.

Also shown are calculations of Salme and Laget. The calculations are described on page 201. Laget's PW+FSI+MEC calculation is not plotted, since it is very close, in

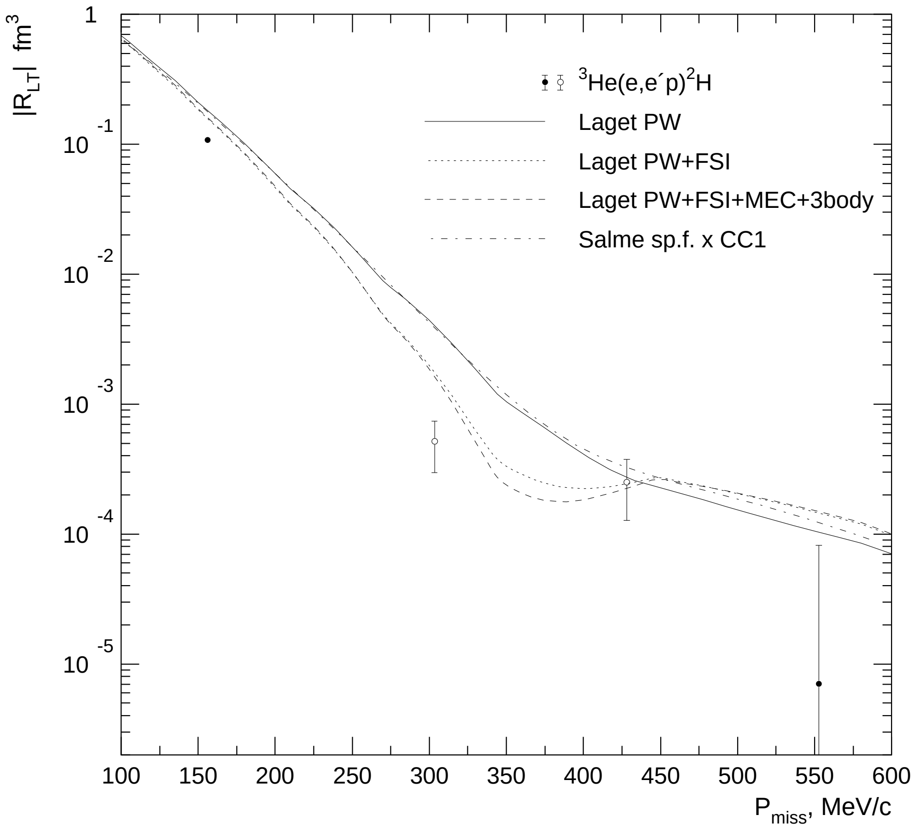

Figure 6-31: Modulus of separated ^{3}He(e,e$'$p)D R_{TL} response function, with (ω, q, P_{miss}) phase space matching between Σ_1 and Σ_2 kinematics only. Theoretical curves and solid points are negative; empty points are positive.

the P_{miss} region shown in the figures, to the full PW+FSI+MEC+3 body calculation.

In Laget's calculations, FSI processes are expressed in all separated response functions, with the largest influence on R_T, especially at $P_{miss} > 300$ MeV/c (up to a 6-fold increase), and on $R_L + R_{TT}V_{TT}/V_L$ (the localized 16-fold "dip" at $P_{miss} \sim 410$ MeV/c), and a lower influence on R_{TL} (the 3-fold "dip"at $P_{miss} \sim 360$ MeV/c). MEC and intermediate Δ formation amplitudes are manifested in a ~ 1.5-fold increase of R_T at $P_{miss} > 300$ MeV/c, and in the change of sign of $R_L + R_{TT}V_{TT}/V_L$ at P_{miss} from 300 to 600 MeV/c. As mentioned above, three-nucleon π double scattering amplitudes do not play a role in the calculations for P_{miss} below 600 MeV/c.

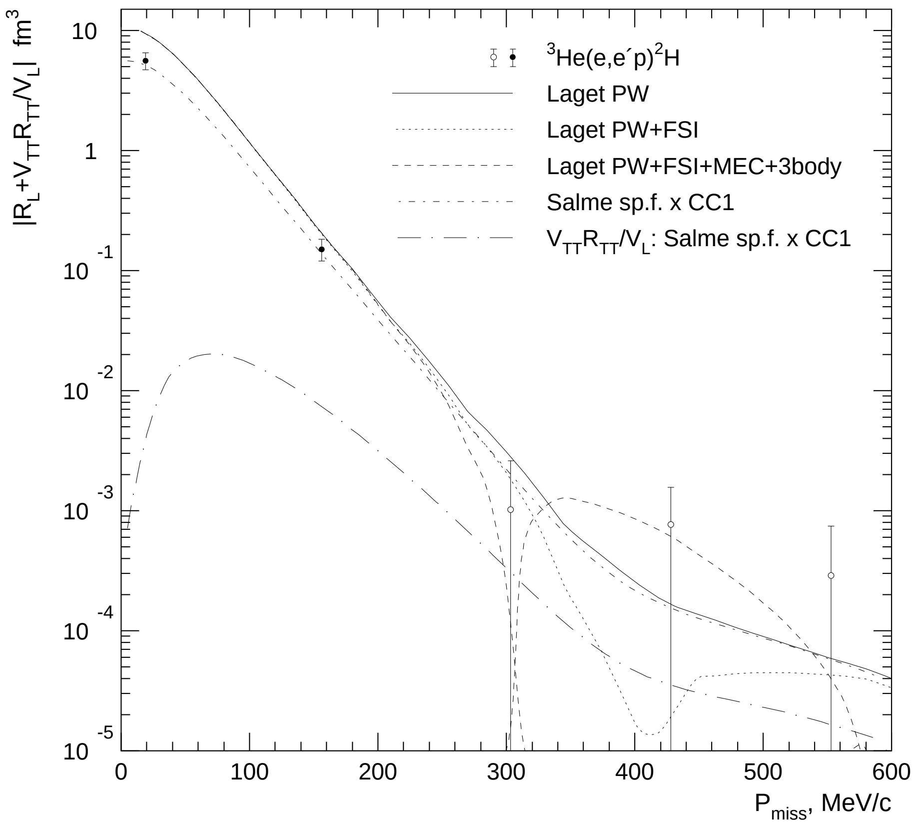

Figure 6-32: Modulus of separated $R_L + V_{TT}R_{TT}/V_L$ combination of ^{3}He(e,e′p)D response functions, with (ω, q, P_{miss}) phase space matching between Σ_1, Σ_2 and Σ_3 kinematics. Solid points are positive, empty points are negative. Theoretical curves are positive, except for Laget PW+FSI+MEC+3 body curve, which is negative for 300 MeV/c $> P_{miss} >$ 580 MeV/c, and positive everywhere else.

Above P_{miss} of 300 MeV/c, Laget's full calculation very well describes both R_T and $R_L + R_{TT}V_{TT}/V_L$ datapoints, indicating the importance of both MEC (and intermediate Δ formation) and FSI in this region. Below P_{miss} of 200 MeV/c, both R_T and $R_L + R_{TT}V_{TT}/V_L$ seem to agree better with the Salme PW calculation.

The separated R_{TL} response function disagrees with all available calculations, in particular, the positive R_{TL} values at $P_{miss} \approx 300$ MeV/c and at $P_{miss} \approx 425$ MeV/c are not reproduced.

The separated response functions are tabulated in Table 6.23.

$P_{miss} \pm \sigma_{Pm}$ MeV/c	$R_T \pm \epsilon_{st}$ fm^3	$R_{LT} \pm \epsilon_{st}$ fm^3	$R_L + V_{TT}R_{TT}/V_L \pm \epsilon_{st}$ fm^3	$\Sigma_{1,2,3} : Q^2 \pm \sigma_{Q^2}$ (GeV/c)^2	$\Sigma_{1,2,3} : \bar{\omega} \pm \sigma_\omega$ MeV
19±5.4	3.262e+01±7.231e-01	-	5.491e+00±8.878e-01	1.5477±0.0225	836.7±6.1
156.2±18.8	7.725e-01±2.397e-02	-1.262e-01±1.750e-02	1.482e-01±3.023e-02	1.5542±0.0359	834.9±9.3
303.4±17.2	1.389e-02±1.478e-03	5.192e-04±7.912e-04	-1.000e-03±1.569e-03	1.5567±0.0356	834.2±9.2
428.1±16.7	4.531e-03±6.629e-04	-3.055e-04±4.332e-04	-7.509e-04±7.816e-04	1.5569±0.0355	834.1±9.1
552.8±15.8	1.190e-03±3.474e-04	-1.268e-04±2.596e-04	-2.833e-04±4.445e-04	1.5569±0.0353	834.2±9.1

$P_{miss} \pm \sigma_{Pm}$ MeV/c	$R_T \pm \epsilon_{st}$ fm^3	$R_{LT} \pm \epsilon_{st}$ fm^3	$R_L + V_{TT}R_{TT}/V_L \pm \epsilon_{st}$ fm^3	$\Sigma_{1,2} : Q^2 \pm \sigma_{Q^2}$ (GeV/c)^2	$\Sigma_{1,2} : \bar{\omega} \pm \sigma_\omega$ MeV
19±5.4	3.248e+01±7.165e-01	-	6.381e+00±6.000e-01	1.5394±0.0561	832.1±22.4
156.2±18.8	7.764e-01±2.239e-02	-1.063e-01±4.209e-03	1.759e-01±1.813e-02	1.5510±0.1169	830.8±22.2
303.4±17.2	1.340e-02±1.427e-03	5.093e-04±2.182e-04	2.201e-03±1.135e-03	1.5504±0.1170	825.1±19.7
428.1±16.7	4.594e-03±6.288e-04	2.470e-04±1.216e-04	3.324e-04±5.103e-04	1.5504±0.1187	826.4±19.5
552.8±15.8	1.211e-03±3.239e-04	-6.920e-06±7.378e-05	-8.953e-05±2.683e-04	1.5513±0.1197	827.4±19.2

Table 6.23: Separated ^{3}He(e,e$'$p)D response functions. Top table: (ω, q, P_{miss}) phase space matching between Σ_1, Σ_2, Σ_3 kinematics. Bottom table: (ω, q, P_{miss}) phase space matching between Σ_1 and Σ_2 kinematics only.

6.5 ^{3}He(e,e$'$p)pn cross sections and spectral functions

Figs. 6-33 through 6-36 show the ^{3}He(e,e$'$p)pn cross sections extracted in the measurements. The corresponding analysis is described in Sec. 5.8.3. The ^{3}He(e,e$'$p)pn cross sections were extracted with the model independent technique only, with ω and q phase space restricted by the contour cut shown in Fig. 5-17. The cross sections were extracted only up to E_{miss} of 30 MeV. E89044 data with E_{miss} above 30 MeV is the subject of thesis of Fatiha Benmokhtar [12].

Also shown in the figures is the factorization (5.19) – (5.20) of the Salme spectral function with the cc1 prescription for the off-shell electron-nucleon cross section. As described in Sec. 5.8, the Salme spectral function reasonably well reproduces the observed relative strengths of the ^{3}He(e,e$'$p)D and ^{3}He(e,e$'$p)pn processes at each P_{miss} value (for $E_{miss} < 30$ MeV). In accord with this statement, as was the case for the extracted ^{3}He(e,e$'$p)D cross sections (Sec. 6.1), the theory reasonably well agrees with the data in the low P_{miss} regime, is slightly above the measured cross sections for P_{miss} from 150 to 300 MeV/c, and is below the cross sections for $P_{miss} > 300$ MeV/c.

Fig. 6-37 shows the ratio of the integral $\int_{7.72MeV}^{20MeV} S_{3bbu} dE_{miss}$ of the extracted ^{3}He(e,e$'$p)pn distorted spectral function (S_{3bbu}) to the extracted ^{3}He(e,e$'$p)D distorted spectral function, for Σ_1 kinematics ($E_{beam} = 4.8$ GeV, the detected proton is back of $\vec{q}$). As seen from the figure, the ratio is rather stable at ~ 0.7, with the exception of the datapoint at $P_{miss} \sim 73$ MeV/c, where the ratio is ~ 0.3. At the low missing momenta, both the Salme spectral function and the data show that the unradiated ^{3}He(e,e$'$p)pn cross section is very narrowly peaked at E_{miss} close to 7.72 MeV. Therefore, the datapoint at $P_{miss} \sim 73$ MeV/c might be subjected to strong averaging effects, for the averaging of the peaked ^{3}He(e,e$'$p)pn cross section with the flat simulation cross section over the E_{miss} bin from 7.72 to 10 MeV (and over the P_{miss} bin from 0 to 120 MeV/c).

The extracted ^{3}He(e,e$'$p)pn cross sections, distorted spectral functions, and the integral of the distorted spectral functions from E_{miss} of 7.72 MeV to 20 MeV, are tabulated in Tables 6.24 though 6.30.

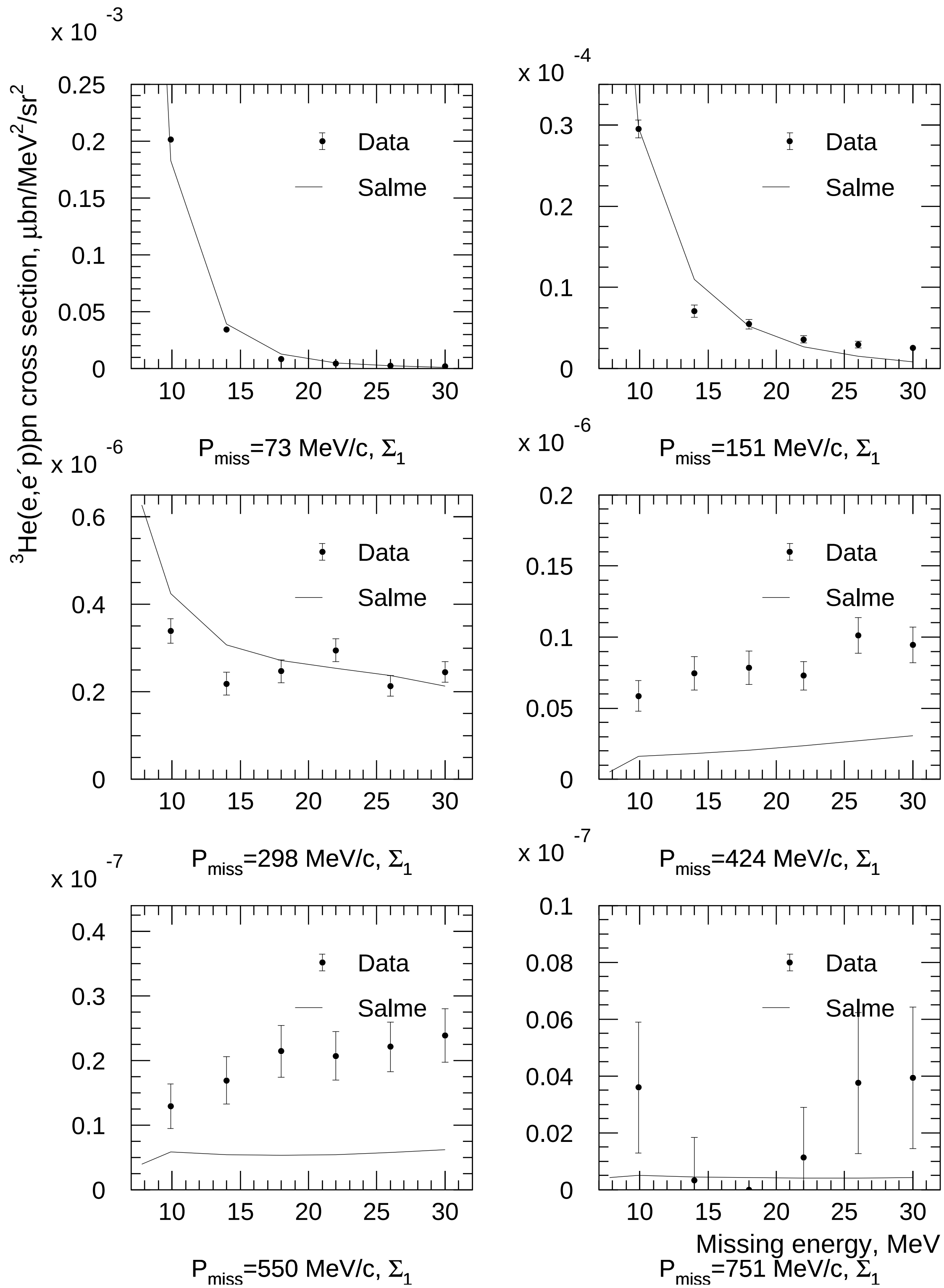

Figure 6-33: ^{3}He(e,e$'$p)pn cross sections extracted at Σ_1 kinematics, and Salme spectral function factorized by the cc1 e-p cross section.

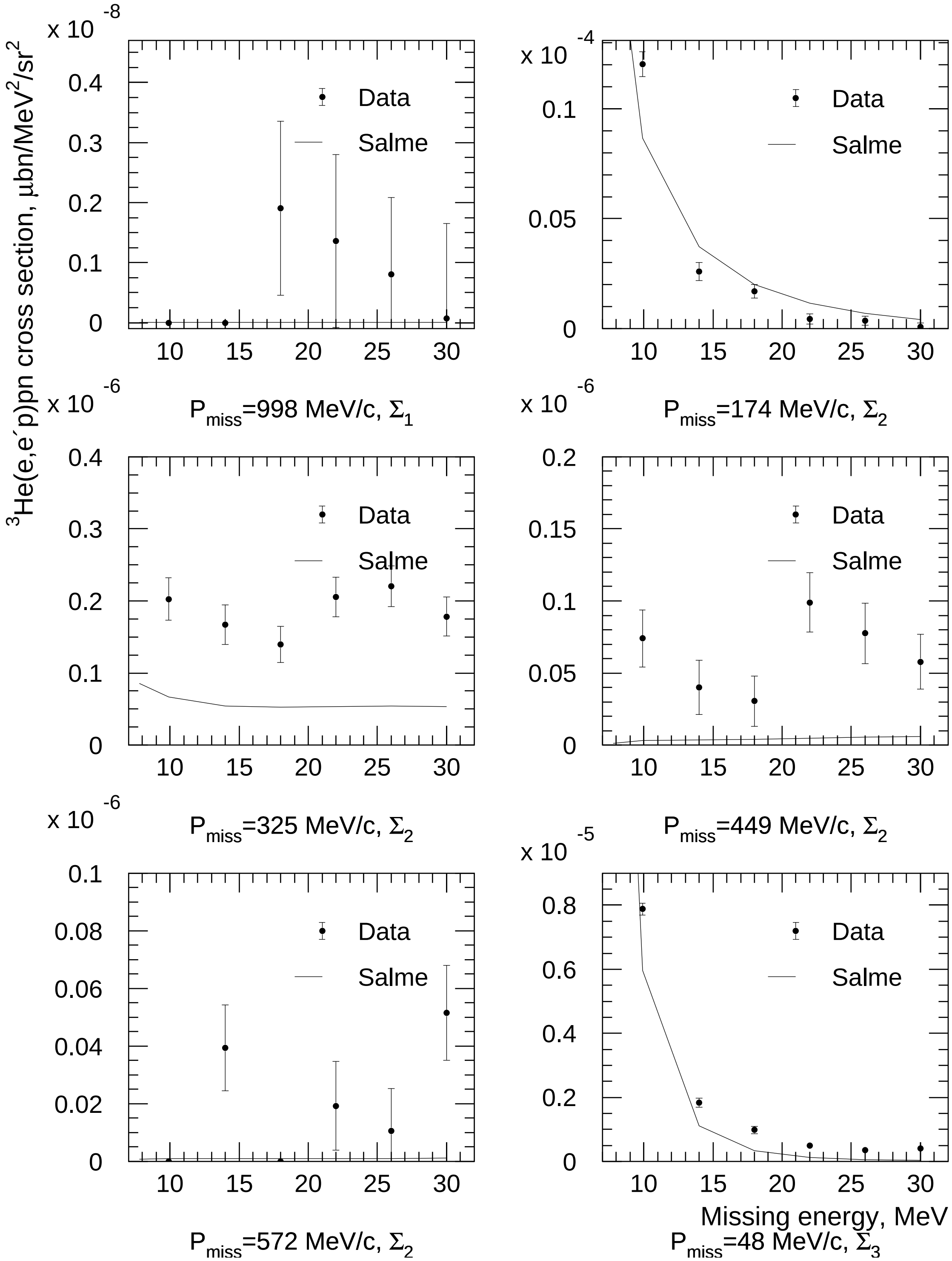

Figure 6-34: ^{3}He(e,e$'$p)pn cross sections extracted at Σ_1, Σ_2 and Σ_3 kinematics, and Salme spectral function factorized by the cc1 e-p cross section.

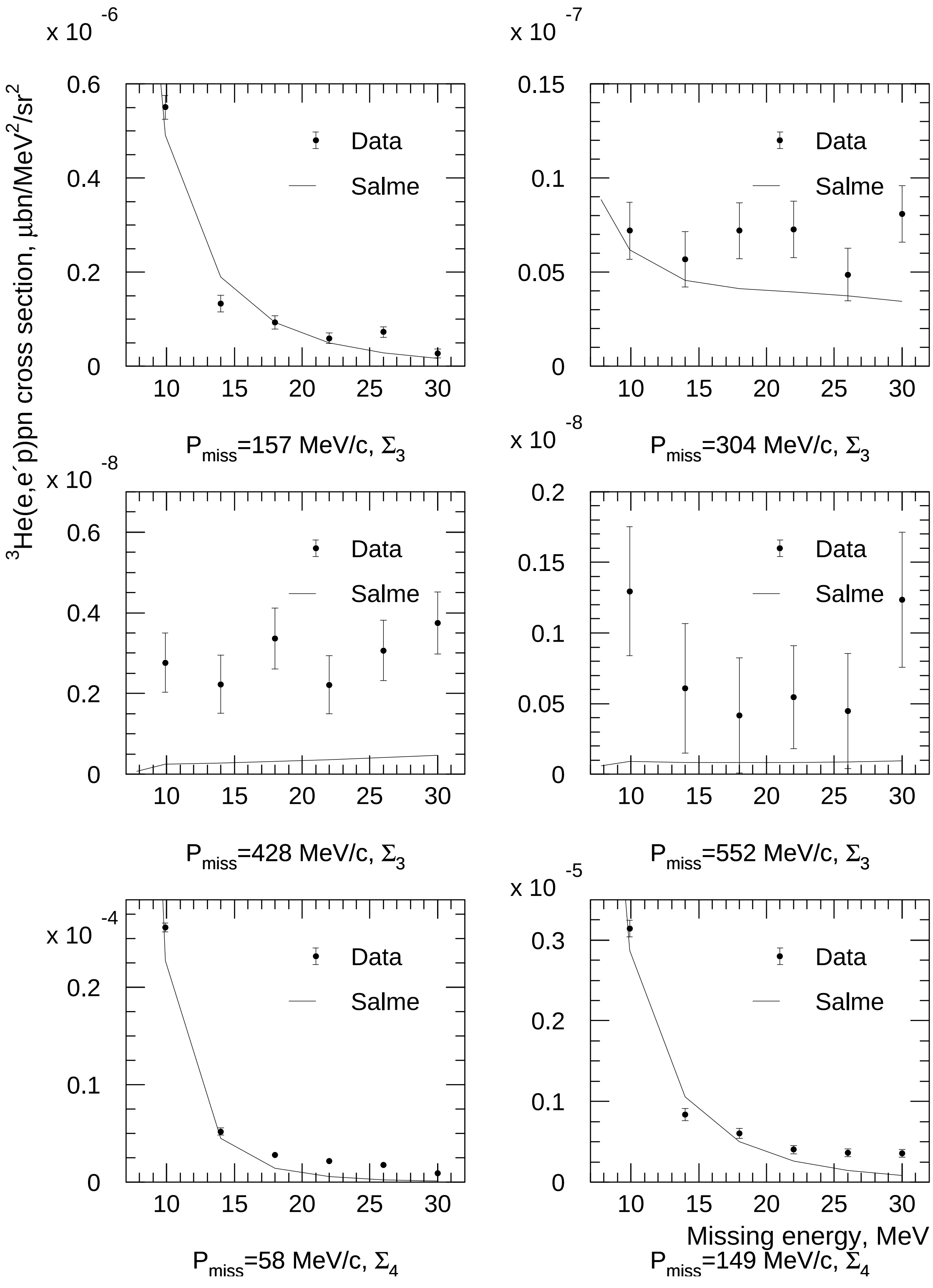

Figure 6-35: ^{3}He(e,e$'$p)pn cross sections extracted at Σ_3 and Σ_4 kinematics, and Salme spectral function factorized by the cc1 e-p cross section.

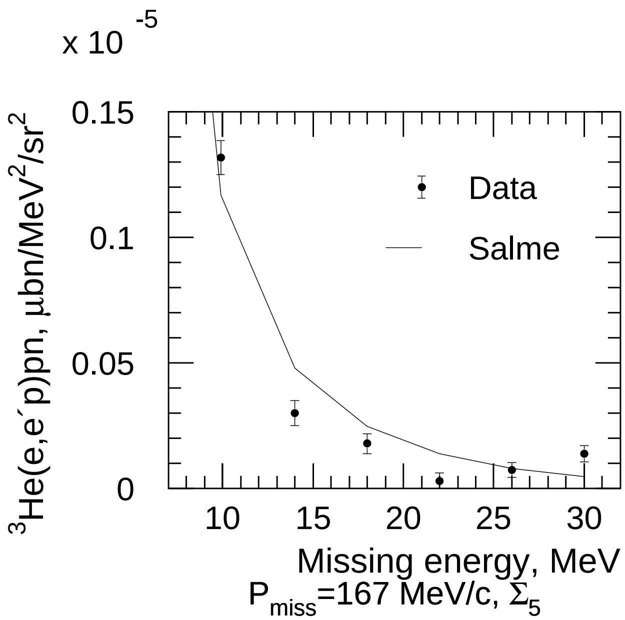

Figure 6-36: ^{3}He(e,e′p)pn cross sections extracted at Σ_5, kinematics, and Salme spectral function factorized by the cc1 e-p cross section.

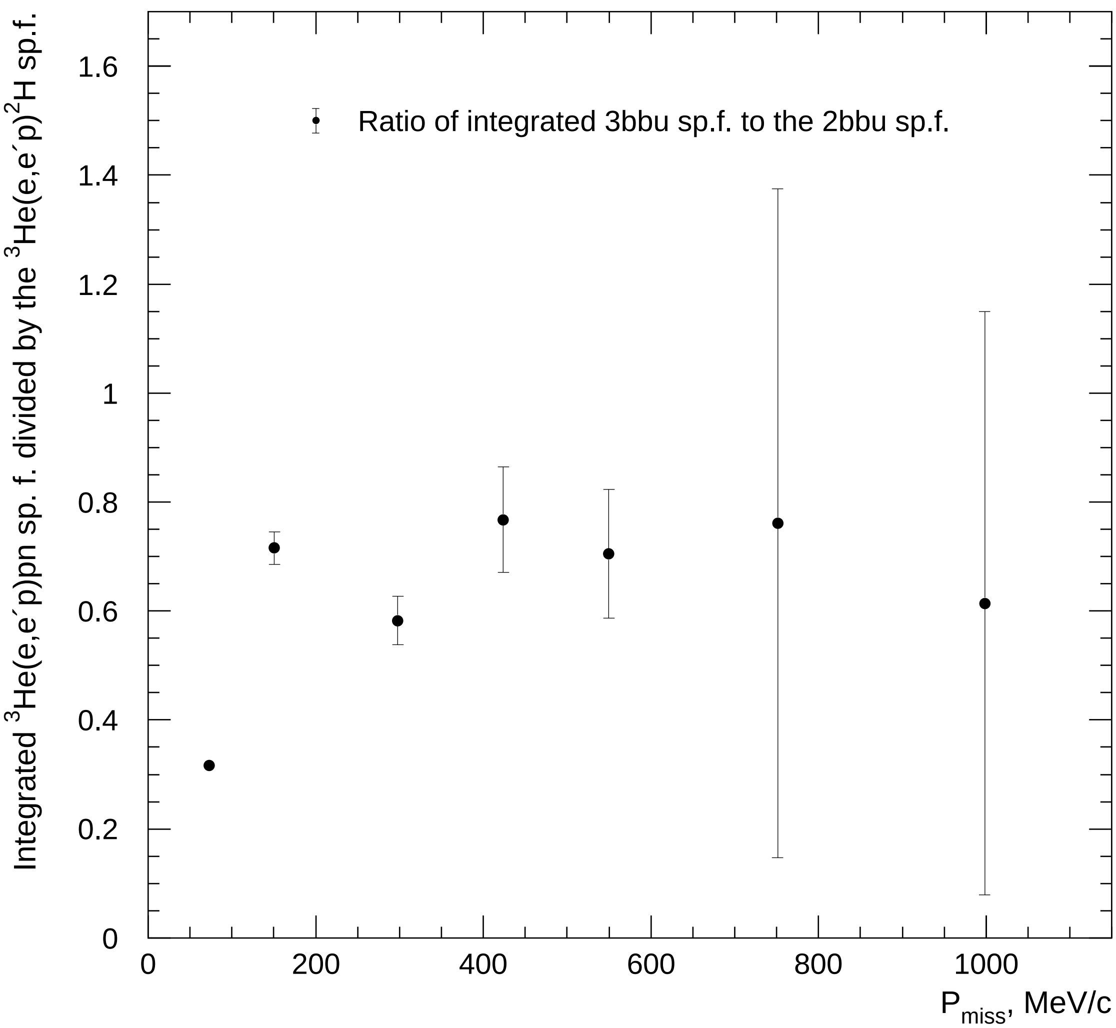

Figure 6-37: The integral $\int_{7.72MeV}^{20MeV} S_{3bbu} dE_{miss}$ divided by the extracted ^{3}He(e,e′p)D distorted spectral function. S_{3bbu} denotes the extracted ^{3}He(e,e′p)pn distorted spectral function. Σ_1 kinematics (beam energy 4.8 GeV, the detected proton back of $\vec{q}$).

$P_{miss} \pm \sigma_{Pm}$ MeV/c	E_{miss} MeV	$\frac{d^6\sigma^{ind}}{dE_f dE_p d\Omega_e d\Omega_p} \pm \epsilon_{st}$ μb MeV^{-2}sr^{-2}	$S_{3bbu}(E_{miss}, P_{miss})$ fm^3/MeV	$\int_{7.72MeV}^{20MeV} S_{3bbu} dE_{miss} \pm \epsilon_{st}$ fm^3	$\bar{Q}^2 \pm \sigma_{Q^2}$ (GeV/c)^2	$\bar{\omega} \pm \sigma_{\omega}$ MeV
72.8±28.6	9.9	1.980e-04±1.3%	6.408e-02	3.289e-01±1.4%	1.5635±0.0789	825.9±13.2
	14.0	3.370e-05±5.7%	1.096e-02			
	18.0	8.215e-06±18.1%	2.682e-03			
	22.0	4.330e-06±28.4%	1.421e-03			
	26.0	2.728e-06±39.9%	9.007e-04			
	30.0	2.254e-06±44.6%	7.493e-04			
150.7±23.5	9.9	2.903e-05±3.8%	8.280e-03	4.958e-02±3.5%	1.5623±0.0789	826.9±13.6
	14.0	6.957e-06±10.9%	1.991e-03			
	18.0	5.378e-06±10.6%	1.545e-03			
	22.0	3.550e-06±12.7%	1.024e-03			
	26.0	2.890e-06±14.1%	8.373e-04			
	30.0	2.478e-06±15.3%	7.211e-04			
297.9±22.9	9.9	3.329e-07±8.3%	7.833e-05	7.689e-04±5.7%	1.5663±0.0828	825.5±13.3
	14.0	2.147e-07±11.8%	5.073e-05			
	18.0	2.431e-07±10.5%	5.769e-05			
	22.0	2.901e-07±8.9%	6.914e-05			
	26.0	2.099e-07±11.1%	5.024e-05			
	30.0	2.409e-07±9.6%	5.794e-05			

Table 6.24: ^{3}He(e,e$'$p)pn cross sections, distorted spectral function and integral of the spectral function from 7.72 MeV to 20 MeV extracted at kinematics 1, 4 and 7; incident electron energy 4805.5 MeV.

$P_{miss} \pm \sigma_{Pm}$ MeV/c	E_{miss} MeV	$\frac{d^6\sigma^{ind}}{dE_f dE_p d\Omega_e d\Omega_p} \pm \epsilon_{st}$ μb MeV^{-2}sr^{-2}	$S_{3bbu}(E_{miss}, P_{miss})$ fm^3/MeV	$\int_{7.72MeV}^{20MeV} S_{3bbu} dE_{miss} \pm \epsilon_{st}$ fm^3	$\bar{Q}^2 \pm \sigma_{Q^2}$ (GeV/c)^2	$\bar{\omega} \pm \sigma_\omega$ MeV
424±21.9	9.9	5.765e-08±18.3%	1.180e-05	1.747e-04±9.4%	1.5649±0.0828	825.4±13.1
	14.0	7.333e-08±15.9%	1.509e-05			
	18.0	7.715e-08±15.1%	1.594e-05			
	22.0	7.156e-08±13.8%	1.486e-05			
	26.0	9.942e-08±12.5%	2.075e-05			
	30.0	9.286e-08±13.2%	1.948e-05			
549.8±22.1	9.9	1.275e-08±26.7%	2.403e-06	3.898e-05±12.6%	1.5711±0.0797	825.7±13.1
	14.0	1.664e-08±21.8%	3.155e-06			
	18.0	2.108e-08±18.8%	4.019e-06			
	22.0	2.037e-08±18.1%	3.903e-06			
	26.0	2.177e-08±17.4%	4.196e-06			
	30.0	2.348e-08±17.3%	4.551e-06			
751.3±22.2	9.9	3.539e-09±64.0%	6.156e-07	2.859e-06±69.4%	1.5694±0.0814	824.2±13
	14.0	3.193e-10±467.6%	5.590e-08			
	18.0	0	0			
	22.0	1.113e-09±155.6%	1.974e-07			
	26.0	3.695e-09±66.0%	6.594e-07			
	30.0	3.877e-09±63.0%	6.964e-07			

Table 6.25: ^{3}He(e,e′p)pn cross sections, distorted spectral function and integral of the spectral function from 7.72 MeV to 20 MeV extracted at kinematics 10, 13 and 28; incident electron energy 4805.5 MeV.

$P_{miss} \pm \sigma_{Pm}$ MeV/c	E_{miss} MeV	$\frac{d^6\sigma^{ind}}{dE_f dE_p d\Omega_e d\Omega_p} \pm \epsilon_{st}$ μb MeV^{-2}sr^{-2}	$S_{3bbu}(E_{miss}, P_{miss})$ fm^3/MeV	$\int_{7.72MeV}^{20MeV} S_{3bbu} dE_{miss} \pm \epsilon_{st}$ fm^3	$\bar{Q}^2 \pm \sigma_{Q^2}$ (GeV/c)^2	$\bar{\omega} \pm \sigma_\omega$ MeV
998.2±20.5	9.9	0	0	1.384e-06±76.2%	1.5699±0.081	825.5±13.4
	14.0	0	0			
	18.0	1.871e-09±76.2%	3.460e-07			
	22.0	1.335e-09±106.1%	2.488e-07			
	26.0	7.888e-10±160.2%	1.481e-07			
	30.0	7.192e-11±2162.5%	1.360e-08			
174.1±29.6	9.9	1.182e-05±4.7%	5.969e-03	3.407e-02±4.6%	1.5789±0.0794	823.8±13
	14.0	2.559e-06±15.5%	1.290e-03			
	18.0	1.667e-06±17.9%	8.393e-04			
	22.0	4.257e-07±54.2%	2.140e-04			
	26.0	3.580e-07±55.1%	1.796e-04			
	30.0	7.427e-08±244.8%	3.717e-05			
324.5±30	9.9	1.992e-07±14.4%	1.261e-04	1.302e-03±9.3%	1.5732±0.0804	824.3±13
	14.0	1.646e-07±16.4%	1.039e-04			
	18.0	1.374e-07±18.1%	8.662e-05			
	22.0	2.022e-07±13.4%	1.273e-04			
	26.0	2.170e-07±12.8%	1.363e-04			
	30.0	1.754e-07±15.4%	1.099e-04			

Table 6.26: ^{3}He(e,e$'$p)pn cross sections, distorted spectral function and integral of the spectral function from 7.72 MeV to 20 MeV extracted at kinematics 29, 5 and 8; incident electron energy 4805.5 MeV.

$P_{miss} \pm \sigma_{Pm}$ MeV/c	E_{miss} MeV	$\frac{d^6\sigma^{ind}}{dE_f dE_p d\Omega_e d\Omega_p} \pm \epsilon_{st}$ μb MeV^{-2}sr^{-2}	$S_{3bbu}(E_{miss}, P_{miss})$ fm^3/MeV	$\int_{7.72MeV}^{20MeV} S_{3bbu} dE_{miss} \pm \epsilon_{st}$ fm^3	$\bar{Q}^2 \pm \sigma_{Q^2}$ (GeV/c)^2	$\bar{\omega} \pm \sigma_\omega$ MeV
448.7±30.1	9.9	7.270e-08±26.6%	5.351e-05	4.326e-04±22.2%	1.5661±0.0805	824±13
	14.0	3.937e-08±47.3%	2.891e-05			
	18.0	3.000e-08±57.4%	2.199e-05			
	22.0	9.731e-08±20.9%	7.118e-05			
	26.0	7.624e-08±27.0%	5.566e-05			
	30.0	5.687e-08±33.1%	4.143e-05			
571.5±30.3	9.9	0	0	1.312e-04±38.0%	1.5693±0.0821	823.8±13.1
	14.0	3.874e-08±38.0%	3.281e-05			
	18.0	0	0			
	22.0	1.897e-08±79.4%	1.601e-05			
	26.0	1.042e-08±138.6%	8.782e-06			
	30.0	5.066e-08±32.0%	4.260e-05			
47.9±19	9.9	7.746e-06±2.4%	1.212e-01	6.912e-01±2.4%	1.556±0.0361	834.4±9.3
	14.0	1.797e-06±7.8%	2.810e-02			
	18.0	9.623e-07±11.4%	1.506e-02			
	22.0	4.799e-07±18.5%	7.514e-03			
	26.0	3.440e-07±22.9%	5.392e-03			
	30.0	3.951e-07±18.7%	6.204e-03			

Table 6.27: ^{3}He(e,e$'$p)pn cross sections, distorted spectral function and integral of the spectral function from 7.72 MeV to 20 MeV extracted at kinematics 11, 14 and 3; incident electron energy 4805.5 MeV and 1253.8 MeV.

$P_{miss} \pm \sigma_{Pm}$ MeV/c	E_{miss} MeV	$\frac{d^6\sigma^{ind}}{dE_f dE_p d\Omega_e d\Omega_p} \pm \epsilon_{st}$ μb MeV^{-2}sr^{-2}	$S_{3bbu}(E_{miss}, P_{miss})$ fm^3/MeV	$\int_{7.72MeV}^{20MeV} S_{3bbu} dE_{miss} \pm \epsilon_{st}$ fm^3	$\bar{Q}^2 \pm \sigma_{Q^2}$ (GeV/c)^2	$\bar{\omega} \pm \sigma_\omega$ MeV
156.5±19.2	9.9	5.411e-07±4.7%	7.937e-03	4.703e-02±4.4%	1.5549±0.036	834.7±9.3
	14.0	1.310e-07±13.5%	1.922e-03			
	18.0	9.136e-08±15.2%	1.341e-03			
	22.0	5.860e-08±19.6%	8.607e-04			
	26.0	7.148e-08±15.5%	1.050e-03			
	30.0	2.703e-08±33.0%	3.976e-04			
303.5±17.6	9.9	7.081e-09±20.9%	9.554e-05	1.094e-03±12.8%	1.5568±0.0362	834.2±9.3
	14.0	5.582e-09±26.0%	7.542e-05			
	18.0	7.076e-09±20.7%	9.572e-05			
	22.0	7.150e-09±20.5%	9.686e-05			
	26.0	4.790e-09±28.6%	6.498e-05			
	30.0	7.963e-09±18.5%	1.082e-04			
428±17.1	9.9	2.719e-09±26.4%	3.448e-05	4.274e-04±15.2%	1.5575±0.0361	834±9.3
	14.0	2.192e-09±32.1%	2.786e-05			
	18.0	3.305e-09±22.4%	4.209e-05			
	22.0	2.179e-09±32.3%	2.781e-05			
	26.0	3.015e-09±24.5%	3.857e-05			
	30.0	3.684e-09±20.6%	4.723e-05			

Table 6.28: ^{3}He(e,e$'$p)pn cross sections, distorted spectral function and integral of the spectral function from 7.72 MeV to 20 MeV extracted at kinematics 6, 9 and 12; incident electron energy 1253.8 MeV.

$P_{miss} \pm \sigma_{Pm}$ MeV/c	E_{miss} MeV	$\frac{d^6\sigma^{ind}}{dE_f dE_p d\Omega_e d\Omega_p} \pm \epsilon_{st}$ μb MeV^{-2}sr^{-2}	$S_{3bbu}(E_{miss}, P_{miss})$ fm^3/MeV	$\int_{7.72MeV}^{20MeV} S_{3bbu} dE_{miss} \pm \epsilon_{st}$ fm^3	$\bar{Q}^2 \pm \sigma_{Q^2}$ (GeV/c)^2	$\bar{\omega} \pm \sigma_{\omega}$ MeV
552.4±16.8	9.9	1.274e-09±35.3%	1.546e-05	1.153e-04±32.6%	1.5581±0.0359	833.9±9.3
	14.0	5.982e-10±75.6%	7.283e-06			
	18.0	4.094e-10±97.8%	4.999e-06			
	22.0	5.356e-10±66.7%	6.559e-06			
	26.0	4.413e-10±90.9%	5.422e-06			
	30.0	1.214e-09±38.8%	1.496e-05			
58.4±26.2	9.9	2.574e-05±1.7%	8.930e-02	4.917e-01±1.9%	1.564±0.0446	826.6±14.2
	14.0	5.099e-06±7.3%	1.775e-02			
	18.0	2.757e-06±11.0%	9.632e-03			
	22.0	2.144e-06±12.8%	7.525e-03			
	26.0	1.744e-06±14.4%	6.153e-03			
	30.0	8.800e-07±26.8%	3.125e-03			
149.2±23.1	9.9	3.092e-06±3.2%	9.494e-03	5.808e-02±3.0%	1.5616±0.0448	827.8±14
	14.0	8.222e-07±8.9%	2.531e-03			
	18.0	5.925e-07±10.0%	1.829e-03			
	22.0	3.948e-07±13.0%	1.222e-03			
	26.0	3.587e-07±13.4%	1.114e-03			
	30.0	3.529e-07±13.6%	1.099e-03			

Table 6.29: ^{3}He(e,e$'$p)pn cross sections, distorted spectral function and integral of the spectral function from 7.72 MeV to 20 MeV extracted at kinematics 15, 33 and 34; incident electron energy 1253.8 MeV and 1953.0 MeV.

$P_{miss} \pm \sigma_{Pm}$ MeV/c	E_{miss} MeV	$\frac{d^6\sigma^{ind}}{dE_f dE_p d\Omega_e d\Omega_p} \pm \epsilon_{st}$ μb MeV^{-2}sr^{-2}	$S_{3bbu}(E_{miss}, P_{miss})$ fm^3/MeV	$\int_{7.72MeV}^{20MeV} S_{3bbu} dE_{miss} \pm \epsilon_{st}$ fm^3	$\bar{Q}^2 \pm \sigma_{Q^2}$ (GeV/c)^2	$\bar{\omega} \pm \sigma_\omega$ MeV
166.7±25.4	9.9	1.295e-06±5.2%	5.982e-03	3.431e-02±5.1%	1.5654±0.0443	825.9±14.1
	14.0	2.963e-07±16.6%	1.367e-03			
	18.0	1.756e-07±21.7%	8.092e-04			
	22.0	3.033e-08±101.1%	1.395e-04			
	26.0	7.193e-08±40.4%	3.303e-04			
	30.0	1.363e-07±23.8%	6.249e-04			

Table 6.30: ^{3}He(e,e$'$p)pn cross sections, distorted spectral function and integral of the spectral function from 7.72 MeV to 20 MeV extracted at kinematics 35; incident electron energy 1953.0 MeV. The detected proton is at angles forward of $\vec{q}$.

6.6 Systematic uncertainties

This section describes the calculation of systematic uncertainties associated with the measurements[8]. Systematic errors are divided into "normalization" uncertainties, which propagate as a multiplicative correction to the extracted cross sections, distorted spectral functions and response functions (the A_{TL} is not subject to the normalization errors), and other uncertainties. In this section we adopt the following notation: the energy of the incident electron – E_i; the horizontal (vertical) angle of the incident electron – ϕ_i (θ_i); the energy of the detected electron – E_e; the horizontal (vertical) angle of the detected electron – ϕ_e (θ_e); the momentum of the detected proton – P_p; the horizontal (vertical) angle of the detected proton – ϕ_p (θ_p).

6.6.1 Normalization uncertainties

The adopted scheme for normalization of the ^{3}He(e,e$'$p) data (i.e. the procedure for determination of the integrated luminosities during the ^{3}He(e,e$'$p) runs) is described in Sec. 4.1. The corresponding to the scheme errors are:

1. The uncertainty in the measured density of the ^{3}He gas in the target. The density was determined in a set of elastic ^{3}He(e,e) measurements at the beam energy of 644 MeV.

2. The error in assuming the stability of the ^{3}He density during changes in the beam energy.

3. The error associated with the luminosity monitoring procedure.

The last two errors are not normalization errors[9], and are described in the next subsection. Here we describe the calculation of the errors associated with the measurement of the ^{3}He density in a set of elastic ^{3}He(e,e) measurements at the beam energy of 644 MeV.

[8] All errors quoted prior to this section are statistical only.

[9] In the sense that these errors do not propagate as an overall correction to *all* results.

Quantity	Sensitivity	Uncertainty	Error
E_i	$1.1\%/(10^{-3}$ rel.)	$2 \cdot 10^{-4}$	0.22%
ϕ_i	1.7 %/mrad	0.1 mrad	0.17%
θ_i	0.006%/mrad	0.1 mrad	0%
ϕ_e	1.7 %/mrad	0.3 mrad	0.51%
θ_e	0.005 %/mrad	2 mrad	0.01%
Sum in quadr.			0.6%

Table 6.31: Kinematic systematic error averaged over acceptance in the ^{3}He(e,e) elastic measurements.

Quantity	Uncertainty
Deadtime	1%
Solid angle	1%
Cut on target length	1.4%
Cut on elastic peak	0.2%
Stat. error	0.5%
^{3}He form factor error	1.5%
Tracking efficiencies	0.5%
Radiative corrections	1%
Accum. beam charge	0.5%
Sum in quadr.	2.8%
Kinematic error	0.6%
Total kin+non-kin in quadr.	2.9%

Table 6.32: Non-kinematic errors associated with the ^{3}He(e,e) elastic measurements, and the total error of the measurements.

Table 6.31 summarizes so called "kinematic errors" for the elastic ^{3}He(e,e) scattering setting with $E_{beam} = 644$ MeV and $Q^2 = 2.9$ fm^{-2}. The kinematic errors are those due to the sensitivity of the elastic ^{3}He(e,e) cross section to E_i, ϕ_i, θ_i, ϕ_e and θ_e, and uncertainties in these quantities. The kinematic errors were determined with the code "systerr" [80], written by K. Fissum and P. Ulmer. This code works in conjunction with the MCEEP simulation, and calculates the sensitivities to a small variation of each of the quantities mentioned above averaged over acceptance. These calculated sensitivities are given in the second column of Table 6.31. The third column of the table gives assumed uncertainties in the measurements of E_i, ϕ_i, θ_i, ϕ_e and θ_e. The fourth column of the table gives the product of the values in the second and in the third columns. The quadratic sum ($\sqrt{\sum \epsilon_i^2}$) of the errors in the fourth column yields the estimate of 0.6% for the kinematic systematic error.

Table 6.32 summarizes non-kinematic errors associated with the ^{3}He density measurements. These errors are added in quadrature with the kinematic systematic error to yield the estimate of 2.9% for the total uncertainty in the measured ^{3}He density (Table 6.32). This error propagates as a normalization factor to the extracted cross sections, distorted spectral functions and response functions.

6.6.2 Uncertainties in the ^{3}He(e,e′p)D analysis

Sensitivities of the ^{3}He(e,e′p)D cross sections to small offsets in E_i, ϕ_i, θ_i, E_e, ϕ_e, θ_e, P_p, ϕ_p and θ_p, averaged over the acceptance with the code "systerr", are presented in the top part of Table 6.33. The right column of the table gives assumed uncertainties in the measured quantities. The row of the table fifth from the bottom gives the quadratic sum[10] of the products of the sensitivities with the corresponding uncertainties[11]. One of the largest contributions to the total error is due to an uncertainty in the reconstructed absolute value of P_{miss}. In perpendicular kinematics, this uncertainty stems mostly from an uncertainty in the direction of $\vec{q}$, and from an uncertainty in the reconstructed direction of the detected proton.

One can distinguish several kinematic situations in which the uncertainty in the reconstructed P_{miss} is largest:

- At the beam energy of 4.8 GeV, the large value of E_e ($\sim$ 4 GeV), translates (with a fixed relative error on E_e) into a large absolute error on E_e, which in turn almost directly translates into the uncertainty in the direction of $\vec{q}$.

- At the high P_{miss} edge of kinematics 1, the accepted ^{3}He(e,e′p) events were close to 90° out-of-plane, and therefore the uncertainty in P_{miss} followed from

[10] I.e., with the formula $\epsilon_{tot} = \sqrt{\sum \epsilon_i^2}$.

[11] The relative uncertainty in E_e was set to be smaller than that for P_p, since in the procedure of calibration of the central momentum of the spectrometers (Sec. 5.7), the reconstructed position of the ^{3}He(e,e′p)D peak in the E_{miss} spectrum at E_{beam} = 4.8 GeV and E_{beam} = 1.9 GeV settings was more sensitive to the electron spectrometer central momentum than to the hadron spectrometer central momentum; as seen from Table 6.33, the uncertainty in E_e at E_{beam} = 1.2 GeV settings practically does not contribute to the total kinematic uncertainty.

Kinematic quantity	Kinematic setting																			Nominal uncert.
	1	4	7	10	13	28	29	5	8	11	14	3	6	9	12	15	33	34	35	
E_i, %/(10^{-3} rel.)	4.6	11.7	6.1	2.4	7.5	1.9	1.7	13.6	3.6	3.3	1.7	1.2	1	1	0.6	1.4	1.5	3.9	3.8	$2 \cdot 10^{-4}$
ϕ_i, %/mrad	3	4.1	1	1.4	0.01	2.4	2.7	11.2	5.7	6.7	5	0.7	3.2	1.3	0.2	1.3	1.3	3.8	6.3	0.1 mrad
θ_i, %/mrad	0.03	0.1	0.1	0.1	0.2	0.1	0.05	0.2	0.04	0.05	0.03	0.02	0.1	0.03	0.006	0.02	0.1	0.03	0.1	0.1 mrad
E_e, %/(10^{-3} rel.)	4.9	9.9	5.2	1.6	5.9	1	0.8	13.5	3.8	4	2.2	0.01	0.7	0.2	0.1	0.1	1.1	3.1	4.1	$5 \cdot 10^{-4}$
ϕ_e, %/mrad	1.8	0.1	1.1	2.1	2.1	2.8	3	6.3	3.9	4.9	3.6	0.2	1.1	0.7	0.4	0.9	0.1	0.6	0.9	0.3 mrad
θ_e, %/mrad	0.005	0.04	0.1	0.1	0.2	0.1	0.05	0.2	0.03	0.04	0.02	0.008	0.02	0.01	0.003	0.006	0.05	0.02	0.1	2 mrad
P_p, %/(10^{-3} rel.)	0.9	0.4	0.02	0.005	0.04	0.1	0.2	1.2	0.3	0.1	0.1	1.9	0.7	0.2	0.03	0.01	1	0.3	0.7	$1 \cdot 10^{-3}$
ϕ_p, %/mrad	1.4	3.8	2	0.6	2.1	0.4	0.3	4.9	1.6	1.9	1.2	1	4.3	2.1	0.6	2.1	1.2	4.4	5.4	0.3 mrad
θ_p, %/mrad	0.03	0.008	0.04	0.02	0.1	0.01	0.005	0.1	0.01	0.007	0.005	0.02	0.1	0.04	0.009	0.02	0.1	0.02	0.1	2 mrad
Sum in quadr., %	2.9	5.6	3	1.2	3.5	1.1	1.1	7.8	2.5	2.7	1.7	1.9	1.6	0.7	0.3	0.8	1.3	2.2	2.9	
Non-kin. error, %	3.4	3.4	3.4	3.4	3.4	3.4	3.4	3.4	3.4	3.4	3.4	3.4	3.4	3.4	3.4	3.4	3.4	3.4	3.4	
Sum in quadr., %	4.5	6.6	4.5	3.6	4.9	3.6	3.6	8.5	4.2	4.3	3.8	3.9	3.8	3.5	3.4	3.5	3.6	4.0	4.5	
Normal. error, %	2.9	2.9	2.9	2.9	2.9	2.9	2.9	2.9	2.9	2.9	2.9	2.9	2.9	2.9	2.9	2.9	2.9	2.9	2.9	
Total error, %	5.4	7.2	5.4	4.6	5.7	4.6	4.6	9.0	5.1	5.2	4.8	4.9	4.8	4.5	4.5	4.5	4.6	4.9	5.4	

Table 6.33: Top part of the table: sensitivities of extracted ^{3}He(e,e$'$p)D cross sections to uncertainties in kinematic parameters, averaged over acceptance. The fifth from the bottom row gives kinematic errors added in quadrature, assuming uncertainties in the right column. The bottom row gives total systematic errors of the ^{3}He(e,e$'$p)D measurements, for each kinematic setting.

Quantity	Error
Deadtime	1%
Solid angle	2%
Cut on target length	1.4%
E_{miss} cut on 2bbu peak	1.5%
Subtraction of 3bbu contrib.	0.3%
Transfer of ^{3}He density	0.5%
Tracking efficiency	1%
Luminosity monit. stat.	$< 0.1\%$
Radiative corrections	1%
Sum in quadrature	3.4%

Table 6.34: Non-kinematic errors associated with the ^{3}He(e,e$'$p)D cross section measurements.

the uncertainties in the reconstruction of θ_e and θ_p, which are substantially larger than those of ϕ_e and ϕ_p.

Naturally, the uncertainty in the reconstructed P_{miss} translates into a larger kinematic error at settings where the cross section varies sharply with P_{miss}, i.e. for P_{miss} from ~ 150 to ~ 300 MeV/c. Combined with the arguments given above, this leads to a conclusion that the kinematic systematic error is the largest at kinematics 4 and 5 ($E_{beam} = 4.8$ GeV, nominal $P_{miss} = 150$ MeV/c), which is confirmed by the values in Table 6.33.

Table 6.34 lists non-kinematic errors associated with the ^{3}He(e,e$'$p)D measurements. Errors in the reconstruction of the phase space volume of kinematic bins were calculated by introducing linear distortions in the ϕ and θ variables in the definition of the acceptance-limiting cut function f_1 (Appendix A.1), and observing changes in the simulated phase space volume due to these distortions. The contribution of the ^{3}He(e,e$'$p)pn reaction channel to the ^{3}He(e,e$'$p)D bins was in general $\sim 3\%$ of the number of detected events in the ^{3}He(e,e$'$p)D bins. This estimate was obtained with the ^{3}He(e,e$'$p) MCEEP simulation, by calculating the number of simulated ^{3}He(e,e$'$p)pn events falling within the ^{3}He(e,e$'$p)D bins, and a comparison to the number of simulated ^{3}He(e,e$'$p)D events falling within the same bins. The error allowed in the subtraction of the 3bbu contribution is estimated at $\sim 0.3\%$. The error due to an uncertainty in the position of the E_{miss} cut on the 2bbu peak was found by varying the position of the cut in a MCEEP simulation and observing changes in the number of events falling in the 2bbu bins. A similar technique was used for the estimate of the error due to an uncertainty in the position of the cut on the reconstructed reaction point along the beam. The error allowed in assuming the stability of the target density during the beam energy changes is estimated at 0.5% (Sec. 4.3).

Kinematic uncertainties of the ^{3}He(e,e′p)D analysis are added with the non-kinematic errors in quadrature in the third from the bottom row of Table 6.33. The bottom row of the table gives the total error of the ^{3}He(e,e′p)D measurements, obtained as the quadratic sum of the normalization error (2.9%) and the errors associated with the ^{3}He(e,e′p)D analysis.

6.7 Summary and conclusions

In this section we summarize obtained results and draw conclusions. The ^{3}He(e,e′p)D and ^{3}He(e,e′p)pn cross sections and distorted spectral functions were measured in perpendicular coplanar kinematics, with ω and q fixed at 837 MeV and 1500 MeV/c respectively (quasielastic peak), at three beam energies of 1.2, 1.9 and 4.8 GeV, up to missing momenta of 1000 MeV/c. The A_{TL} asymmetry and R_T, $R_L + R_{TT}V_{TT}/V_L$ and R_{TL} response functions were separated for the ^{3}He(e,e′p)D reaction channel up to missing momenta of 550 MeV/c. The obtained dataset significantly extends currently available data on the quasielastic ^{3}He(e,e′p) reaction, both in the momentum transfer and in the missing momentum.

In the low P_{miss} regime, available calculations based on Faddeev-type wave functions overestimate the ^{3}He(e,e′p)D cross sections, while a reasonable agreement is observed for calculations based on variational wave functions. It is concluded, that the worse performance of the Faddeev-type calculations of the wave function is likely to be due to their well-known underbinding of the ^{3}He nucleus by $\sim$ 0.7 MeV; the variational calculations reproduce the ^{3}He binding energy by construction.

For P_{miss} from 100 to 740 MeV/c, strong final state interactions effects, in general consistent with available calculations, are observed. The effect is quenching below P_{miss} of about 300 MeV/c, and vastly enhancing the ^{3}He(e,e$'$p)D cross section above 300 MeV/c. Based on Laget's diagrammatic expansion [6, 5], to a lower degree MEC and/or isobaric currents are expressed above the missing momentum of 250 MeV/c. However, in a Glauber-type FSI calculation of Ciofi degli Atti and Kaptari [81], all (and even more than) the observed strength for P_{miss} from 300 to 600 MeV/c is explained only by FSI. Therefore, at present it cannot be conclusively stated on the role of MEC and isobaric currents in this region.

At missing momenta from 740 to 1035 MeV/c, the ^{3}He(e,e$'$p)D reaction channel strength is observed to be far above than that predicted by available theories. It has been suggested that it could be due to multiple scattering experienced by the knocked-out proton on its bound neighbors. Understanding processes in this very interesting region needs further theoretical work. In general, it is concluded that nucleonic models of the ^{3}He structure seem to work quite well in quasielastic kinematics at the very short ($\sim$ 0.1 fm) wavelength of the exchanged photon, at least up to missing momenta of $\sim$ 740 MeV/c.

The measured ^{3}He(e,e$'$p)D A_{TL} asymmetry exhibits a strong oscillation-type enhancement for P_{miss} from 220 to 480 MeV/c. Qualitatively, the enhancement is reproduced in all available calculations including FSI. However, quantitatively, the observed A_{TL} behavior is not reproduced by the theories. Based on the character of Udias's and Vignote's very preliminary calculations [82], it can be suggested that some of the enhancement is due to dynamical relativistic effects, but more theoretical calculations are necessary to draw a conclusive statement.

Above P_{miss} of 300 MeV/c, the measured ^{3}He(e,e$'$p)D R_T and $R_L + R_{TT}V_{TT}/V_L$ response functions are very well reproduced by Laget's diagrammatic expansions including lowest-order FSI, MEC and intermediate Δ formation amplitudes, indicating the importance of these process in this region. Below P_{miss} of 200 MeV/c, a disagreement with Laget's calculations is observed, which, as mentioned above, might be due to the underbinding of the ^{3}He nucleus by Faddeev-type calculations of the wave function. However, it should be noted that the convergence of low-order diagrammatic expansions is not guaranteed, especially at higher missing momenta [2].

The measured ^{3}He(e,e$'$p)D R_{TL} response function is not reproduced by available calculations, in particular in its positive sign for P_{miss} from 300 to 450 MeV/c. As well as for the A_{TL}, the main hope in reproducing the R_{TL} behavior in this region is in the correct treatment of FSI and relativity in the calculations.

The observed up to E_{miss} of 30 MeV strength of the ^{3}He(e,e$'$p)pn reaction channel relative to the strength of the ^{3}He(e,e$'$p)D reaction channel at each P_{miss} value is, in the first approximation, very well reproduced by the Salme spectral function. Analysis of the E89044 data for E_{miss} above 30 MeV will be presented elsewhere [12].

The extracted dataset presents a long-anticipated systematic study of electrodisintegration of ^{3}He in the (e,e$'$p) reaction at high momentum transfers. The dataset presents a challenge for theoretical work, after which more conclusions may be drawn.

Appendix A

Analysis programs

This section describes the definition of the spectrometer acceptance at (e,e′p) kinematic settings with the R-function cut (Sec. 5.3) and PAW programs written for extraction of the ^{3}He(e,e′p)D cross sections, both for the "model independent" and the "cc1-averaging" extraction procedures (Sec. 5.8).

A.1 Acceptance definition with R-functions

The following is the definition of the "cut function" f_1 constructed with the R-function technique (Sec. 5.3). The cut on the cut function f_1, together with the cut on the reaction point along the beam (Sec. 5.4) and the cut on the reconstructed out-of-plane angle (Sec. 5.1), restricted coincidence events to a flat acceptance region of both spectrometers. Below, f_1 is defined as a PAW function. This definition was used in restricting experimentally reconstructed events to the flat acceptance region. An equivalent definition was coded into the simulation code MCEEP and was used to restrict simulated events to an identical acceptance region.

```
REAL FUNCTION rfcut()
include ?
REAL F1,F2
REAL sp_cut
```

```
      F1=sp_cut(y_tgth,ph_tgth,th_tgth,dph)
      F2=sp_cut(y_tgte,ph_tgte,th_tgte,dpe)
      rfcut=PROD(F1,F2)
      END

* Definition of cut on one spectrometer
      REAL FUNCTION sp_cut(y_tgth,ph_tgth,th_tgth,dph)
      REAL C1,C2,C3,C4,C5,C6,C7,C8,C9,C10,C11,PROD
      REAL D1,D2,D3,D4,D5
      REAL E1,E2
      REAL y_tgth,ph_tgth,th_tgth,dph
* Definition of hyperplanes forming initial domain
      C1=-0.0137*ph_tgth+0.0502-th_tgth
      C2=0.0502+th_tgth
      C3=-0.136*y_tgth+0.02518-0.991*ph_tgth
      C4=y_tgth*0.136+0.02518+0.991*ph_tgth
      C5=-0.975*dph+0.0396-0.220*th_tgth
      C6=dph+0.0409+0.068*th_tgth
      C9=-0.421*dph-0.907*th_tgth+0.0561
      C7=-dph*0.1776+0.984*ph_tgth+0.0237
      C8=-dph*0.1738+0.0236-0.985*ph_tgth
      C10=0.319* y_tgth-0.948*ph_tgth+0.0336
      C11=-0.319*y_tgth+0.948*ph_tgth+0.0336

* Pairwise products of hyperplane functions
      D1=PROD(C1,C2)
      D2=PROD(C3,C4)
      D3=PROD(C5,C6)
      D3=PROD(C9,D3)
      D4=PROD(C7,C8)
      D5=PROD(C10,C11)

      E1=PROD(D1,D2)
      E2=PROD(D3,D4)
      E2=PROD(E2,D5)

      sp_cut=PROD(E1,E2)
      END

* Definition of R-function corresponding to logical AND
      REAL FUNCTION PROD(X,Y)
      REAL X,Y

      PROD=MIN(X,Y)
* Below are alternative definitions of R-functions
```

```
* corresponding to logical AND
*      PROD=X+Y-SQRT(X*X+Y*Y+2*0.9*X*Y)
*      PROD=X+Y-SQRT(X*X+Y*Y)
      RETURN
      END
```

A.2 Fitting programs

The following PAW program was used for adjustment of weights w_i assigned to the vertex E_{miss} simulation bins until the yield simulated within each asymptotic E_{miss} bin was equal to the yield detected experimentally (the procedure is described in Sec. 5.8). The program operates on a PAW HBOOK file [73, 72], containing:

- Ntuple 10: real coincident data (variables: E_{miss}, P_{miss}, Q^2, ω).
- Ntuple 11: accidental coincident data (variables: E_{miss}, P_{miss}, Q^2, ω).
- Ntuple 12: simulation (variables: E_{miss}, P_{miss}, Q^2, ω, vertex values of E_{miss}, P_{miss}, Q^2, ω, vertex cross section $sigma$ and MCEEP internal weight $numer\_wt$ assigned to each event [55]).

Events in the ntuples are restricted by cuts summarized in Sec. 5.1. The difference between the "cc1-averaging" and the "model independent" procedures is in the file "fillh1.f"[1] called by the program, which either fills the simulation histograms by weighting each event by the weight $numer\_wt$, or by $numer\_wt/sigma$.

The file "fillh2.f" fills histograms with the vertex values of E_{miss}, P_{miss}, Q^2 and ω. The file "diff.f" executes the Kolmogorov test of shape compatibility of two histograms. The files listed below were used for extraction of the ^{3}He(e,e$'$p)D cross sections at kinematics 4. Programs used at other kinematic settings were similar.

"do_fit.kumac":

```
macro do_fit
* Loop over Pmiss bins
```

[1] Listed below.

```
do pc=100,250,10
cut $10 [pc]<=prmag<$EVAL([pc]+10)
fname=$substring($cutexpand(out$10),1,$index($cutexpand(out$10),'<')-1)
* Define Emiss bins
nch=14
v/cre chan($EVAL([nch]+1)) R 0.5 7.72 9.72 11.72 13.72 15.72 \\
17.72 19.72 21.72 23.72 25.72 27.72 29.72 31.72 40
bins 20 ! [nch] chan
do i=21,38
hi/co 20 [i]
enddo
*Start fitting 2bbu peak position (Sigma1 and Sigma2 kinematics only)
1d 50 ! 1000 -3 7
call hbarx(0);
hi/co 50 51
hi/co 50 52
1d 60 ! 500 2 7
hi/co 60 61
v/cre dat(1000) R
v/co dat date
v/co dat mc
v/co dat mce
nt/plot 10.miss_m-1  $10 -50
nt/plot 11.miss_m-1  $10 -52
nt/plot 12.miss_m numer_wt&&$10 -51
sub 50 52 50
get/cont 50 dat
get/err 50 date
get/cont 51 mc
get/err 51 mce

maxv=0
maxi=0
do i=0,400
put/cont 60 dat($EVAL(501-[i]):$EVAL(1000-[i]))
put/err 60 date($EVAL(501-[i]):$EVAL(1000-[i]))
put/cont 61 mc(501:1000)
put/err 61 mce(501:1000)
res=$CALL('diff.f(1)')
if [res]>[maxv] then
maxv=[res]
maxi=[i]
endif
enddo
miss_sh=[maxi]*0.01-1
```

```
* At this point, miss_sh is the Emiss shift between data and simulation
* Below, apply shift globally fitted to all Pmiss bins
miss_sh=([pc]-118.5)*0.0063405815265
mess [miss_sh]
* End 2bbu peak position fitting

* Fill data histograms
nt/plot 10.miss_m+[miss_sh] $10 -20
nt/plot 11.miss_m+[miss_sh] $10 -21
* Subtract accidentals (widths of real and accidental windows
* is the same at kinematics 4)
sub 20 21 22 ! ! E
v/cre h22e([nch]) R
get/err 22 h22e

v/cre str([nch],[nch]) R
v/cre strd([nch]) R
* Fill simulation histograms
nt/plot 12.miss_m $10&&fillh1.f([nch])>0 ! ! ! ! 21

do i=1,[nch]
get/cont $EVAL([i]+22) str(1:[nch],[i])
v/inp strd([i]) str([i],[i])
enddo

v/cre coef([nch]) R [nch]*1
v/co coef data
v/co coef sim

* Start iterative calculation of weights assigned to simulation bins
ctr=1
difr=1
do k=1,1000
op/reset 37
do i=1,[nch]
add $EVAL([i]+22) 37 37 coef([i])
enddo

get/cont 22 data
get/cont 37 sim

v/co coef coefs

vsub data sim data
vmult coef strd coef
```

```
vadd data coef data
vdiv data strd coef

do l=1,[nch]
IF coef([l])<0 THEN
v/inp coef([l]) 0
ENDIF
enddo

hi/pl 22
hi/pl 37 s

* If weights did not change in 20 iterations, break out from the loop
difrs=$EVAL(difr)
SIGMA difr=vmax(abs(coefs-coef))
if $SIGMA(difr)=[difrs] then
ctr=[ctr]+1
else
ctr=1
endif
if [ctr]>20 then
breakl
endif
*mess $SIGMA(difr) $EVAL([difrs]) $EVAL([ctr]) $EVAL([k])
enddo
* End iterative calculation of weights assigned to simulation bins

do i=1, [nch]
1d $EVAL(1000+[i]*10) ! 2000 500 1500
1d $EVAL(1001+[i]*10) ! 2000 0 3
1d $EVAL(1002+[i]*10) ! 2000 0 1500
1d $EVAL(1003+[i]*10) ! 2000 0 45
enddo
v/cre val(3) R
v/cre hist(2000) R
v/cre absc(2000) R
v/write chan [fname] '30(F5.2,X)' O

* Fill simulation histograms with vertex Emiss, Pmiss, Q^2 and omega
nt/plot 12.missm_v $10&&fillh2.f([nch])>0 ! ! ! N 21
zon 1 4;hi/pl 1010;hi/pl 1011;hi/pl 1012;hi/pl 1013;

do i=1,[nch]
v/cre val(3) R
v/inp val(1) coef([i])  * This is the adjusted weight
```

```
v/inp val(2) $EVAL(str([i],[i])*coef([i]))

* Calculate statistical errors for weight i
op/reset 37
do j=1,[nch]
if [i]<>[j] then
add $EVAL([j]+22) 37 37 coef([j])
endif
enddo
sub 22 37 37
div 37 $EVAL([i]+22) 37
get/err 37 coefs

if coef([i])<>0 then
v/inp val(3) $EVAL(coefs([i])/coef([i])*val(2))
else
v/inp val(3) 0
endif
* End calculation of statistical errors for weight i

v/write val [fname] 'E20.10,2X,F10.2,2X,F10.2' ' '

v/cre val(4) R

* Write out mean, variance, etc, for Emiss, Pmiss, Q^2, omega
get/cont $EVAL(1000+[i]*10) hist;absci 1010 absc;exe do_fit#mean
v/write val [fname] '4X,F10.5,2X,F10.5,2X,F10.5,2X,F10.5' ' '

get/cont $EVAL(1001+[i]*10) hist;absci 1011 absc;exe do_fit#mean
v/write val [fname] '4X,F10.5,2X,F10.5,2X,F10.5,2X,F10.5' ' '

get/cont $EVAL(1002+[i]*10) hist;absci 1012 absc;exe do_fit#mean
v/write val [fname] '4X,F10.5,2X,F10.5,2X,F10.5,2X,F10.5' ' '

get/cont $EVAL(1003+[i]*10) hist;absci 1013 absc;exe do_fit#mean
v/write val [fname] '4X,F10.5,2X,F10.5,2X,F10.5,2X,F10.5' ' '
enddo
v/cre val(2) R [miss_sh] [maxv]
v/write val [fname] 'F10.5,2X,F14.9' C
zon 1 1
enddo
* End loop over Pmiss bins
return

* This macro computes mean, variance, etc, for histograms
```

```
macro mean
SIGMA pr=hist*absc
SIGMA half=abs(hist-maxv(hist)/1.99999)
SIGMA point=lvmax(hist)
v/del temp
v/co half(:$SIGMA(point)) temp
SIGMA low=absc(lvmin(temp))
v/del temp
v/co half($SIGMA(point):) temp
SIGMA hi=absc(lvmin(temp)+point-1)
*mess $SIGMA(vsum(pr)/vsum(hist)) $SIGMA(absc(lvmax(hist))) \\
$SIGMA(low) $SIGMA(hi)
SIGMA sq=pr*absc
devia=$SIGMA(vsum(sq)/vsum(hist))-$SIGMA(vsum(pr)/vsum(hist))* \\
$SIGMA(vsum(pr)/vsum(hist))
v/inp val $SIGMA(vsum(pr)/vsum(hist))  $SIGMA(low) $SIGMA(hi) \\
$SIGMA(sqrt([devia]))
return
```

Files called by the program listed above: “fillh1.f”, “fillh2.f”, “diff.f”:

“fillh1.f”:

```
      REAL FUNCTION fillh1(nch)
      include ?
      VECTOR chan
      INTEGER nch, I

      DO I=1, nch
         IF (missm_v .ge. chan(I) .and. missm_v .lt. chan(I+1))THEN
      CALL HF1(22+I,miss_m,NUMER_WT)
* In 'model independent' procedure, the previous line is replaced by
*      CALL HF1(22+I,miss_m,NUMER_WT/SIGMA)
         ENDIF
      ENDDO

      fillh1=1.
      END
```

“fillh2.f”:

```
      REAL FUNCTION fillh2(nch)
```

```
include ?
REAL Q2_V

VECTOR chan
INTEGER nch, K

Q2_V=(qmag_v**2-omega_v**2)/1000000.

DO K=1, nch
   IF (missm_v .ge. chan(K) .and. missm_v .lt. chan(K+1))THEN
   IF (miss_m .ge. chan(K) .and. miss_m .lt. chan(K+1))THEN

CALL HF1(1000+K*10,OMEGA_V,NUMER_WT/SIGMA)
CALL HF1(1001+K*10,Q2_V,NUMER_WT/SIGMA)
CALL HF1(1002+K*10,PRMAG_V,NUMER_WT/SIGMA)
CALL HF1(1003+K*10,MISSM_V,NUMER_WT/SIGMA)

   ENDIF
   ENDIF
ENDDO

fillh2=1.
END
```

"diff.f":

```
real function diff()
call hdiff(60,61,diff,' ')
if(diff .le. 1.)then
else
   diff=0.
endif
end
```

Appendix B

MySQL database

B.1 Filling MySQL database with scaler readouts

This section describes several of the most useful Perl programs written for filling the MySQL database with scaler readouts (Sec. 4.6). At the end of each run, readouts from 304 scalers were appended to file "scaler_history_e89044.dat". A MySQL table filled with the end-of-run scaler readouts for all E89044 runs was created in three steps. First, the MySQL table was created (Sec B.1.1). Then, the file "scaler_history_e89044.dat" was preformatted (Sec. B.1.2). Finally, a Perl script read the preformatted file and entered the scaler values into the created MySQL table (Sec. B.1.3).

B.1.1 Creating table with scaler columns

The order of scaler readouts in the file "scaler_history_e89044.dat" is the same as the order of the scaler names in the electron and hadron spectrometer scaler configuration files (named "scaler.config"). These files were first edited to produce a file containing a scaler name on each line. Then, MySQL table "scaler" with a single column "run" was created and the 304 scaler columns were added to the table by the following Perl script:

```
#! /usr/bin/perl
use DBI;
my ($dsn) = "DBI:mysql:data:localhost"; # data source name
my ($user_name) = "root";  # user name
my ($password) = "passw"; # password
my ($dbh, $sth);           # database and statement handles
my (@ary);                 # array for rows returned by query
# connect to database
$dbh = DBI->connect ($dsn, $user_name, $password, { RaiseError => 1 });

open (FILE, "sc_columns_mod");
while(<FILE>){
# issue query
    if ($_=~/^o/){
        $n++;
        $_="em"."$n";
    }
    $sth = $dbh->prepare ("alter table scaler add $_ int");
    $sth->execute ();
    $sth->finish ();
}
$dbh->disconnect ();
```

Within the program listed above names “o” (preassigned to unused scalers) are renamed to the names “emN”, where index N counts unused scalers.

B.1.2 Reformatting scaler_history file

The file “scaler_history_e89044.dat” contained some auxiliary information not relating to the scaler readouts. This information was fitered out by the following Perl script:

```
#! /usr/bin/perl
while (<STDIN>){
  if ($_=~/^[-]?\d+$/){print;}
  if ($_=~/number (\d{4})/){print "$1\n";}
}
```

This script filters through lines that contain only numbers (the scaler values) and substitutes lines mentioning a run number by the run number.

B.1.3 Filling the database

The following script read the file created as described in the previous section and entered the values in the MySQL database:

```
#! /usr/bin/perl
use DBI;
my ($dsn) = "DBI:mysql:data:localhost"; # data source name
my ($user_name) = "root";  # user name
my ($password) = "passw"; # password
my ($dbh, $sth);           # database and statement handles
my (@ary);                 # array for rows returned by query
# connect to database
$dbh = DBI->connect ($dsn, $user_name, $password, { RaiseError => 1 });

open (FILE, "sc_filter_out");
while(<FILE>){
# issue query
    if($n != 304){$arr[$n]="$_";
      $n++;}
    else {$arr[$n]="$_";
          $out=join ',',@arr;
          $sth = $dbh->prepare ("insert into scaler values($out)");
          $sth->execute ();
          $sth->finish ();
          $n=0;
    }
}
$dbh->disconnect ();
```

This script uses the fact that (in the E89044 setup) the number of scalers read out at the end of each run was exactly 304.

Appendix C

Trigger electronics block diagrams

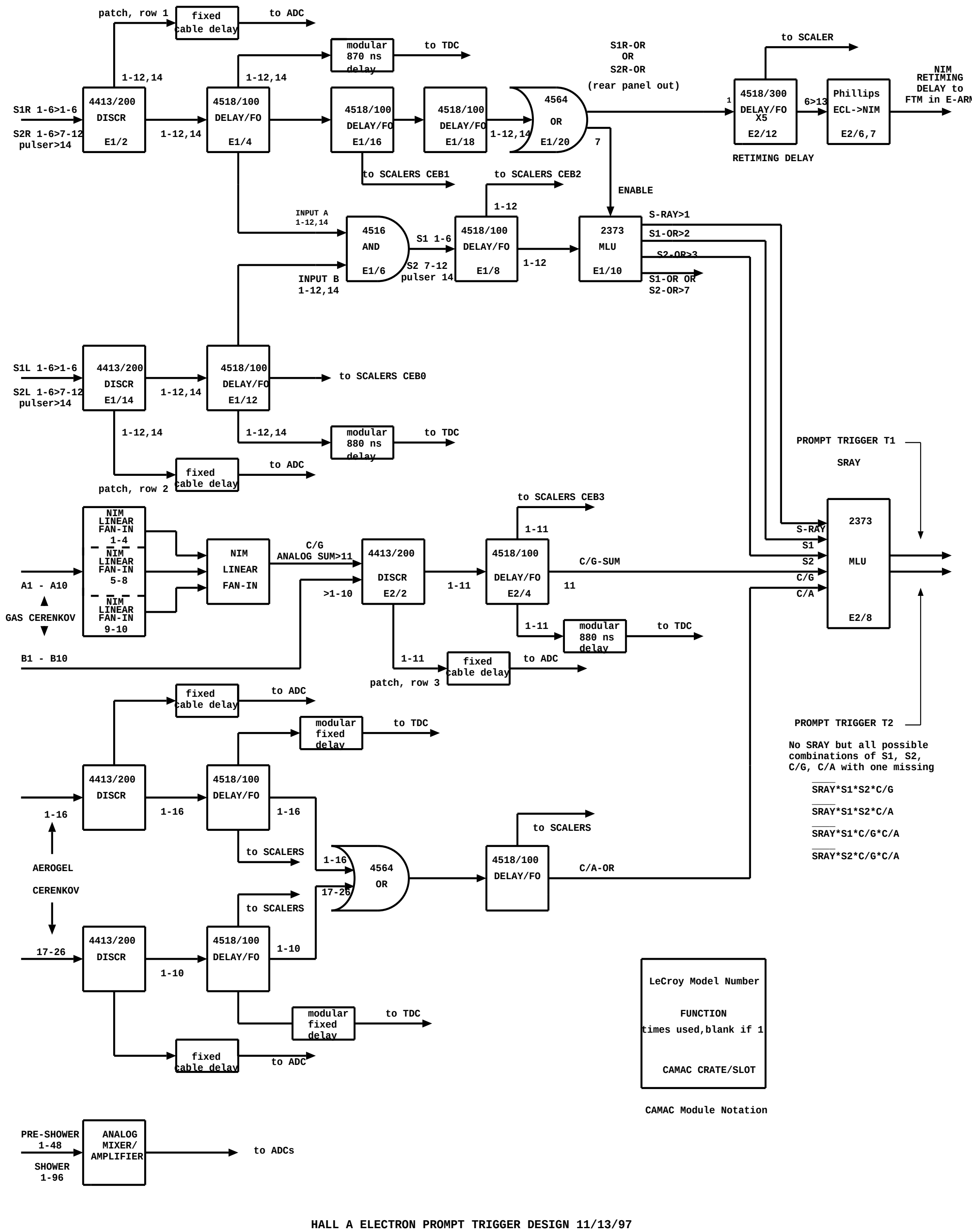

Figure C-1: Block diagram of setup of the electron singles trigger.

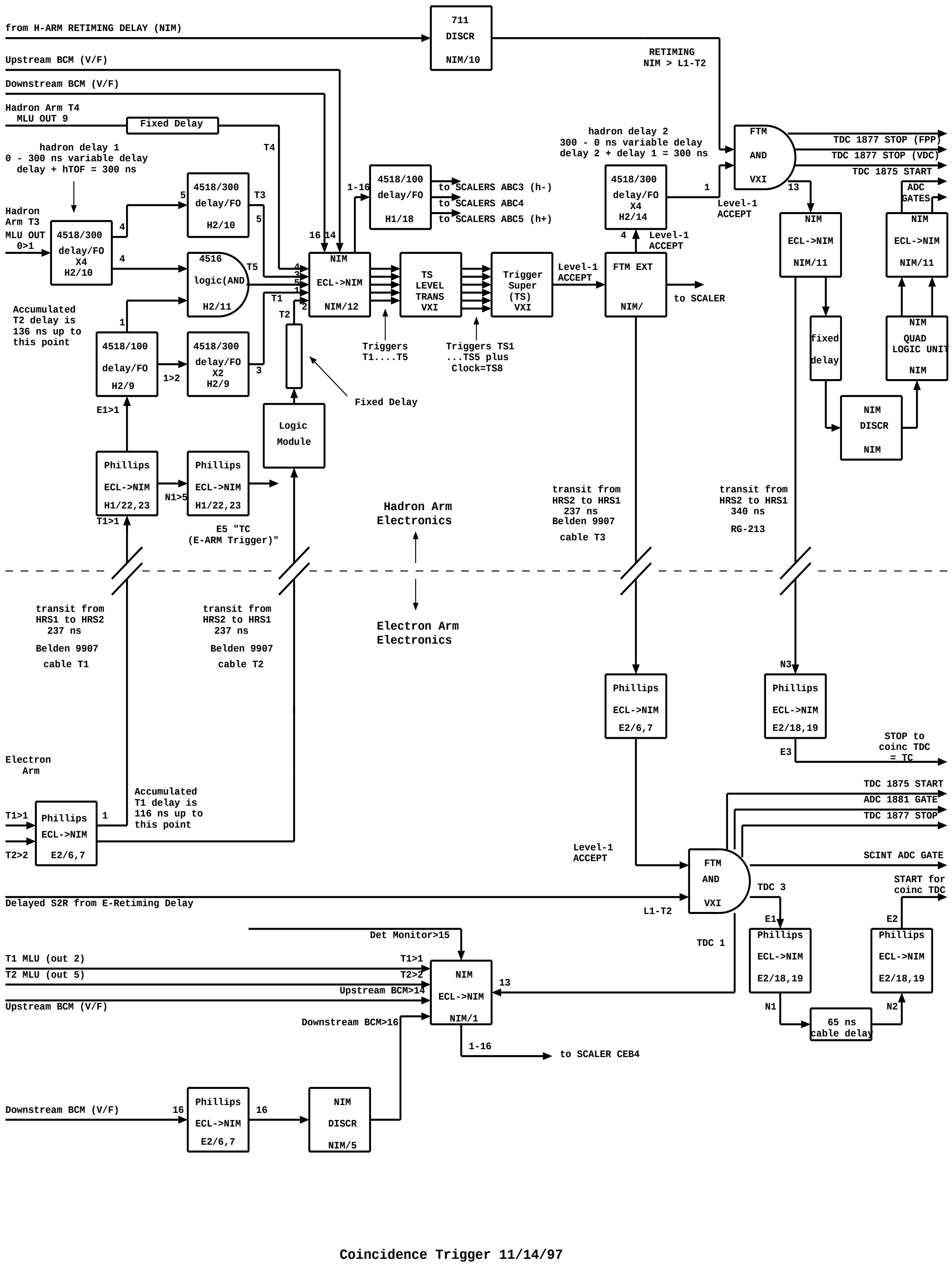

Figure C-2: Block diagram of coincidence circuit of the coincidence trigger.

Bibliography

[1] J. D. Walecka, *Electron Scattering for Nuclear and Nucleon Structure,* Cambridge Monographs on Particle Physics, Nuclear Physics and Cosmology, v. 16 (Cambridge University Press, 2001).

[2] J. J. Kelly, Adv. Nucl. Phys. **23**, 75 (1996).

[3] J. Carlson and R. Schiavilla, Rev. Mod. Phys. **70**, 743 (1998).

[4] S. Frullani and J. Mougey, Adv. Nucl. Phys. **14**, 1 (1984).

[5] J.-M. Laget, arxiv: nucl-th/0303052 (2003).

[6] J.-M. Laget, Nucl. Phys. A **579**, 333 (1994).

[7] R. J. Glauber and G. Matthiae, Nucl. Phys. **B21**, 135 (1970).

[8] J. Ryckebusch *et al.*, arxiv:nucl-th/0305066 (2003).

[9] J. Caballero *et al.*, arxiv: nucl-th/0211019 (2002).

[10] J. A. Caballero, T. W. Donnelly, E. Moya de Guerra, and J. M. Udias, Nucl. Phys. **A632**, 323 (1998).

[11] J. Udias and J. R. Vignote, Phys. Rev. C **62**, 034302 (2000).

[12] F. Benmokhtar, PhD thesis, Rutgers University, in preparation.

[13] E. Penel, PhD thesis, LPSC, Grenoble, France, in preparation.

[14] J. Heisenberg and H. P. Blok, Ann. Rev. Nucl. Part. Sci. **33**, 569 (1983).

[15] A. Johansson, Phys. Rev. **136**, B1030 (1964).

[16] V. A. Goldshtein, Nucl. Phys. **A392**, 457 (1983).

[17] E. Jans *et al.*, Phys. Rev. Lett. **49**, 974 (1982).

[18] P. H. M. Keizer *et al.*, Phys. Lett. **B197**, 29 (1987).

[19] C. Marchand *et al.*, Phys. Rev. Lett. **60**, 1703 (1988).

[20] J. E. Ducret *et al.*, Nucl. Phys. **A553**, 697 (1993).

[21] J. M. L. Goff *et al.*, Phys. Rev. C **55**, 1600 (1997).

[22] R. E. J. Florizone *et al.*, Phys. Rev. Lett. **83**, 2308 (1999), nucl-ex/9908004.

[23] B. F. Gibson and G. B. West, Nucl. Phys. B **1**, 349 (1967).

[24] R. E. J. Florizone, PhD thesis, MIT, 1999.

[25] T. de Forest, Jr., Nucl. Phys. **A392**, 232 (1983).

[26] J. Alcorn *et al.*, Nucl. Instrum. Methods Phys. Res. A (2003), "Basic instrumentation for Hall A at Jefferson Lab", to appear soon.

[27] Jefferson Lab and Hall A webpages, http://www.jlab.org/, http://hallaweb.jlab.org/.

[28] C. Hyde-Wright, L. Todor, and G. Laveissiere, Jefferson Lab Tech. Note 01-001, (2001).

[29] E. Offerman *et al.*, *ESPACE: Event Scanning Program for Hall A Collaboration Experiments, v. 2.9β*, 2000.

[30] A. Saha, private communication.

[31] http://hallaweb.jlab.org/equipment/targets.html.

[32] K. G. Fissum *et al.*, Nucl. Instrum. Methods Phys. Res. **A474**, 108 (2001).

[33] E. A. J. M. Offermann *et al.*, *The Hall A sextupole crisis: an evaluation of the magnitude of the problem and possilbe solutions*, 1995.

[34] M. Iodice *et al.*, Nucl. Instrum. Methods Phys. Res. **A411**, 223 (1998).

[35] N. Liyanage, Jefferson Lab Tech. Note 02-012, (2002), http://www.jlab.org/~nilanga/physics/optics.ps.

[36] N. Liyanage, PhD thesis, MIT, 1999.

[37] J. Gao, PhD thesis, MIT, 1999.

[38] N. Liyanage, private communication.

[39] http://coda.jlab.org/.

[40] http://hallaweb.jlab.org/equipment/daq/daq_trig.html.

[41] http://www-esd.fnal.gov/esd/catalog/intro/introfb.htm.

[42] http://www-esd.fnal.gov/esd/catalog/intro/introvme.htm.

[43] http://www.windriver.com/products/wxworks5/.

[44] http://www.aps.anl.gov/epics/.

[45] A. Kozlov, Scintillator trigger efficiency, in *Hall A data analysis workshop*, Jefferson Lab, 2001, http://hallaweb.jlab.org/data_reduc/AnaWork2001/kozlov/.

[46] P. Ulmer, private communication.

[47] R. Veenhof, *Garfield, a drift-chamber simulation program: User's Guide Version 5.18*, CERN, 1995, http://consult.cern.ch/writeup/garfield/.

[48] Z. Chai, PhD thesis, MIT, 2003.

[49] F. Benmokhtar *et al.*, *Spectrometer Setups*, Report to E89044 collaboration, (2000).

[50] M. Jones, *Report of Electronic Deadtime*, (2000), http://www.jlab.org/~jones/e91011/report_on_deadtime.ps.

[51] B. Povh, K. Rith, C. Scholz, and F. Zetsche, *Particles and Nuclei*, 2nd ed. (Springer-Verlag, 1999).

[52] A. Amroun *et al.*, Nucl. Phys. **A579**, 596 (1994).

[53] E. A. J. M. Offermann *et al.*, Phys. Rev. C **44**, 1096 (1991).

[54] C. R. Otterman *et al.*, Nucl. Phys. **A435**, 688 (1985).

[55] P. Ulmer, *MCEEP: Monte Carlo for Electro-Nuclear Coincidence Experiments, v.3.4*, 2000.

[56] W. Leo, *Techniques for Nuclear and Particle Physics Experiments* (Springer-Verlag, 1987).

[57] R. Sternheimer, M. Berger, and S. Seltzer, At. Data Nucl. Data Tables **30**, 261 (1984).

[58] J. S. Schwinger, Phys. Rev. **75**, 898 (1949).

[59] E. Borie and D. Drechsel, Nucl. Phys. **A167**, 369 (1971).

[60] J. A. Templon, C. E. Vellidis, R. E. J. Florizone, and A. J. Sarty, Phys. Rev. C **61**, 014607 (2000).

[61] Y. S. Tsai, Rev. Mod. Phys. **46**, 815 (1974), errata.

[62] G. R. Lynch and O. I. Dahl, Nucl. Instrum. Methods Phys. Res. **B58**, 6 (1991).

[63] J. LeRose, Forward transfer functions of Hall A spectrometers, (2002), http://hallaweb.jlab.org/news/minutes/tranferfuncs.html.

[64] V. L. Rvachev, *Theory of R-functions and Some Applications* (Naukova Dumka, Kiev, Ukraine, 1982), in Russian, 566 pp.

[65] V. L. Rvachev and T. I. Sheiko, Appl. Mech. Rev. **48(4)**, 151 (1995).

[66] V. L. Rvachev, T. I. Sheiko, V. Shapiro, and I. Tsukanov, Comp. Mech. **25**, 305 (2000).

[67] V. Shapiro, Technical Report, Cornell University, (1991), http://sal-cnc.me.wisc.edu/Research/meshless/R-functions/R-functions.html.

[68] M. M. Rvachev, Jefferson Lab Tech. Note 01-055, (2001).

[69] M. M. Rvachev, Geometrical acceptance through R-functions, in *Hall A data analysis workshop*, Jefferson Lab, 2001, http://hallaweb.jlab.org/data_reduc/AnaWork2001/marat_rfunc.html.

[70] V. A. Rvachev, Russian Math. Surveys **45**, 87 (1990).

[71] K. Avinash and V. L. Rvachev, Found. of Physics **30(1)**, 139 (2000).

[72] CERN, Geneva, Switzerland, *HBOOK Reference Manual, v.4.24*, 1995.

[73] CERN, Geneva, Switzerland, *PAW: Physics Analysis Workstation, An Introductory Tutorial*, 1995.

[74] T. W. Donnelly and A. S. Raskin, Ann. Phys. **169**, 247 (1986).

[75] A. S. Raskin and T. W. Donnelly, Ann. Phys. **191**, 78 (1989).

[76] A. Picklesimer, J. W. V. Orden, and S. J. Wallace, Phys. Rev. C **32**, 1312 (1985).

[77] A. Kievsky, E. Pace, G. Salme, and M. Viviani, Phys. Rev. C **56**, 64 (1997).

[78] J.-M. Laget, private communication.

[79] J. Udias *et al.*, Phys. Rev. C **48**, 2731 (1993).

[80] K. Fissum and P. Ulmer, Jefferson Lab Tech. Note 02-015, (2002).

[81] C. Ciofi degli Atti and L. P. Kaptari, private communication.

[82] J. M. Udias and J. R. Vignote, private communication.

Acknowledgments

My graduate studies in the US, all in all, have been a great experience. I would like to express my gratitude to everyone who has made it very enjoyable and educational. I apologize for unintentionally omitting anyone.

I've been lucky to have Prof. Bill Bertozzi as my research and thesis supervisor. Bill's deep practical knowledge of physics, enthusiastic attitude and care for students were inspirational throughout my time with the Nuclear Interactions Group at MIT. I would like to thank Bill for that, for tremendously helpful advice and guidance throughout the research, and for reading and correcting the thesis. I also would like to thank Norma Bertozzi for her hospitality.

I would like to thank Shalev Gilad for his additional supervision of my work, active participation in the analysis and valuable advice. I thank everyone in the Hall A collaboration for making the E89044 experiment a success. The experiment has been a highly collective effort, made possible by an outstanding work of the Hall A staff, JLab staff, and the many contributors from universities. I would like to thank the whole team of original, past and present spokespersons for the experiment, Marty Epstein, Jean Mougey, Robert Lourie, Arun Saha, Michael Kuss and Eric Voutier, for their excellent planning and efforts in upholding the experiment. I would like to thank my fellow PhD students Fatiha Benmokhtar and Emilie Penel for a fruitful and pleasant collaboration.

I thank Douglas Higinbotham for being of extraordinary help in my research. Doug has been invaluable on great many occasions, from troubleshooting the analysis to coding the ^{3}He elastic form factors in the simulation code and maintaining the MySQL database. I thank Arun Saha and Joe Mitchell for the beam energy measurements. I thank Michael Kuss for implementing the "burst mode" readout of the beam position in ESPACE, for maintaining the ^{3}He target, and for providing a cheerful spirit to the experiment. I thank Jean Mougey for sharing his deep expertise with me and for his huge contributions to the planning and analysis of the experiment.

I thank George Chang for calculating the effects of changes in the target density on the resolution and for the simulation of the proton absorption. I thank Mark Jones and Bob Michaels for their measurement of the electronic deadtime. I thank Paul Ulmer for developing the simulation code MCEEP and for being always available to discuss the code and techniques of data analysis in general. I thank Jeff Templon for the excellent treatment of the radiation in MCEEP. I thank Kevin Fissum for writing the "systerr" code, for his contributions to planning the experiment, for teaching me how to handle the wire chambers, and for being a good friend and officemate at the Trailer City at JLab. I thank Nilanga Liyanage and Zhengwei Chai for calibrating the optics databases, and for being good friends. I thank Nilanga for teaching me the calibration procedures during Zhengwei's and my calibration of the databases for the E94010 experiment.

I thank Konrad Aniol, Dimitri Margaziotis, Marty Epstein and the CalState L. A. group for constructing the ^{3}He target. I thank the JLab team of experts (Paul Brindza and others) for developing the target gas system. I thank Konrad for his planning of the luminosity monitoring scheme and the elastic scattering measurements, and for his analysis of the target performance. I thank the core analysis team, Fatiha, Emilie, Marty, Arun, Doug and Eric for the weekly conference calls that powered the progress of the analysis. I thank Marty for providing a deep level of thinking and reflection, for his efforts at improving the analysis, and for sharing his comprehensive expertise.

My deep appreciation goes to Jean-Marc Laget, C. Ciofi degli Atti, L. M. Kaptari, Javier Vignote and J. M. Udias for the theoretical calculations without which the thesis would not be complete. I would like to thank Mark Jones, Xiaodong Jiang, Bob Michaels, John LeRose and Bogdan Wojtsekhowski for introducing me to the Hall A operation and the experimental techniques. Indeed, my understanding of Hall A is rooted in lunchtime discussions with Mark, Xiaodong, Bob, John, Bogdan and many others at the JLab cafeteria. Just in my first two weeks at Hall A, Bob made me feel like an expert in the data acquisition system. Mark was the source of truly expert advice which I'm sure I wouldn't have gotten anywhere else.

I would like to thank my colleagues at the Nuclear Interactions Group at MIT, Simon Sirca, Riad Suleiman, Juncai Gao, Nilanga Liyanage, Peter Monaghan, Xiaochao Zheng, Zhengwei Chai, Alexander Skabelin, Yuan Xiao, Doug Higinbotham, Zilu Zhou and Bin Zhang for friendship and a productive working environment.

I would like to thank the cheerful gang of JLab grad students, Hovanes, Pibero, Jose, Agus, Hovanes II, Hovanes III, Gagik, Carlos, Fefo, Jordi, Paolo, Pibero, Rikki, Olivier, Antonin, Julie, Emilie, Fatiha, Kevin, Antoine, Jason, Bin, Xiaochao, Zhengwei, Peter and others for friendship and for the great times we spent together.

I would like to thank my MIT and Harvard friends, Konstantin Anikeev, Alexander Rakitin, Sergei Dzhosyuk, Sergei Bashinskii, Oleg, Tatiana, Alexey and Andrew Shpyrko, Igor Shpyrko, Alexander Skabelin, Kristjan Gulbrandsen, Dmitri Pouchine, Maria Springer, Alexander Demurov, Ilia Sigalov, Michael Slutsky, Boris Iyutin, Mikhail Voropaev, Alexander and Yelena Rabiner, Alexander and Olga Shirokov, Wang Xu, Feng Xiong and Olexei Motrunich, and friends at other universities, Alexander Tumanov, Peter Puzynia, Akakii Melikidze, Alexey Sedov, Igor Lugach, Sergei and Olga Zalyubovsky, Vadim Stakhurskii, Sergei Dobrovolskii, Ilia Lebenedko and others for friendship and the good times we had in the US, Moscow and Vinnitsa. I would like to thank MIT for providing a pleasant and challenging intellectual environment, and for excellent classes. I thank Joanne Gregory, Elsye Luc, Sheela Hulsoor and Lauren Saragosa for organizational help.

I thank Prof. Bill Donnelly and Prof. Aron Bernstein for serving on my thesis committee and for providing very valuable comments.

I especially thank my high school math and physics teachers, Viacheslav Andreyevich Yasinsky and Dmitrii Mikhailovich Vlasov, for superb teaching and a great jump-start to science that they gave me.

My deepest gratitude goes to my parents, Michael and Lila Rvachov, to my brothers Alex and Timur, to all my relatives and to Julia for everything they have done for me. I also thank Julia for love, understanding and help that carried me through the writing.